UNIVERSITÉ DE GENÈVE
Département de physique nucléaire et corpusculaire

FACULTÉ DES SCIENCES
Professeur Allan CLARK

Measurement of the Inclusive b-jet cross section in $p\bar{p}$ collisions at CDF RunII

and

Development of silicon microstrip detectors for the ATLAS Silicon Tracker

THÈSE

présentée à la Faculté des sciences de l'Université de Genève
pour obtenir le grade de Docteur ès sciences, mention physique

par

Monica D'Onofrio
d' Italie

Thèse N° 3673

GENÈVE
Atelier de reproduction de la Section de physique
2005

Contents

Abstract

In the past twenty years, the study of events with bottom quark has led to many important Tevatron results – as the discovery of the top quark – and it will be as well crucial at the LHC for the search of new physics phenomena.
In particular, measurements of the beauty production cross section at hadron colliders provide an important quantitative test of strong interaction dynamics as foreseen in the Standard Model. The publication of "controversial" results on this topic, *i.e.* by CDF and DØ in RunI, has led to many developments in the theoretical calculations, but also in the experimental approach, resulting in a better agreement between data and theory. Up to now, CDF measurements have mainly considered B-hadrons: in this thesis work we instead make use of jets, to explore a wider energy range and thus extend current knowledge of bottom production. The present measurement of the b-jet cross section is based on about 300 pb^{-1} of data, collected by the CDF experiment from February 2002 to September 2004. A cone-based iterative MidPoint algorithm is used for jet reconstruction; the jet energy scale is corrected to compensate for energy losses at calorimeter level, in order to have a final experiment-independent measurement. The analysis exploits the good tracking capabilities of the detector and relies on b-jet identification made by secondary vertex reconstruction.
The measured cross section covers a range in transverse momentum between 38 and 400 GeV/c and it extends for more than 6 order of magnitudes, thus dramatically improving previous hadron collider results. A first comparison with one of the existing theoretical calculations implemented for b-jet production, shows an agreement within $\pm 1\sigma$ between data and theory. Nevertheless, the large theoretical uncertainties could be an indication of a major role played by not-included higher order contributions; thus a Next-to-Leading Order perturbative QCD calculation might not be considered conclusive for theoretical comparison with high-P_T b-jets production cross section.

The new generation of hadron collider experiments, for example ATLAS, obviously takes advantage of the knowledge developed at the Tevatron, for instance concerning the techniques and the tools used for b-jet identification. In this sense, the study of the Inner Tracker system performance and in particular of the Semi Conductor Tracker (SCT), can be considered one of the fundamental issues in the construction of the apparatus. The second part of this thesis work reports some of the crucial tests performed during the development of the silicon microstrip detectors composing the SCT.
The Semi Conductor Tracker consists of four cylindrical barrel layers of silicon strip detectors and of 18 disks in the forward and backward direction. Four different module designs

exist, one for the barrel and three (inner, middle and outer) for the rings of the disks. LHC operating conditions result in very challenging performance specifications for the SCT modules and the limitations mainly concern the accepted noise and noise occupancy level, the tracking efficiency, the timing and the power consumption. A series of several end-cap module pre-production prototypes have been built and extensively tested on single module test benches as well as on beam tests. In particular, the electrical performance measurements made on these end-cap module pre-production prototypes are summarised here, with special emphasis on the results of electrical tests after irradiation and on test beam analysis. The present work has led to the definition of a final forward module design (K5), judged satisfactory by the SCT collaboration to pursue the real module production. In addition, an alternative module layout (KB) has been studied: a functional design of this kind provided the SCT with a viable back-up solution in case the development of a fully functional baseline module had not been achieved.

Résumé

Ce travail de thèse est composé de deux parties. Après une brève introduction théorique, la première partie décrit les mesures de section efficace de production de jets b dans des collisions $p\bar{p}$ de $\sqrt{s} = 1.96$ TeV dans le centre de masse, réalisées par l'expérience CDF. Le détecteur CDF et ses divers composants sont d'abord présentés, puis la stratégie d'analyse utilisée est expliquée en détail. La mesure est basée sur environ 300 pb^{-1} de données, collectées entre février 2002 et septembre 2004. L'analyse utilise des jets dans la région de rapidité centrale ($|\mathrm{Y}| < 0.7$) reconstruits avec l'algorithme "MidPoint" pour des impulsions transverses P_T^{jet} allant jusqu'à 400 GeV, et exploite les bonnes capacités de reconstruction de traces du détecteur CDF pour identifier les jets b en reconstruisant le vertex secondaire avec l'algorithme SecVtx. Les résultats obtenus sont conparés avec les prédictions théoriques.

La deuxième partie de ce travail commence par la description de l'expérience ATLAS (A Toroidal LHC Apparatus) au collisionneur LHC (Large Hadron Collider), avec un intérêt particulier porté au détecteur à micro-pistes de silicium SCT. Les tests électriques extensifs réalisés dans la phase de développement des modules destinés à équiper les disques (modules "forward") sont présentés. Ces nombreux tests ont été réalisés, aussi bien sur des modules irradiés que non irradiés, sur des bancs de tests en laboratoire aussi bien qu'en tests faisceau. Ce travail a abouti, après des études détaillées de plusieurs prototypes successifs, à l'élaboration d'une version satisfaisante de ces modules forward (K5), ainsi qu'au développement d'une solution alternative à la version officielle (module KB) parfaitement fonctionnelle. Ces modules, partie intégrante du détecteur de traces interne d'ATLAS, sont essentiels pour la détection des particules contenant des quarks b, dont la connaissance est cruciale à de nombreux égards dans l'étude de la physique du modèle standard et au-delà.

Introduction théorique

Le Modèle Standard (SM) des interactions électro-faibles et fortes décrit les interactions entre les particules élémentaires en utilisant la théorie quantique des champs. Jusqu'à présent, le Modèle Standard a connu un succès remarquable par ces prédictions, qui ont été vérifiées expérimentalement.

Les interactions sont basées sur le groupe de symétrie de jauge $SU(3)_C \otimes SU(2)_L \otimes U(1)_Y$, qui décrit les interactions électromagnétiques, faibles et fortes, par l'échange de champs de jauge. En particulier, la Chromodynamique Quantique est la théorie de jauge des interactions fortes : le groupe de couleur $SU(3)_C$ sur lequel cette théorie se fonde,

implique l'existence de 8 gluons, médiateurs de l'interaction. La portée de l'interaction forte est caractérisée par la constante de couplage forte α_s, qui décroît lorsque le module carré du quadri-moment d'impulsion $|Q^2|$ transférée lors de la collision augmente. Les sections efficaces de la QCD peuvent être approximées par des développements en série de α_s : si α_s est suffisamment petit, la théorie des perturbations est justifiée. L'énergie dans centre de masse au Tevatron est déjà suffisamment élevée pour permettre des mesures de précision des prédictions de QCD, et spécialement pour la production de quarks bottom. Les mesures de la section efficace de production des jets b fournissent ainsi un important test quantitatif de la QCD, puisque l'on s'attend à ce que les données soient correctement décrites par les calculs au second ordre ("next-to-leading order": NLO) en α_S.

L'expérience CDF au Tevatron

Le Tevatron est un collisionneur de type proton-antiproton situé au Fermi National Laboratory (FERMILAB) à Chicago (Etats-Unis). Son énergie dans le centre de masse est de $\sqrt{s} = 1.96$ TeV, ce qui en fait le collisionneur atteignant la plus haute énergie jusqu'à la mise en service du Large Hadron Collider (LHC).

CDF est l'une des deux expériences multifonctionnelles construites afin de permettre l'étude de collisions $p\bar{p}$ au Tevatron. C'est un détecteur cylindrique avec une symétrie avant-arrière, conçu pour couvrir le plus d'angle solide possible autour du point d'interaction. On utilise un système de coordonnées polaires où r est la distance mesurée à partir du point d'interaction, ϕ est l'angle azimutal se trouvant dans le plan perpendiculaire à la direction du faisceau, et θ est l'angle polaire qui définit la pseudorapidité $\eta = -\ln\tan\frac{\theta}{2}$.

En partant du point d'interaction, on peut identifier trois parties principales du détecteur:

- Les détecteurs de traces de particules chargées : Layer 00 (L00), le Silicon Vertex Detector (SVX II), l'Intermediate Silicon Layer (ISL) et le Central Outer Tracker (COT).
- Les calorimètres électromagnétiques et hadroniques.
- Les chambres à muons : le Central Muon Detector (CMU), le Central Muon Upgrade (CMP) et le Central Muon Extension (CMX).

Le détecteur de vertex au silicium est la première couche cylindrique autour du tube à vide du Tevatron. Il est composé de L00, SVX et ISL. Il s'agit de détecteurs à bandes ou "microstrips" au silicium. L00, étant à 1.35 cm, est la couche la plus proche du point d'interaction. Le SVX est composé de trois cylindres de 29 cm de longueur, qui – montés ensemble – mesurent au total 96 cm. Chaque cylindre est divisé en douze sections azimutales de 30^o, chacune contenant cinq couches de détecteurs au silicium, qui mesurent la position des traces dans le plan $r-\phi$. Le SVX permet la reconstruction précise des points d'interaction secondaires des particules avec un court temps de vie, comme les particules B. Il mesure le paramètre d'impact avec une précision allant jusqu'à 40 μm lorsqu'on inclut

les signaux provenant du L00. Le ISL qui se trouve entre le SVX et le COT prolonge la couverture des détecteurs au silicium à des valeurs de pseudorapidité allant jusqu'à 2.0.

Le COT est une chambre à dérive de 310 cm de long avec un rayon intérieur de 44 cm et un rayon extérieur de 132 cm. Elle est composée de 96 couches alternant des fils de mesure axiaux et stéréo. Le COT est capable de reconstruire les traces des particules dans la région de $|\eta| < 1.0$ avec une impulsion transverse supérieure à 400 MeV/c. Les détecteurs de traces se trouvent à l'intérieur du champ magnétique de 1.4 T produit par un aimant solénoïdal placé autour d'eux.

Le système de calorimétrie est évidemment fondamental pour la reconstruction des jets. Il est composé d'une partie électromagnétique et d'un partie hadronique, basées toutes deux sur la technologie des scintillateurs, et il mesure le passage des particules avec $|\eta| < 3.64$. Les chambres à muons sont situées à l'extérieur des calorimètres électromagnétiques et hadroniques. Dans la région centrale ($|\eta| < 0.6$) le CMU est constitué de quatre couches de chambres à dérive. Derrière 60 cm d'acier additionnels se trouvent les quatre plans de chambres à dérive du CMP. La couverture des chambres à muons est complétée par le CMX qui couvre la région $0.6 < |\eta| < 1.0$. Les chambres à muons incluent aussi des scintillateurs qui permettent de mesurer avec précision le temps exact de passage de la particule.

Enfin, le système de déclenchement est composé de trois niveaux consécutifs, chacun diminuant le nombre d'événements d'un ou deux ordres de grandeur.

Section efficace inclusive de jets b à CDF

L'utilisation de jets pour la production de quark b dépasse la limite atteinte par les mesures précédentes, qui utilisaient les désintégrations exclusives de hadrons B, et permet ainsi d'explorer une large gamme d'impulsions transverses. De plus, on s'attend à ce que les corrections dues aux effets de fragmentation auxquels les calculs théoriques sont sensibles, soient petits pour les jets.

La mesure de la section efficace différentielle de jets b se fonde sur environ 300 pb^{-1} de données, collectées entre février 2002 et septembre 2004. L'analyse utilise des jets dans la région de rapidité centrale ($|\mathrm{Y}| < 0.7$) et considère des impulsions transverses allant jusqu'à 400 GeV/c. Les jets sont des flots de hadrons dans les processus de diffusion dure; c'est-à-dire que pour calculer les sections efficaces des jets en utilisant la QCD perturbative, la définition des jets doit satisfaire à de fortes contraintes pour garantir la validité de la théorie des perturbations. Ceci signifie que la définition doit être indemne de divergences infrarouges (les propriétés des jets ne peuvent pas dépendre de la présence de partons arbitrairement "mous"), d'anomalies collinéaires (les propriétés des jets ne peuvent pas changer lorsqu'on remplace un parton par un ensemble de partons collinéaires portant la même impulsion totale), et collinéairement factorisables (les propriétés des jets devraient être insensibles aux partons émis collinéairement à la direction du faisceau).

Expérimentalement, l'algorithme MidPoint remplit ces conditions, et est donc utilisé pour reconstruire les jets. L'algorithme MidPoint est une procédure basée sur un cône qui utilisent les signaux du calorimètre comme germes pour reconstruire les agrégats, puis

ensuite les jets; son nom provient du fait qu'il place explicitement un autre germe à un point milieu en énergie, entre deux germes quelconques.

La rapidité Y et l'angle azimuthal ϕ sont utilisés comme position du jet lorsqu'est calculée sa séparation des autres particules ou autres jets, alors que l'énergie du jet est définie en terme d'impulsion transverse P_T.

Les échantillons de base pour l'analyse sont les cinq ensembles de données avec jets nommés Single Tower 05 (ST05), Jet20, Jet50, Jet70, Jet100, où les nombres 20,50..... désignent les seuils du déclencheur sur l'énergie transverse du jet.

Le comportement de chaque échantillon a été étudié afin de définir un seuil et ainsi un intervalle d'impulsion transverse P_T des jets pour lequel les effets dus à l'inefficacité du déclencheur peuvent être négligés. Ainsi, la sélection des événements requiert des jets au dessus d'un tel seuil en $P_T^{\rm jet}$, en plus d'autres exigences pour rejeter les rayons cosmiques et le bruit de fond.

L'impulsion transverse des jets mesurée est par définition biaisée par les effets du détecteur (pertes en calorimétrie, efficacité finie du détecteur, effets de lissage dus à la résolution finie du détecteur). Ces jets sont communément appelés jets calorimétriques, et ils dépendent de façon évidente de l'expérience. Lorsque l'on compare les sections efficaces ou d'autres résultats de mesures avec les prédictons théoriques, les jets impliqués sont reconstruits en utilisant les particules stables (hadrons) ou les partons. Les jets calorimétriques doivent alors être corrigés des effets du détecteur.

La procédure pour trouver la correction moyenne utilise la simulation. Dans les échantillons Monte Carlo (on a utilisé principalement les jets de Monte Carlo de Pythia Version A), pour former des jets au niveau hadronique, on utilise les informations provenant des particules stables et on implémente le même algorithme "MidPoint": ces jets peuvent être comparés à ceux reconstruits avec les informations fournies par le calorimètre. En effectuant un ajustement dans l'espace Y-ϕ entre les jets hadroniques et calorimétriques, on trouve la corrélation, et une fonction de correction est extraite dans la gamme complète de P_T: l'effet est de l'ordre de 15-20% à basse impulsion transverse P_T et décroît jusqu'à 10% pour les bas P_T.

Une fois les jets reconstruits et corrigés, il est nécessaire d'identifier les jets de saveur b (i.e. ceux contenant un hadron avec un quark bottom). L'une des techniques développées à cette fin tire partie de la longue durée de vie des hadrons B. Le temps de vie moyen est de l'ordre de 1.5 ps, et la distance propre $c\tau$ est donc d'environ 450 μm: en considérant l'important boost relativiste des événements pris en compte, le hadron B parcourt une distance de l'ordre de quelques millimètres avant de se désintégrer. Les produits de désintégration proviennent alors d'un vertex secondaire, déplacé par rapport au point d'interaction primaire.

La totalité des trajectoires des produits de désintégration ne peut pas être reconstruite à cause de la présence de particules neutres ou de la complexité considérable des états finaux. Néanmoins, il est possible d'utiliser des techniques plus inclusives, qui exploitent les performances du détecteur silicium de vertex pour distinguer entre les traces qui dérivent d'un vertex primaire et celles qui proviennent de traces déplacées. L'algorithme SecVtx,

utilisé dans la présente analyse, applique une sélection sur le paramètre d'impact des traces et reconstruit un vertex secondaire à partir des traces sélectionnées.

L'efficacité de reconnaissance des b est alors définie comme la fraction de jets b identifiés par rapport à tous les jets b pour chaque intervalle $P_T^{\rm jet}$ donné. Puisqu'il n'est pas possible de la mesurer directement avec les échantillons de données de jets, l'algorithme Monte Carlo est utilisé pour décrire la dépendance en énergie et l'acceptance géométrique de la reconnaissance, et un facteur d'échelle, mesuré dans un large échantillon indépendant ayant un contenu en saveur lourde important, est déterminé pour prendre en compte les imperfections dans les simulations (i.e. la différence dans l'efficacité d'identification des traces et la résolution, les incertitudes des modèles de désintégration des hadrons B, etc...) L'efficacité de reconnaissance des b obtenue est autour de 45% pour des valeurs basses et intermédiaires de P_T, et elle décroît jusqu'à 30% pour des valeurs élevées de P_T.

Un aspect négatif d'une telle procédure réside dans le fait que les hadrons charmés sont aussi caractérisés par un parcours propre intermédiaire ($c\tau \simeq 200$ μm), et il est donc difficile de distinguer les hadrons b des hadrons c. De plus, les jets légèrs peuvent aussi être incorrectement identifiés. Il est alors nécessaire d'extraire le contenu en saveur b des jets sélectionnés. La technique adoptée dans l'analyse présentée ici considère la forme de la masse invariante des traces utilisées pour trouver le vertex secondaire, comme quantité discriminatrice. Bien qu'une reconstruction complète de la masse invariante des hadrons ne soit pas possible à cause de la présence de particules neutres et de pertes d'énergie dues à la résolution en énergie du détecteur, la masse du vertex secondaire est plus dure pour les jets b que pour les jets c, ou les jets legèrs. Les distributions fournies par les données sont interpolées par une combinaison linéaire des deux composantes (jets b et non b). Les figures 1 (à gauche) montrent la distribution en masse du vertex secondaire telle qu'extraite des données, comparée à la prédiction, ainsi que les schémas-types pour les masses b et non b, normalisés à la fraction provenant du fit, pour un intervalle en P_T. Ce fit est en fait réalisé en considérant indépendemment chaque intervalle de P_T des jets, et la figure 1 (à droite) montre la fraction de jets b identifiés dans la gamma complète de P_T: les erreurs statistiques et l'erreur systématique totale sont indiquées.

La section différentielle des jets b au niveau des particules est

$$\left.\frac{d^2\sigma_{\rm b-jet}}{dp_T dY}\right|_i = \frac{N^i_{\rm tagged} f^i_b C^i_{\rm unfold}}{\epsilon^i_{\rm b-tag} \Delta Y \ \Delta p^i_T \int \mathcal{L}}$$

pour chaque intervalle d'impulsion transverse du jet, où $N^i_{\rm tagged}$ est le nombre de jets identifiées en utilisant l'algorithme d'identification des jets b; f^i_b est la fraction de jets b parmi les jets identifiés extraits des données: $\epsilon^i_{\rm b-tag}$ est l'efficacité de reconnaissance des b ($= \epsilon^i_{\rm b-tag\,MC} \times$ SF). $C^i_{\rm unfold}$ est le facteur de correction spécifique aux jets b pour chaque intervalle. ΔY est l'intervalle de rapidité des jets; Δp^i_T est la taille de l'intervalle d'impulsion transverse du jet; $\int \mathcal{L}$ est la luminosité intégrée définie pour chaque ensemble de données.
Les facteurs de correction additionnels $C^i_{\rm unfold}$ sont nécessaires car la procédure pour trouver les corrections moyennes pour les jets a été implémentée seulement pour des événements avec des jets positivement identifiés; tous les jets identifiés ne contiennent pas un quark b,

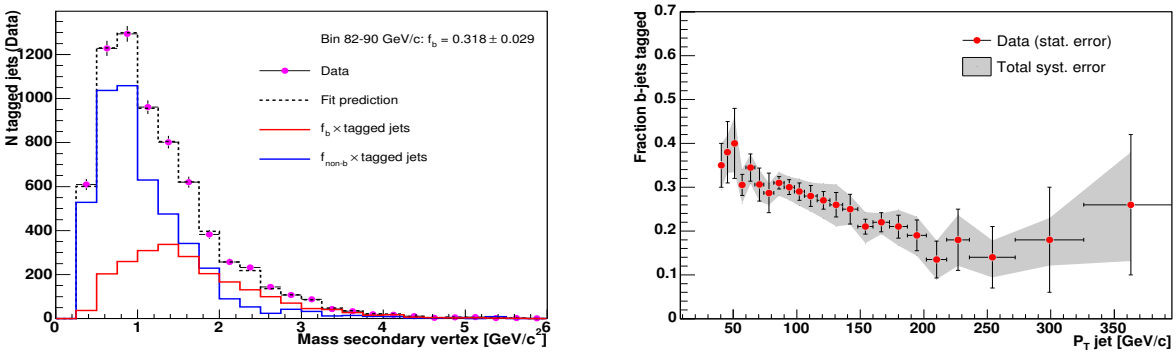

Figure 1: A gauche: distribution en masse des vertex secondaires extraite des données, et superposée à la courbe prédite par les "patrons" Monte Carlo pour les jets b et non b, pour des intervalles en P_T de 82-90 GeV/c. A droite: fraction des jets b identifiées dans les données, en fonction de l'impulsion transverse P_T de la jet: l'erreur totale du fit est indiquée, et les erreurs totales systématiques sont superposées.

et les différences entre les jets avec saveur b et les jets ordinaires doivent donc être prises en compte. Par ailleurs, C^i_{unfold} corrige la section efficace des effets de lissage dus à la résolution finie du détecteur; ces facteurs sont calculés intervalle par intervalle en comparant la section efficace des jets b au niveau calorimétrique et hadronique telle qu'elle est donnée par la simulation Monte Carlo.

La section efficace de jets b mesurée au niveau des particules est montrée figure 2 en fonction de l'impulsion transverses P_T corrigée dans la gamme allant de 38 à 400 GeV: les incertitudes systématiques sont superposées à la distribution.

Les sources principales d'erreur systématique proviennent de l'échelle d'énergie des jets et de la fraction de jets b identifiés. La section efficace est aussi comparée avec les prédictions au second ordre (NLO) pour la production de jets b (cf. aussi le rapport données/NLO de la figure 3). L'accord est bon pour des jets au dessous de 100 GeV/c, mais se dégrade pour des jets d'impulsions transverses plus élevées, bien que les incertitudes systématiques des données et de la théorie se recouvrent. La forte dépendance des prédictions théoriques en fonction du choix de renormalisation et d'échelle de factorisation montre que les contributions d'ordre supérieure, non incluses ici, pourraient jouer un rôle majeur. Pour cette raison, un calcul au second ordre de la théorie des perturbations en QCD ne devrait pas être considéré comme concluant dans la comparaison théorique avec la section efficace de production des jets b à haut P_T.

L'expérience ATLAS au LHC

Le projet LHC est un collisionneur pp qui est en cours de construction au Conseil Européen de Recherche Nucléaire (CERN). Il représente la prochaine étape dans l'évolution des accélérateurs à hautes énergies, ayant une énergie du centre de masse de $\sqrt{s} = 14$ TeV.

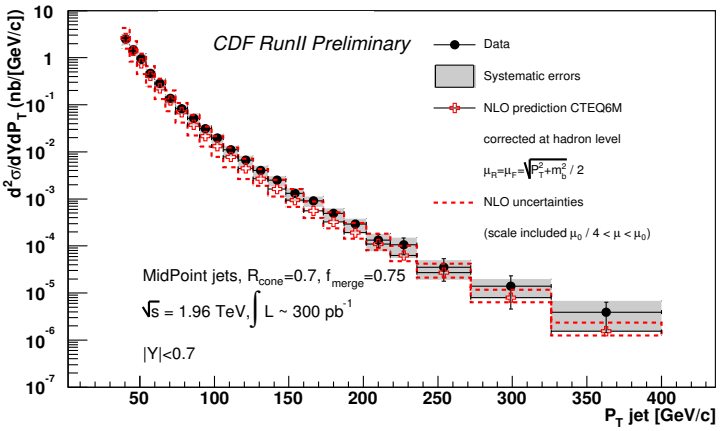

Figure 2: Section efficace différentielle mesurée: les calculs NLO sont superposés.

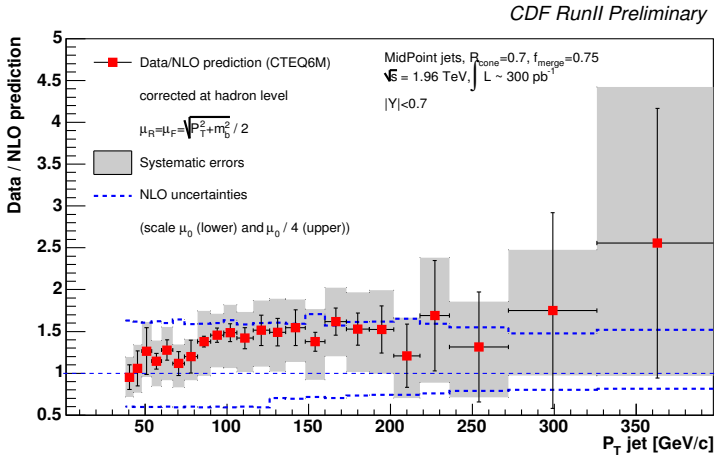

Figure 3: Rapport données/NLO: la bande grise représente les erreurs systématiques sur les données, les lignes bleues les incertitudes théoriques, incluant les dépendances d'échelle.

ATLAS, qui est un détecteur plurifonctionnel, a beaucoup de similitudes dans sa construction avec CDF. En partant de l'intérieur vers l'extérieur on trouve les composants suivants:

- Les détecteurs de traces de particules chargées (Inner Tracker): les détecteurs au silicium à pixels (Pixels), le Semiconductor Tracker (SCT) et le Transition Radiation Tracker (TRT).
- Les calorimètres électromagnétiques et hadroniques.
- Les chambres à muons.

La partie intérieure du Inner Tracker est constituée de détecteurs au silicium à pixels, arrangés en trois cylindres à des rayons de 5.05 cm, 8.85 cm et 12.25 cm, et de trois disques de chaque côté du détecteur central. Ces détecteurs fournissent une précision de 50 μm dans

le plan $r - \phi$ et de 400 μm le long de la direction du faisceau. De 30 cm à 52 cm du tube à vide contenant le faisceau se trouvent les quatre couches du SCT, ainsi que neuf disques de chaque côté du détecteur central. La partie cylindrique ("avant-arrière") du SCT est constitué de 2112 (1976) modules au silicium qui contiennent aussi l'électronique nécessaire pour la lecture de bandes de silicium. Les modules de la partie cylindrique mesurent le passage d'une particule avec une précision de 19 μm dans le plan $r - \phi$ et 700 μm le long de la direction du faisceau. L'élément extérieur du système de traceurs d'ATLAS est le TRT, une chambre à fils. La partie centrale contient 50000 fils, et les 36 disques des régions "avant-arrière" en contiennent 320000. Par rapport aux détecteurs au silicium la résolution est moindre (170 μm), mais cela est équilibré par le nombre important de points de mesure, typiquement 36 par trace. Le TRT permet la reconnaissance des électrons grâce à leur radiation de transition caractéristique (d'où le nom du détecteur). Entre les traceurs de particules et les calorimètres se trouve le solenoïde supraconducteur qui crée un champ magnétique de 2 T dans le volume des traceurs.

Les calorimètres, qui couvrent la région de $|\eta| < 3.2$, sont basés sur la technologie d'argon liquide et des tuiles de scintillateurs plastiques. Ils sont entourés par les chambres à muons qui occupent l'espace jusqu'à un rayon de 11 m et jusqu'à $\pm$23 m dans la direction du faisceau. Différentes technologies sont utilisées pour les chambres à muons remplissant différentes tâches. Des "Monitored Drift Tubes" et des "Cathode Strip Chambers" sont utilisés pour les mesures de précision, alors que pour les déclenchements des "Resistive Plate Chambers" et des "Thin Gap Chambers" sont prévus. ATLAS prévoit un système de déclenchement à trois niveaux, similaire à celui de CDF.

Développement du détecteur à micro-pistes de silicium SCT

Le détecteur à micro-pistes de silicium SCT est constitué de quatre cylindres concentriques et de 18 disques en fibre de carbone, équipé au total de 4088 modules.

Chaque module consiste en une paire de senseurs micro-pistes de silicium, collés dos à dos avec un angle stéréo de 40 mrad, et attachés à une partie électronique appelée "hybride". Ce dernier est constitué d'un circuit flexible cuivre-polyimide laminé sur un substrat carbone-carbone, et porte les puces de lecture.
De nombreux tests ont été réalisés dans la phase de développement des modules destinés à équiper les disques (modules "forward"). Les conditions d'opération extrêmes du LHC imposent des contraintes très exigeantes sur les performances électriques – notamment – de ces modules, en particulier sur le bruit, le niveau d'occupation en bruit, l'efficacité de reconstruction des traces, le temps de réponse et la consommation électrique. L'électronique de lecture des modules SCT étant binaire, le niveau d'occupation en bruit, au point d'opération (1 fC) est particulièrement important et il doit impérativement être significativement inférieur à l'occupation en signal, pour assurer que le taux de bruit n'affecte pas la transmission des données ni la reconstruction des traces. La limite prévue en niveau d'occupation en bruit de 5×10^{-4} impose que le niveau du discriminateur de l'électronique

frontale de lecture est fixé à 3.3 fois le rms en bruit.

Après des études détaillées de plusieurs prototypes successifs, on est arrivé à l'élaboration d'une version satisfaisante de ces modules forward (K5).

Les modules non irradiés sont bien en deça des spécifications, avec un niveau d'occupation en bruit qui n'excède pas 4×10^{-5}, et ce, dans le cas le plus défavorable des modules externes. La figure 4 montre un exemple de niveau d'occupation en bruit pour la face supérieure d'un module non irradié.

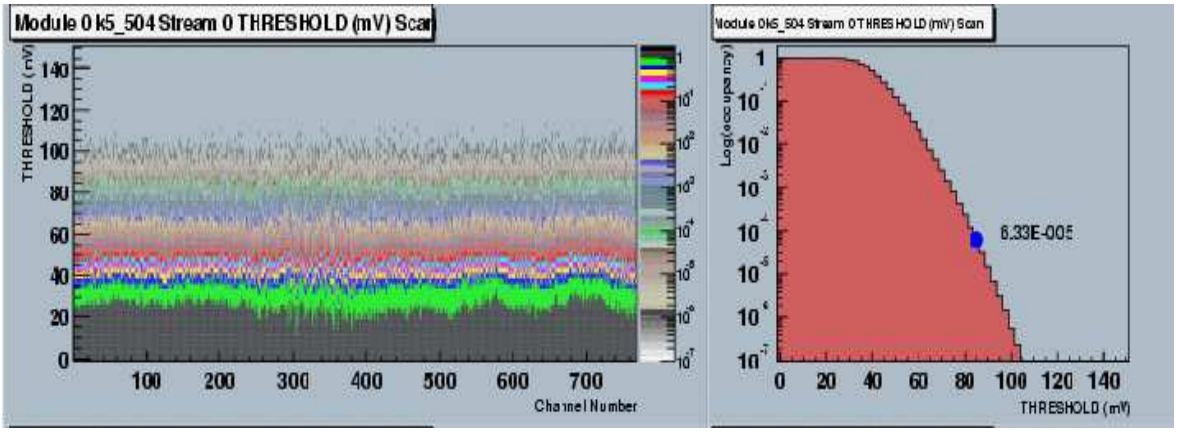

Figure 4: Example de niveau d'occupation en bruit pour la face supérieure d'un module non irradié: sur la gauche, est présentée la distribution bidimensionnelle de l'occupation en fonction du seuil par canaux, et sur la droite on peut voir la projection de l'occupation en bruit en échelle logarithmique pour la face complète, qui a bien la forme attendue. Le point indique le point de fonctionnement à 1 fC, tel qu'il est identifié par la procédure d'ajustement ("trimming").

Il est aussi important de tester les performances des modules après irradiation. Les dégats causés par les radiations touchent à la fois l'électronique de lecture et des détecteurs de silicium, et conduisent à une augmentation du bruit, en même temps qu'à une augmentation du courant de fuite des détecteurs. La température de fonctionnement augmente ainsi, rendant encore plus crucial un bon système d'évacuation de la chaleur et de refroidissement.

Certains des modules des disques ont été irradiés grâce au faisceau de proton de 24 GeV du SPS au CERN. Le niveau d'occupation en bruit augmente jusqu'à atteindre $1.\times10^{-3}$, bien au delà des spécifications du SCT. La limite nominale d'occupation en bruit peut être récupérée en augmentant le seuil du discriminateur jusqu'à au moins 1.2 fC.

Les résultats des tests électriques obtenus ont été jugés suffisamment satisfaisants par la collaboration SCT pour s'engager dans la production massive, et les modules des disques ont passés avec succès leur revue finale ("Final Design Review") en décembre 2002.

Bien que l'hybride K5 verifie les spécifications du SCT, quatre versions antérieures d'hybrides montraient des instabilités inacceptables. C'est pour cette raison que la possibilité de construire un module "forward" basé sur l'hybride des modules des cylindres – nommé "KB", et assemblé suivant la configuration "forward", avec des détecteurs ayant la

géométrie adaptée aux disques – a été considérée par certains instituts de la collaboration.

Un premier prototype a été construit avec succès en septembre 2001, suivi de huit autres modules externes en configuration finale, assemblés et entièrement testés. Le niveau d'occupation en bruit de ces modules à un seuil de 1 fC est entre $\approx 2 \times 10^{-6}$ et $\approx 10^{-5}$, satisfaisant ainsi parfaitement les spécifications requises.

Les tests réalisés sur des prototypes irradiés font apparaître aussi un comportement satisfaisant. On peut donc en conclure que ce dessin de module aurait fourni une solution de rechange satisfaisante au cas où la version officielle de l'hybride "forward" n'aurait pas été terminée à temps.

Enfin, les modules à micro-pistes SCT d'ATLAS ont aussi été mesurés en tests faisceau, afin d'évaluer leur performance en tant que détecteurs de particules. Le faisceau est habituellement composé de pions de 180 GeV/c, avec une contamination mineure par des muons. Les modules sont disposés suivant une ligne, avec un système de télescopes: l'analyse conventionnelle des tests faisceau du SCT est en fait fondée sur la comparaison entre la réponse réelle des modules et la position attendue des traces, extrapolées à partir des télescopes.

Les mesures de base du test faisceau ont été adaptées à l'électronique de lecture binaire du SCT, et consiste en des balayages du seuil du discriminateur dans la gamme 0.7-6.0 fC. Environ 20 000 événements sont enregistrés à chaque valeur du seuil, fournissant ainsi une courbe d'efficacité (appelée courbe en "s"). A 1 fC, l'efficacité doit être supérieure à 99% pour satisfaire aux exigences du SCT. Par ailleurs, il est possible dans les tests faisceaux, de mesurer la résolution spatiale, la réponse à des traces arrivant avec des angles extrêmes, etc... Les mesures ont aussi établi les performances de reconnaissance de traces du dessin final des diverses géométries des modules SCT.

Part I

Measurement of the inclusive b-jet cross section at CDF

In the first part of this thesis work, the measurement of the inclusive b-jet cross section is presented. It is based on about 300 pb^{-1} of data, collected by the CDF experiment from February 2002 to September 2004. The measured cross section covers a range in transverse momentum between 38 and 400 GeV/c and it extends for more than 6 order of magnitudes, thus dramatically improving previous hadron collider results. A first comparison with one of the existing theoretical calculations implemented for b-jet production, shows an agreement within $\pm 1\sigma$ between data and theory. Nevertheless, the large theoretical uncertainties could be an indication of a major role played by not-included higher order contributions; thus a Next-to-Leading Order perturbative QCD calculation might not be considered conclusive for theoretical comparison with high-P_T b-jets production cross section.

Analysis steps are presented in detail, as support for the Physics Review Letter foreseen to be published soon.

Chapter 1

Standard Model and Bottom Production

Measurements of the b-jet production cross section at $p\bar{p}$ colliders provide an important quantitative test of Quantum Chromodynamic (QCD). Data on b-quark production are expected to be adequately described by perturbative expansions in the strong coupling constant α_S. Presently available for this process are calculations at next-to-leading order (NLO).

In the first part of this Chapter – sections 1.1 and 1.2 – the Standard Model and in particular the theory describing strong interactions, QCD, is summarized. In section 1.3 an overview of Bottom production is presented together with a description of the theoretical calculation developed to determine b-jet cross section at NLO. Finally, section 1.4 presents the uncertainties related to the theory prediction, mainly related to the choice of renormalization and factorization scales, as well as to the Parton Distribution Functions (PDF).

1.1 The Standard Model

The Standard Model [1] (SM) describes matter in terms of its fundamental constituents and their interactions. It has been extensively tested by experiments and, so far, all measurements have agreed with predictions within experimental errors.

Three of the four fundamental interactions in nature are described by the Standard Model: strong, weak and electromagnetic. Matter is built of three types of particles: leptons and quarks, which are all fermions (spin $\frac{1}{2}$), and bosons (spin 1), which mediate the interactions above.

There are three generations of leptons, each of which consists of a charged particle (electron, muon and tau) and a neutral partner (electron, muon and tau neutrinos). The generations are arranged by a mass hierarchy, whose source is unknown. In an analogous manner, three generations of quarks exist, each consisting of a charge +2/3 quark (up, charm, and top) and a charge -1/3 quark (down, strange, and bottom).

Elementary particles can be represented as fields: the theory based on them uses a Lagrangian formalism and is referred to as a gauge theory [2]. In that, the fields are described by representations of an abstract symmetry group, and the interaction between the fields, mediated by the gauge bosons (or quanta), is induced by the requirement that the Lagrangian is invariant with respect to arbitrary transformations of the fields. Transformations may be applied in all space-time locations ("global") or vary from one point to another ("local").

In the language of gauge theories, electromagnetic interactions are characterized by a $U(1)$ gauge symmetry, weak interactions by an $SU(2)$ symmetry, and strong interactions by an $SU(3)$ symmetry. Thus, the Lagrangian of the Standard Model is invariant under the symmetry:

$$SU(3) \otimes SU(2) \otimes U(1) \tag{1.1}$$

The group $SU(3)$ implies 8 mediators of the strong interaction (*gluons*). The Electro-Weak (EW) sector $SU(2) \otimes U(1)$ [3] is governed by bosons $W^{\pm}$ and Z for the weak interaction and by the photon γ for the electromagnetic interaction – the gauge theory for the $U(1)$ symmetry being the Quantum Electrodynamics (QED).

Gravity is not incorporated in the Standard Model as a quantized theory. Gravitation is assumed to be mediated by a massless spin 2 particle, the graviton (G).

Quarks carry colour charge, electric charge and therefore can interact via the strong force as well as the electroweak and the gravitational forces, coupling with the gluons, photons and $W^{\pm}$ and Z bosons. All leptons are subject to the weak interactions but only charged leptons interact electromagnetically.

In the context of the Standard Model, all massive particles acquire their mass by coupling to an additional scalar field, called the Higgs boson [4], that has yet to be seen.

Table 1.1 summarizes basic properties of the Standard Model particles: in particular, the considerable ranges given for the quark masses reflect the difficulties in dealing with masses of strongly interacting particles which are not observable as free fields. They have to be understood as mass parameters of the theory rather than mass contributions to the bound states corresponding to the observable hadrons.

Particles	Mass [MeV/c^2]	Spin	Charge/e	Coulor states
down (d)	4-8	1/2	-1/3	3
up (u)	1.5-4	1/2	+2/3	3
strange (s)	80-130	1/2	-1/3	3
charm (c)	1150-1350	1/2	+2/3	3
bottom (b)	4100-4900	1/2	-1/3	3
top (t)	174300	1/2	+2/3	3
e^-	0.511	1/2	-1	0
ν_e	< 0.000003	1/2	0	0
μ^-	105.66	1/2	-1	0
ν_μ	< 0.19	1/2	0	0
τ^-	1777	1/2	-1	0
ν_τ	< 18.2	1/2	0	0
γ	0	1	0	0
$W^\pm$	80419	1	± 1	0
Z	91188	1	0	0
gluon (g)	0	1	0	8
Higgs (H)	> 114000	0	0	0
Graviton (G)	0	2	0	0

Table 1.1: Particles of the minimal Standard Model: the first group contains quarks, the second the leptons and the last one the gauge bosons. All charges are given in units of the positron charge. The gravitational force (thus the Graviton field G) is also considered. The graviton and Higgs boson are the last two un-observed particles (in bold).

1.2 Quantum Chromodynamics

From *ep* scattering experiments, it is clear that protons are not fundamental particles of nature. With the advent of accelerators, many different hadronic particles appeared. In 1964 it was noted by Gell-Mann [5] and Zweig [6] that these particles could be arranged in multiplets of $SU(3)$. They also proposed the existence of new mathematical entities, named quarks, such that by fitting them into the elements of this fundamental representation and by making appropriate compositions with them, one could build up the whole spectrum of hadrons (*quark model*). A classification was made separating particles with a quark and an anti-quark, the $Mesons$, and particles with 3 quarks, the $Baryons$.
However, several questions remained unexplained within this quark model. Among them:

- the Δ^{++} particle should not exist as it has a symmetric wave function, therefore obeys the wrong statistics. Its wave function is:

$$|\Delta^{++}> \;\sim\; |u^{\uparrow}u^{\uparrow}u^{\uparrow}> \tag{1.2}$$

  which is apparently totally symmetric: in space, flavor and spin. However, according to Fermi-Dirac statistics it should be antisymmetric as it corresponds to a state with identical fermions.

- Some observables computed using the quark model differ from experimental measurements by a factor 3. The ratio of quark pair production:

$$R_{e^+e^-} \equiv \frac{\sigma(e^+e^- \to hadrons)}{\sigma(e^+e^- \to \mu^+\mu^-)} \tag{1.3}$$

  should be equal to 2/3 according to the quark model, but the measured value is 2 (below $\sqrt{s} \sim 3$ GeV). This can only be explained with a number of quarks 3 times more numerous than expected.

The puzzles posed by these (and other) problems was solved assuming that a new quantum number exists, called *colour*, conceptually similar to electrical charge. This quantum number is actually a source of colour field, that glues the quarks together to form the observed hadrons, motivating the name *gluons* for the quanta.

The evident existence of a field theory of strong interactions based on the colour charge of the quarks, makes it natural to assume an invariant Lagrangian under an $SU(3)$ gauge symmetry. The derived theory is the *Quantum Chromodynamics* (QCD) [7] and the Lagrangian has the form:

$$\mathcal{L}_{QCD} = \sum_f \overline{q}_f \; (i\gamma^\mu D_\mu - m_f) \; q_f - \frac{1}{2} Tr(G^{\mu\nu} G_{\mu\nu}) \tag{1.4}$$

where the q_f are the fermions and f is the colour index. D_μ and $G_{\mu\nu}$ are matrices defined as:

$$D_\mu = \partial_\mu + i g_S G_\mu \qquad and \qquad G_{\mu\nu} = \partial_\mu G_\nu - \partial_\nu G_\mu + i g_S [G_\mu, G_\nu] \tag{1.5}$$

with $G_\mu = \sum_f G^f_\mu \lambda_f/2$, being λ_f the 8 Gell-Mann (3×3) matrices: the quark states transform under the fundamental representation of the group, and $\lambda_f/2$ are the eight generators of $SU(3)$ symmetry, indeed the gluons.

Colour charge of strong interactions is analogous to the electric charge of electromagnetic interactions in many respects, *i.e.* the forces are mediated by massless, vector particles. However, electromagnetism is an Abelian $U(1)$ gauge theory, with two types of charge and an uncharged mediating boson. QCD is a non-Abelian gauge theory, with six types of charge (colour or anti-colour) and a charged (coloured) mediating boson. As gluons carry colour, they can self-couple unlike photons in QED. This difference turns out to be crucial in understanding the features of the quark interactions at short distances, and it leads to two phenomena explained in the following: asymptotic freedom and colour confinement.

The interaction strength of strong interaction is governed by the coupling constant g_S or equivalently $\alpha_S = g_S^2/(4\pi)$. If the coupling parameter is sufficiently small, one can use perturbative expansions to calculate theory predictions reliably. Indeed, a very important property of QCD is that the size of the strong coupling parameter varies with the size of the characteristic momentum transfer in a process.

In quark interactions, at the first order of QCD expansion (Leading Order), quarks interchange a gluon as shown in figure 1.1 (a). The bare color charge of the quark behaves as the electric charge of a particle immersed in a dielectric medium: the charge exerts a potential, at distances larger than or comparable with molecular dimensions, which is smaller than the Coulomb potential in free space. Thus, the dielectric introduces a *shielding* effect. Actually, also in vacuum, the test charge continually emits and reabsorbs virtual photons that can temporarily produce e^+e^- pairs, again producing a shielding effect: this is an intrinsic feature of QED. In a similar way, quark-antiquark pairs produce a shielding effect on the value of a test quark (color charge): the leading order process is modified by higher order loop diagrams in which the loops consist again of quarks or gluons (figure 1.1 (b) and (c)). However, the gluon-loop contribution produces an *anti-shielding effect*, where the possibility to have mediator self-couplings is a specific feature of QCD, as a non-Abelian gauge theory. The self-coupling of the gluons "spreads out" the color charge, and this effect

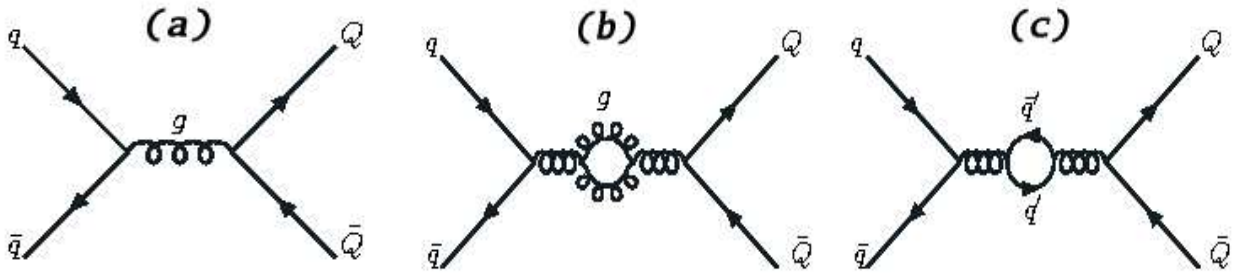

Figure 1.1: QCD quark interaction processes: (a) is at leading order, (b) and (c) are higher order loop diagrams, consisting of gluons (b) and quarks (c).

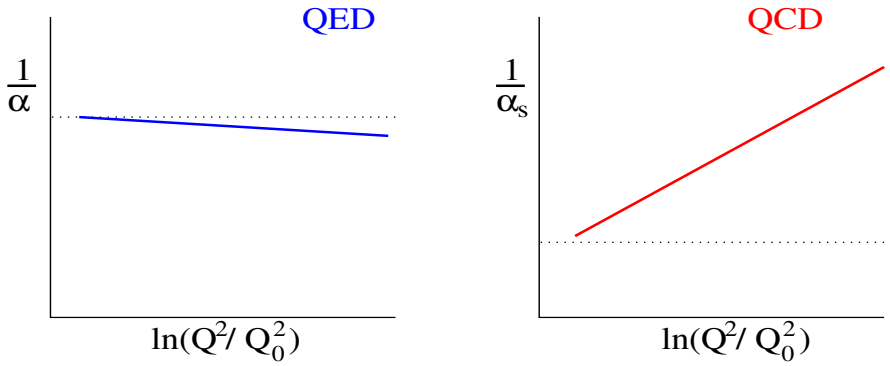

Figure 1.2: Reciprocal of the running coupling constant as function of Q^2, for (left) QED, and (right) QCD.

becomes larger as Q^2 increase[1].

The coupling α_S at the given interaction $|Q^2|$, is expressed in terms of another value of α_S at a reference scale Q_0^2. In the leading-logarithm approximation:

$$\alpha_s(|Q^2|) = \frac{\alpha_s(Q_0^2)}{1+\beta_0\alpha_s^0(Q_0^2)\ln(Q^2/Q_0^2)} = \frac{1}{\beta_0 \ln(Q^2/\Lambda^2_{QCD})} \tag{1.6}$$

where $\beta_0 = (11n - 2f)/12\pi$ (with n is the number of colors, f is the number of flavor participating to the process at the given $|Q^2|$) and in the second expression we have made the substitution $\Lambda^2_{QCD} = Q_0^2 \exp[-1/\beta_0\alpha_s(Q_0^2)]$.

Thus, provided the number of quark flavors is below 16, it follows that $\alpha_S(|Q^2|)$ decreases as Q^2 increase. As for $Q \to \infty$, $\alpha_S(|Q^2|) \to 0$, that is the quarks behave as if free: this phenomenon is called *asymptotic freedom*. Figure 1.2 shows the behaviour of $1/\alpha_S$ as a function of $\ln(Q^2/Q_0^2)$, on the right, together with the one of $1/\alpha$(QED), on the left: in quantum electrodynamics there is no anti-shielding effect because of the Abelian nature of the theory, where self-photon coupling are not allowed, thus, α(QED) is almost constant up to a certain scale, to increase at very high $|Q^2|$.

Thanks to asymptotic freedom, QCD can be treated with perturbation theory under the hypothesis $|Q^2|$ is high enough to have a small α_s, which is the case for $|Q^2|$ higher than few GeV^2. However, this breaks down when higher order corrections are calculated in the ultraviolet region, corresponding to large loop momenta: such a feature is characteristic of QCD but also of QED, that contains divergent terms associated with integrals over intermediate states. Nevertheless, for QED is found that these divergences can always be absorbed into redefinition of "bare" lepton charges and masses – which are anyway arbitrary and unmeasurable – as being equal to the physically measured values. This property is called *renormalizability*: the parameters are renormalized such that they exactly cancel the infinities resulting from higher order corrections in any calculation.

[1] $|Q^2|$ is defined as the absolute squared four-momentum transferred in a parton-parton collision.

Also in QCD, the infinite parts of the corrections can be absorbed, through the choice of a renormalization procedure, into the parton masses and the coupling parameter α_S. Somehow, equation 1.2 already show the dependence of α_S by a "reference scale" $|Q_0^2|$. The introduction of a "renormalization scale" (μ_R) is then required. Many different renormalization schemes (RS) exist to regulate the divergences of the theory: the most commonly used one is the modified minimal subtraction ($\overline{MS}$) [8].

It should be noticed that μ_R is a pure mathematical tool and no physical consequences can result from the choice: physical quantities, such as the cross section calculated to all order in perturbation theory, do not depend on RS. Any changes due to the explicit dependence on μ_R have to be reabsorbed by changes in the renormalized parameters, such as α_s and the mass. It follows that a truncated series does exhibit RS dependence: in particular, at NLO, the dependence is completely given by one condition, which can be taken to be the value of the renormalization scale μ_R.

In a high energy collision, quarks evolve initially as free particles, so perturbative QCD can be used. Nevertheless, free quarks are not observed in nature and only colour singlet objects have been seen. This is explained by *colour confinement*. The coupling of the strong force gets large at a scale $\Lambda_{QCD} \simeq 300$ MeV, that is approximately the scale where QCD is non-perturbative, because the strong coupling constant $\alpha_s \to 1$; this corresponds to the situation when the quarks reach a separation of around 10^{-15} m (the typical size of hadrons). As the force between coloured objects increases with distance, eventually enough potential energy is present to create a $q\bar{q}$ pair out of the vacuum. This process continues until the quark hadronizes into a color singlet object. The simplest color singlet is a meson, the next simplest a baryon. While the first part of the shower can be treated in perturbative QCD, the hadron cascade is produced in a non-perturbative way: this process, called *hadronisation* and represented in figure 1.3, is then described by phenomenological models such as the Peterson model[9], the Lund model[10] etc.

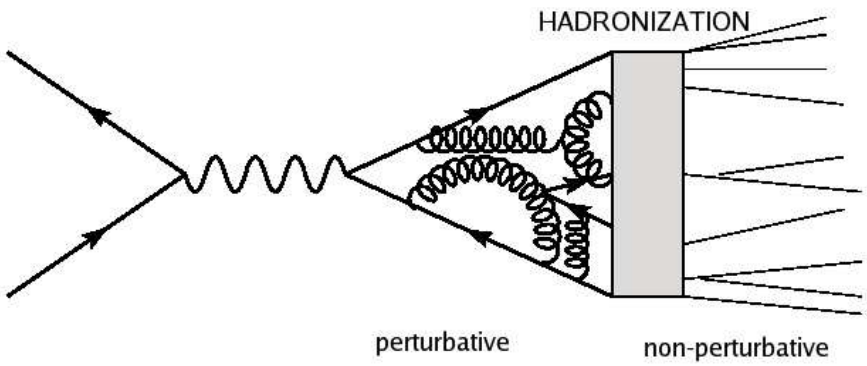

Figure 1.3: Schematic of the hadronisation process in a high energy collision.

1.3 Bottom production

The factorization theorem[11] states that hadron-hadron cross sections can be expressed as a convolution of two pieces, the partonic cross sections, calculable in perturbative QCD, and parton momentum distributions, not calculable but universal, and therefore process independent.

Thus, the cross section for a certain interaction can be defined as:

$$\sigma_{ab}(p_A, p_B) = \sum_{ij} \int dx_i dx_j F_i^A(x_i, \mu_F) F_j^B(x_j, \mu_F) \hat{\sigma_{ij}}(x_i p_A, x_j p_B, \mu_R, \mu_F, \alpha_s(\mu_R)) \quad (1.7)$$

where $\hat{\sigma_{ij}}$ is the parton level cross section between the partons in each hadron (the calculable piece), x_i and x_j are the fractions of the proton momentum p_A and anti-proton momentum p_B carried by partons i and j, F_i^A and F_j^B are the parton distribution functions (PDF), that indeed describe the momentum distribution of the partons inside the incoming hadrons. These contain a dependence on a factorization scale μ_F, in a certain sense analogous to μ_R. Quarks inside the proton are not free constituents, but they have interactions through gluon exchange and emission. These interactions are reabsorbed up to a certain scale, namely the factorization scale μ_F, and therefore removed from the single parton cross section $\hat{\sigma_{ij}}$. In other words, the scale is introduced to separate long-distance (soft) and short-distance (hard) contributions to equation 1.7, in such a way that all long-distance physics (non-perturbative) is contained within the proton PDF, whilst all short-distance physics (calculable in pQCD) is contained within the hard-subprocess.

Starting from the calculable piece of the hadron-hadron cross section, b-quark production [12] can be written as an expansion in α_s:

$$\hat{\sigma_{ij}} = \alpha_s^2(\mu) G_{ij}^{(0)}(\hat{s}, m_b) + \alpha_s^3(\mu) G_{ij}^{(1)}(\hat{s}, m_b) + O(\alpha_s^4) \quad (1.8)$$

where μ_R and μ_F are chosen to be equal, the total cross section being the sum of all contributing processes.

At leading order, the heavy quark (namely bottom and charm, in general defined as Q) cross section in hadronic collisions gets contributions from the processes below:

$$\begin{aligned} g + g &\rightarrow Q + \bar{Q} \\ q + \bar{q} &\rightarrow Q + \bar{Q} \end{aligned}$$

At Next-to-leading order additional contributions come from the radiative corrections to the processes above and the amplitudes of the processes below:

$$\begin{aligned} g + g &\rightarrow Q + \bar{Q} + g \\ q + \bar{q} &\rightarrow Q + \bar{Q} + g \\ q + g &\rightarrow Q + \bar{Q} + q \end{aligned}$$

Figure 1.4 shows Feynman diagrams for leading order processes (top and middle) and some of the next-to-leading order contributions. Traditionally, the NLO terms are grouped into

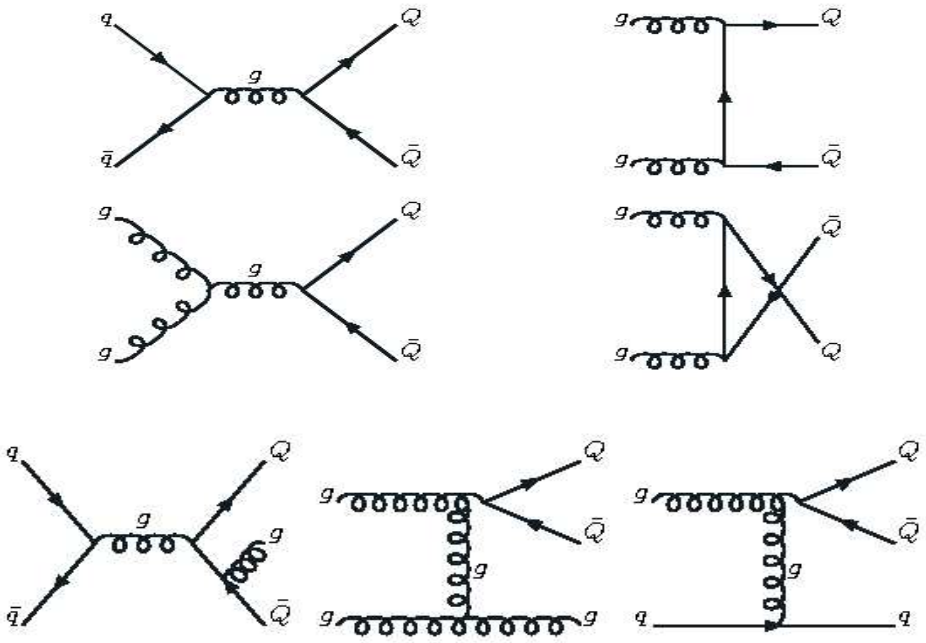

Figure 1.4: Leading order and some Next-to-Leading order diagrams for heavy quark production.

three categories: flavor creation, flavor excitation and gluon splitting. In perturbation theory, the three categories are not independent, due to interference terms among them. Nevertheless, flavor creation, flavor excitation and gluon splitting are still useful concepts in describing bottom hadroproduction, as they have a minimal overlap in phace space. At NLO, flavor creation consists of the $2\rightarrow2$ processes, in addition to diagrams which add gluon radiation to the $2\rightarrow2$ terms. Flavor excitation includes diagrams in which a initial state gluon splits into $b\bar{b}$ pair before interacting with the parton from the other hadron, putting the bottom quarks on-shell. Gluon splitting consists of diagrams where a gluon splits into a $b\bar{b}$ pair after interacting with the parton from the other hadron.

A study of b-quark production is carried out regardless of the event structure in which the quark is produced, so it is not compatible with possible experimental measurement. The principle of colour confinement states that coloured objects (such as b-quark) must bind with other quarks and gluons to produce a colorless object, or hadronize. Therefore, the real observable quantities are b-hadrons, whose energy can be measured independently of the momentum fraction carried by the b-quark(s) from hard interactions, and jets containing one or more b-hadrons, thus b-quarks.

The calculation of parton properties brings the difficulty of treating the emission of collinear gluons, which at high momentum cause large logarithms $\log(p_T/m)$ to appear at

any order in the perturbative expansion of the b-quark ${p_T}^2$ distribution. To include these logarithms, one has to re-sum them, and this can be done including the log terms into another piece, known as fragmentation function, to be convoluted with the hadron-hadron cross section again thanks to the factorization theorem.

Fragmentation functions give the probability that a parton produces a final hadron carrying a fraction z of the primary parton's momentum. This fraction is defined as

$$z = \frac{E(B) + p_{||}(B)}{E_b + p_b} \tag{1.9}$$

where $E(B)$ and $p_{||}(B)$ are the bottom hadron's energy and momentum parallel to the bottom quark direction and E_b and p_b are the bottom quark's energy and momentum. Because of the non-perturbative nature of the hadronisation process, fragmentation functions are described by models. However, they also have the property to be independent of the hard-subprocess, so they are universal.

Nevertheless, the implementation of models might lead to major uncertainties. Part of the long-standing "discrepancy" found between NLO theory and CDF and DØ data for B-meson production cross section measurements has been ascribed to a non accurate treatment of the fragmentation properties of the b-quark. This is briefly described in the section 1.5.

1.3.1 b-jets

Calculations based on jets should be less sensitive to the details of the analysis of large logarithms, because jets contain both b-quark(s) and collinear gluons[13]. In the following, we will focus on these observables to study bottom production.

A detailed description of the jet definition and the associated reconstruction algorithm, as treated experimentally, is given in section 3.2. In the NLO calculation algorithm [14] used here, a bottom quark jet is defined as a cone containing at least one b-quark. The definition of the jet kinematical variables is made in terms of the those related to the partons inside the jet. A "measurement function", called S, is computed in order to obtain the differential b-jet cross section $d\sigma_{AB}$ (A and B are initial massless partons) as the sum of two terms,

$$d\sigma_{AB} = d\sigma_{AB}^{quark} + d\Delta_{AB} \tag{1.10}$$

where $d\sigma_{AB}^{quark}$ is the b-quark cross section at next-to-leading order, $d\Delta_{AB}$ takes into account the fact that, in the final state, an additional parton is present, thus the jet does not coincide with the b-quark.

As a consequence of the initial processes considered, 3 different "kinds" of jets are possibly built: a jet only containing one b-quark if there are no other partons that end up in the same cone, a jet with one b-quark plus a light parton (gluon or light quark), or jets

[2] Transverse momentum p_T is defined as $p_T = p\sin\theta$, with θ the angle of the particle with respect to the beam.

with both b and $\bar{b}$ inside. The first two kinds will be referred as single b-jets, the last as double b-jet or $b\bar{b}$-jet.

The measurement function S depends on the jet algorithm and resummation scheme adopted: in this calculation, a Snowmass-like scheme[15] is used (see also 3.2.2), although a slight variation is adopted since b-quarks are treated with mass. Thus, the kinematical variables defining the jet are the transverse energy E_T, and the pseudo-rapidity η[3]. The NLO calculation algorithm has been adapted to have a differential cross section in rapidity instead of pseudo-rapidity[4], and in P_T instead of E_T, to use the same kinematic variables adopted in the data measurement. We also consider jets with cone size R=0.7 produced in the central region $|Y| < 0.7$, in order to correctly reproduce the acceptance of the data analysis.

The main parameters entering in the calculation are the b-quark mass, the renormalization and factorization scale, and the parton distribution function. The mass is chosen to be m_b=4.75 GeV/c^2, and we consider $\mu_R = \mu_F = \mu$, with $\mu = \mu_0/2$, where $\mu_0 = \sqrt{p_T^2 + m_b^2}$. Finally, we use PDF CTEQ6M.

Figure 1.5 shows the initial state composition of the b-jet cross section considering the different components of the production processes: $gg \to b$-jet (upper right), $q\bar{q} \to b$-jet (lower left), $qg \to b$-jet (lower right). The total is shown on the upper left plot. Two different b-jet curves are presented for each production process: single b-jet and double b-jet; for the comparison b-quark cross sections is also shown. Production through gg and qg channels is dominant at P_T below 200 GeV/c: in particular, gluon-gluon initial states dominate especially because of the large number of gluons at low momentum with respect to the number of quarks and antiquarks in the proton, together with the fact that gg interaction is $\hat{t}$ channel, whereas the quark-antiquark interaction is $\hat{s}$ channel. On the other hand, at higher momentum b-quarks are mostly produced by annihilation of light quarks. Since the $b\bar{b}$-jet contribution is a result mainly of gluon splitting, as expected it is suppressed for the $q\bar{q}$ channel, while it is dominant in case of gg and qg channels.

The differential cross section output of the NLO algorithm, shown in figure 1.5, refers to the production of a single heavy-flavor jet, either containing b or $b\bar{b}$-jets (i.e. no $\bar{b}$-jets contribution). To use the same prescription of data, b-jets must be defined as jets containing either a b-quark or a $\bar{b}$-quark, jets containing both being counted only once. The

[3] The pseudo-rapidity η is defined as

$$\eta = -ln\,(\tan(\frac{\theta}{2}) \tag{1.11}$$

being θ the angle between the direction of the particle and beam axis.

[4] The rapidity Y is defined as

$$Y = \frac{1}{2} ln(\frac{E + p_z}{E - p_z}) \tag{1.12}$$

where E and p_z are respectively the total energy and the longitudinal momentum of the particle. It is approximately equal to η for $p \gg m$, where p is the momentum and m the mass of the particle; however, differently from η, rapidity is Lorentz invariant in the longitudinal direction, thus is a preferable kinematical variable in case of experimental jet definition (see section 3.2.1).

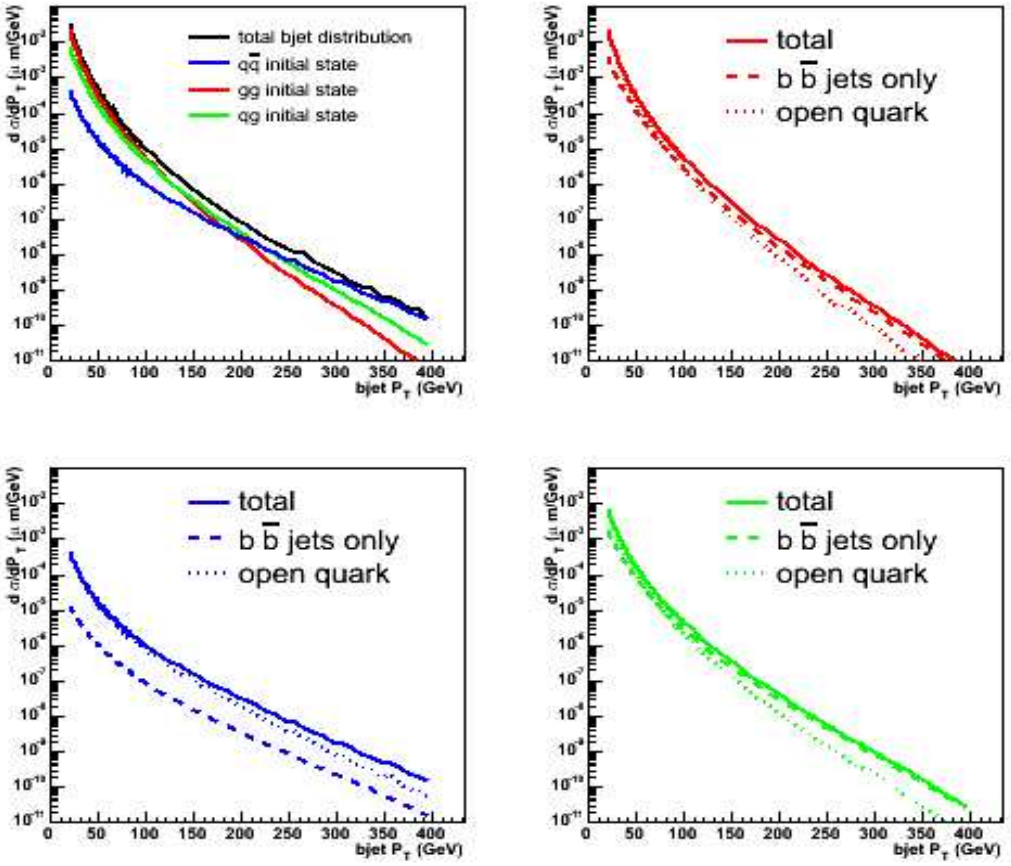

Figure 1.5: Initial state composition of the b-jet production processes as calculated for $\mu_R = \mu_F = \mu_0/2$ and reconstruction cone radius R = 0.7 (upper left). Different components of the production processes are also shown: $gg \to bjet$ (upper right), $q\bar{q} \to bjet$ (lower left), $qg \to bjet$ (lower right). The total is showed on the upper left plot.

cross section to be compared with a measurement result is obtained by subtracting the contribution of the $b\bar{b}$-jets from twice the total b-jet rate.

Figure 1.6 shows the predicted P_T distribution of b-jets for Tevatron conditions as in the performed analysis. Together with the differential cross section, we present also the contribution of $b\bar{b}$-jets only: as already underlined, the latter content plays a major role for intermediate energy range, because of the dominance of gluon splitting contribution as a source of heavy quarks. At very high energy values the $b\bar{b}$-jet content decreases since the most likely production process for heavy quarks is via light quark annihilation. The rate of $b\bar{b}$-jets with respect to all b-jets is also shown in figure 1.7 as a function of jet P_T, and it increases to 45% in the intermediate transverse momentum region.

1.4 Theory uncertainties

The major sources of uncertainty are the choice of the renormalization and factorization scale μ and the parton distribution functions. The uncertainty associated to the mass of the b-quark can be considered, in a first stage, negligible since we are dealing with jets with a much larger energy.

The b-jet cross section calculation in perturbative QCD at fixed order is affected by a dependence on the choice of the scale. If the whole expansion were known, the result would be formally independent of the value chosen for μ, the residual μ dependence present at any finite order being compensated by the higher order terms. This residual dependence can thus be considered an estimate of the magnitude of higher order effects.

In the differential cross section for b-jets there are two "mass" scales, the transverse momentum of the jet and the mass of the b-quark: for this reason the natural choice for μ is to be of the order of $\sqrt{P_{T\,b}^2 + m_b^2}$.

Figure 1.8 shows the dependence of the theory prediction with respect to the choice of scale. We consider $\mu_0/2$ as the baseline scale and show the ratios with b-jet cross sections calculated using μ_0, $2\mu_0$ and $\mu_0/4$, as a function of transverse momentum. Below 250 GeV/c the difference is remarkable, being also 40-50%, while at very high P_T the dependence on the scale is reduced. This effect is partially attributed to the fraction of b-quark ending up in the same jet-cone and so to the behavior of the gluon splitting contribution that is only present at Leading Order. In a regime where this contribution is suppressed, like at high energy, the scale dependence is lower. Thus, the uncertainty related to the scale choice shows that the impact of higher-order contributions could be quite large.

However, it should also be noticed that the assumption of identifying renormalization and factorization scales is conventional, but not supported by physical motivations [16]. Some studies [17] have been carried out in this sense, showing that at NLO the cross section $\sigma_{tot}(b\bar{b}, \mu_R, \mu_F)$ depends, indeed, on these two scales in quite different ways.

The other main source of uncertainty in the theoretical calculation is related to the PDF. Parton Distribution Functions are universal global fits extracted from experimental results, that describe the internal structure of the proton, independently of the process, in

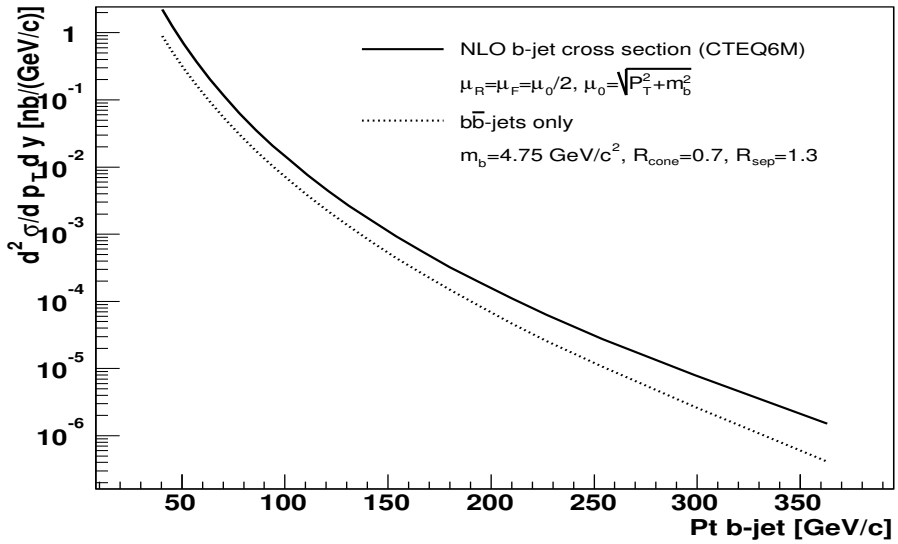

Figure 1.6: b-jet cross section as obtained by the NLO algorithm. Total cross section and $b\bar{b}$-jets only contribution are reported.

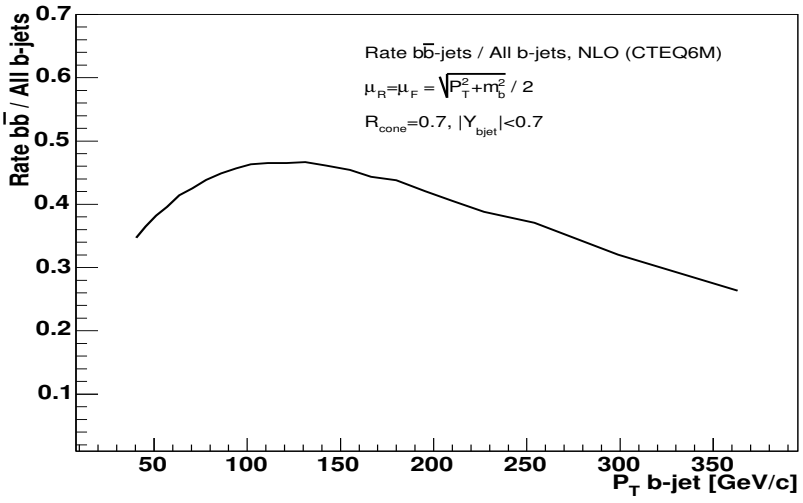

Figure 1.7: Rate of $b\bar{b}$-jets with respect to all b-jets, as a function of jet P_T.

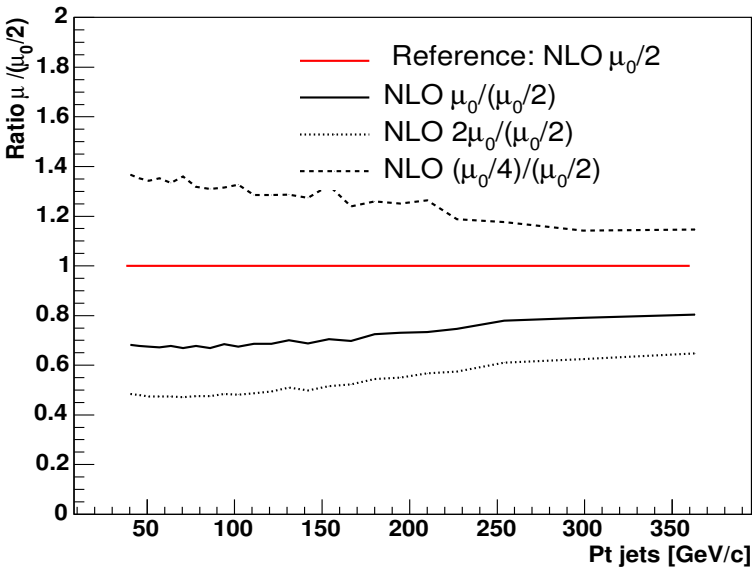

Figure 1.8: Ratios of b-jet cross sections from NLO algorithm obtained using as renormalization and factorization scales μ_0, $2\mu_0$ and $\mu_0/4$, with respect to $\mu_0/2$.

terms of momentum distributions of the partons inside the proton itself. Several sets of PDF exist, calculated by different groups, such as CTEQ [18], MRST [19], Alekhin [20].

CTEQ6M parton distribution functions (chosen here) use the Standard $\overline{MS}$ scheme, and are distributed as 20+1 PDF sets, consisting of a central value (best fit), and eigenvector basis sets in the plus and minus directions along each eigenvector. Fits are obtained by using the same coupling strength $\alpha_s(Mz)$=0.118 and the NLO running α_s formula.

From these PDF sets it is possible to calculate the best estimate of the physical quantity we are considering (in this case, the cross section) and the range of uncertainty. According to [18], the uncertainty can be computed from the formula:

$$\Delta X = \frac{1}{2}(\sum_{i=1}^{20}[X(S_i^+) - X(S_i^-)]^2)^{1/2} \tag{1.13}$$

where X is the observable, and $X(S_i^{\pm})$ are the predictions for X based on the PDF sets $S_i^{\pm}$. The contribution of PDF uncertainties to this cross section varies between 7%(low transverse momentum) and 20% (high transverse momentum): the dominant contribution to the error is given by eigenvector 15, related to the gluon distribution at high x. Since the factorization scale μ_F and renormalization scale μ_R are correlated to structure functions and the coupling constant, there is a residual dependence of the PDF on the scale μ: for instance, in case of μ=$\mu_0/2$, PDF systematics are 1-2% higher than in the case of μ_0.

1.5 Past measurements of bottom production at hadron colliders

The first measurement of the bottom production cross section at hadron colliders was performed by the UA1 collaboration [21]. The analysis used semi-leptonic decays of bottom hadrons to muons in order to measure the integrated quark cross section with $p_T^b > p_T^{min}$ at $\sqrt{s} = 630$ GeV: although a slight excess of the measurement relative to the NLO QCD prediction, results were considered consistent with the theory within the prediction uncertainty.

The bottom cross section was studied by the DØ and the CDF collaborations (see for instance [22, 23, 24] and [25]) at the Tevatron with $\sqrt{s} = 1800$ GeV: figure 1.9 shows the integrated bottom quark cross section with $p_T^b > p_T^{min}$ from CDF, where the measurement used semi-leptonic decay and bottom decays to J/ψ mesons. All results showed about a factor 3 excess with respect to the theoretical expectation.

The publication of these "controversial" measurements in RunI has led to many developments both in the theoretical calculations beyond NLO and the experimental approach, resulting in a better agreement between data and theory. A major role, concerning theoretical improvements, has been played by the implementation of the so called Fixed-Order with Next-to-Leading-Log (FONLL) calculation [27], where the resummation of $\log(p_T/m_b)$ terms with the next-to-leading logarithmic accuracy is matched with a fixed order NLO calculation. Also, there have been substantial changes in the bottom fragmentation function as extracted from experimental data and for the used Parton Distribution Functions (now CTEQ6M).

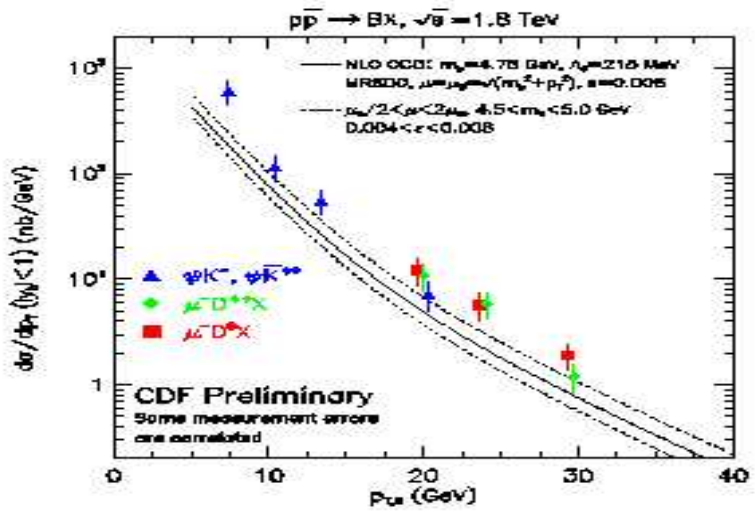

Figure 1.9: Cross section measurement of bottom production at the Tevatron as published by CDF: the measured B meson differential cross section is shown with theoretical prediction superimposed.

A measurement of the B-hadron production cross section [26] has been performed by CDF, using data corresponding to an integrated luminosity of 39.7 pb^{-1}. The differential cross section of the B-hadrons over the transverse momentum range from 0 to 25 GeV/c is shown in figure 1.10. The most recent theoretical calculations are also superimposed, showing a remarkable agreement with data.

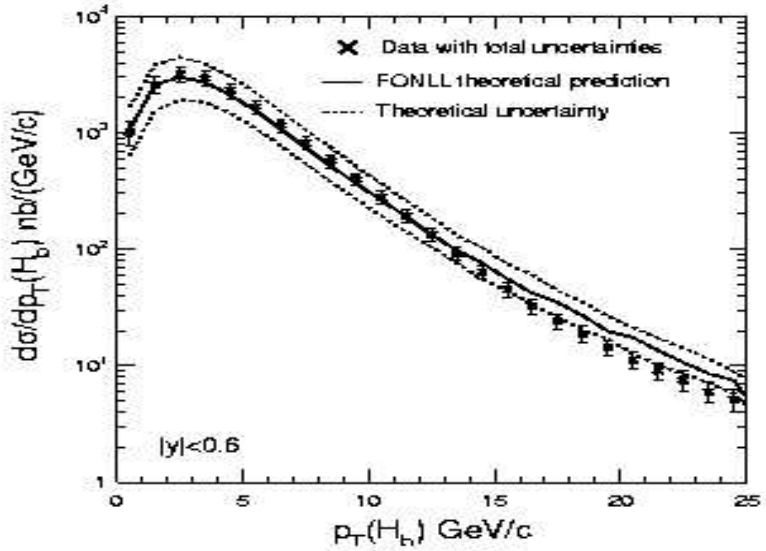

Figure 1.10: B-hadron production cross section as a function of B-hadron p_T. The crosses with errors bars are the data with systematic and statistical error added. Theoretical prediction is superimposed.

Chapter 2

The CDF experiment

Located about 35 miles west of Chicago, Illinois, the Fermi National Accelerator Laboratory (Fermilab) is one of the main particle physics facilities in the world. It was built in the late 1960's, funded by the Department Of Energy of the United States. During the past 40 years several experiments have made important contributions to the understanding of the Standard Model of Fundamental Particles and Forces. In 1977, the Fermilab experiment E288 observed a new particle, the Upsilon, composed of a new kind of quark and its anti-matter partner, giving the first evidence for the existence of the bottom quark. In 1995 the CDF and D0 experiments at the Tevatron proton-antiproton Collider completed the quark sector of the SM with the observation of the top quark. The RunII of the Tevatron started in March 2001, designed to meet the goals of the new particle physics frontiers, involved a complete upgrade of the full Fermilab accelerator complex.

In this Chapter we briefly describe the Tevatron accelerator and the CDF experimental apparatus.

2.1 The Fermilab Tevatron

The Fermilab accelerator complex, as shown in Figure 2.1, is composed of five different accelerators - the Cockroft-Walton, the Linac, the Booster, the Main Injector, and the Tevatron - which, working in cascade, accelerate in opposite directions bunches of protons and antiprotons to an energy of 980 GeV. The total energy available in any proton-antiproton collision is then 1.96 TeV. The cross section will depend on this value which also sets the upper threshold to the mass of particles which can be produced.

Another key parameter in collider experiments is the luminosity, which determines the number of collisions per unit time. For a certain process with a cross section σ the number of events in a time interval ΔT is given by the relation

$$N = \sigma \cdot \int_{\Delta T} L dt = \sigma \mathcal{L}, \tag{2.1}$$

where $\mathcal{L}$ is the "integrated luminosity" collected in the time interval ΔT.

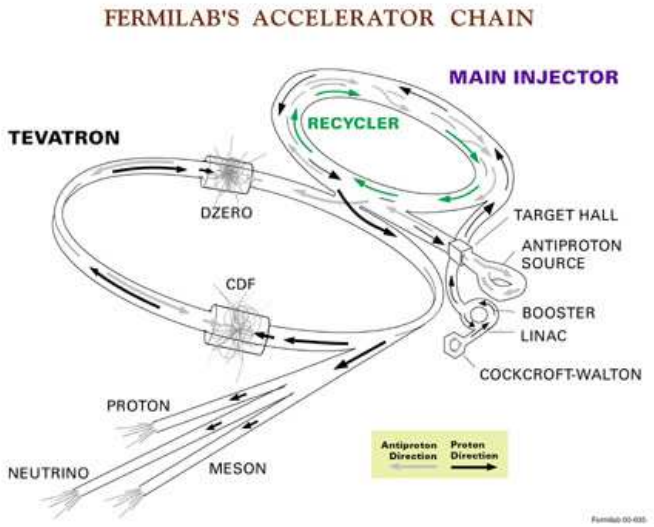

Figure 2.1: A schematic drawing of the Fermilab accelerator complex.

The Run II upgrades on both the accelerator and the detector were driven by the consideration that, in order to improve the potential discovery and reach a better sensitivity for high precision measurement, the number of events collected by the Tevatron experiments had to be increased.

To achieve this goal the Tevatron was redesigned to provide an higher luminosity. Moreover, the center of mass energy of the proton-antiproton system has been increased by 10%, which translates into a higher interaction cross section for most physical processes.

The higher Tevatron instantaneous luminosity is due to to the increase of the number of bunches in each beam as well as to the greater number of protons and antiprotons per bunch. In fact the instantaneous luminosity $\mathcal{L}$ is proportional to:

$$\mathcal{L} \sim \frac{f B N_p N_{\bar{p}}}{2\pi(\sigma_p^2 + \sigma_{\bar{p}}^2)}, \tag{2.2}$$

where f is the revolution frequency, B the number of bunches in each beam, N_p and $N_{\bar{p}}$ the number of protons and antiprotons per bunch, σ_p and $\sigma_{\bar{p}}$ the transverse beam size at the interaction point. Although the instantaneous luminosity is proportional to the number of particles per bunch, its value is limited from above by the number of interactions per bunch crossing, which is also related to the number of particles. This limitation is due to the superposition of several $p - \bar{p}$ interactions within the same bunch crossing, resulting in an increase of the event complexity.

The average number of interactions per bunch crossing is shown in Figure 2.2 as a function of the instantaneous luminosity for different number of bunches.

From the plot it is evident that, at a fixed instantaneous luminosity, to keep the number of interactions per bunch reasonably small, the number of bunches in each beam has to

be increased. More bunches results in a shorter interval between each interactions. This time interval is the clock of the whole apparatus: accelerator and detectors. Presently the Tevatron is running with 36×36 bunches, resulting in a bunch crossing interval of 396 ns.

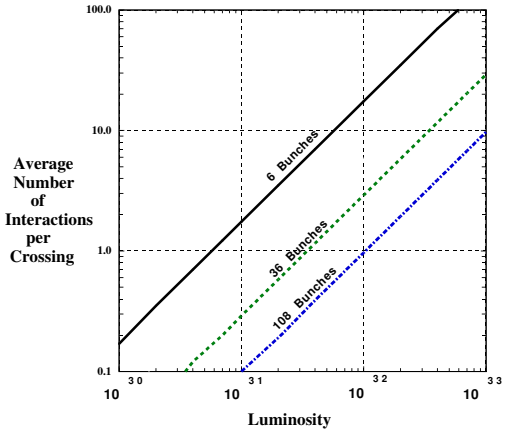

Figure 2.2: Average number of interactions per bunch crossing as a function of the instantaneous luminosity for different beam conditions.

2.1.1 Production and injection of protons and boosting

Protons are extracted from negatively ionized hydrogen gas. Hydrogen molecules are passed through a magnetron, which extracts ions, consisting of two electrons and one proton, and accelerates them to the energy of 25 KeV. These ions are then accelerated using the potential difference supplied by the Cockroft-Walton preaccelerator, which produces a H^- beam of 750 keV. The H^- ions subsequently enter the second stage of the accelerator process, the Linac.

The Linac is a linear accelerator about 150 m long, which increases the energy of the H^- to 400 MeV, using radio frequency cavities. The ion beam is then injected in the Booster, a small synchrotron having 150 m of diameter, where ions are merged with the already circulating protons. Then this combined beam is focused on a thin carbon sheet, which strips the H^- of their two electrons. The resulting protons, using radio frequency cavities, are here packed into bunches and accelerated to 8 GeV. Protons are now ready to be transfered into the Main Injector.

2.1.2 Main Injector

The Main Injector replaces the old Main Ring, and it was designed to fulfill the new operational requirements needed by the Tevatron Run II.

The Main Injector is a synchrotron of 3 Km of circumference, where protons and antiprotons are accelerated to 150 GeV before injection into the adjacent Tevatron. The

main feature of this new synchrotron, compared to the Main Ring, is the larger particle acceptance to accommodate bunches from the Booster. Another important capability of the Main Injector consists in the possibility of decelerating antiprotons, when the Tevatron is not in a collide mode. With this functionality antiprotons can be recovered and stored until a new run starts.

2.1.3 Antiproton production and cooling

Antiprotons are produced by dumping onto a nickel target a 120 GeV proton bunch extracted from the Main Injector. Among the variety of particles generated in the collision, antiprotons of about 8 GeV energy are produced and collected through lithium lenses and dedicated magnetic field. Antiprotons are then injected into the Debuncher Ring, where, by means of the "stocastical cooling" technique, their momentum spread is reduced, while they are collected as a continuous beam. Subsequently antiprotons are sent to the Accumulator, where they are further cooled and stacked into bunches. The stacking rate, thanks to the Run II upgrades, has been increased by a factor of 3 with respect to Run I, resulting in higher luminosity. When a sufficient number of antiprotons is available, they are accelerated to 150 GeV and, together with the protons, transfered to the Tevatron for the ultimate acceleration stage before the collisions.

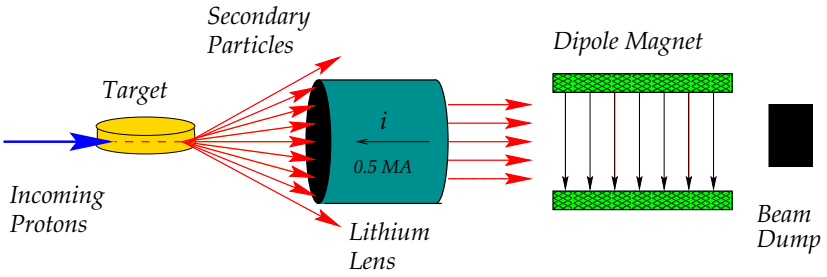

Figure 2.3: Schematic diagram which illustrates the antiproton production and selection chain.

2.1.4 Tevatron

The Tevatron is a proton-antiproton synchrotron collider. It is situated a few meters underground and its circumference is about 6 km. The Tevatron receives the protons and the antiprotons in the same beam pipe, where the two beams circulate in opposite directions. The Tevatron makes use of superconducting dipole magnets and quadrupole focusing magnets to provide a stable circular orbit for the protons and antiprotons.

Once 36 bunches of protons and 36 of antiprotons ("a store") are circulating in the Tevatron the beam energies are ramped up together to 0.98 TeV. The two beams, kept spatially separated during the acceleration stage, are then forced to collide in two regions

around the ring. In these regions, where the two experiments D0 and CDF are located, a collision takes place every 396 ns.

The luminous region in CDF has a dispersion of about 30 cm in the directions of the beams ($\sigma_z \sim 30$ cm) due to the geometrical configuration of the bunches. The transverse section of the beams is approximately circular and has a gaussian dispersion $\sigma_t^{beam} \sim 30$ μm.

Tevatron performance and future prospective

The accelerator has been running since March 2001. Many problems were identified during the start-up period: the efficiency of the machine was severely limited, for instance, by beam-beam effects. The major losses were those of anti-protons during the squeeze, besides smaller but significant anti-proton losses also occurred at 150 GeV and during acceleration. Most of these losses have been overcome by changing the helices to increase the beam separations, with smaller antiproton emittance. In addition, other improvements have been implemented upgrading the accumulator stochastic cooling and modifying the proton beam loading compensation in Main Injector.

At present the instantaneous initial luminosity is topping out at 1.2×10^{32} cm^{-2}s^{-1} (see figure 2.4), which is very close to what was nominally expected (about 0.9×10^{32} cm^{-2}s^{-1} for first 3 years and 1.6×10^{32} cm^{-2}s^{-1} afterwards). The 1fb^{-1}-goal of integrated luminosity was achieved in summer 2005. However, due to the problems of the first 2 years of running, the integrated luminosity delivered is lower than expectation (see figure 2.5), although it will still be possible to reach the foreseen 4.4-8.6 fb^{-1} integrated luminosity by 2009.

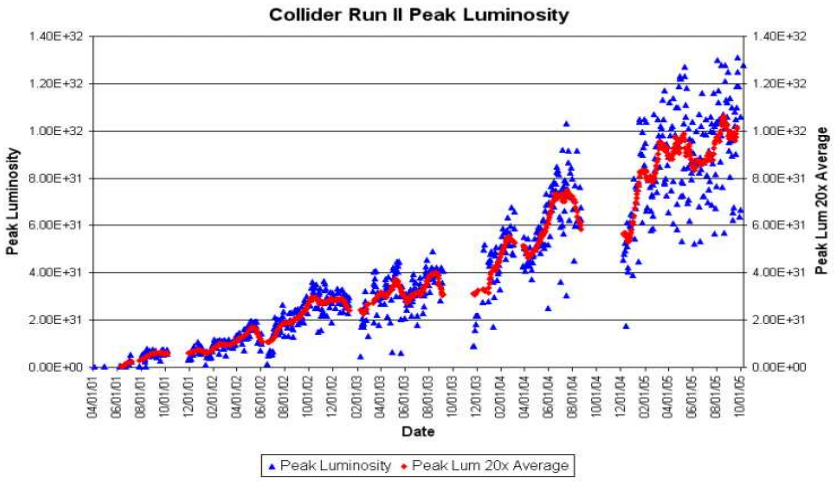

Figure 2.4: Instantaneous luminosities at the start of the stores though the October 2005.

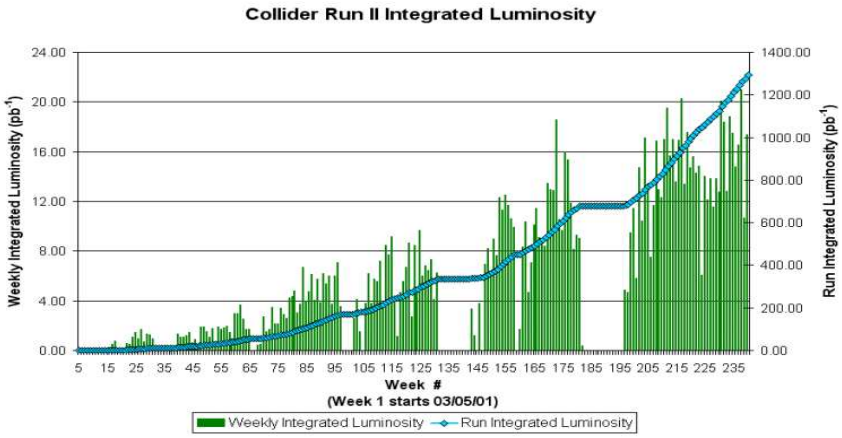

Figure 2.5: Delivered luminosity by the Tevatron since the start of RunII until October 2005.

2.2 Collider Detector at Fermilab

The CDF II detector (figure 2.6), located at one of the six nominal interaction regions of Tevatron, is a general purpose detector which combines precision charged particle tracking

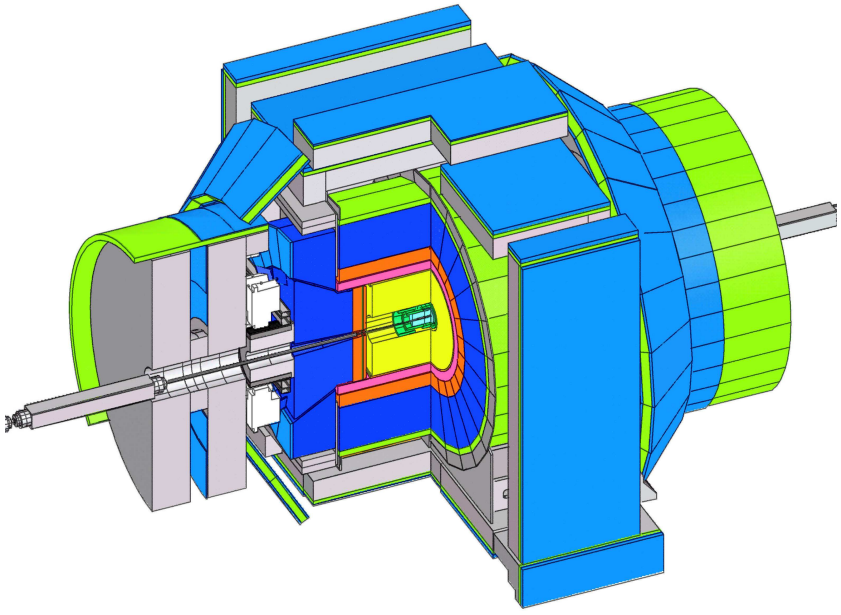

Figure 2.6: CDF Run II detector view.

with fast projective calorimetry and fine grained muon detection. It measures approximately 27 m from end-to-end, is about 10 m high, and weighs over 5000 tons. A schematic view of

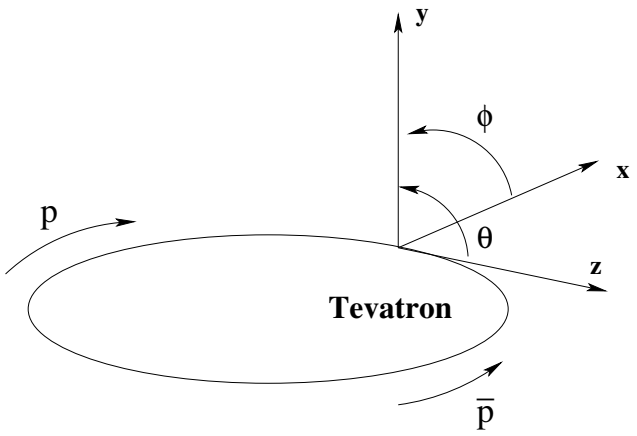

Figure 2.7: CDF Run II detector view.

conventionally used coordinates, related to one quadrant of the CDF II detector, is given in Figure 2.7. The right-handed coordinate system is defined with respect to the proton beam direction which gives the z-axis, the y-axis points vertically upward, and the x-axis lies on the plane defined by the Tevatron ring. The origin of the coordinate system is placed at the nominal interaction point that coincides with the center of the detector. The azimuthal angle (ϕ) is measured counterclockwise from the Tevatron plane, the polar angle (θ) is defined with respect to the positive z-axis, and the pseudo-rapidity (η) is as usual defined as:

$$\eta = -\ln\left[\tan\left(\frac{\theta}{2}\right)\right]. \tag{2.3}$$

To work with the new high luminosity and therefore with the high collision rate of Run II the CDF experiment underwent significant upgrades with many new features. In the following sections a description of the various subdetectors involved in this analysis is given as well as an overview of the major changes in the trigger and in the data acquisition system. A complete description of the CDF detector can be found in [28]: a longitudinal view of half of the CDF RunII detector is shown in figures 2.8.

2.2.1 Central Tracking System

The Central Tracking System (figure 2.9 shows a schematic $r-z$ section view) is designed to reconstruct the trajectories of charged particles coming from the interaction vertex. The whole system is composed of four subsystems that, coming from the nearest to the beam pipe, are the Layer 00 (L00), the Silicon Vertex Detector (SVXII), the Intermediate Silicon Layers (ISL) and the Central Outer Tracker (COT). The two innermost Silicon detectors provide an excellent 3D vertex measure inside $|\eta < 2|$, ISL allows forward tracking in a

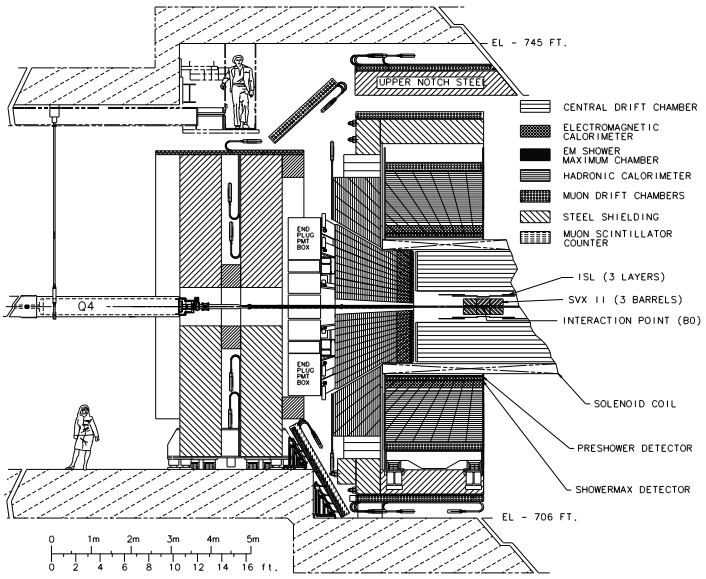

Figure 2.8: Longitudinal view of half of the CDF Run II detector.

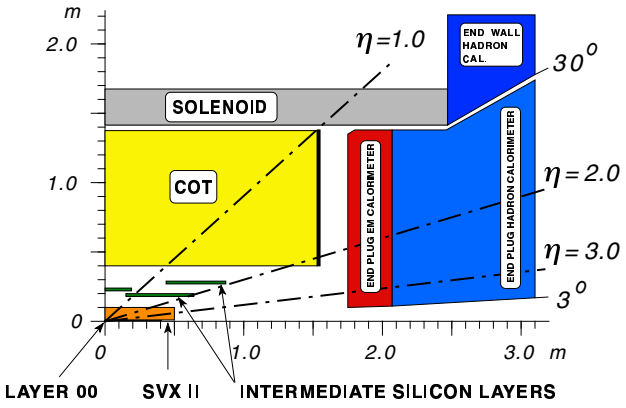

Figure 2.9: Schematic drawing of the tracker $r-z$ section of the CDF Run II tracker.

wider η range than the COT , and the COT completes the tracking in the central region ($|\eta| < 1$) before the particles hit the calorimeter. All these devices are placed inside a solenoidal magnetic field of 1.41 Tesla parallel to the beam line. The field is uniform to 0.1% in the region $|z| < 150$ cm and $r < 150$ cm. The solenoid and the cryogenic equipment represent 0.85 radiation length (X_0).

The curvature of the charged particles interacting with the magnetic field allows the extraction of precise information on the particle momentum as well as the sign of the charge. According to the Lorentz force, the transverse momentum of a reconstructed track

is given by:

$$p_T = B \cdot |q| \cdot e \cdot \rho, \tag{2.4}$$

where q is the particle charge, e is electron charge, B the magnetic field and ρ the radius of the helicoidal trajectory. The resolution of the whole tracking system on the track curvature has been estimated to be 0.68×10^{-4} cm^{-1}, which translates into a momentum resolution of $\sigma_{p_T}/P_T^2 \sim 6 \times 10^{-3}[\mathrm{GeV/c}]^{-1}$.

Silicon Vertex Detector (SVXII)

In Run I a silicon detector was used for the vertex reconstruction and tracking. This device is crucial for heavy flavor detection and has made possible the observation of the top quark and the measurement of its mass, as well as a wealth of b physics studies previously unfeasible in hadron colliders.

In Run II the overall vertex detector was redesigned to deal with the higher luminosity and the shorter bunch crossing with respect to Run I. This upgrade was also intended to allow the determination of precise 3D track impact parameters [1] over a wider acceptance range. This capability is crucial to provide b-tagging for studies of top production, supersymmetry searches and the search for the Higgs boson. SVX II and the associated trigger upgrades are also of great benefit to the CDF B physics program. Other features of SVX II are the improvement of the purity and efficiency of the tracking, in particular stereo tracking, and of the angular acceptance.

The SVX II is a silicon microstrip detector, made of thin silicon wafers. On the wafer surface several narrow lines of impurity atoms are implanted to form closely spaced strips. Diode junctions are thus created between the wafer and the strips. Applying a voltage with the proper polarity to the diode increases the depletion depth. The depletion junction, a free charges zone with strong electric field, is the actual sensitive region of the microstrip detector. When an ionizing particle passes through this region electrons are promoted to the conduction band which generates an electrical signal on a few strips. The strips are then read out by fast electronics revealing, to within a fraction of the strip spacing, where the particle intercepted the wafer along one dimension.

The whole detector coverage along z is driven by the spread of the primary interaction along this axis. SVXII consists of three 32 cm long cylindrical barrels, for a total length of 96 cm, providing a geometrical acceptance greater than 70%. The pseudorapidity coverage is $|\eta| < 2$. SVXII is characterized by 12-fold symmetry in ϕ, each containing five layers. These layers consist of double side silicon wafers (ladders) mounted with staggered radii to provide some overlap between adjacent ladders. The innermost layer is placed at a radius of 2.4 cm, while the outermost is at a radius of $\sim$ 10.7 cm. Three of the 5 layers have on one side the microstrips aligned to the beam while on the other side orthogonal. The remaining two instead have the strips on the two sides with a small-angle stereo. These strips are spaced in $r\phi$ by approximately 60 to 65 microns, depending on layer, and have implant widths of

[1] The impact parameter is defined as the closest distance between the primary vertex and the track helix in the transverse (d_0) and longitudinal (z_0) plane.

14 to 15 microns. The stereo strips of the SVX II are spaced by $(141, 125.5, 60, 141, 65)$ microns, and have implant widths of 20 microns for the 90° strips and 15 microns for the small-angle stereo layers. This design allows both a good resolution on the z-position of secondary vertices and an enhanced 3D pattern recognition. The length of each ladder is 29 cm, each divided into two half-ladders that are read out independently. The readout electronics consists of hybrid chips that are mounted directly to the silicon surface at each end of the half-ladder. The choice of electronics located on the silicon sensors was made to fulfill the requirement of a fast response and low occupancy detector. The high speed is for example required in order to use the SVX data in the Level 2 vertex trigger processor (SVT). The electronics inside the detector implied additional material within the active sensitive volume, for example cables and cooling tubes. This increases the multiple scattering of a particle worsening the pattern recognition capability. To partially mitigate this effect and improve the lever arm, another layer of silicon at small radius (Layer 00) was added to SVX II.

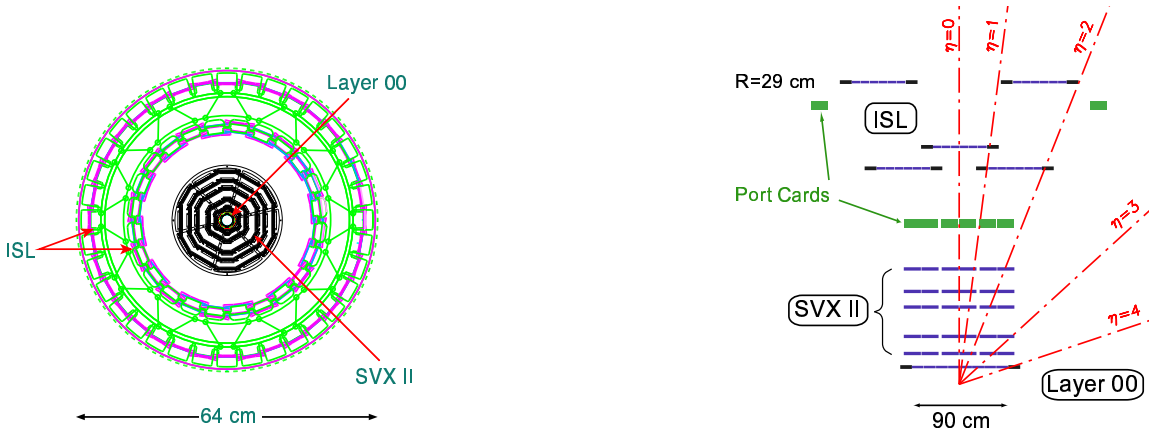

Figure 2.10: Schematic $r-\phi$ (left) and $r-z$ (right) views the Run II CDF silicon detector.

Layer 00 (L00)

L00 is a radiation tolerant, single-side axial-strip silicon layer, placed immediately outside the beam pipe at R$\sim$ 1.5 cm. Being so close to the interaction region L00 is expected to improve noticeably the impact parameter resolution (see section 3.1). The improvement of impact parameter resolution leads to a substantial improvement in b-tagging performance.

Intermediate Silicon Layers (ISL)

The Intermediate Silicon Layers were designed both to improve the tracking capabilities in the region $|\eta| < 1$ where tracks are based on the SVX II and on the COT and to allow silicon stand-alone tracking outside the COT η coverage. In the central η region the ISL consists of a single layer of silicon placed at a radius of 22 cm, while in the forward region

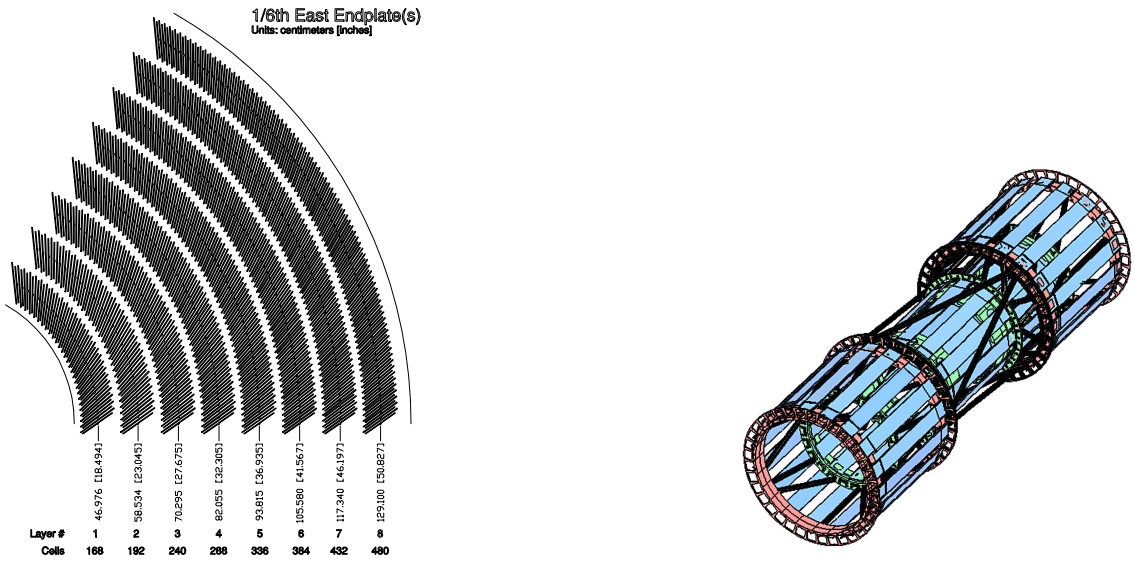

Figure 2.11: Intermediate Silicon Layer.

($1.0 < |\eta| < 2.0$), where the COT coverage is incomplete or missing, it has two layers of silicon at radii of 20 cm and 28 cm.

The ISL was developed using many features already studied for the SVX II. For example the data acquisition, power supplies and cooling system are nearly the same for these two detectors. Nevertheless the large surface area of silicon needed by the ISL required some simplification of the SVX II technology to minimize the subdetector cost. The lower occupancy and the lower radiation damage allowed the use of longer strips and wider readout pitch. This directly reflects in a smaller number of readout channels and chips reducing the cost of the front-end electronics and data acquisition.

The basic ISL unit is the ladder. Each ladder is made of three silicon detectors bonded together to form a single electrical unit. The readout hybrids are not mounted on the silicon as for the SVX II, but they are glued onto the edge of the mechanical support. Two ladders are paired to form a module $\sim$ 55 cm long. A silicon sensor consists of double-sided microstrip detectors with axial strips on one side and small angle stereo strips on the other. To reduce the number of channels the readout pitch is twice the strip pitch. The intermediate strips are not read out but contribute to the resolution via charge sharing.

A description of tracking performance is given in section 3.1.

Central Outer Tracker (COT)

The COT detector is an open cell drift chamber, placed immediately after the ISL in a region between the radii of 40 and 138 cm from the beam pipe. It consists of eight superlayers which cover the $|\eta| < 1$ region. Each superlayer groups 12 planes of sense wires alternated with layers of potential wires. To reconstruct tracks in three dimensions, four of the eight superlayers (axial) have wires along the axial direction, while the remaining four (stereo)

Resolution	COT	COT + SVXII + ISL
$\delta p_T/p_T^2[(GeV/c)^{-1}]$	3×10^{-3}	1×10^{-3}
$\delta d[\mu\text{m}]$	600	30
$\delta z_0[\mu\text{m}]$	5×10^3	30
$\delta\cot\theta$	6×10^{-3}	4×10^{-3}

Table 2.1: Resolution on various track parameters as obtained by the COT and by the COT + SVXII + ISL.

have wires tilted of $\pm 3°$ with respect to the axial direction; the superlayers are alternated starting with a stereo superlayer.

To cope with the high luminosity and the event pile-up keeping the device occupancy to reasonable values, the cell size was reduced by a factor of four with respect to Run I. Moreover the chamber is filled with a mixture of Argon and Ethane in proportions of 50:50, which, with a drift velocity of $\sim 100\mu m/\text{ns}$, ensures a faster response of the COT.

2.2.2 Time of Flight Detector

The CDF II detector has been equipped with a Time Of Flight(TOF) detector dedicated to particle identification. It is placed immediately outside the tracking system, and it consists of scintillator bars 3 meters long which cover the COT active volume. The thickness of these bars (4 cm) is constrained by the limited space between the COT and the solenoid, while the width (4 cm) has been determined by resolution and occupancy studies.

A particle reaching the TOF detector produces scintillation light which is collected by photomultiplier tubes attached to both sides of each bar. The pulse-height signal collected is used in coincidence with the T_0 of the event, to determine the time interval between the production and the detection of the particle. Moreover this signal gives a measurement of the z coordinate of the particle on the TOF detector.

This device is of particular importance in B physics, for which it is used to discriminate between protons, kaons and pions. With a time-of-flight resolution of 100 ps, the system is able to provide 2 standard deviation separation between $K^{\pm}$ and $\pi^{\pm}$ for momenta $p < 1.6\,GeV/c$, complementing the specific ionization energy loss dE/dx measured with the COT.

2.2.3 Calorimetry system

The CDF calorimetry system, located immediately outside the solenoid, is devoted to measure the energy and the direction of neutral and charged particle escaping the tracking region.

The calorimetry is designed to absorb these particles degrading their energy through electromagnetic and hadronic interactions. It is organized into two subsystems: the inner electromagnetic and the outer hadronic section, optimized to better react, respectively, to

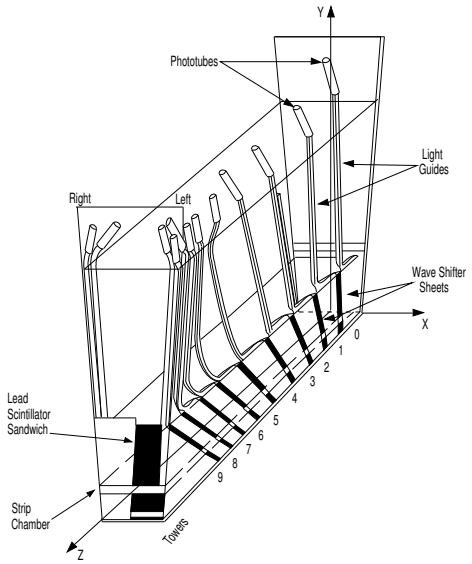

Figure 2.12: Perspective view of a CEM module.

electromagnetic and hadronic interacting particles. Both the subsystems are segmented in towers, which, projecting toward the centre of the detector, provide spatial information on the particle direction. Each tower consists of layers of passive material alternated with scintillator tiles. Particles, gradually absorbed by the passive material, leave a signal in the scintillators which is read by means of wavelength shifters (WLS) and carried through light guides to photomultiplier tubes. The CDF calorimetry systems, divided in central ($|\eta| < 1.1$) and forward ($1.1 < |\eta| < 3.64$) regions, are described in the following sections.

Central Calorimeter

The Central Calorimeter, apart from some upgrades on the readout electronics to match the time requirements imposed by Run II, is the same as in Run I.

It consists of two halves joined at $\eta = 0$, which cover the central region $|\eta| < 1.1$.

The Central ElectroMagnetic (CEM) subsystem is a sampling calorimeter made of lead sheets separated by polystyrene scintillator. Each half is organized in 24 wedges in ϕ, subtending an angle of 15^0. Each wedge is segmented with steps of $\Delta\eta = 0.11$ in 10 projective towers.

Behind the CEM are placed the Central and the End Wall Hadronic calorimeters (respectively CHA and WHA). The last subsystem is intended to cover the gap between the central and the plug hadronic sections. The transverse segmentation of the hadronic calorimeter is designed to match the geometry of the CEM. Towers, made of acrylic scintillator sandwiched between iron sheets, use a readout scheme similar to the one used in CEM.
To increase the spatial resolution of the calorimeter two proportional chambers are embedded in each wedge of CEM. The Central Electromagnetic Strip chamber (CES), placed 5.9

Electromagnetic Calorimeter		
	Central	Plug
Thickness	19 X_0, 1λ	21 X_0, 1 λ
− per sample(abs.)	0.6 X_0	0.8 X_0
− per sample(scint.)	5 mm	4.5 mm
Light yield	160 p.e. / GeV	300 p.e. / GeV
Stochastic resolution	11.6 %/ $\sqrt{E[GeV]}$	14 %/ $\sqrt{E[GeV]}$
Sampling resolution	14 %/ $\sqrt{E[GeV]}$	16 %/ $\sqrt{E[GeV]}$
Hadronic Calorimeter		
	Central	Plug
Thickness	4.5 λ	7 λ
− per sample(abs.)	1 in (central) 2 in (end wall)	2 in
− per sample(scint.)	6 mm	6 mm
Light yield	40 p.e. / GeV	39 p.e. / GeV
Resolution	75% / $\sqrt{E[GeV]}\oplus$ 3%	80% / $\sqrt{E[GeV]}\oplus$ 5%

Table 2.2: Characteristic of the CDF II calorimeter.

radiation lengths (X_0) deep in the EM towers, consists of wires in the $r-\phi$ plane and cathode strips in the z direction. It measures the charge deposition approximately at the depth of the maximum electromagnetic shower development. The pulse-height and the tri-dimensional spatial position of this signal allow a better reconstruction of electromagnetic objects.

The Central Pre Radiator (CPR) wire chamber, occupying the interspace between the magnetic coil and CEM, acts as a shower presampler. This detector is a very useful tool in the pion-photon discrimination.

Although the signal coming from both these wire chambers has to be integrated over several beam crossings, this turns out not to be a problem thanks to the low occupancy of this device ensured by its granularity.

Plug calorimeter

The plug calorimeter, which extends from $|\eta| > 1.1$ to $|\eta| < 3.64$, substitutes the Run I gas calorimeters. The new calorimeter, based on a similar design to that of the central calorimeter, consists of a lead-scintillator electromagnetic section followed by an iron-scintillator hadronic section.

The electromagnetic calorimeter contains an embedded Shower Maximum Detector (SMD) placed at a radial depth of $\sim 6X_0$. This device consists of 16 detector sectors each covering 45^0 in ϕ, with two layers of strips per sector. To keep the occupancy acceptable each sector is divided in two segments in pseudorapidity.

In addition the first layer of the electromagnetic calorimeters can be read out separately, acting as a pre-shower detector.

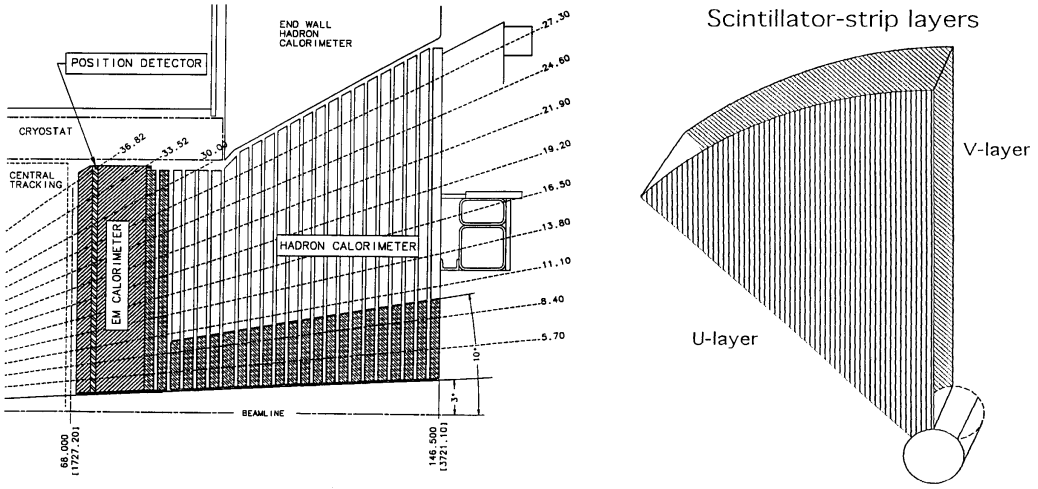

Figure 2.13: $r - z$ view of the plug calorimeter (left), and the SMD module (right).

The active elements of both calorimeters are scintillating tiles, which are arranged in projective towers. Groups of 48 or 28 towers (for $|\eta| < 2.11$ and $|\eta| > 2.11$) are organized in 12 concentric η sectors, with η ranging from 0.1 to 0.64 according to the increasing pseudorapidity.

As in the central calorimeter the active elements are read out using a wavelength shifter, optical cables then route the light from the tiles to the photomultiplier tubes. Each photomultiplier collects the light from the whole tower.

2.2.4 Muon detection

The last device surrounding the whole CDF II detector is the muon system. Thanks to the their high penetration power muons can escape the calorimeter reaching the muon chambers, while all the other particles are absorbed in the inner detectors (a part for invisible neutrinos).

The muon system is organized into 4 subsystems which cover different η regions – Central Muon Detector (CMU), Central Muon Upgrade (CMP), Central Muon Extension (CMX) and Intermediate Muon System (IMU) – allowing triggering and identification of muons up to $|\eta| < 1.5$. Each subdetector consists of several layers of active material where the muon signal is collected. The system relies on proportional wire chambers to provide tracking information, and scintillator counters for triggering. Minimal detectable muon transverse momentum is 1.4 GeV/c for CMU, CMX and IMU, while is 2.2 GeV/c for the CMP subsystem.

2.2.5 Trigger and data acquisition system

Trigger systems have crucial importance in hadron collider experiments. The collision rate, proportional to the huge $p\bar{p}$ inclusive cross section, is in fact much higher than the rate that data can be stored on tape. At CDF Run II the collision rate is of the order of 7 MHz, while the tape writing speed is limited to less than 70 events per second. The role of the trigger selection system is to effectively filter the interesting events among the large amount of "minimum bias" background. As discussed in the Section 2.1.4 the clocking of the whole experiment has changed since Run I, and thus the trigger system had to be redesigned.

The CDF trigger system has an architecture based on three decision levels. The rejection rate at each level is such that more sophisticated event processing is allowed at the next level with a minimum dead-time. The main characteristics of the three trigger levels are detailed in the following.

Level 1

The Level 1 trigger (L1) selection is based on a number of physics objects (primitives) constructed from the raw detector signals. To guarantee enough time for transmission and processing of the information coming from the various subdetectors, a L1 latency time of 5.5 μs has been chosen. Each subdetector is equipped with a local data buffering system able to accommodate the 42 events expected during such a period. L1 primitives are constructed by means of dedicated hardware, designed to analyze signals from the calorimeters, tracking chambers and muon detectors.

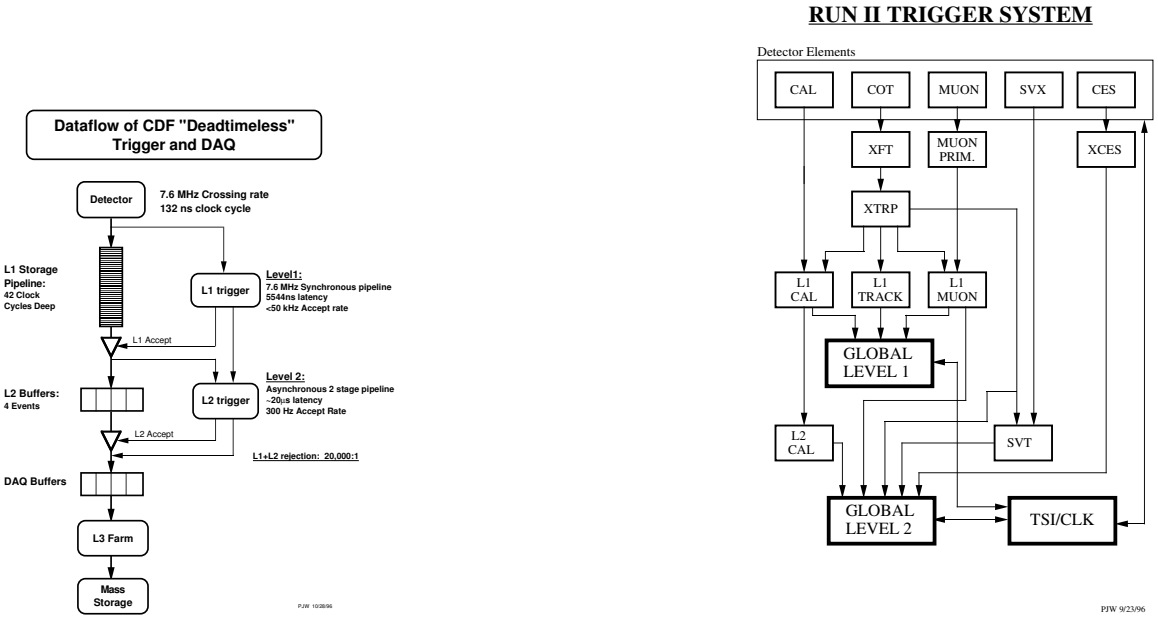

Figure 2.14: CDF pipelines and buffers trigger architecture (left). Block diagram of the Run II trigger system.

The most significant upgrade with respect to Run I is the new hardwired algorithm of track finding named eXtremely Fast Tracker (XFT). XFT analyzes the COT signals, returning track p_T and ϕ_0 by means of $r-\phi$ pattern recognition. These quantities are then used to better identify electron and muons, extrapolating and matching XFT tracks to calorimeter towers and to muon chambers. This task is performed by the dedicated unit XFTP.

The calorimeter informations used at level one, are the calorimeter tower signals grouped in pairs along η (trigger tower). Using the electromagnetic and the total transverse energy of these trigger towers, electron/photon and jets primitives are defined. Moreover using all the energy deposited in the trigger towers above 1 GeV the $\not\!\!E_T$ is computed.

The maximum L1 accepted rate is $\sim$ 20 KHz, while the typical one is about 12 KHz.

Level 2

Events accepted by L1 are then processed by the Level 2 trigger (L2). At this level event informations are collected into one of the four L2 buffers. When L2 is processing an event, the buffer where the event is stored is not accessible by L1; if all the four buffers are full the experiment incurs a dead-time. To overcome this problem each separate L2 buffer is connected to a two-step pipeline taking approximatively 10 μs. In the first step single detector informations are processed, and subsequently combined at the second stage to take a trigger decision. In this way the dead-time is less than 10% even at full L1 accepted rate.

At L2 all the L1 primitives are recalculated with higher precision. In particular, the cluster finder L2CAL combines a contiguous region of calorimeter towers with energy above 100 MeV to form clusters; for each cluster found, the total electromagnetic and hadronic energies are calculated and recorded, together with the tower multiplicity and the space coordinates of the seed tower. The information on the impact parameter are instead provided by the Silicon Vertex Tracker (SVT) [29]. The SVT is an hardwired algorithm, implemented into dedicated processors which, for the first time in hadron collider experiment, allows to trigger on long living particles, using a selection based on track impact parameter. The resolution after correcting for SVX alignment and beam line position has been found to be $\simeq 50\,\mu$m, as resulting by the convolution of the SVT resolution ($35\,\mu$m) and the beam spot wide ($30\,\mu$m).

The typical L2 accepted rate is between 100 and 300 Hz, depending on the luminosity.

Level 3

The Level 3 (L3) trigger is structured in two steps. First, for the events selected by L2, the informations from all the subdetectors are structured in one data block. This is then passed to the L3 Linux farm, where the whole event is reconstructed almost at the offline analysis level. Some variables like global event observables, might not be calculated due to the long processing time required. Then a trigger decision to whether or not store permanently the event is taken. Finally a trigger path is defined by making a unique combination of L1, L2 and L3 requirements.

Events that pass the Level 3 trigger are monitored in real time in the control room and are then stored on tape in Feynman Computer Center and organized in *datasets*, depending on the 3-level trigger path used to select the data.

2.2.6 Collected Luminosity for data analysis

The luminosity at CDF is measured both online and offline with the Cherenkov Luminosity Counters (CLC), using the process of inelastic $p\bar{p}$ scattering. Two CLC modules exist, installed at small angles in the proton and antiproton directions, with rapidity coverage between 3.75 and 4.75. Each module consists of 48 thin, long Cherenkov counters, filled with isobutane: counters are arranged around the beam-pipe in three concentric layers.

The online luminosity shows up in real-time and takes into account multiple interactions automatically but does not include further possible corrections or refinements, which are done offline. Every CDF event contains both the online and offline luminosity information – the average instantaneous luminosity and the integrated luminosity up to that event. It is then possible to find the integrated luminosity for a given dataset.

The systematic error of the luminosity measurement is dominated by the uncertainty of the elastic $p\bar{p}$ cross section, of the CLC acceptance and the related stability, together with uncertainties on beam losses, beam position and statistics. The total systematic error on the luminosity is $\delta L/L \simeq 6\%$.

Figure 2.15 shows luminosity measurements (integrated) as collected by the CDF experiment until the beginning October, 2005. However, the analysis presented in this thesis uses $\sim$ 350 pb^{-1} of data (until September 2004), mainly because of the time that is necessary to process the data. In addition, a further selection is needed to remove any bias resulting from malfunctioning detectors, thus bad runs are not considered in the analysis.

Figure 2.15: Up-to-date Luminosity measurements for runs which have Physics* in the run-type, so that they can be potentially used for analyses (as a function of the date).

Chapter 3

Event reconstruction

The Bottom production cross section measurement is performed using as observables the jets. Results are based on 300 pb^{-1} of data collected with inclusive calorimetric jet trigger implemented at CDF. This chapter describes the procedures used to reconstruct event's relevant quantities for the measurement: charged particle trajectories (tracks) and jets, in respectively section 3.1 and 3.2. After defining, in sections 3.3 to 3.5, the main data samples and their luminosities (plus other control samples used in the analysis, Monte Carlo samples and z-vertex algorithm), in section 3.6 the implemented event selection is reported. Finally, corrections on the transverse energy of the jets for detector effects and multiple interactions are described in section 3.8.

3.1 Tracking reconstruction

The detection and tracking of charged particles is an essential part of this (and many other) analyses: for instance, the reconstruction of primary and secondary vertices depends on the software capabilities to define the direction and curvature of the particles' path (helix), together with their momenta.

Tracking algorithms can either use combined informations from COT and Silicon detector, or use standalone inputs from one of the two sub-systems. The main procedures implemented are summarized in the next subsections.

3.1.1 COT tracking

The Central Outer Tracker is able to reconstruct particle trajectories and their momenta up to $|\eta| < 1$ (maximal coverage of the drift chamber). The pattern recognition algorithm is performed according to many successive steps [30], summarized below.

- In each of the eight superlayers, hits in three consecutive wires are grouped and fitted to a straight line by the method of the least squares. These segments are listed in decreasing p_T and used as seeds. Other hits in the superlayer within a distance of $\simeq$

1 mm from the segment (20 ns in road time considering a drift time of 55 μm/ns) are added to the straight line fit using an iterative procedure. Seed-segments defined in this step can use axial or stereo superlayer hits.

- Tracks are initially reconstructed using axial ($r - \phi$) superlayer seed-segments only. The segments with good angle and position matches are then linked together to form axial tracks. To increase the reconstruction efficiency, two algorithms are run in parallel for this purpose:
  - the "segment-segment linking" algorithm, that matches segments from different superlayers and does a fit on all hits in the segments using a χ^2 minimization;
  - the "histogram linking" algorithm, that starts with one segment position and the beam position, makes a circle fit to these points and considers a band of ± 1 cm around this circle. It then looks for any hit within this band: a 200 μm-binned histogram is filled with the radius (the distance to the center of the track circle) of each hit. If the most populated bin contains more than 10 hits, a track is made out of those hits. Finally, the procedure attempts to add other hits within 750 μm of the track and re-fits it: if the fit succeeds and the track has at least 20 axial hits (15 if the seed segment is SL4), the track is added to the track collection.

  Track duplicates (reconstructed by both algorithms) are removed.

- In a second step of pattern recognition procedure, stereo angle superlayer information is added to the axial tracks. Again two algorithms are implemented, this time running sequentially:
  - the stereo-segment linking algorithm matches stereo segments to existing axial tracks starting from the outer stereo superlayer; thus it performs a re-fitting of the track to estimate the z and cotθ helix parameters and then continues the procedure looking to inner layers.
  - Following this re-definition, the hit linking algorithm tries to recover stereo information for axial tracks that failed the stereo-segment matching. To do this, stereo tracks are used to reconstruct the z-coordinate of vertex seeds in the event and scans the cot θ parameter of the helix for the best hit usage.

- Finally, tracks are refitted to take into account any underestimation of the material used in the procedures above, variations in the value of the applied magnetic field etc; also, a refit is necessary to obtain the best energy loss corrections.

The tracking efficiency is a function of the track transverse momentum: it is found to be above 99% for tracks with $P_T > 1.5$ GeV/c ($P_T > 1.35$ GeV/c in case of isolated muons), while it decreases down to 95% for 500 MeV/c tracks.

3.1.2 Silicon Detector Tracking

Tracking algorithms using silicon information are either standalone or combine silicon and COT inputs. The main features of these procedures are summarized below.

- The Silicon clustering algorithm (Si-standalone) uses the strip data from the silicon detectors and produces a set of strip clusters that represent charge deposited by a single particle as it traverses the silicon, considering that particles often deposit charge among several adjacent strips. The profile of the resulting "cluster" depends upon many factors, including the strip pitch, angle of incidence of the track, type of charge carrier, diffusion of charge carriers in the silicon, and magnetic field to name a few. The purpose of the clustering algorithm is to identify groups of contiguous strips that represent the charge from a single particle, gather them into a strip cluster (hit) and estimate the exact location of the track impact. Once this set has been identified as a cluster, the position and resolution of the track are calculated.

- Outside-in Algorithm (OI) tracking takes COT tracks and extrapolates them into the silicon detectors, adding hits via a progressive fit. Only tracks with at least three hits are kept. As each layer of silicon is encountered (going from the outside in), a "road" is established around the seed track: the road is four standard deviations wide, based on the error matrix of the track. Hits that are within the road are added to the track, and the track parameters and error matrix are refit with this new information. A new track candidate is generated for each hit in the road, and each of these new candidates are then extrapolated to the next layer in, where the process is repeated. As the extrapolation proceeds, the track error matrix is inflated to reflect the amount of scattering material encountered. At the end of this process, there may be many track candidates associated with the original COT track. The candidate that has hits in the largest number of silicon layers is chosen; if more than one candidate has the same number of hits, the χ^2 of the fit in the silicon is used as discriminating quantity.

One of the most important track features for b-tagging algorithm is the impact parameter resolution, since this quantity is used to select displaced tracks, thus heavy flavor candidates (see next Chapter). The single track impact parameter resolution is about 40 μm including a 30 μm contribution from the beamline. This is a considerable improvement with respect to the past (when $\sigma_{d_0} \simeq$ 50-60 μm), thanks to the introduction of Layer 00 information in track reconstruction. Figure 3.1 shows the impact parameter resolution as a function of track P_T with and without Layer 00 hits included in the track reconstruction, for the region corresponding to SVX Readout (high passive material density): the improvement is particularly visible at low P_T, where multiple scattering is the dominant component. On the other hand, the improvement is less pronounced but still remarkable in the low material density region (see figure 3.2).

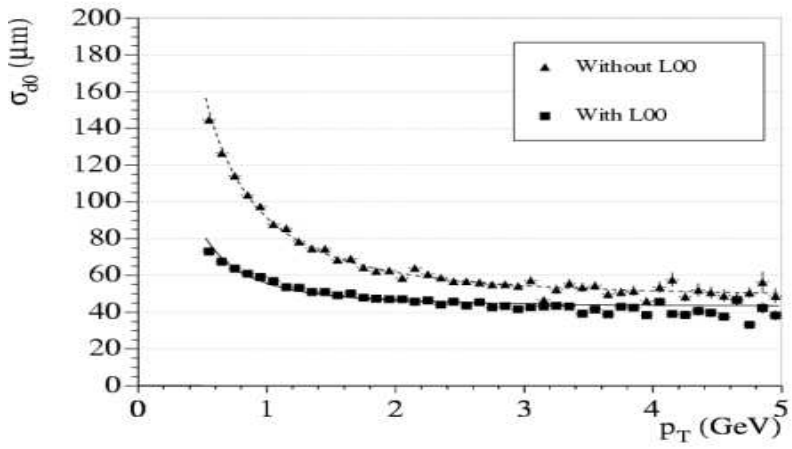

Figure 3.1: Impact parameter resolution (σ_{d_0}) in μm as a function of the P_T for tracks passing through passive material without Layer 00 hits (triangles) and with Layer 00 hits (squares).

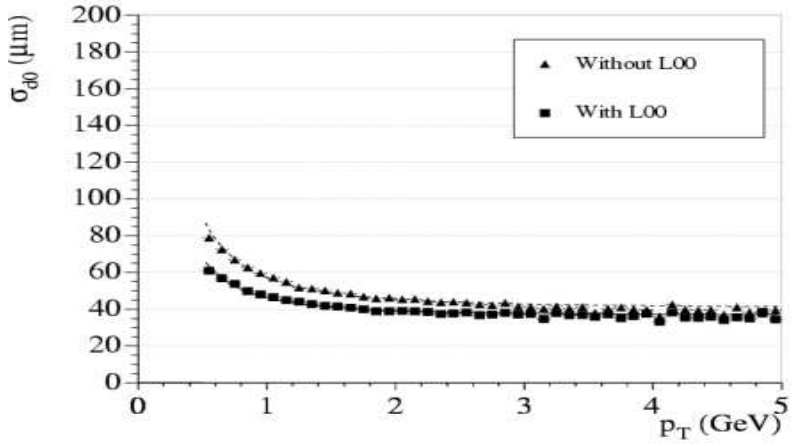

Figure 3.2: Same as figure 3.1, for tracks passing through silicon only.

3.2 Jet reconstruction

A jet is a collimated flow of hadrons in hard scattering processes, whose energy, mass and momentum can then be related to a collection of partons in a perturbative QCD calculation. Each "particle" i, associated with a calorimeter cell (tower) or a hadron at the experimental level, and with a parton in a QCD calculation, carries a 4-momentum p_i^μ, which we take to be massless. Differences in the properties of reconstructed jets when going from the parton to the hadron or calorimeter level are a major concern for a good jet algorithm. The task is to select a set of particles which are emitted close to each other in angle and combine their momenta to form the momentum of a jet. The selection process is called the "jet algorithm" and the momentum addition rule is called the "recombination scheme". We

consider here cone algorithms. These kinds of procedures are intended to cluster all energy within a given radius, R, around a point to form a jet: all particles whose trajectories lie in an area $A = \pi R^2$ of η-ϕ space, where η is the pseudorapidity are considered. In principle one simply searches for all such stable cones to define the jet content of a given event. In practice, this is not possible because of limited computing resources, so we define a clustering iterative process to search for stable cones, thus to start with only those cones centered around the most energetic particles in the event. Usually the seeds are required to pass a certain threshold (few hundred MeV): the E_T-weighted centroids are calculated for the particles in each seed-cone and then the centroids are used as centers for new cones in the η-ϕ space. Unfortunately, nothing prevents the final stable cones from overlapping. A single particle may belong to two or more cones. As a result, a procedure must be included in the cone algorithm to specify how to split or merge overlapping cones.

To compute jet cross sections by using QCD perturbation theory, the definition of jets should also fulfill strong constraints to guarantee its perturbative safety. This means that the definition has to be infrared safe (jet properties cannot depend on the presence of arbitrarily soft partons), collinear safe (jet properties cannot change by replacing a parton with a set of collinear partons carrying the same total momentum) and collinearly factorisable (jet properties should be insensitive to partons radiated collinearly to the beam direction). If the jet definition is not perturbatively safe we cannot perform calculations at fixed order in perturbation theory because they are affected by uncancelled infrared divergences[1]. Naively a jet algorithm should be both infrared and collinear safe: the effect of infrared radiation on the cluster momentum vanishes in the infrared limit, and the energy measured for the jet is the same whether a single particle/tower is at the core of the cone or whether there has been collinear splitting. Prescriptions to select cones can easily violate this expectation.

For example, figure 3.3(a) shows how two particles can be emitted with a certain separation in (η-ϕ): suppose this is higher than the cone radius R (therefore the two particles/towers are assigned to different jets) but smaller than $2R$. In figure 3.3(b) the same scenario is shown but with a third soft particle (such as a "soft gluon") emitted between the two original particles. Drawing an additional cone related to the third particle, we can see that this encompasses all three particles and they will be classified in the same jet. Since the presence of a soft particle changes the classification of hard event, the related jet algorithm is infrared unsafe and thus not sufficient to describe perturbative QCD where an arbitrary number of soft gluons can be radiated at sufficiently high orders.

In a similar way, a infinite number of collinear splittings occurs at higher order in perturbation theory. Figure 3.4 illustrates a possible problem: the difference between the situations shown on the right and left plots is that the central and hardest parton may split in two almost collinear partons. On the left side the distance between the lateral partons

[1]In full QCD theory the perturbative divergences are regularized by small physical cutoffs related to hadron masses and finite experimental resolutions: these cutoffs are always present, independently of the jet definition. However, in case of perturbative safe definition, their effects are suppressed by some inverse power of the jet transverse energy, thus they are small. This power suppression does not work in perturbative unsafe jet definitions.

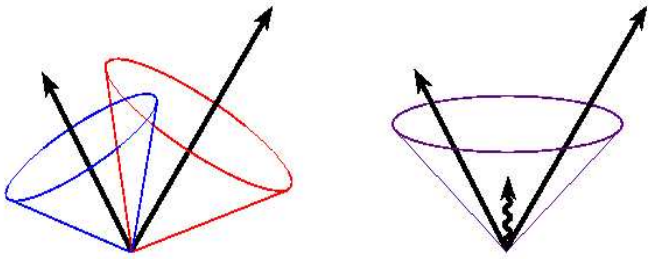

Figure 3.3: Example for a situation which can lead to infrared problems in an unsafe cone algorithm.

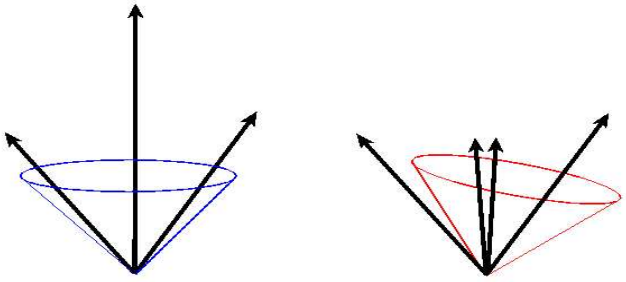

Figure 3.4: Example for a situation which can lead to collinear problems in an unsafe cone algorithm.

is larger than R but the three hard partons all fall within a cone of radius R around the central one that is the highest energy particle: all three partons are recombined in the same jet. Suppose that collinear splittings make the right hand parton the one with largest E_T (right plot): drawing the first cone around the highest E_T parton will recombine it with the two central partons and a separate jet is likely to be assigned to the remaining fourth parton. Thus we have that a difference in the jet number that depends on the presence or absence of collinear splitting and that must be avoided because the incomplete cancellation of the logarithmic divergences of real emission and virtual combinations will lead to a collinear unsafe jet algorithm. One can eliminate such ambiguities by making the selection or ordering of jet definition cones independent of the E_T of individual particles.

3.2.1 The MidPoint algorithm

During the Tevatron RunII QCD workshop[31] the two experiments CDF and D0 agreed to use the MidPoint algorithm. MidPoint is a seed-cone procedure: it gets its name from the fact that it explicitly places another seed at the energy-weighted midpoint between any two seeds (towers or particles). This aims to reduce the number of events which are reconstructed differently by theorists and experimentalists. In particular in the case of figure 3.3, MidPoint would find the higher energy, single jet solution as would the theoretical analysis. Besides this, the number of jets reconstructed strongly depends on soft energy

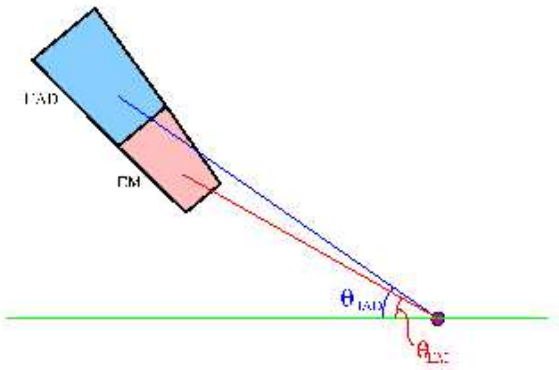

Figure 3.5: Schematic of a single CDF calorimeter tower.

deposition: the inclusion of extra midpoints eliminates these soft effects because observables no longer depend on whether soft emission actually took place. Thus, the procedure is infrared and collinear safe.

The MidPoint algorithm in CDF uses the so called *E-scheme* (or *4-vector*) as the recombination scheme; a tower (or a hadron or a parton) i is clustered into a cone and eventually into a jet if the separation in rapidity-azimuthal angle $(Y - \phi)$ satisfies the following condition:

$$i \subset: \sqrt{(Y^i - Y^c)^2 + (\phi^i - \phi^c)} \leq R \tag{3.1}$$

where c denotes the cone variables. The kinematic variables of a cluster of particles is given by direct addition of the 4-momenta of the individual massless particles i:

$$p^\mu = (E, p_x, p_y, p_z) = \sum_i p_i^\mu. \tag{3.2}$$

Since the resulting clusters have a clearly defined mass, we must distinguish transverse energy E_T from transverse momentum p_T, and pseudorapidity η from rapidity Y. We define

$$p_T = \sqrt{p_x^2 + p_y^2}, \qquad \phi = \tan^{-1}\frac{p_x}{p_y}, \qquad Y = \frac{1}{2}\ln\frac{E + p_z}{E - p_z}, \tag{3.3}$$

The rapidity Y and the azimuthal ϕ are used as the position of the jet when calculating its separation from other particles or jets. Note that in this scheme one does not use the scalar E_T variable. The 4-vector variables defined above display the desired Lorentz properties so that rapidity and transverse momentum are the kinematic variables used to define the jets in the analysis. In this way, phase space boundaries will exhibit the required stability necessary for all-order resummations.

In the case of experimental inputs, the MidPoint algorithm uses as seeds simply calorimeter towers in which the energy deposition exceeds a certain predefined limit (0.3 GeV for

this analysis). Figure 3.5 shows the schematic of a single CDF calorimeter tower, each tower consisting of an electromagnetic (EM) and a hadronic (HAD) component. For each tower the 4-vectors for the hadronic and electromagnetic compartments are constructed as below:

$$\begin{aligned} \mathbf{P}^{\text{tower}} &= (P_x, P_y, P_z, E)_{\text{Had}} + (P_x, P_y, P_z, E)_{\text{EM}} \\ Y^{\text{tower}} &= \frac{1}{2}\ln\left(\frac{E^{\text{tower}} + P_z^{\text{tower}}}{E^{\text{tower}} - P_z^{\text{tower}}}\right) \end{aligned} \tag{3.4}$$

where:

$$\begin{aligned} P_x(\text{Had/EM}) &= E_{\text{had/em}}\, sin(\theta_{\text{had/em}})\, cos(\phi) \\ P_y(\text{Had/EM}) &= E_{\text{had/em}}\, sin(\theta_{\text{had/em}})\, sin(\phi) \\ P_z(\text{Had/EM}) &= E_{\text{had/em}}\, cos(\theta_{\text{had/em}}) \end{aligned}$$

Polar angles $\theta_{\text{had/em}}$ are calculated with the correct Z vertex of the event; the azimuthal angle ϕ is the same for the hadronic and electromagnetic tower compartments.

3.2.2 The JetClu algorithm

In RunI, but also in many analyses in RunII, the algorithm implemented to reconstruct jets is JetClu: it is also cone-based and similar to MidPoint for the iterative procedure implemented, without midpoints addition. One of the main differences between the two algorithms is the so called "ratcheting": with this feature, a jet cone always contains the original seed towers that initiated it (precluster), even if the subsequent clustering steps place these seeds outside the stable jet cone. this can be the case, for example, for close jets, where one is more energetic than the other. The advantage of ratcheting is to prevent that energy associated with hard scattering is finally unclustered in any of the jet; nevertheless, such a procedure cannot be modelled in perturbation theory and the algorithm is consequently not infrared and collinear safe. For instance, in the case of figure 3.3, JetClu would reconstruct two distinct jets.

In addition to this feature, JetClu uses the *Snowmass* scheme: this recombination scheme was largely used in RunI and still adopted today, but has some disadvantages. In particular it leaves the question of jet mass open by only defining the total transverse energy, rapidity and azimuthal angle of a set of parton momenta as the E_T weighted sums of individual particle variables. For the original massless particle $E_T i{=}P_T i$ and $\eta_i = Y_i$. The corresponding recombined variables for a cluster of particles are then given by the total transverse energy, the pseudorapidity and azimuthal angle

$$E_T = \sum_i E_{Ti}, \qquad \eta = \sum_i \frac{E_{Ti}}{E_T}\eta_i, \qquad \phi = \sum_i \frac{E_{Ti}}{E_T}\phi_i. \tag{3.5}$$

Note that the designation of η as pseudorapidity is purely conventional: it corresponds to neither the real pseudorapidity nor the rapidity of the massive cluster and is approximately equal to either only in the limit of small cluster mass ($<< E_T$). The concomitant loss

of Lorentz invariance is a serious disadvantage of the Snowmass convention, together with problems related to resummation calculations.

3.2.3 Splitting and Merging

As underlined before, one feature that generally affects cone algorithms is the merging/splitting procedure whereby two cones separated by less than twice the cone radius are merged into a single jet. This is done if their overlapping transverse momentum is larger than a fraction $f_{\rm merge}$ of the total momentum of either of the two cones. For MidPoint $f_{\rm merge}$ was initially agreed to be to 50% for both the CDF and D0 experiments in RunII but recently it was agreed to change this limit at CDF to 75%. JetClu uses 75%.
The splitting/merging procedure is iterative in the case of MidPoint, and there is no limitation in the number of jets involved. Starting from the highest P_T jet, jets are merged until the overlap fraction is lower than the threshold. This can sometimes lead to many jets being merged into a single jet. The use of the lower, 50%, merging fraction as well as the iterative procedure were seen to lead to a small fraction of jets which spanned huge areas of the detector (with ΔR sometimes as large as 2.5). This issue was investigated and it was decided to change the merging/splitting fraction to 75% while leaving the iterative merging procedure.

3.3 Data Samples

The analysis presented in this document relies on data collected from February 2002 through September 2004. The primary samples for this analysis are the five jet datasets[2] having different transverse energy E_T threshold. Other control samples, used to study specific jet corrections or properties of the b-tagging algorithm include the Minimum Bias trigger and electron trigger with nominal 8 GeV E_T^{ele} threshold.

3.3.1 Inclusive jet samples

Details of the trigger paths, related to the three trigger levels, for the five jet datasets are shown in Table 3.1. To reduce the bandwidth, at each trigger level a prescale is applied: values of nominal prescale factors (PS) are also shown in parenthesis.

At Level 1, events with a single tower of transverse energy above a given threshold (5 or 10 GeV) are selected for all trigger paths. With the exception of ST05, at Level 2 a cut on transverse energy of the calorimetric clusters is applied, with thresholds of respectively 15, 40, 60 and 90 GeV. Finally at Level 3, jets are reconstructed, assuming the event vertex coordinates are at zero, using the JetClu algorithm. Events with $E_T^{\rm jet}$ above a fixed threshold (20, 50, 70 and 100 GeV) are selected. ST05 does not have selection cuts on Level 2 cluster or Level 3 jet energy but is heavily prescaled at Level 2.

[2]Data are reprocessed with the version 5.3.1 of CDF software using version 5.3.3_nt for the analysis

Path	L1(PS)	L2(PS)	L3
ST5	ST05(20/50)	AUTO_ACC(1hz,300,600,1000)	–
Jet20	ST05(20/50)	CL15(12,25)	J20
Jet50	ST05(20/50)	CL40(1)	J50
Jet70	ST10(1)	CL60(8)	J70
Jet100	ST10(1)	CL90(1)	J100

Table 3.1: Trigger paths and nominal prescales (in brachets) for the five jet datasets used in this analysis: Single Tower 05 (ST05), Jet20, Jet50, Jet70, Jet100, where the 20,50 .. number refers to the trigger threshold on the jet transverse energy.

The different datasets with the related luminosity used and the calculated prescale are reported in table 3.2, the quoted values referring to data required to pass the good run criteria: bad runs are excluded from the dataset in order to remove any bias resulting from malfunctioning detectors[3]. The total integrated luminosity of runs included in the good run list is 346 pb^{-1}: values reported in table 3.2 are different for each dataset since a further requirement is applied on the number of events, which must be the same for each run in the database and in the used ntuples. This additional requirement is applied to avoid miscalculation of the luminosity: as a consequence, the official 6% uncertainty can be considered the only source of error for the integrated luminosity.

Trigger	dataset	Lum. pb^{-1}	<Prescale>
ST5	gjs00d	310.6	11717
J20	gjt10d	253.1	503
J50	gjt20d	301.2	22.9
J70	gjt30d	264.9	8
J100	gjt40d	303.7	1

Table 3.2: Datasets used with their corresponding integrated luminosity after bad run removal and relative average prescale. The luminosity values are not corrected here for the 1.019 correction factor used to calibrate common CDF/DØ luminosity counting.

The prescale factors of certain datasets (ST05, Jet20 and Jet50) have changed during data taking period: those are directly extracted from each event according to the trigger path name and an average prescale factor is calculated. For ST05, in particular, the prescale at L2 for 10.8% of the events (run<147879, corresponding integrated luminosity 6.9 pb^{-1}) was dynamic giving a maximum allowed bandwidth of 1 Hz. Figure 3.6 on the left shows the prescaled cross section (σ_{PS}) for the range of runs with unknown PS: the average σ_{PS} is about 150 pb. Assuming the total unprescaled cross section to be constant, we extrapolate

[3]version 7.0 good run list with silicon, means requiring the silicon tracker working

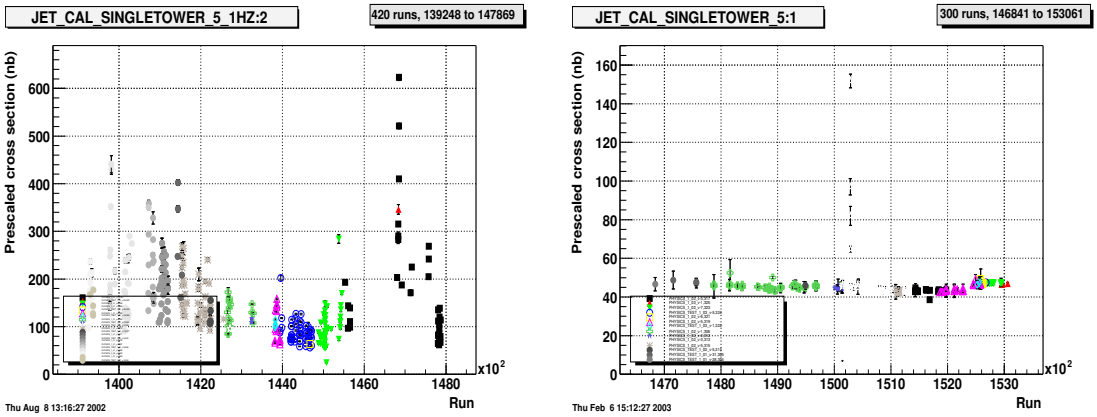

Figure 3.6: Prescaled cross section for Single Tower 05 trigger, related to the range of runs with unknown prescale (left), and a reference one, with PS at L2 of 300. The L1 prescale is constant (= 20) in both cases.

an average prescale of 80 using the value of σ_{PS} for a bunch of runs with known L2 PS (PS=300) shown in the same figure, on the right. Clearly the approximation of this simple calculation only allows to fix a central value, but even assuming the uncertainty of this method to be 100% and combining it to the 6% on the integrated luminosity, the overall systematic uncertainty increases only to 6.2% for ST05 dataset. The raw inclusive jet P_T distribution for the five triggers after prescale correction is shown in figure 3.7.

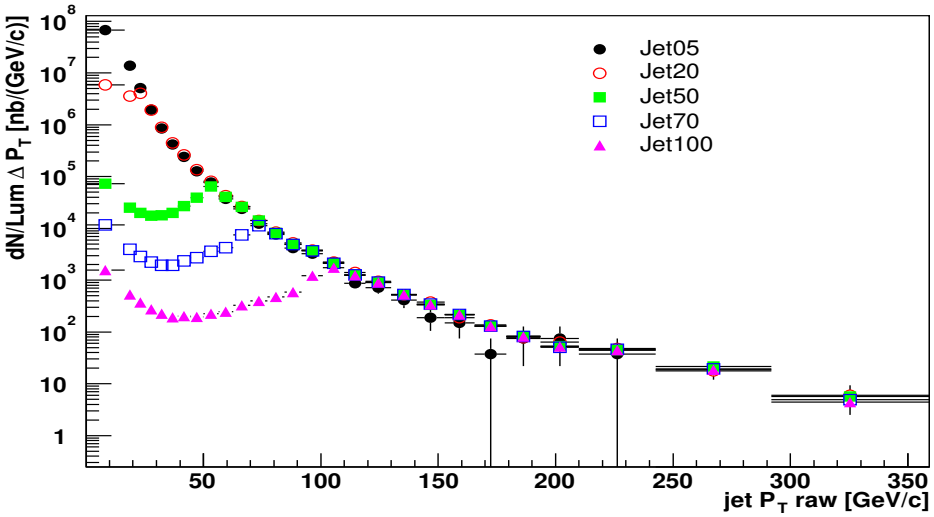

Figure 3.7: Raw inclusive jet P_T distribution for the five trigger datasets after prescale correction: below the trigger threshold, the number of jets is suppressed as expected.

3.3.2 8 GeV electron trigger

At the Level 1 of the trigger, calorimeter towers are clustered in pairs so that the effective $\eta - \phi$ segmentation is $0.2 \times 15°$. At least one trigger tower is required to have E_T >8 GeV, with an E_{HAD}/E_{EM} ratio less than 0.125. At least one track with P_T >8 GeV/c is required to point to this tower. At level 2, the trigger towers are clustered and the total E_T cluster must be larger than 16 GeV. Finally, at level 3 a full event reconstruction and electron identification is performed. A 3-dimensional COT track of P_T >8 GeV/c must point to a cluster of E_T >8 GeV with $E_{HAD}/E_{EM} < 0.125$. The electron identification cuts are:

- E_T >9 GeV, P_T >8 GeV,
- 0.5< E/P <2, where E is the total energy of the electron calorimeter cluster and P is the electron momentum measured from the track,
- Had/Em <0.05, where Had(EM) is the energy of the electron in the hadronic (electromagnetic) calorimeter,
- L_{shr} <0.2, where L_{shr} is a variable related to the EM shower shape; the energy deposited in the two towers adjacent to the tower at the center of the cluster is compared to the one expected from test beam data, thus

$$L_{shr} = 0.14 \times \frac{\sum_i (E_i^{obs} - E_i^{exp})}{\sqrt{(0.14\sqrt{E_E M})^2 + \sum_i (\delta E_i^{exp})^2}} \tag{3.6}$$

- The shower maximum detector (CES) is used to reject possible hadron contamination: the track is required to match the CES cluster in both axial ($|\Delta Z|$ <3 cm) and azimuthal ($|\Delta X|$ <3 cm) directions; the shape of the CES cluster is required to be similar to the one evaluated from test beam data (χ^2_{CES} <10).

About 200 pb^{-1} of data, after the removal of bad runs, are used in the analysis: since the sample has only been used for checking, the use of the full dataset has not been necessary.

3.4 Jets Monte Carlo samples

Monte Carlo event samples are used in this analysis to determine the response of the detector (and related correction factors on the measured jet energy), to find b-tagging efficiency and b-flavor content etc. The generated samples are passed through a full detector simulation, based on GEANT3[32], where the GFLASH[33] package is used to simulate the energy deposition in the calorimeters. Reconstruction of jet and track related quantities is obtained using the same software version as for the data. Samples of simulated inclusive jet events have been generated using Pythia 6.203[34] and Herwig 6.4[35] Monte Carlo generators. The Pythia samples (used as default, while Herwig ones are considered as control samples) have been created using a special tuning to better simulate the underlying event. The set of parameters, denoted as Tune A, has been optimized using CDF RunI data. CTEQ5L[36]

are the PDF functions used. The used samples are associated to datasets called Pt18, Pt40, Pt60, Pt90, Pt120, Pt150, Pt200, Pt300, where the name indicates the P_T cut at the level of the hard scattering. Before any selection, the MC content in term of $b\bar{b}(c\bar{c})$ pair production at the level of the hard scattering is on average about 4%(11%), for both Pythia and Herwig samples. In addition, Pythia Monte Carlo samples filtered in order to have at least 1 b-quark in the initial parton list have been produced: those samples are completely equivalent to the inclusive ones but for the b-filter, and they are mainly used to extract the b-flavor content from the data (see section 4.5).

3.5 Z-vertex reconstruction

At level 3, jets are reconstructed using JetClu algorithms and assuming the primary vertex coordinates to be zero. It is then necessary to rebuild offline the jets using the appropriate vertex and reconstruction procedure.

The z-vertex algorithm has been developed to measure the z-position of interactions due to collisions. At the stage of jet reconstruction, informations related to the transverse (xy) plane primary vertex are not used, since in first approximation the vertex coincides with the beam axis; thus, the problem is reduced to finding its z-coordinate.

Once z is defined, each calorimetric tower 4-momentum is calculated according to equations 3.4 and 3.5, thus used to reconstruct jets using the MidPoint algorithm.
The procedure is seed-driven and to reduce the fake rate uses vertices created upstream as input and associates to them tracks reconstructed in the event. Two lists of primary vertex candidates are considered, the one created by `PVFinder` - a pre-tracking finder which attempts to find vertices using the 2D hits from small-angle stereo layers - and a COT based vertex collection `COT Standalone vertices`. The collections are then merged to provide a single list of seeds. To reconstruct primary vertices the Z-vertex finder uses a subset of tracks. The tracks are selected and classified as follows:

- COT-only and COT+SVX tracks with at least 3 axial and 3 stereo COT segments (good COT tracks) and χ^2(COT)/DOF$<$ 4: track quality[4];
- SVX-only tracks with at least 5 axial and 3 (z+small angle stereo) SVX hits and χ^2(SVX)/DOF$<$8: track quality 4. COT+SVX tracks found by inside out algorithm are required to pass the same requirements as good SVX tracks;
- tracks with at least 2 axial and 2 stereo COT segments and χ^2(COT)/DOF$<$ 4 AND at least 4 axial and 3 (z+sas) SVX hits and χ^2(SVX)/DOF$<$ 8 : track quality 2.

The highest P_T COT track also makes a vertex, to increase the efficiency of vertex finding. In this case, the quality assigned to the track is 12. All the participating tracks are also required to have impact parameter $\mid d_0 \mid \leq$ 1cm. The list of the reconstructed seed vertices

[4]The quality of the track is a flag defined in order to have good vertices only with specified combinations: *i.e.*, since a good vertex should have quality 12, at least 2 quality-6-tracks must be used.

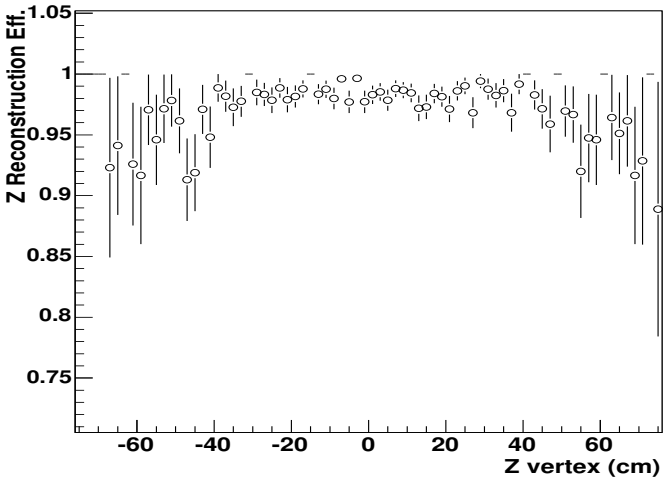

Figure 3.8: Efficiency to find a good primary vertex (closer than 3 cm from the true one at generator level) for W events Monte Carlo, used to test the Z-vertex finder.

is pruned: 2 seeds are merged if the distance between them is less than 3 cm. For each vertex its quality code is defined as Σ (tracks$_{qual}$): a good vertex has a quality above or equal to 12. A list of z-vertex candidates is made and in the case that two or more are found, it is chosen the vertex with highest total scalar sum of transverse momentum, *i.e.* in order to maximize the efficiency. Additional vertices are used to correct the jet energy for multiple interaction effects (see section 3.8.2).

The performance of the algorithm has been tested on Monte Carlo samples. For example, figure 3.8 shows the case of W boson Monte Carlo samples, with W decaying in electron and neutrino - the most challenging kind of events to identify a primary vertex, since they are poorly populated in tracks and have an undetected neutrino: the efficiency to find a vertex closer than 3 cm from the true one at generator level is above 95% for $|Z|$ <50 cm. For inclusive jet samples, the relative efficiency is above 99%.

3.6 Event selection

Events are required to pass the following criteria:

- At least one good primary vertex, reconstructed in the range $|Z_v| < 50$ cm. Proton and antiprotons are delivered in bunches which extend for about 50 cm in the beampipe direction. As a consequence, the distribution of the z-vertex position is approximately Gaussian with $\sigma \simeq 30$ cm, centered near z=0 cm. Thus, a selection on z assures good energy measurement of the jets; besides, events are in this way selected within the acceptance limit in the b-tagging algorithm. Finally, the selection on primary vertex allows the removal of cosmic rays.

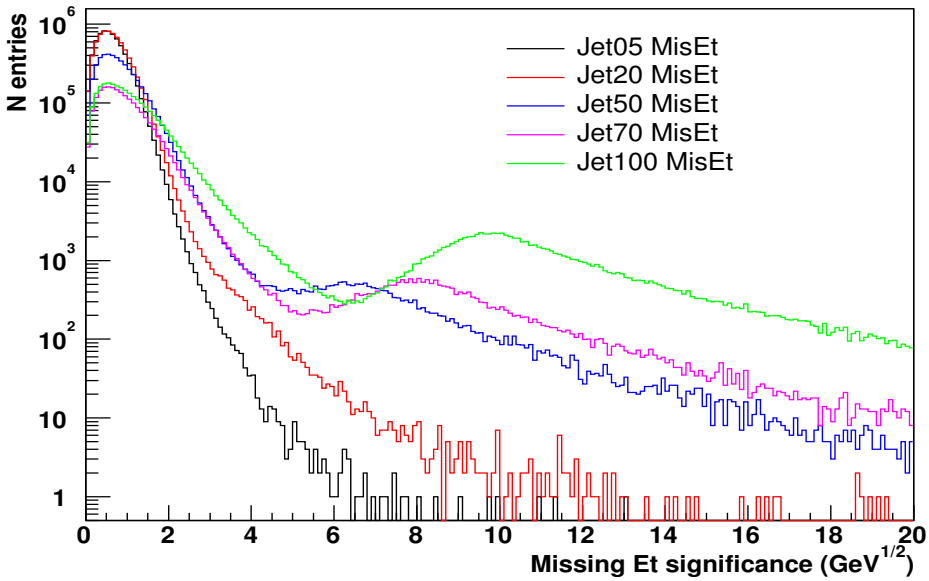

Figure 3.9: Missing E_T significance for ST05, Jet20, Jet50, Jet70 and Jet100 data.

- Missing E_T significance (MetSig) below a value X (GeV$^{1/2}$), where X depends on the data sample; MetSig is defined as $E_T^{\text{missing}}/\sqrt{\Sigma E_T}$, where E_T^{missing} is the missing transverse energy and ΣE_T the total transverse energy of the event. A cut on missing E_T significance, together with primary vertex selection previously described, rejects most of the background from cosmic rays. Distributions of missing Et before cuts are shown in figure 3.9. The second peak in the distribution comes from events with high missing E_T and small total energy, clearly related to cosmic ray background. The cuts are at 2, 3.5, 5., 6., 7. GeV$^{1/2}$ for ST05, Jet20, Jet50, Jet70 and Jet100 respectively.

- At least one jet with rapidity in the central range $|Y|$ <0.7 and P_T^{jet} above the trigger efficiency threshold of each data sample used (see section 3.7 for trigger efficiency range).

3.7 Trigger efficiency

The behaviour of each trigger sample has been studied in order to define a range of P_T of jets where effects due to trigger inefficiency can be neglected and trigger bias avoided. Besides, the Level 3 trigger uses the JetClu algorithm to define jets and the transverse energy is calculated with an event z-vertex of 0; thus, it is necessary to measure the trigger efficiency for jets reconstructed using MidPoint algorithm and with the proper value of the z vertex .

For each dataset, the efficiency is calculated using an inclusive jet sample with a lower

trigger threshold (e.g. Jet20 is used for Jet50, Jet50 for Jet70 etc.), or an independent trigger path: this is the case for ST05, for which the high P_T muon trigger (`bhptmu` dataset) is used.
The efficiency of a given trigger, defined as a function of jet P_T for inclusive jets in the datasets used, is the fraction of events, in each single bin in P_T, that has the corresponding trigger bits (L1&L2&L3) set. To avoid that prescales affect the efficiency, we factorize it as follow:

$$\epsilon_{\text{trigger}} = \epsilon_{L1unPS} \times \epsilon_{L1PS \to L2unPS} \times \epsilon_{L2PS \to L3}$$

where ϵ_{L1unPS} refers to the L1 efficiency, $\epsilon_{L1PS \to L2unPS}$ and $\epsilon_{L2PS \to L3}$ are the efficiency between L1PS and L2 unprescaled, and L2PS and L3 respectively. Plots in figure 3.10 show the distributions of $\epsilon_{\text{trigger}}$ for all the five data samples used as a function of jet P_T. Notice that for ST05, in order to increase statistics, events with only the L1 unprescaled trigger bit are considered. To model $\epsilon_{\text{trigger}}$, the efficiency curve is fitted with a function of the form:

$$\text{eff}(x) = \frac{P_0}{1 + e^{(-P_1(x+P_2))}} \tag{3.7}$$

The P_T value where the distribution is above 99% is chosen as the threshold used in the event selection for the corresponding data sample. Above this threshold the trigger is assumed to be fully efficient. The results for each trigger path are shown in table 3.7 as the range of the corresponding dataset used in the analysis. ST05 is the only trigger that will be used also in a range below the 99% threshold. To take into account this effect, the efficiency function extrapolated from the fit is used to re-weight each jet entry; nevertheless, the effect is below 1%, since $\epsilon_{\text{trigger}}$ predicted for the lower-edge value of first and second bin of the P_T spectrum (30 GeV/c for 30-34.5 bin and 34.5 GeV/c for 34.5-39 bin) are 96.75% and 98% respectively.

Trigger	99% Eff P_T (GeV/c)	Range (GeV/c)
ST05	38±1	30-44.5
J20	43±1	44.5-70.
J50	67±1	70.-100.9
J70	89±1	100.9-140.9
J100	123±1	$>$ 140.9

Table 3.3: From figure 3.10, for each trigger the measured jet P_T of crossing the 99% trigger efficiency threshold is reported (first column): the error comes from the binning definition (1 GeV/c bin) of the curve. The second column of the table shows the range in measured jet P_T used from each dataset

.

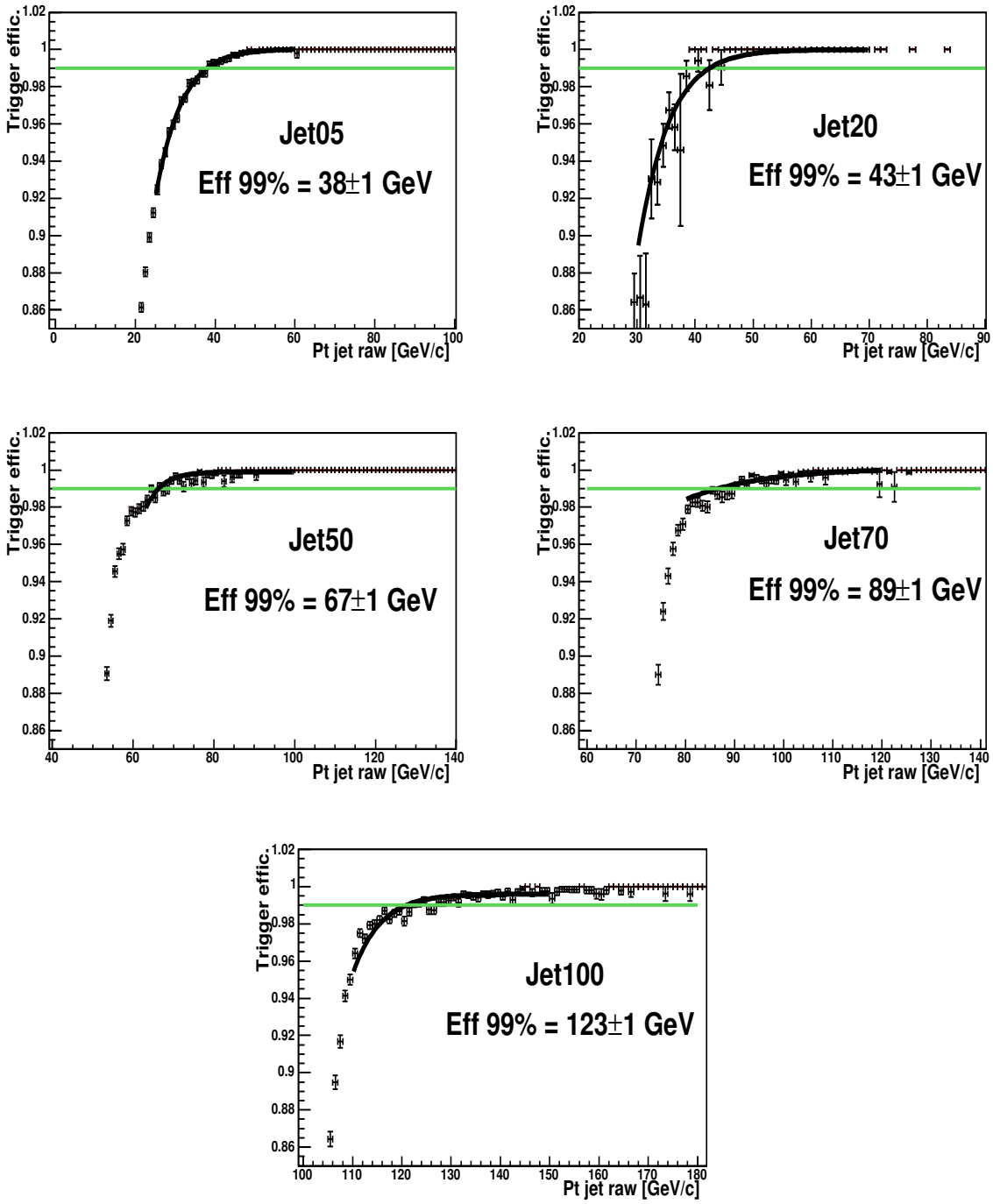

Figure 3.10: Trigger efficiency as a function of jet P_T for inclusive jets in the five jet trigger dataset used.

3.8 Jet P_T correction

The measured transverse momentum of the jets is by definition biased by detector effects. These jets are commonly referred as *calorimeter* jets, and they are experiment-dependent. When comparing cross sections or other measurement results with theoretical expectations, the involved jets are reconstructed using particles (hadrons) or partons, and they should be independent of the experiment (referred as *hadronic* or *particle* jets): figure 3.11 shows the sketch of jets at parton, particle and calorimeter level. Detector effects can be summarized as follow:

- the presence of cosmics, noise and beam halo;
- calorimetry losses;
- the finite efficiency of the detector;
- smearing effects due to the finite resolution of the detector.

Background events are suppressed with the selection cuts described in section 3.6. To take into account the detector inefficiency and calorimetry losses, it is necessary to use the Monte

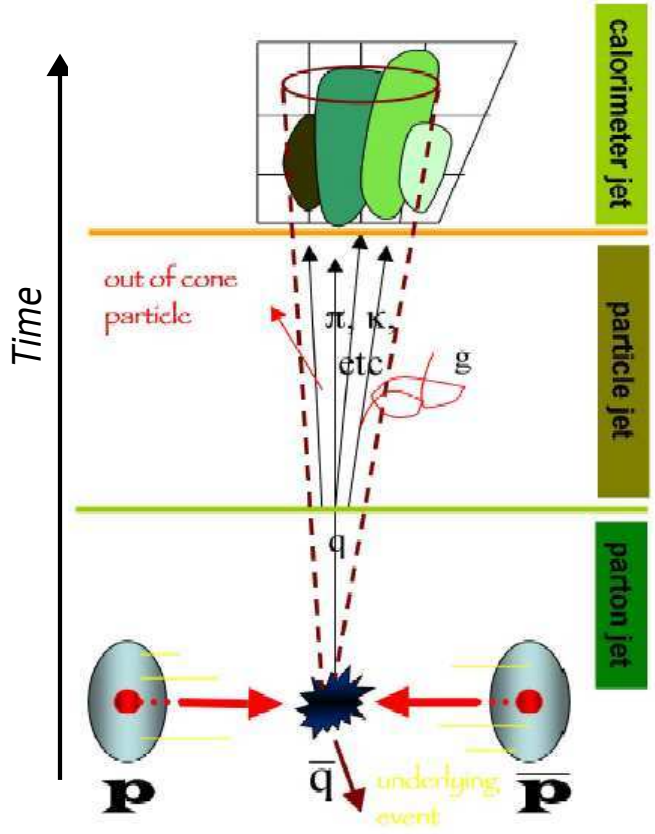

Figure 3.11: Development of the jet: from flow of partons (partonic jet) to stream of stable particles (hadronic jet), until the measured jet (calorimeter jet).

Carlo samples.

It is important to underline that the procedure to find average correction factors has been implemented only on a subset of events, containing a positively tagged jet (see Chapter 4 for b-tagging algorithm definition and features). Not all tagged jets contain a b-quark, so that differences between b-flavor jets and ordinary jets must be taken into account. For example, about 23% of b-hadrons decay semileptonically, so there is an underestimation of the parton energy due to lost neutrinos. On the other hand, transverse energy correction factors for tagged b-jets might be biased due to the selection on charged tracks required to pass P_T cuts.

For these reasons, additional corrections due to the b-flavor content in the jet must be considered: together with the smearing effects due to the finite resolution of the detector, these factors are calculated bin by bin using an unfolding procedure explained in section 5.2.

3.8.1 Average Jet P_T correction

The comparison between data and Monte Carlo for jets in the central region shows that there is a good agreement for most general quantities (see Appendix). Thus, it is possible to use Monte Carlo events to define the average detector effects on the jet energy and to correct the P_T scale. With the MidPoint algorithm, it is possible to form jets at the hadron level in MC, using information from stable particles in the HEPG bank. Those jets can then be compared to jets reconstructed with calorimetric information (energy deposited in the towers). At the hadronic level, particles with momentum above 1 GeV are used as seeds. No further selections are applied on other particles included in the proto-jet reconstructions and the same jet kinematics scheme is used.

In order to extract the correction factors to compensate for energy losses at calorimeter level, we use a procedure to match hadronic and calorimetric jets in the Y-ϕ space. For each calorimetric jet i (generic) in a rapidity range $|Y|$ <0.7 (no cut in Y is applied on the hadronic jet):

- define $\Delta Y[i,j]$, $\Delta\phi[i,j]$ for each hadronic jets j in the event and consequently the resulting $\Delta R[i,j]=\sqrt{\Delta Y^2[i,j]+\Delta\phi^2[i,j]}$;
- take the minimal $\Delta R[i,j] = \Delta R_{MIN}[i]$; a combination i,j is accepted if $\Delta R_{MIN} <$ 0.7 (cone radius);

For the transverse momentum, the correlation between the calorimetric jet P_T and the corresponding hadronic jet P_T is found using MC samples with different P_T hard cuts and considering only regions far from the MC generation cut, in order not to bias the correlation ($P_{T\,min}$=$P_{T\,MCcut}$ + about 20 GeV). The efficiency of the calorimeter for detecting jets with P_T above 20-30 GeV is about 100%, thus for each hadronic jet there is always a matched calorimeter jet.

The procedure has been implemented only for events with a positively tagged jet, so these corrections are not to be considered valid for b-jets, but for general tagged ones,.

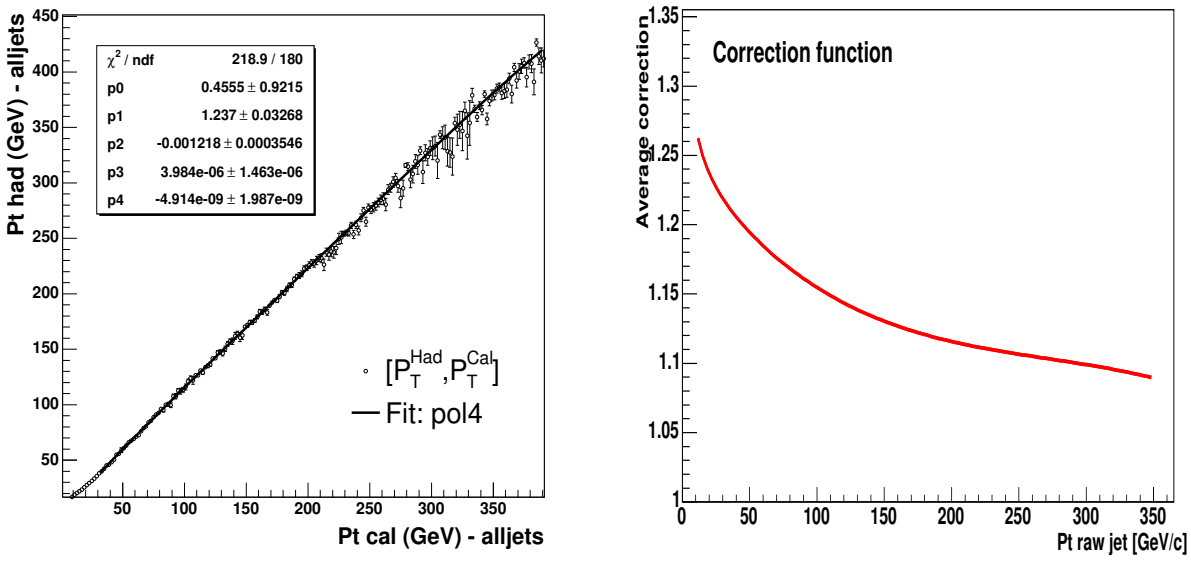

Figure 3.12: Profile P_T^{CAL} VS P_T^{HAD} for merged MC sample: for each sample with hard scattering cut equal to PtMCcut, we consider only jet with $P_{T\,min}$=$P_{T\,MCcut}$ + about 20 GeV.

The resulting correlation shown in figure 3.12 (left) is fitted to fourth-order polynomial in $< P_T^{\mathrm{CAL}} >$:

$$P_0 + P_1 * P_T^{jet}(CAL) + P_2 * P_T^{jet}(CAL)^2 + P_3 * P_T^{jet}(CAL)^3 + P_4 * P_T^{jet}(CAL)^4$$

The applied correction is shown in figure 3.12(right): the effect is of the order of 15-20% at low P_T and 10% at high P_T.

3.8.2 Multiple interaction correction

An additional correction is required to take into account multiple interactions (called UEM from Underlying Event).

At high luminosities a single collision of a proton and antiproton bunch may result in more than 1 $p\bar{p}$ interaction which leads to additional energy deposited in the calorimeter and extra reconstructed tracks. To correctly reconstruct energies of the jets produced in the hard interaction, energy corresponding to the additional interactions needs to be subtracted from the total energy measured in the calorimeter. This correction requires knowledge of the number of additional interactions occurring in a given bunch crossing and thus reconstructing not only one but multiple primary vertices.

The good performance of the Z-vertex finder algorithm allows to use the information of number of vertices per event to identify the multiple interaction contribution.

Figure 3.13 shows the average number of vertices as a function of the instantaneous luminosity for different data samples (Minimum Bias, Jet samples, high P_T electron samples,

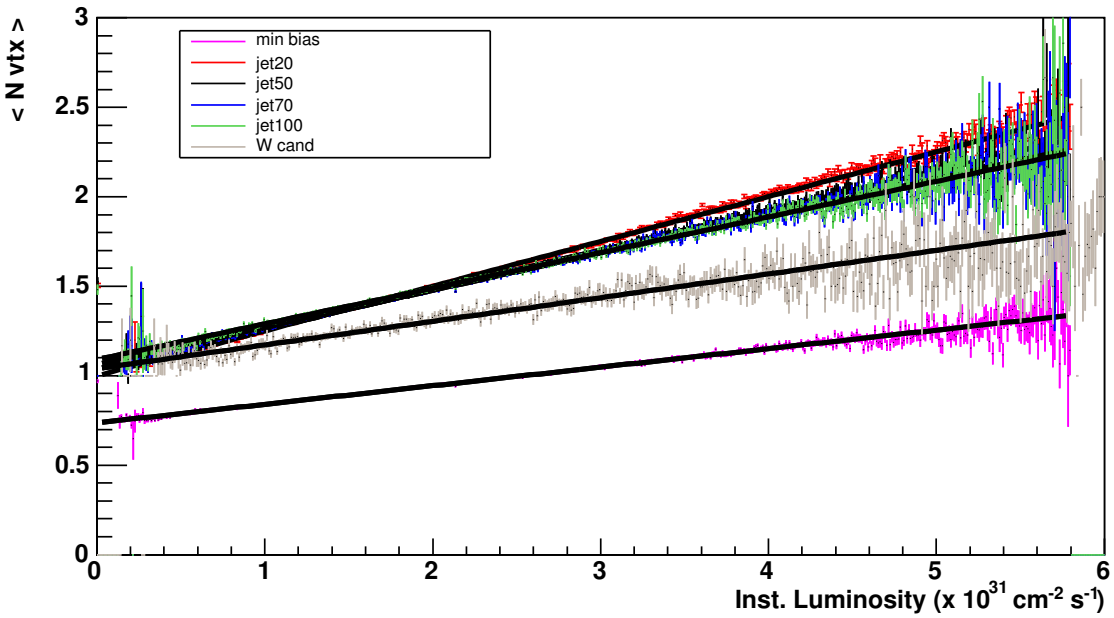

Figure 3.13: Average number of vertices as a function of instantaneous luminosity.

used to reconstruct W bosons events): the correlation between the number of vertices and $\mathcal{L}_{inst}$ is consistent with the assumption that these vertices do characterise the number of interactions observed in a given event. As expected, there is at least one vertex in jet high P_T electron samples by definition of the trigger, that requires an hard interaction. Minimum Bias data are instead inelastic hadron-hadron events that contains both hard and soft interactions. Although dominated by the latter, the hard interaction component play a non negligible role and gives a bias correlated to trigger effects, resulting in an offset of the $< N_{vtx} >$ distribution as a function of instantaneous luminosity.

To extrapolate the multiple interaction correction, the minimum bias dataset is used; jet samples and the high P_T sample are only used as a check on the minimum bias measurement and to quote a systematic error. Details on the methodology and checks are reported elsewhere [37]: here only the basic results for MidPoint jets with 0.7 cone are shown.

The tower P_T and jet P_T used for the measurement has been corrected using the primary vertex as the interaction point. The multiple interaction correction is here measured by considering the minimum bias momentum in a cone placed randomly in (Y, ϕ) with the constraint that $0.1 < |Y| < 0.7$. The cone energy is measured as a function of the number of good quality vertices in the events (NQ12Zv). The towers that are within the cone must be summed in a manner consistent with the MidPoint jet algorithm clustering, according to equations 3.4 and 3.5.

The energy that needs to be removed from the raw jet P_T for each additional vertex in a jet event is found to be $f_{UEM} = 0.93$ GeV/c. Figure 3.14 on the top show the average P_T of a random cone of radius 0.7 as a function of good vertices. The correction is of the

form $UEM = f_{UEM} \times (N_{vtx} - 1)$. The uncertainty given on this factor is about 15% and it is dominated by the dependency on instantaneous luminosity changes: the correlation between f_{UEM} and luminosity is shown in figure 3.14 on the bottom.

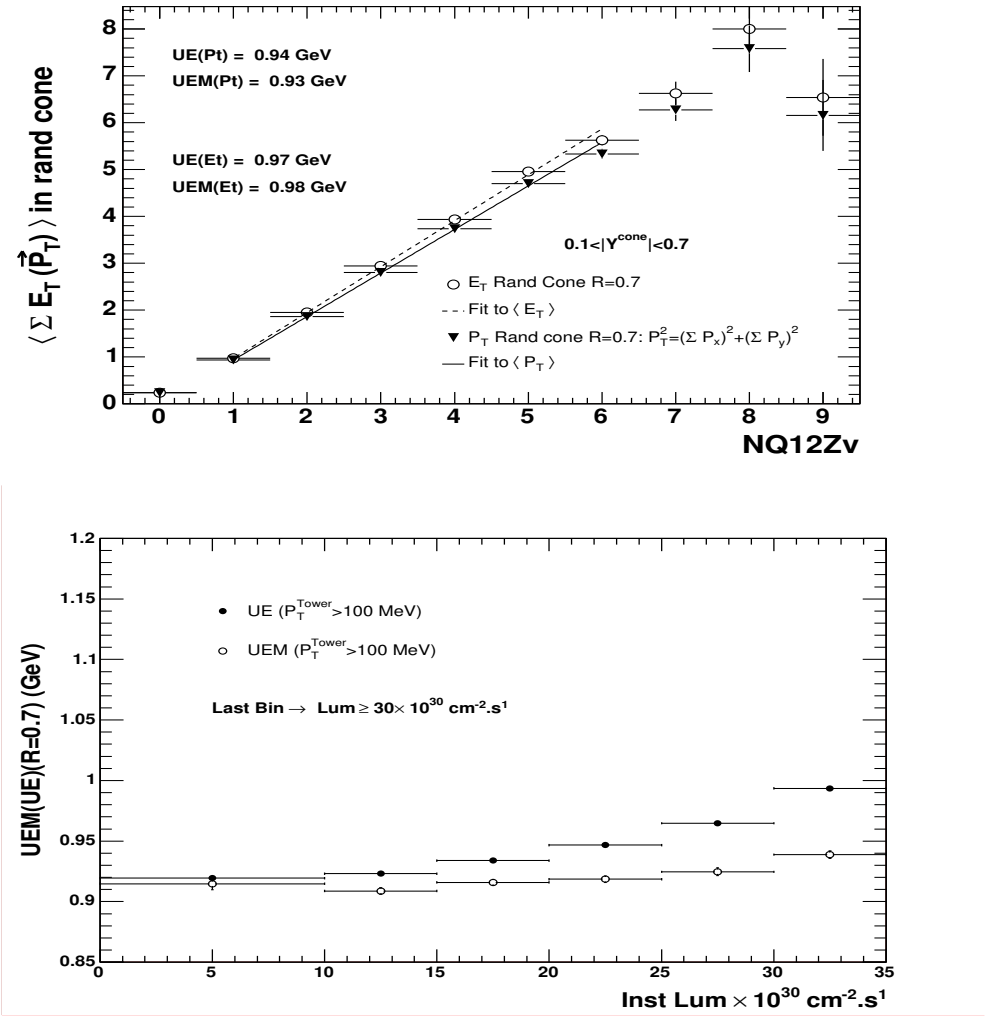

Figure 3.14: On the top: Linear fit to minimum bias momentum and energy *vs* number of good quality vertices. On the bottom: variation as a function of instantaneous luminosity.

3.8.3 Binning definition

From the results on the average jet transverse momentum correction, we can extract the transverse momentum resolution, using the quantity:

$$\kappa = \frac{P_T^{\mathrm{HAD}} - P_T^{\mathrm{CAL}}(\mathrm{Corr})}{P_T^{\mathrm{CAL}}(\mathrm{Corr})}$$

While the mean of the distribution gives a consistency check on the hadron scale correction, the standard deviation $\sigma(\kappa)$ multiplied by the $P_T^{\mathrm{CAL}}(\mathrm{Corr})$ gives the 1σ bin width in corrected jet P_T: the bin size for the b-jet cross section is defined according to this 1σ resolution and also taking into account the requirement that the trigger efficiency has to be above 99% for each dataset.

The definition of P_T^{jet} bins is reported in table 3.4. Figure 3.15 shows, on the top, $\sigma(\kappa)$, and on the bottom, $\sigma(\kappa)$ multiplied by the $P_T^{\mathrm{CAL}}(\mathrm{Corr})$, as a function of $P_T^{\mathrm{CAL}}(\mathrm{Corr})$.

DATA sample	**Range**	**Bin**
ST 05	38-43	5
	43-48	5
	48-54	6
JET20	54-60	6
	60-67	7
	67-74	7
	74-82	8
JET50	82-90	8
	90-98	8
	98-106	8
	106-116	10
JET70	116-126	10
	126-136	10
	136-148	12
Jet100	148-160	12
	160-173	13
	173-187	14
	187-202	15
	202-218	16
	218-236	18
	236-272	36
	272-326	54
	326-400	74

Table 3.4: Binning sizes used for corrected P_T: the used data sets for the different bins are also specified.

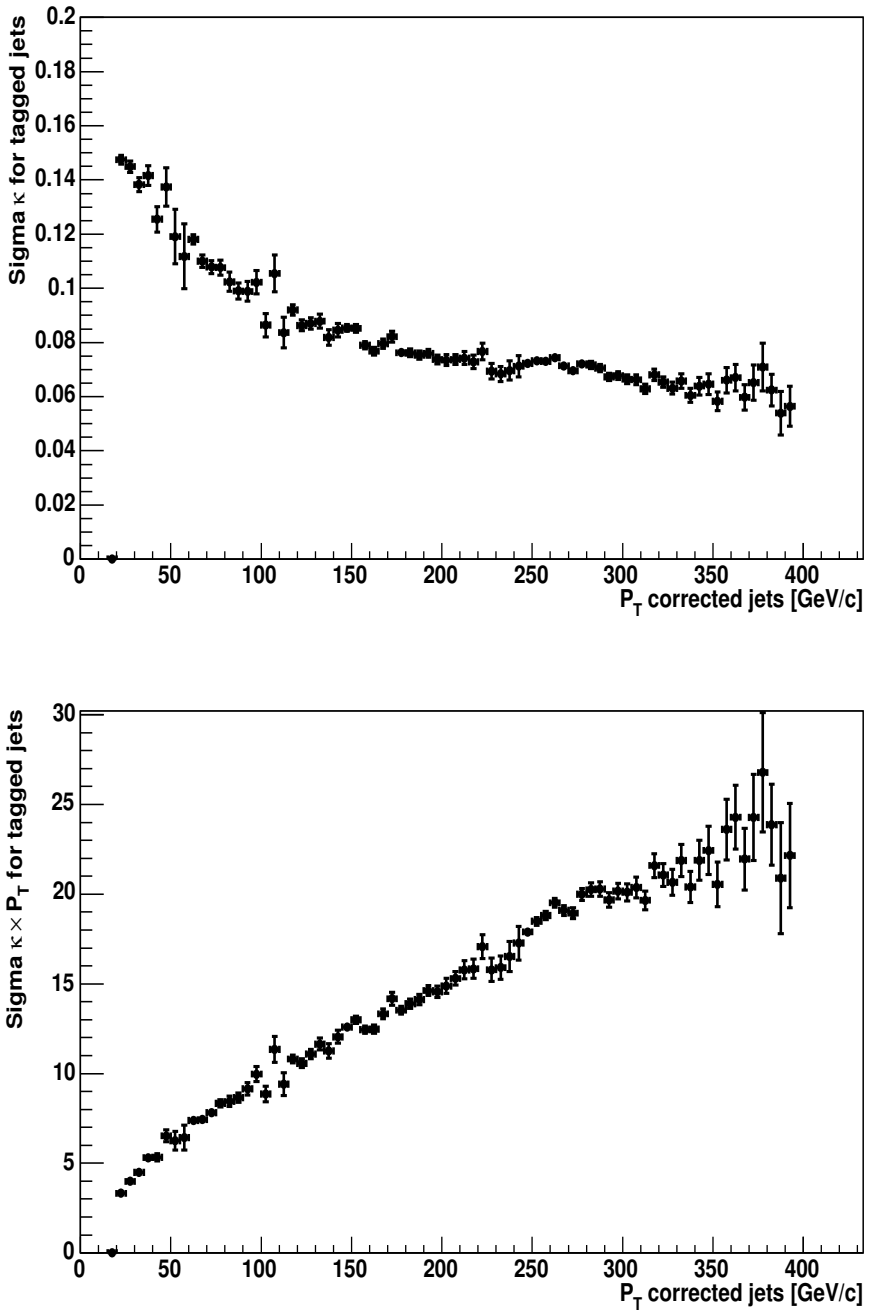

Figure 3.15: On the top: $\sigma(\kappa)$ from gaussian fit, as function of tagged jet transverse momentum: this is the $P_T^{\rm CAL}$(Corr) resolution, used to set the bin width. On the bottom: $\sigma(\kappa)$ multiplied by $P_T^{\rm CAL}$(Corr).

Chapter 4

Tagging b-jets

The b-jet identification is made using secondary vertex reconstruction: the analysis exploits the good tracking capabilities of the detector to select displaced tracks that are more likely to result from B-hadron decay products. To distinguish tracks of a secondary vertex from prompt tracks deriving from the interaction point, it is also necessary to have a good measurement of the primary vertex. In the previous chapter the procedure to define the z-coordinate of the primary vertex was described: in section 4.2 we report some details on the procedure used to define with high precision the 3-D primary vertex coordinates. In section 4.3 the SecVtx algorithm used to define secondary vertices is described, while in section 4.4 the performance is summarized, with a description of the methods used to find the b-tagging efficiency and the related systematic errors. Finally in section 4.5 the fraction of b-flavor jets in tagged jets is extracted and results and systematic uncertainties are reported.

4.1 Techniques to identify b-jets

Identifying b-flavor jets (i.e. jets containing a bottom flavor hadron) is fundamental for a b-jet cross section measurement. Many techniques have been developed for this purpose.

The so-called "soft lepton tagger" identifies low momentum electrons or muons coming preferentially from B-hadron semileptonic decays, and attempts to disentangle them from prompt leptons. Limitations of this methodology are mainly related to the low semileptonic branching ratio (about 11% per lepton flavor) and to the difficulties in identifying low momentum leptons in the wide jet transverse momentum range considered in this measurement.

Other techniques currently used take advantage of the long life-time of the B-hadrons; it is of the order of 1.5 ps, a proper path length $c\tau$ of 450 μm: considering the usual large relativistic boost of the events, a B-hadron travels a few millimeters before decaying. The decay products then derive from a secondary vertex displaced from the primary interaction point.

Not all the decay particle trajectories can be reconstructed because of the presence of

neutral particles or generally very complex final states. Nevertheless it is possible to use more inclusive techniques that exploit the silicon vertex tracker to distinguish between tracks deriving from the primary or secondary vertex. The SecVtx algorithm, used for this analysis and described in the next sections, applies a selection on track impact parameter and reconstructs a secondary vertex from the selected tracks. One drawback of this procedure is that charm hadrons are also characterized by intermediate ($c\tau \simeq 200\ \mu m$) proper path length, so it is difficult to distinguish b from c-hadrons. For this reason the SecVtx algorithm is actually a "heavy flavor tagger" and further selections are needed to extract the real bottom flavor content of the analysed sample.

4.2 Primary Vertex Finding

The z-vertex algorithm described in the previous chapter gives a first estimation of the interaction point to reconstruct jets. The event-by-event primary vertex algorithm uses this information as a starting point (z-seed), together with the average beamline, to give a better estimate of the primary interaction point, also providing the position in the XY plane. By default, the beamline is the time-dependent SVX beamline read from the CDF database.

Tracks within a ± 1 cm window from the z-seed are considered: the procedure starts fitting a vertex using all the tracks in this window, where tracks are also required to have an impact parameter significance, relative to the average beam position, $|d_0/\sigma_{d_0}| < 3$: d_0 is the impact parameter and σ_{d_0} is its uncertainty (including the beam position error). If a track added to the fit results giving a $\chi^2 > 10$ it is removed from the procedure ("pruning"). The 3-dimensional primary vertex position is determined, with a precision of the order of 10-20 μm, by the fit performed on the tracks passing the initial pruning, iterated until no tracks below the χ^2 cut are found. In case no tracks survive the selections, the beam position is assumed as the primary vertex.

Figure 4.1 shows the distribution of primary vertex x and y coordinates for events passing the selection requirements of section 3.6 for the Jet50 dataset: the interaction point in the XY plane changes in time and does not coincide with the coordinate origin (0,0). The CDF Monte Carlo simulation has been tuned to represent the data in a realistic way: in the figure Pythia Tune A Monte Carlo results (from Pt60 sample) are also superimposed; the simulation and data agree, although some beam configurations are not reproduced[1]. Such a difference, together with other simulation issues, might imply a different b-tagging performance in data and Monte Carlo that must be taken into account.

[1]Beam positions are simulated using information on 732 runs, corresponding to an integrated luminosity of about 250 pb^{-1}. For details see [38].

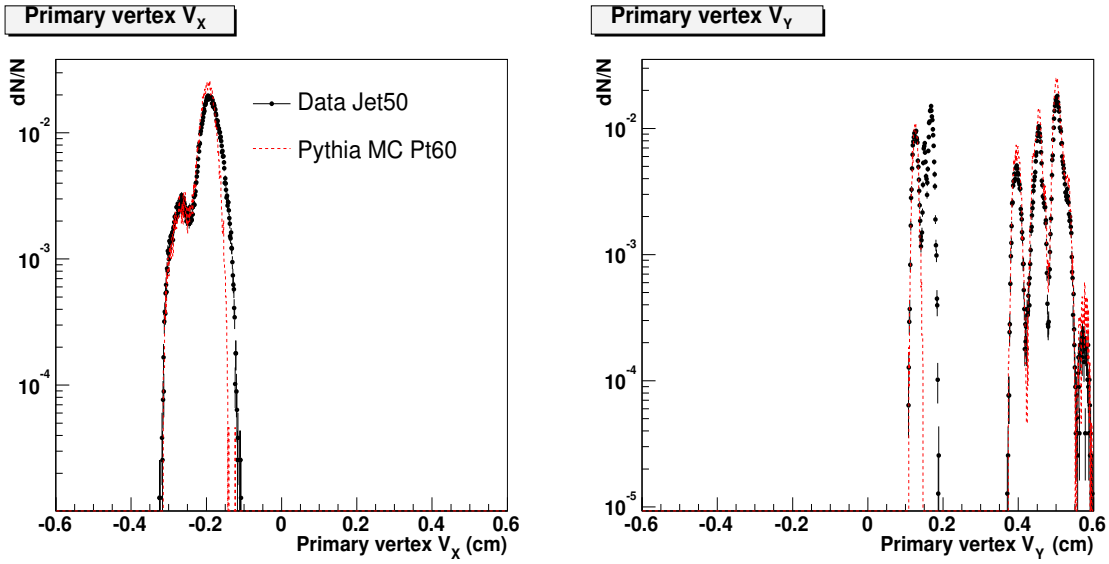

Figure 4.1: Primary vertex x (on the left) and y (on the right) coordinates for events selected from Jet50 dataset – black circles – compared with Monte Carlo simulations – red dashed line – : some beam configurations are not reproduced in Monte Carlo, although there is a general agreement with data.

4.3 The SecVtx Algorithm

To identify jets containing bottom hadrons, the algorithm used for this analysis is SecVtx. The procedure starts by considering each jet in the event located in the central part of the detector ($|\eta|$ <2), and tracks within the jet, in a cone of radius

$$\Delta R = \sqrt{(\eta_{track} - \eta_{jet})^2 + (\phi_{track} - \phi_{jet})^2} < 0.4$$

(generally called sub-cone). Though the SecVtx algorithm has been optimized for jets with a cone R=0.4, jets of this analysis have a cone size 0.7; nevertheless, we still consider only tracks inside a sub-cone 0.4 to reconstruct secondary vertices since, on average, tracks used for secondary vertex tagging of heavy flavor jets are closer to the jet axis, while soft tracks on the edge of the jet cone might lead to the reconstruction of a fake secondary vertex despite the tracks coming from a light quark jet.

Tracks are required to pass selection cuts to reject the poorly reconstructed ones: obviously only jets with at least two of these tracks can produce a displaced vertex, and those are defined as "taggable" jets.

Most of the reconstructed tracks originate directly from the primary interaction point (prompt tracks). Displaced tracks are typically decay products of long life-time particles as B and D hadrons but also strange particles such as K_S and Λ; in addition, they can be either mis-reconstructed because of multiple scattering in the detector material, or secondary particles produced by nuclear interactions in the material.

In order to identify tracks mostly coming from heavy flavor hadron decays, some selection cuts are applied:

- $P_T(\text{track}) > 500$ MeV/c: soft tracks are more likely mis-reconstructed due to multiple interactions with material;
- $|d_0| < 0.3$ cm: the upper limit on the impact parameter value removes most of the tracks produced by nuclear interactions, since they are often produced far away from the beam in the detector material;
- $|z_0^{\text{track}} - z_{\text{PrimaryVertex}}| < 5$ cm: as the previous one, this requirement removes mostly tracks coming from nuclear interactions;
- to reject particles resulting from K_S and Λ decays, the invariant mass of a pair of tracks is reconstructed and explicitly compared with that of the strange hadrons.

Tracks within the 0.4 sub-cone and passing these requirements are labelled as good and classified in different categories, made in terms of track fit χ^2, the number of Silicon hits, the number of missing SVX axial hits (identified extrapolating the track in active modules of the silicon detector), the number of good silicon hits (defined as not containing defective strips, made of a maximum of five strips, not to be shared with other tracks).
Not all tracks have the same "weight" in the tagging procedure. SecVtx algorithm uses a two-pass approach to find a secondary vertex where different kinds of tracks are used in two stages:

- First (Pass 1), at least three tracks with $P_T > 500$ MeV/c and $|d_0/\sigma_{d_0}| > 2.5$ are required: out of them, an attempt to reconstruct a secondary vertex is made, where at least one of the tracks used in the fit must have $P_T > 1$ GeV/c. The tracks considered must fulfill the requirements described in table 4.1.
- If there are no reconstructed vertices in the first pass, a second attempt (Pass 2) is performed using tighter track requirements ($P_T > 1$ GeV/c and $|d_0/\sigma_{d_0}| > 3$, plus one track with $P_T > 1.5$ GeV/c), but with looser particle multiplicity (two displaced tracks are enough). Track requirements in terms of hits and χ^2 are again summarized in table 4.1.

For each taggable jet, the multiplicity of good tracks inside the jet-cone such that $\Delta R_{\text{jet}-\text{trk}} < 0.4$ (top-left), together with Pass 1 (top-right) and Pass 2 (bottom-left) track multiplicities, is shown in figure 4.2. The bottom-right plot refers to tracks effectively used to reconstruct the secondary vertex in jets positively tagged (average $\simeq 2.6$): about 27% tracks are used to make a first attempt of secondary vertex reconstruction at Pass 1, while about 13% are considered in the second attempt (Pass 2). Displaced tracks used in finally positive tag jets are about 2% of the total.

Once a secondary vertex is reconstructed, additional selections are applied on the distance between the primary and secondary vertex: for this purpose, the quantity L_{xy} is used, defined as the distance between primary and secondary vertex in the r-ϕ plane. Figure 4.3

SecVtx Track Selection			
N hit	3 hits	4 hits	$\geq$5 hits
Pass 1	gd=3; m=0; χ^2 <12 gd=3; m$\leq$2; χ^2 <6 gd=2; m=0; χ^2 <6	gd=4; m=0; χ^2 <18 gd=4; m$\leq$1; χ^2 <12 gd=4; m$\leq$2; χ^2 <6 gd=3; m=0; χ^2 <12 m$\leq$1; χ^2 <6	gd=5; χ^2 <18 gd=4; χ^2 <12 χ^2 <12; m$\leq$1
Pass 2	gd=3; m$\leq$1; χ^2 <6 Hit on SVX L0 or L1	gd=4; m$\leq$1; χ^2 <6 gd=4; m=0; χ^2 <6	gd=5; χ^2 <12; m$\leq$12 χ^2 <6; m$\leq$0

Table 4.1: SVX hits requirement, where "gd" is the number of good hits, and "m" is the number of missing hits. In addition, associated COT tracks must have a total of at least 19 axial hits and 16 stereo hits.

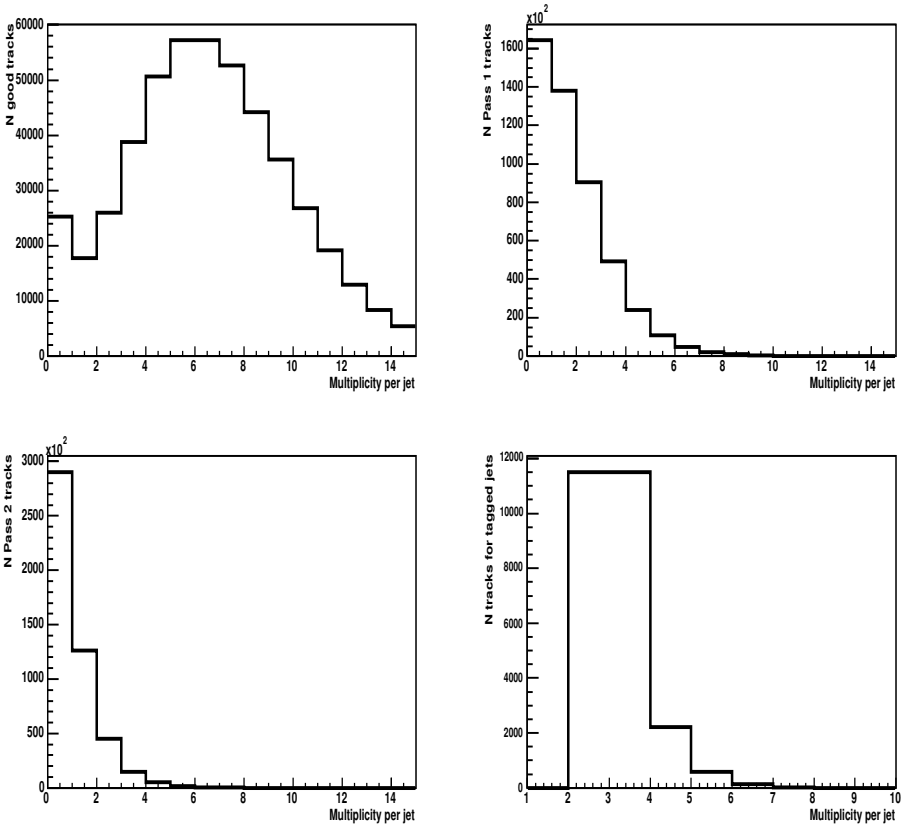

Figure 4.2: From top to bottom (Jet50 dataset taken as example): multiplicity of good tracks inside jets within a 0.4 sub-cone (top-left), Pass 1 (top-right) and Pass 2 (bottom-left) track multiplicities; bottom-right plot refers to tracks effectively used to reconstruct secondary vertex in jets positively tagged.

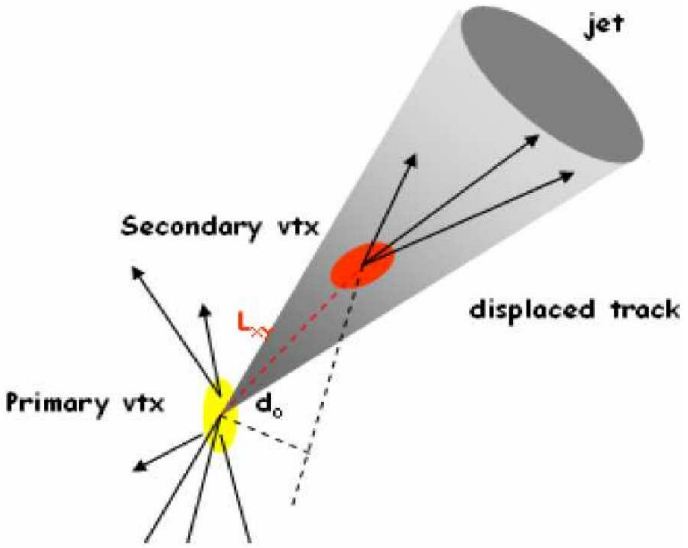

Figure 4.3: Scheme of a secondary vertex within a jet cone and distance from the primary vertex (L_{xy})

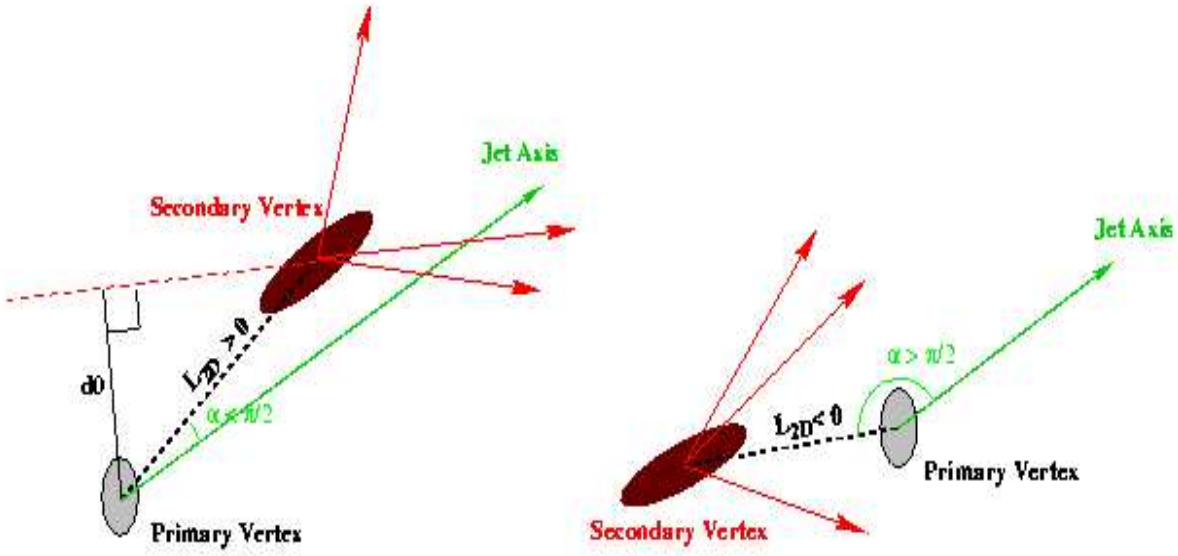

Figure 4.4: Schematic view of positive and negative SecVtx tag.

shows the scheme of a secondary vertex within a jet cone and the distance from the primary vertex (L_{xy}). The selections of the SecVtx algorithm are actually performed on L_{2D}, the projection of L_{xy} onto the jet axis[2]. The sign of L_{2D} is defined with respect to the jet direction by the angle α between the jet axis and the secondary vertex vector: if α is below(above) $\pi/2$, L_{2D} is positive(negative). This is also used in the selection: displaced vertices from heavy flavor decays are more likely to have a large and positive L_{2D}, while mis-tagged vertices usually present a smaller displacement with respect to the primary interaction point and L_{2D} is supposed to be randomly positive or negative, thus symmetric around 0. A secondary vertex is then required to have $L_{2D}/\sigma_{L_{2D}} > 7.5$ for positive tag jets, and $L_{2D}/\sigma_{L_{2D}} < -7.5$ for negative tag jets, where $\sigma_{L_{2D}}$ is the total estimated uncertainty on L_{2D}.

Figure 4.4 shows a schematic view of positive and negative SecVtx tags. Additional requirements on L_{2D} are finally applied to make a further rejection of vertices found because of material interactions:

- $|L_{2D}| < 5$ cm, with $|L_{2D}| < 2$ cm for two-track vertices;
- |pseudo-$c\tau$| < 1 cm, defined as $|L_{2D}| \times M_{\text{sec.vtx}}/p_T^{\text{sec.vtx}}$, where $M_{\text{sec.vtx}}$ and $p_T^{\text{sec.vtx}}$ are respectively the mass and the momentum of the secondary vertex, reconstructed from the tracks used in the fit;
- $|z_{\text{sec.vtx}} - z_{\text{prim.vtx}}| < 5$ cm.

Positively tagged jets are the b-flavor jet candidates considered in this analysis; negatively tagged jets are typically used as an estimate of mis-tag rate.

4.4 B-tagging efficiency

The b-tagging efficiency is the fraction of positively tagged b-jets with respect to all b-jets in a given P_T^{jet} bin. To directly measure the b-tagging efficiency in the inclusive jet samples, one should determine their heavy flavor content before and after the tagging procedure and this is not possible.

The approach CDF has adopted up to now [39] is to use a calibration sample of jets, whose heavy flavor fraction can be measured independently of the tagger, and to derive the per-jet tagging efficiency in the data for that sample. However, the measured efficiency cannot be directly used, because in general jets from other samples have different features (for example energy, rapidity, tracking multiplicity) from the jets in the calibration sample. So, the b-tagging efficiency is also derived from a Monte Carlo simulation, specifically generated to match the data of the calibration sample, and the ratio between the efficiencies as found in data and Monte Carlo is extracted. Finally, this ratio, called Scale Factor (SF), is used to correct the b-tagging efficiency derived from Monte Carlo samples generated to

[2]Sometimes this quantity is also referred as L_{xy} since the difference is quite small and they can be treated as equivalent in first approximation.

match the specific jet samples used in the analysis. In other words, the simulation is used to describe the energy dependence and geometrical acceptance of the tagger, while the scale factor takes into account imperfections in the Monte Carlo such as the difference in tracking efficiency and resolution, uncertainties in B-hadron decay models etc.

The calibration sample commonly used is the 8 GeV inclusive electron data sample described in 3.3.2: the enhancement in heavy flavor content – thanks to the sensitivity of the trigger to semileptonic decays of bottom and charm hadrons – allows a measurement of the b-jet fraction and the b-tagging efficiency in the data, using techniques independent of displaced vertices, based on the good electron identification capability of the detector.

This approach has been currently used in the experiment (for example in $t\bar{t}$ cross section measurements) and a common Scale Factor is used in all the analyses where SecVtx b-tagging is involved. Nevertheless, substantial differences between these analyses and the b-jet one, such as the use of JetClu jets with cone 0.4 rather than 0.7 MidPoint jets, imply the necessity to prove that one can use the official CDF Scale Factor value, regardless the jet clustering and cone size implemented. This is demonstrated in section 4.4.1: a scale factor value for MidPoint 0.7 electron jets is found using two different methodologies to derive the b-tagging efficiency; it is then compared to that obtained using JetClu 0.4 jets and thus to the official CDF result as obtained using the same Monte Carlo simulation samples.

The Scale Factor reported in 4.4.1 is 10% lower that effectively used in the analysis – that is finally the one determined for common use in the CDF collaboration. This difference is mainly related to the choice of Monte Carlo simulation taken to match the 8 GeV electron data sample: considering also more recent samples generated for this purpose, the extracted Scale Factor is found closer to 1. Checks have been made in this sense (in section 4.4.2) to estimate our sensitivity to the Monte Carlo samples; however, the main purpose of this study is to demonstrate the independence of the Scale Factor on the jet reconstruction algorithm, and not the determination of the value itself.

Although the implemented approach relies on Monte Carlo for the energy dependence, the P_T range covered by the direct b-tagging efficiency measurement is much smaller than the one considered in this analysis. Thus, section 4.4.3 reports the results of a dedicated comparison data/Monte Carlo of some important "tagging variables" in inclusive jet samples, performed to parametrize the Scale Factor in different P_T regions and thus extrapolate its dependence in P_T. In this way, a specific systematic error for the energy dependence is defined.

4.4.1 B-tagging efficiency from electron sample

Data and Monte Carlo samples used in this study are:

- Data: the 8 GeV inclusive electron sample as in 3.3.2: an integreted luminosity of 200 pb^{-1} after bad run removal.
- Monte Carlo: the Herwig 2→2 sample (3.8M events): to match the data, parton events have to pass through a filter requiring an electron with P_T >7 GeV/c and $|\eta| < 1.3$.

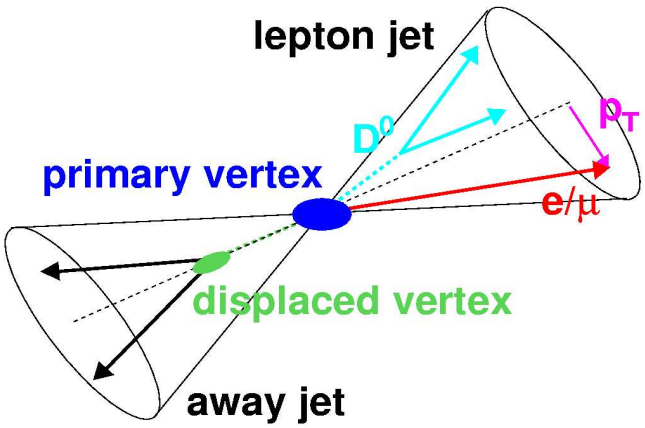

Figure 4.5: Schematic view of dijet events as selected in the Scale Factor measurement: the away jet is usually required to be tagged to enrich the sample in b-flavor content.

Events with at least 2 jets are required, where one jet is the so-called electron jet (ejet), the other one the so-called away jet (ajet). A sketch of typical dijet event is shown in figure 4.5. In addition to the standard electron identification described in 3.3.2, further requirements are:

- electron ID:
  - electron is not isolated $\rightarrow$ $\mathrm{Iso}_{0.4}=(E^{0.4}_{EM}+E^{0.4}_{HAD})/E_{electron}$ >0.1
  - if several electrons pass these requirements, pick the highest E_T one.
- Electron jet:
  - P_T >15 GeV/c (measured energy – not corrected for detector effects)
  - closest jet to electron in Y-ϕ
- Away jet:
  - P_T >15 GeV/c (measured energy)
  - $\Delta\phi\,[ej, aj]$ >2
  - if several jets pass cuts above, pick the away jet with largest $\Delta\phi\,[ej, aj]$.

No simulation for electron trigger effects on the Monte Carlo is applied: this results in higher yield of electron jets with respect to the official tag counts. This choice is motivated by our purpose, since the change in the b-tagging efficiency and SF calculated omitting the trigger biased region is negligeble.

The identification of converted photons mimicking electrons is also important, especially because the rate of conversions can be used to estimate the light flavor content (mis-tag)

directly from the data. A conversion is selected when a pair of tracks satisfy the following conditions:

- opposite sign
- $|\Delta cot\theta|$ <0.04
- $|\Delta\, XY|$ <0.2 cm

A second loop to remove fake conversions is also applied. Figure 4.6 shows the $|\Delta\, XY|$ distribution before the cuts are made and the conversion radius with peaks corresponding to known detector structures: for example, at about 15 cm radius peak corresponding to SVX readout material is clearly visible, as is also the COT inner cylinder at 40 cm.

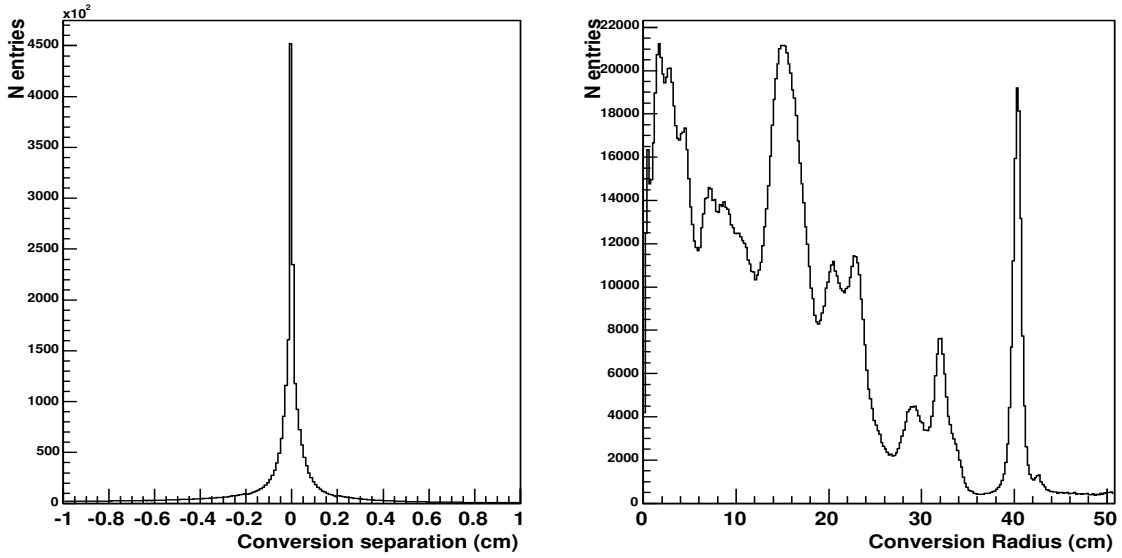

Figure 4.6: Conversion separation (left) and conversion radius (right)

In figure 4.7 comparisons of the Monte Carlo with the data for the electron and away jets P_T distribution are presented, with and without conversion removal. The agreement is fair, except for the range 15-19 GeV of electron jet P_T distribution, where the trigger is not implemented in the Monte Carlo. Figures 4.8, 4.9 show some event kinematic quantities relevant for SecVtx for both electron and away jets: number of good, Pass1, Pass2 tracks, number of tracks used to reconstruct secondary vertex in positively tagged jets, mass of secondary vertex, L_{2D} distribution and $c\tau$ distribution, the latter for electron jets positively and negatively tagged. Electrons identified as conversions are vetoed, since the data contain many more than the Monte Carlo sample. The number of tracks passing the selections of SecVtx is generally smaller in data than in Monte Carlo because the simulation does not properly describe underlying events and does not include minimum bias or beam halo effects

and therefore does not reproduce correctly low momentum tracks. Consequently, the Monte Carlo is more "efficient" than real data, and we expect a Scale Factor lower than 1.

Methods

The advantage of using an electron jet sample with respect to an inclusive sample is the enrichment of heavy flavor content. Nevertheless the sample is far from being pure and only one quarter of the electron jets are expected to be b (or c) flavor jets, mainly because of fake electrons or photon conversions.
To further enhance the fraction of b hadrons, one can apply the additional requirement to have the away jet positively tagged, but also in this case the fraction of heavy flavor-electron jets is not 100%: an away jet can be mis-tagged, or a tagged c-jet, or it could contain $b\bar{b}$ pairs from gluon splitting and therefore we do not expect to have a b-electron jets on the other side. However, the most straightforward method to define the b-tagging efficiency consists in measuring the number of electron-jets before (N^{a+}) and after SecVtx tagging (N^{e+}_{a+}), together with the fraction of b-flavor jets in both cases ($F^b_{bef\,tag}$ and $F^b_{aft\,tag}$ respectively), in the sub-sample with tagged away jet. Also, electron-jets identified as photon conversions are vetoed. The b-tagging efficiency is then defined as

$$\epsilon_b = \frac{N^{e+}_{a+}}{N^{a+}} \frac{F^b_{aft\,tag}}{F^b_{bef\,tag}}, \tag{4.1}$$

and we refer to this approach as the *single-tag method*. It allows to measure directly the b-jet tagging efficiency, the contamination of c-jets being negligible. However, the drawback is the poor statistics of the sub-sample, and consequently the difficulty to extract the b-fraction.

For this reason, another method has been developed for top quark measurements, the so-called *double-tag method*. One advantage of this approach is the possibility to extract, with better precision and with a small dependence on Monte Carlo simulation, the heavy flavor content of the calibration sample: the fraction is measured in the entire sample and then extrapolated to the tagged away-jet sub-sample, using the number of identified electron conversions. Details of the derivation of the efficiency computation can be found elsewhere[40]. The b-tagging efficiency from the double-tag method is defined as:

$$\epsilon_b = \frac{(N^{e+}_{a+} - N^{e-}_{a+}) - (N^{e+}_{a-} - N^{e-}_{a-})}{(N_{a+} - N_{a-})} \frac{1}{F^a_B} \tag{4.2}$$

where F^a_B, the heavy flavor ratio in the away tagged events, is:

$$F^a_B = 1 - \frac{(\frac{N^{a+}_c - N^{a-}_c}{N^{a+} - N^{a-}} - \frac{N^{e+}_c - N^{e-}_c}{N^{e+} - N^{e-}})}{\frac{N_c}{N_{ej}} - \frac{N^{e+}_c - N^{e-}_c}{N^{e+} - N^{e-}}} (1 - F_B). \tag{4.3}$$

The subscript "c" refers to events with an identified electron conversion, $\pm$ refers to the number of away or electron jets that represent the positive or negative tagging nature of the jets and N_{ej} is the total number of electron-jets. It should be noted that the double-tag

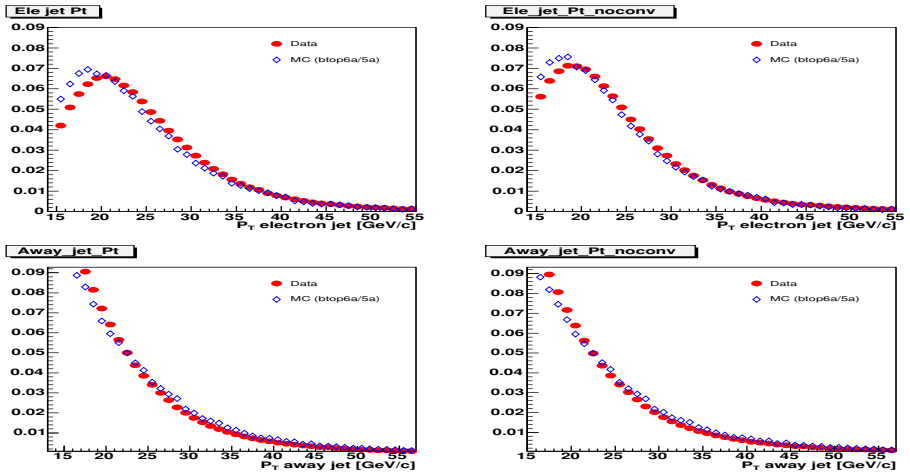

Figure 4.7: P_T of electron and away jet (on the left all events, on the right after conversion pairs removal): comparison Data/Monte Carlo for MidPoint cone 0.7 jets.

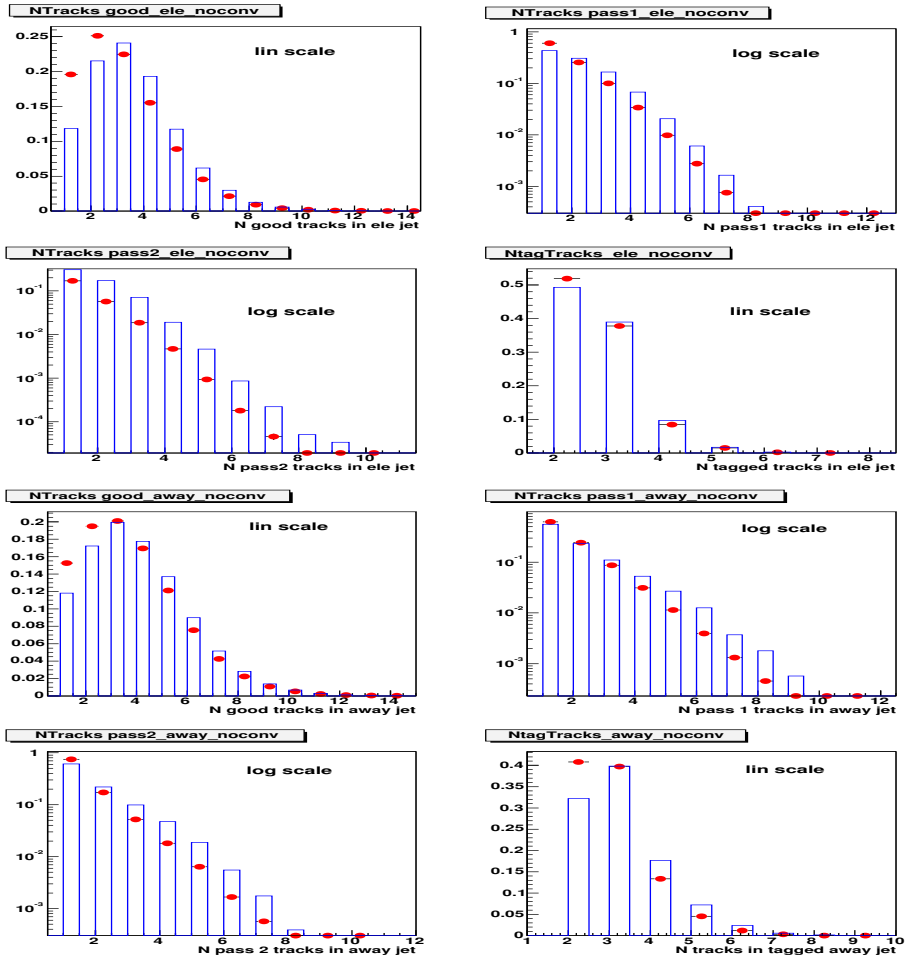

Figure 4.8: Number of tracks for electron and away jet (conversion pairs removed): comparison Data/Monte Carlo for MidPoint cone 0.7 jets. The poor agreement for low track multiplicity jets is assumed to be related to the simulation, that does not reproduce correctly low momentum tracks.

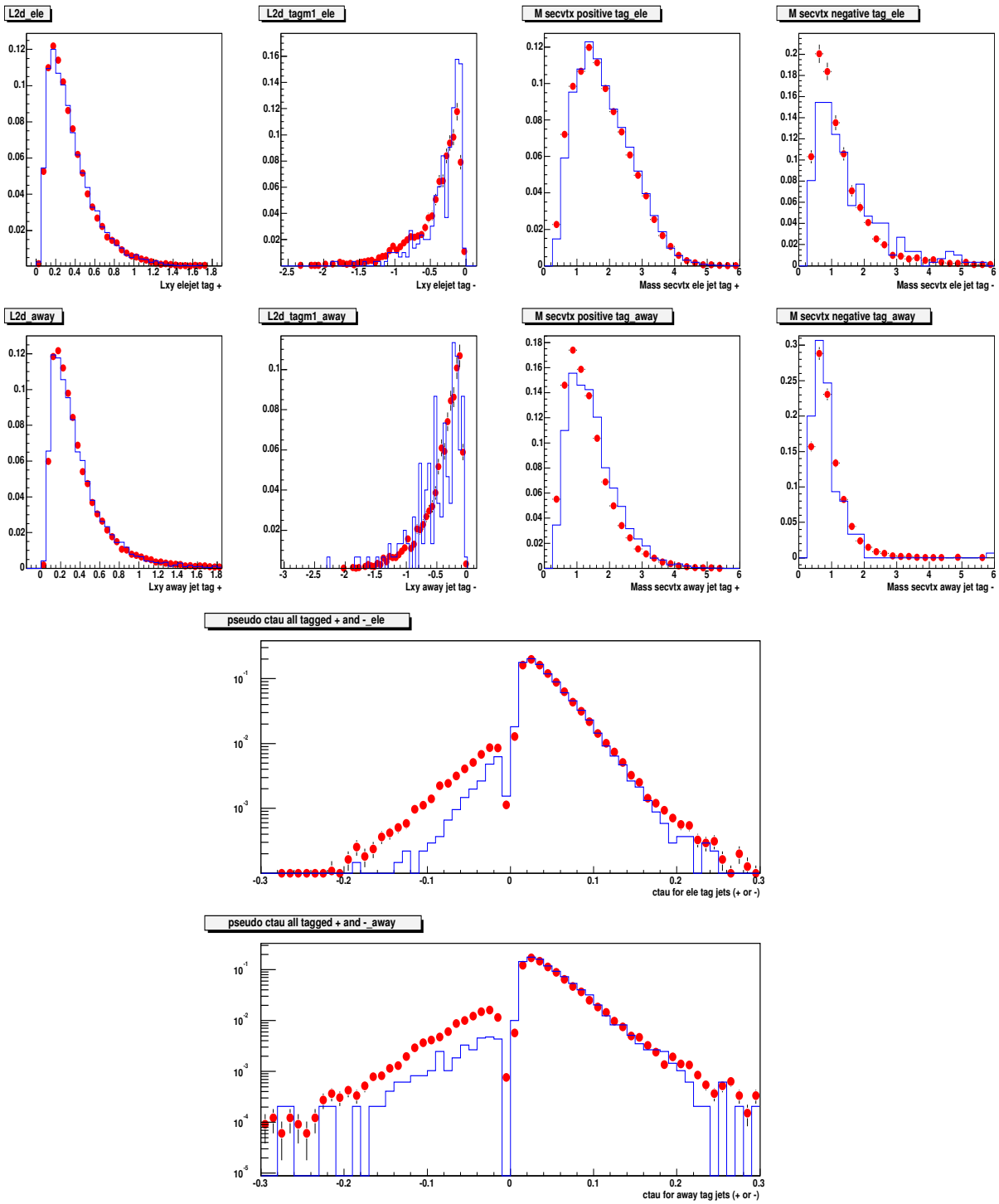

Figure 4.9: L_{2D}, $M_{Sec.vtx}$, $c\tau$ distributions for electron and away jet (conversion pairs removed): comparison Data/Monte Carlo. It is clear that the Monte Carlo simulation does not reproduce correctly the negatively tagged jets of the data.

method uses as an input the heavy flavor fraction content of the electron jets F_B=F_b+F_c, before any tagging requirement, and not only F_b as in the single tag method.
To measure the fraction of b-jets before tagging in the electron jets many techniques have been adopted, *e.g.* reconstruction of $D_0 \to K\pi$ decays or to identify muons from semileptonic D decays, giving a final value of F_B=0.259±0.064. The official Scale Factor, as obtained using the same Monte Carlo simulation samples and applying the double-tag method, is SF = 0.809±0.060.

This value is compared, in the following, with results from both of the approaches presented. Nevertheless, different procedures are also used to extract the fraction of heavy flavor jets.
For the fraction of b or $b+c$ jets in electron jets, independently of the tagger, the P_T^{rel} of the electron with respect to the electron jet axis is used as a discriminant parameter. Being invariant with respect to a boost along the jet axis, P_T^{rel} is a measurement of the transverse momentum of the electron with respect to this axis. In the rest system of the B-hadron, the electron coming from its decay gets a significant momentum due to the mass difference of the B-hadron and its decay products. This momentum is lower when considering a D- or light hadron decay, because of the lower mass difference with decay products. Thus, the shape of P_T^{rel} distributions can be used to disentangle different contributions to the electron jets.
The fraction of b-jets (or heavy flavor jets) after tagging uses the invariant mass of the tracks used to reconstruct the secondary vertex as the discriminating quantity; the method will be extensively explained in section 4.5.
In both cases, the data distribution is fitted to find the coefficients of a linear combination of the 2 components (b and non-b) with the ROOT routine TFractionFitter[44].

Results

Table 4.2 summarizes the tag counts and conversion yields found in data and Monte Carlo both for MidPoint cone=0.7 jets and for JetClu cone=0.4 jets. Those values have then been used to calculate the b-tagging efficiency with both methods.

- *Single tag method* (conversion removed, fake conversion removed):

$$\epsilon^b_{data} = \frac{N^{e+}_{a+}}{N^{a+}} \frac{F^b_{aft\,tag}}{F^b_{bef\,tag}} = 0.265 \pm 0.018,$$

  where $F^b_{bef\,tag}$ = 0.68±0.04 (away jet tagged), $F^b_{aft\,tag}$ = 0.98±0.04 (ele+away jet tagged). The fractions are extracted from a fit to P_T^{rel} and to the mass of the secondary vertex respectively; the distributions are shown in figure 4.10, with Monte Carlo templates normalized to data, and the fit results superimposed. The Monte Carlo single b-tag efficiency is $\epsilon^b_{MC} = 0.326 \pm 0.011$, thus the corresponding Scale Factor is

$$SF = 0.813 \pm 0.062$$

MPoint 0.7	Data	Monte Carlo
N_{ej}	1197104	68118
N_{a+}	29428	4725
N_{a-}	3445	150
N_{e+}	52105	13278
N_{e-}	2668	298
N_{a+}^{e+}	4820	1374
N_{a+}^{e-}	104	13
N_{a-}^{e+}	225	31
N_{a-}^{e-}	9	1
N_{c}	345445	10374
N_{c}^{a+}	4914	357
N_{c}^{a-}	1008	17
N_{c}^{e+}	3626	697
N_{c}^{e-}	710	19

JetClu 0.4	Data	Monte Carlo
N_{ej}	659868	44847
N_{a+}	19316	3324
N_{a-}	2197	96
N_{e+}	31526	9176
N_{e-}	1596	193
N_{a+}^{e+}	3320	1035
N_{a+}^{e-}	74	11
N_{a-}^{e+}	152	23
N_{a-}^{e-}	6	1
N_{c}	202045	7301
N_{c}^{a+}	3555	283
N_{c}^{a-}	709	12
N_{c}^{e+}	2371	516
N_{c}^{e-}	457	11

Table 4.2: Summary of data/Monte Carlo ele samples results for (*on the left*) MidPoint cone 0.7 (merge fraction 0.75) and for (*on the right*) JetClu cone=0.4.

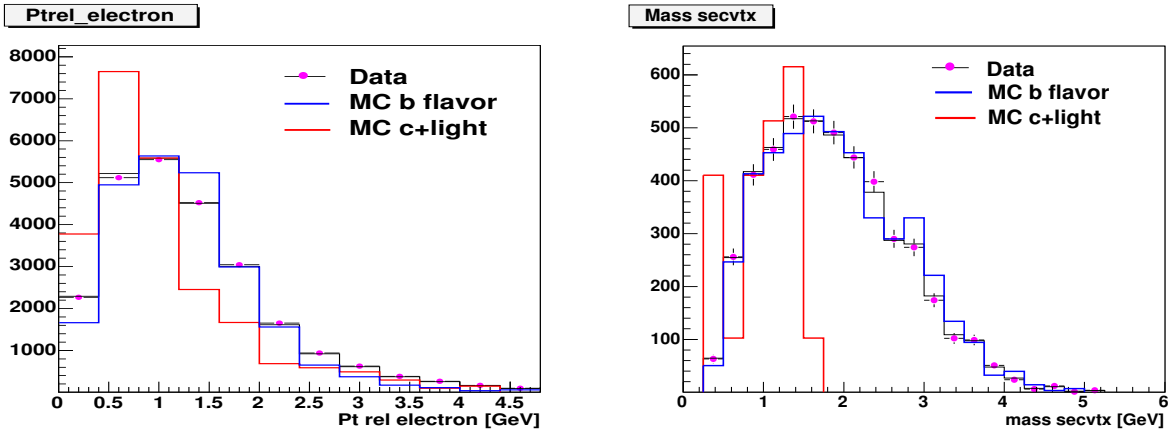

Figure 4.10: *Left:* P_T^{rel} of the electron with respect to the jet for away jet tagged events. *Right:* Mass of the secondary vertex for ele+away tagged jets.

Results for JetClu cone 0.4 jets are also computed for comparison. After measuring $F_{bef\,tag}^{b} = 0.66 \pm 0.04$ and $F_{aft\,tag}^{b} = 0.97 \pm 0.04$, the efficiencies and the corresponding scale factor are:

$$\epsilon_{JC04,\,data}^{b} = 0.288 \pm 0.017, \quad \epsilon_{JC04,\,MC}^{b} = 0.357 \pm 0.013, \rightarrow SF_{JC04} = 0.807 \pm 0.055$$

The two values SF and SF_{JC04} are in good agreement within the error. Figure 4.11 shows the b-tagging efficiency (left) and the SF (right) as a function of the electron jet P_T: the first bin is not considered in the fit because is the most affected by trigger

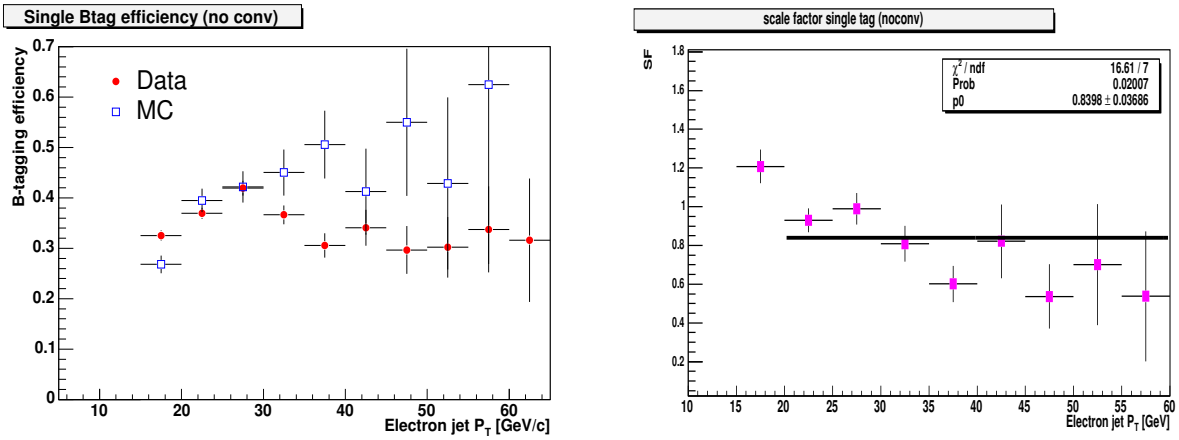

Figure 4.11: B-tagging efficiency comparison Data/Monte Carlo for MidPoint cone 0.7 jets (left) and SF (right)

threshold effects. To check the independence of the scale factor from these effects, the b-tagging efficiency considering only electron jets above 19 GeV/c is calculated:

$$\epsilon^b_{MC} = 1039/2502 = 0.415 \pm 0.015, \qquad \epsilon^b_{data} = 0.334 \pm 0.019$$

with $F^b_{bef\,tag} = 0.68 \pm 0.04$, $F^b_{aft\,tag} = 0.98 \pm 0.04$ as before.
The Scale factor is 0.810 ± 0.060, consistent with the previous result of 0.813 ± 0.062.

- *Double tag method:* Using equations 4.2 and 4.3, we find

$$\epsilon^B_{data} = 0.234 \pm 0.012,$$

with $F^B_{bef\,tag} = 0.36 \pm 0.03$ as the fraction of heavy flavor before tagging, found using the electron $P_{T\,rel}$; using equation 4.3 only, we can extract the heavy flavor ratio in the away tagged events: $F^a_B = 0.740 \pm 0.035$. Figure 4.12, on the left, shows templates and fit results for P^{rel}_T of electron with respect to the jet, used to calculate the fraction for $F^B_{bef\,tag}$. Again, Monte Carlo templates are normalized to the data, and data and the fit results are superimposed. $F^B_{bef\,tag}$ fit presents some additional uncertainties, especially due to the templates used for P^{rel}_T of light flavor, very different between data and Monte Carlo. Thus, we try to directly extract F^a_B using the secondary vertex mass distribution of away jets (see fig. 4.12 on the right).

Using the resulting value from the fit of F^a_B, the evaluated b-tagging efficiency found is compared to the Monte Carlo prediction:

$$\epsilon^B_{data} = 0.240 \pm 0.014, \qquad \epsilon^B_{MC} = 0.302 \pm 0.015$$

and the corresponding scale factor is 0.80 ± 0.06. For comparison, we report the results obtained using jet algorithm JetClu (jet cone 0.4) and repeating the same fitting procedure on templates: the heavy flavor fraction before tagging is found to

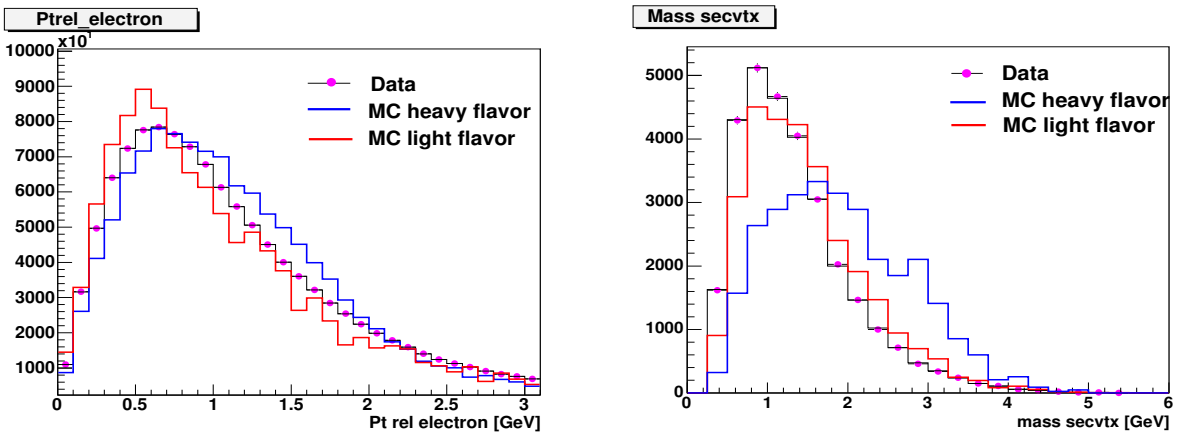

Figure 4.12: *Left:* P_T^{rel} of electron with respect to the jet templates with Data distribution and fit prediction superimposed. *Right:* Templates of secondary vertex mass for away tagged jets superimposed to Data distribution and fit prediction.

be $F^B_{bef\ tag} = 0.232 \pm 0.033$, and $F^a_B = 0.675 \pm 0.04$ as extracted from equation 4.3. This is again compared to the predicted b-tagging efficiency in the Monte Carlo for JetClu jets with cone 0.4:

$$\epsilon^B_{data\ JC04} = 0.267 \pm 0.013, \qquad \epsilon^B_{MC\ JC04} = 0.325 \pm 0.018$$

and scale factor is then $SF_{JC04} = 0.82 \pm 0.06$.

Table 4.3 summarizes the b-tagging efficiency and the corresponding Scale Factor, for MidPoint cone 0.7 jets and JetClu cone 0.4 jets, considering results of single tag method (first 2 lines, labelled as (S)) and double tag method (central 2 lines, labelled as (D)). The last line presents the official JetClu cone 0.4 results, as obtained considering the same Monte Carlo samples as in the present study: the agreement is very good, proving that performance of the tagger does not depend on jet clustering or the cone size implemented.

It is important to underline that the official scale factor reported in table 4.3 is not the one finally used in this analysis and in other CDF measurements: the updated Scale Factor value is $SF = 0.909 \pm 0.060$, and it has been obtained after improving Monte Carlo sample simulation and combining different methods. A detailed description of the used Scale Factor and relative systematics is reported in section 4.4.2.

4.4.2 Used Scale Factor and systematics

The 10% increase between the used Scale factor and that reported as official in table 4.3 is mainly related to the choice of Monte Carlo simulation samples taken to match the 8 GeV electron data trigger. In particular, including more recent samples (anyhow identical to the previous ones in terms of detector simulation and performance), a remarkable difference has been observed with respect to the first Herwig Monte Carlo sample generated in 2003

Jet Reconstruction	ϵ^b_{data}	ϵ^b_{MC}	SF
MidPoint 0.7 (S)	0.265 ± 0.018	0.326±0.011	0.813±0.062
JetClu 0.4 (S)	0.288 ± 0.017	0.357±0.013	0.807±0.055
MidPoint 0.7 (D)	0.240 ± 0.014	0.302±0.015	0.80±0.06
JetClu 0.4 (D)	0.267 ± 0.013	0.325±0.018	0.82±0.06
JetClu 0.4 (official)	0.276 ± 0.011	0.338 ± 0.012	0.816±0.059

Table 4.3: B-tagging efficiency and corresponding Scale Factor, for MidPoint cone 0.7 jets and JetClu cone 0.4 jets, considering results of single tag method (first 2 lines, labelled as (S)) and double tag method (central 2 lines, labelled as (D)). The last line present the official JetClu cone 0.4 results, as obtained considering the same Monte Carlo samples as in the present study.

(named `btop6a`) and corresponding to about half of the 3.8M events used in the present study (the other subsample named `btop5a`).

To evaluate this difference, the two Monte Carlo samples `btop5a` and `btop6a` have been studied separately. The values of b-tagging efficiency, together with the extracted Scale Factor, are reported in table 4.4: since the data are not very sensitive to the difference between the two Monte Carlo samples, we consider the same b-tagging efficiency in data calculated before. The SecVtx algorithm performs more efficiently for `btop6a` sample than for `btop5a`, thus the Scale Factor found in the latter case is closer to 1: this discrepancy has been partially related to uncertainties due to B decay tables, but it has not yet been completely understood. The new Monte Carlo samples produced to obtain the final official scale factor show features similar to the `btop5a` sample.

sample	ϵ^b_{data}	ϵ^b_{MC}	SF
`btop5a`(D)	0.240 ± 0.014	0.284±0.018	0.85±0.07
`btop5a`(S)	0.265 ± 0.018	0.308±0.015	0.86±0.07
`btop6a`(D)	0.240 ± 0.014	0.322±0.018	0.75±0.07
`btop6a`(S)	0.265 ± 0.018	0.350±0.017	0.76±0.07

Table 4.4: B-tagging efficiency and corresponding Scale Factor, considering separately two Monte Carlo subsamples.

The final Scale Factor is also the result of a combination of different techniques. In particular, a measurement using a sample of jets containing muons was studied to avoid the sensitivity of electron scale factor methods to fake electrons and conversions. The muon scale factor [41] is also measured using a double-tag method by selecting events with a jet that contains a well identified muon opposite another jet in azimuth: figure 4.13 shows the b-tagging efficiency in data and Monte Carlo as a function of muon-jet E_T, and the corresponding Scale Factor.

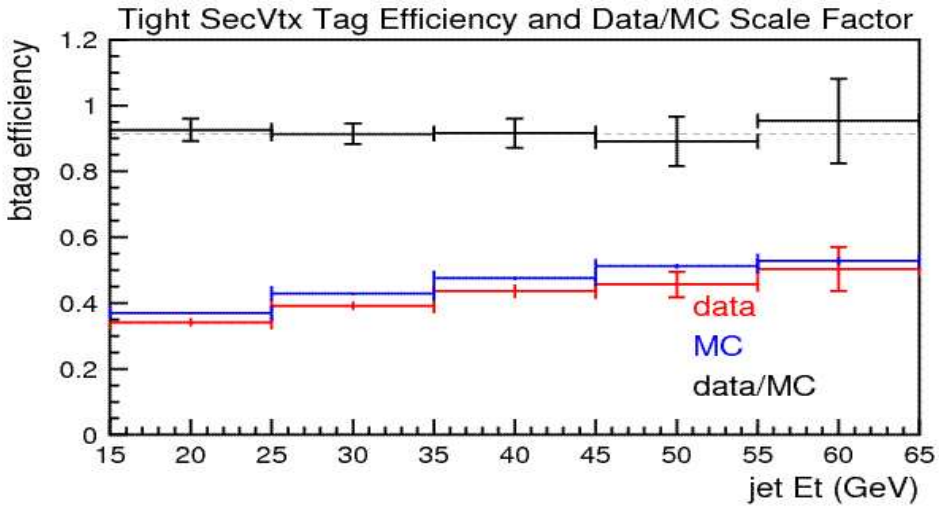

Figure 4.13: B-tagging efficiency in the data(red) and Monte Carlo(blue) using the muon technique and corresponding Scale Factor, as a function of jet E_T (JetClu algorithm, cone size 0.4).

The error quoted above is a combination of statistical and systematic errors, although the latter are dominant.
Several sources of systematics are included, and the most important are summarized below:

- Mistag asymmetry: the double tag method extensively uses information related to negative tag jets. Based on the assumption that, for mis-tagged jets, the L_{2D} distribution is symmetric, as well on the approximation that no heavy flavor jets are negatively tagged, the double tag method uses the neg-tag rate[3] as the background estimate. Figure 4.14 shows the negative tag rate for the data, compared to total negative tag rate as well as positive and negative mis-tag rates in the Monte Carlo: the mis-tag asymmetry is very pronounced, and there is a non negligible heavy flavor content in negatively tagged jets. Also, the negative tag rate has been evaluated with an uncertainty, in data, of about 10-20%. Considering different values of asymmetry correction factors f (20% for data, from 20% to 100% for Monte Carlo), the effect on the efficiency is always small. The corresponding systematic uncertainty is 3%, and another 3% is added to take into account uncertainties of the conversion rate.

- Hadronic *vs* semileptonic decays: the b-tagging efficiency is measured for lepton jets. Uncertainties on the semileptonic decay branching ratio as well as possible differences in the scale factor due to the lower charged particle multiplicity of semileptonic B-hadron decays are found to be about 3%.

- P_T dependence: a 4-5% uncertainty has been estimated in top measurements. Since the energy dependence uncertainty is the dominant source of systematics in the

[3]Positive(negative) tag rate is defined as the ratio between positive(negative) tagged jets and the total number of jets, calculated for each bin in P_T.

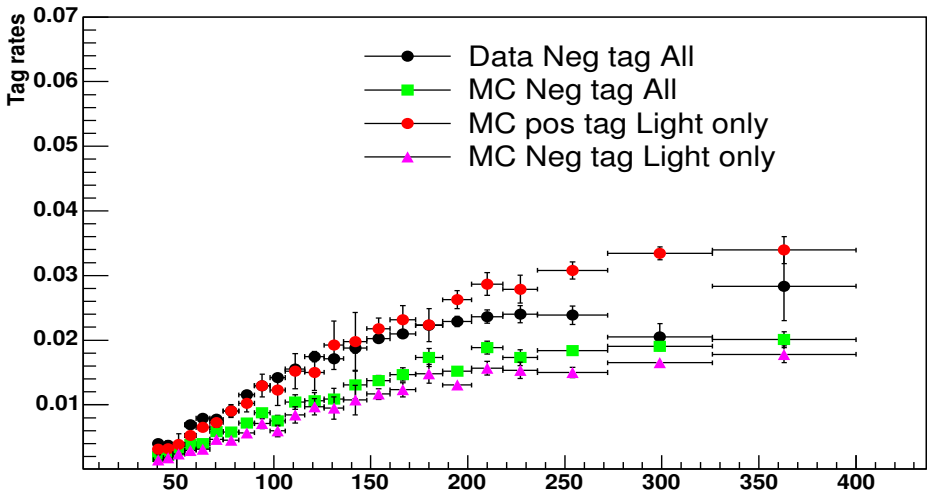

Figure 4.14: Data negative tag jets rate is shown as function of jet P_T, superimposed to Monte Carlo Pythia Tune A predictions for negative tag rate, positive mis-tag rate and negative mis-tag rate.

present analysis, a careful study is described in the following section, taking into account the very wide jet P_T range of this measurement.

- b-quark multiplicity in the jet cone: the b-tagging efficiency depends on the b-quark content of the tagged jet, *i.e.* if within a jet cone one or two b-quarks are included. The study that has been made and the evaluated systematic uncertainty are described in section 4.4.4.

The b-tagging efficiency obtained from the Monte Carlo dijet samples and scaled to match the data is shown in figure 4.15 as a function of the jet P_T: the total systematic error (including contributions presented in next section) is reported on the figure (grey band).

4.4.3 P_T dependence

From a distribution such as that presented in figure 4.11, it is not possible to deduce whether or not the scale factor is constant over the wide jet P_T range that we consider for the present analysis. To study the effect of P_T dependence above 60 GeV/c, only inclusive jet data samples and Monte Carlo dijet (Pythia) samples can be used. The same event selection used in the analysis is implemented, so that only central jets are considered ($|Y| < 0.7$). Figures 4.16 show the positive (POS, top plots) and negative (NEG, bottom plots) tag rate for all jet samples (on the left) and Monte Carlo samples (on the right). Differently to what is used in the analysis, the measured jet P_T is considered in these distributions and in those following presented in this section; the choice is irrelevant for the purpose of this study, since jets are corrected in the same way for data and Monte Carlo.

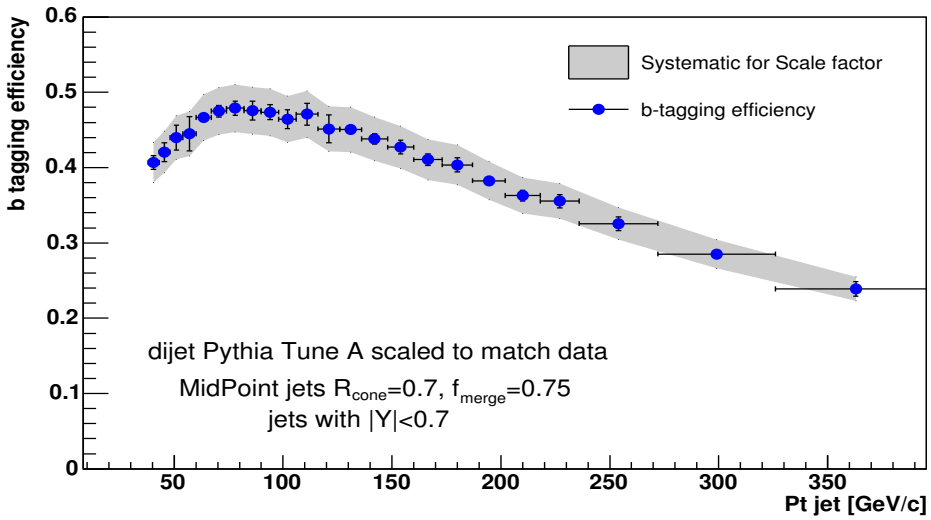

Figure 4.15: The b-tagging efficiency from Pythia Tune A Monte Carlo, rescaled to match the data: the systematic error band comes from the scale factor systematic error.

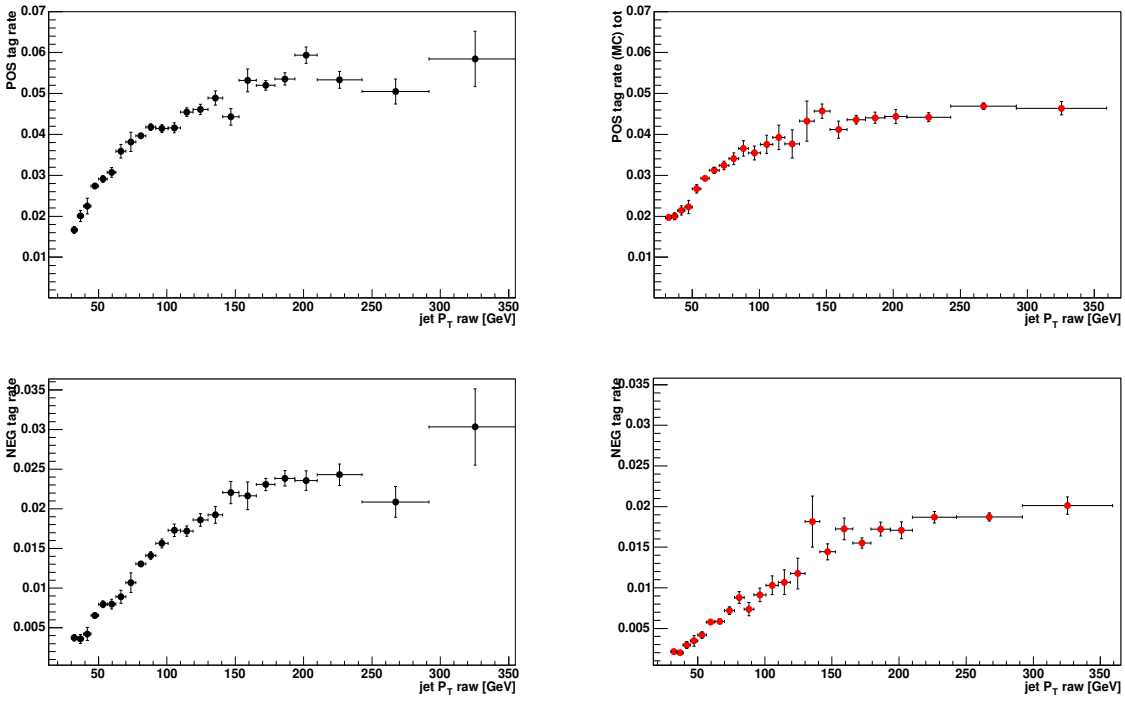

Figure 4.16: P_T jet dependence of POS (top) and NEG (bottom) tag rate for data (left column) and Monte Carlo (right column) jets.

One method to determine the P_T dependence of the scale factor uses the slope of the

ratio of tag excess rates Data/Monte Carlo (figure 4.17). Performing a fit we obtain a slope of $+(0.0008 \pm 0.0002)$, (fit range 30-350 GeV). This estimation is however not conclusive and is affected by large uncertainties, because it assumes that the evolution versus jet P_T of the b-jet fraction before and after tagging is well modeled by the Monte Carlo.

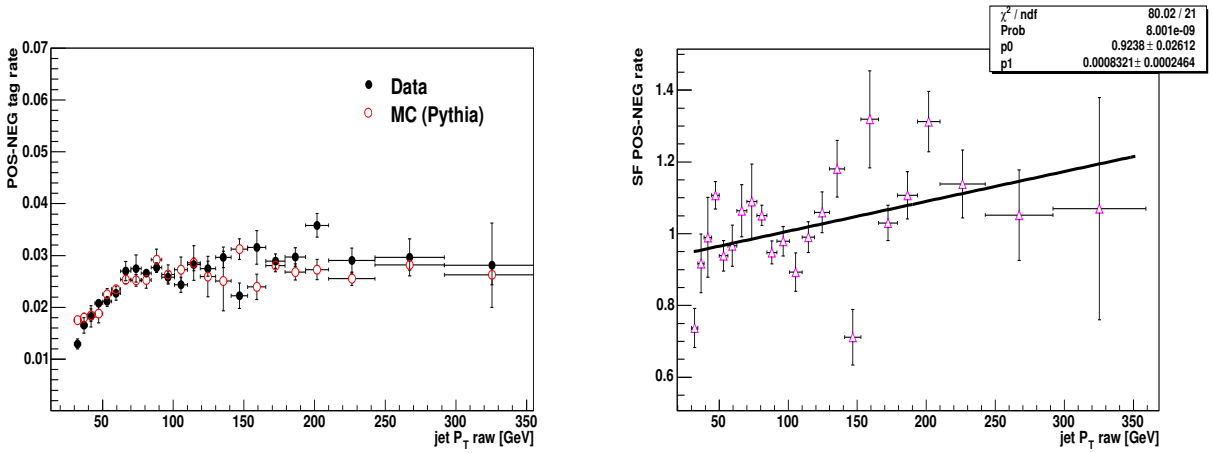

Figure 4.17: Jet P_T dependence of POS-NEG rate (on the left) and Data/Monte Carlo ratio (on the right).

We then consider some other relevant variables on which the b-tagging efficiency depends, and compare their behavior as a function of P_T in the data and Monte Carlo. In particular, for data we consider general jets, for which the b-flavor jet content is unknown; the variables are compared with Pythia Monte Carlo jets, considering separately the case of general jets and tagged b-jets.
The variables initially considered here are:

- Number of good tracks
- Number of pass 1 tracks
- Number of pass 2 tracks
- Number of tracks used for secondary vertex reconstruction in tagged jets (called N tag tracks)
- Number of COT hits
- Number of SVX hits

Figure 4.18 show the profiles and the Data/Monte Carlo ratios, as a function of jet P_T, for the number of good, pass 1, pass 2 and tag tracks: all jets are considered in Monte Carlo. In the range between 30 and 350 GeV/c, the fluctuation of the ratio is of the order of 3% for good tracks, 6% for pass1 tracks, 5% for pass2 tracks, 8% for tracks used in positive tagged jets; for the not reported COT and SVX hit distributions in good tracks, the fluctuation of

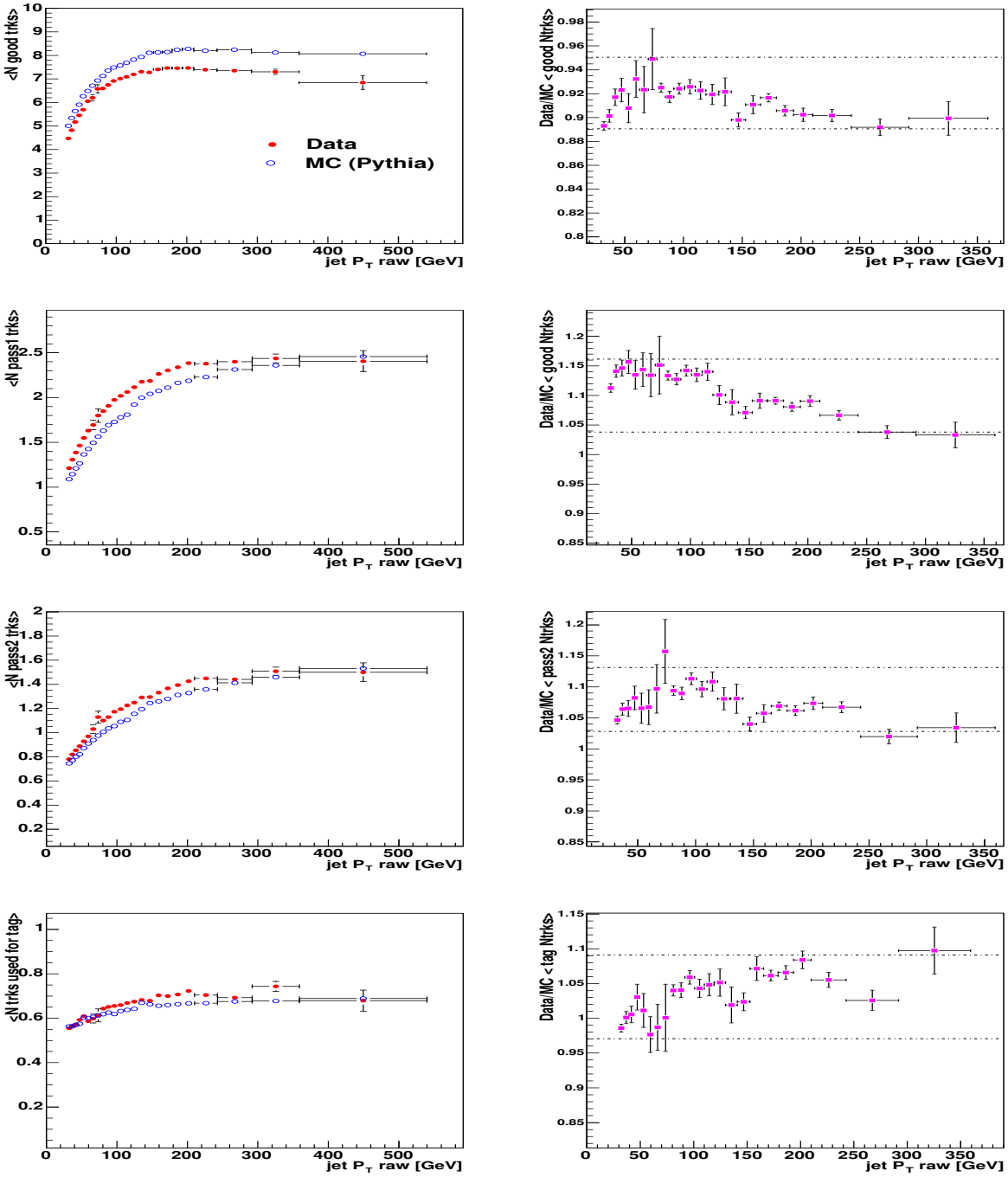

Figure 4.18: *On the left* Average distribution as function of Jet P_T of N good, pass1, pass2, N tag tracks: Data are red filled circles, Monte Carlo blue empty circles. *On the right* Ratio Data/Monte Carlo. In case of Monte Carlo general jets are considered.

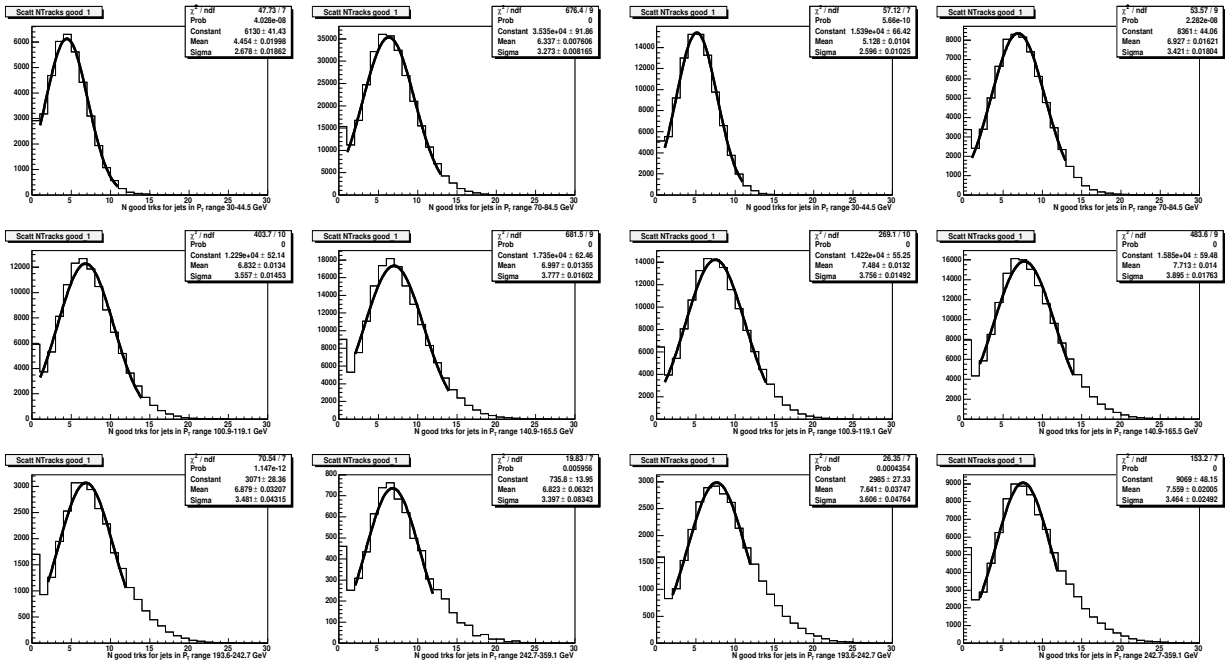

Figure 4.19: Distribution of N_{gtrk} for the 6 different energy ranges considered for Data (on the left) and Monte Carlo (on the right).

the ratio is less than 2%.

In order to check the impact of those fluctuations on the tagging efficiency, let us consider the first variable, the number of good tracks (N_{gtrk}). We study the positive tag rate in Data and Monte Carlo as a function of number of good tracks in 6 finite jet P_T ranges, covering the whole spectrum of the analysis: the correlations are fitted with a linear fit between N_{gtrk}=2 and 11. The N_{gtrk} distributions in each P_T bin (shown in fig. 4.19) can be fitted with a gaussian and the mean is the expected value for the number of good tracks. We finally extract the predicted tagging efficiency (for each P_T range) resulting from the linear fit, together with the relative variation if a 3% fluctuation is applied to $<N_{gtrk}>$ (figure 4.20).

Results are shown in table 4.5: the induced variation is approximately constant as a function of P_T both for Data and Monte Carlo, and it is about 5%.

Although more conclusive than the simple fit on (POS-NEG) tag rate distribution over the jet P_T, the performed parametrization still considered all tagged jets, and it constrains the general tagging efficiency rather than the b-tagging one. Thus, the same check is made considering only b-jets in the Monte Carlo samples. Figure 4.21 shows the comparison of $N_{gtrk}^{all-jet}$ *vs* jet P_T in data and N_{gtrk}^{b-jet} *vs* b-jet P_T in Monte Carlo (on the left) and the relative ratio (on the right). The maximal fluctuation is 4%. The Monte Carlo b-tagging efficiency is calculated as a function of N_{gtrk}^{b-jet} in the usual 6 finite jet P_T ranges: the expected value for the number of good tracks, extracted from the gaussian fits in figure 4.22 on the left,

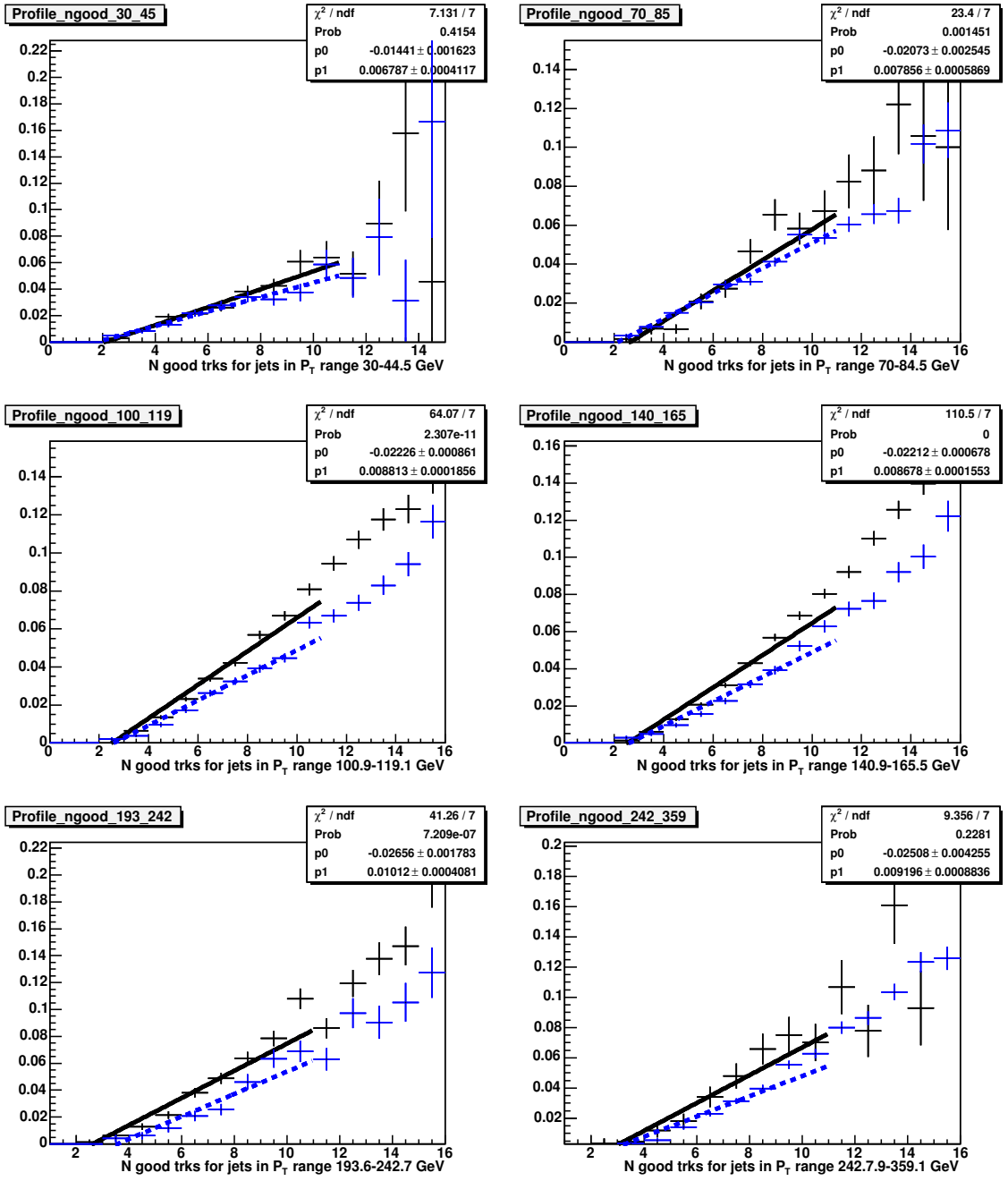

Figure 4.20: Tagging rate as a function of Number of good tracks: the solid line is the fit related to Data, the dashed line is referred to Monte Carlo.

is varied by ±4% and the corresponding b-tagging efficiency variation is determined (figure 4.22 on the right). Results are summarized in the last column of table 4.5: again the induced variation is approximately constant as a function of P_T and it is less than 5%.

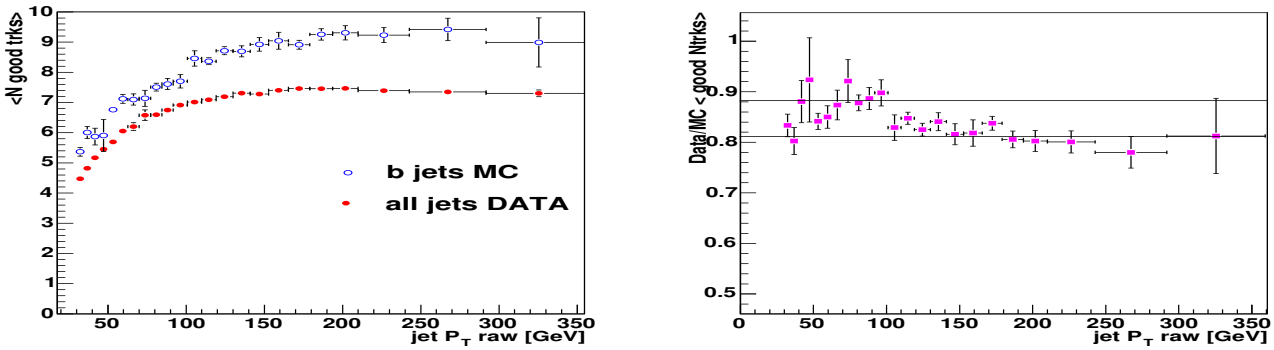

Figure 4.21: *On the left*: Profile of N_{gtrk} VS P_T for Data and b-jets in Monte Carlo. *On the right*: Ratio Data/Monte Carlo.

We therefore associate this 5% uncertainty to the Scale Factor, independent of P_T.

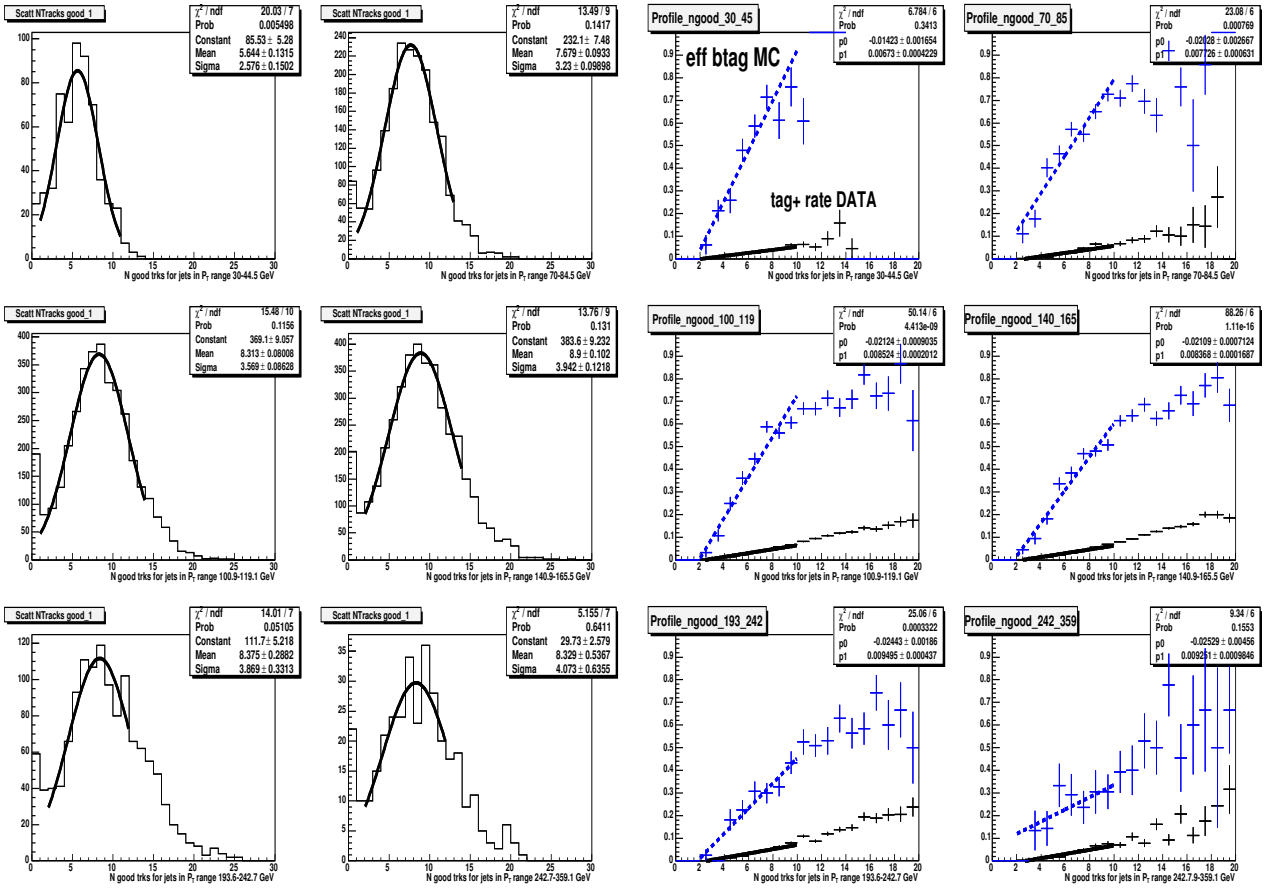

Figure 4.22: *On the left*: Distribution of Number of good tracks in b-jets for each P_T bin. *On the right*: B-tagging efficiency for MC (tagging efficiency for Data) as a function of Number of good tracks for each P_T bin.

P_T range	Data	Monte Carlo	Monte Carlo (b-jet)
30.0-44.5	±6%	±4.5%	±5%
70.0-84.5	±5%	±4%	±6%
100.9-119.1	±5%	±4%	±4%
140.9-165.5	±5%	±4%	±4%
193.6-242.7	±5%	±5%	±4%
242.7-359.1	±5%	±5%	±3%

Table 4.5: Prediction of tagging (b-tagging) efficiency variation when a 3% (4% for b-jet MC) fluctuation is associated to the $<N_{gtrk}>$.

4.4.4 Dependence on b-quark multiplicity in jet cone

An additional source of systematic uncertainty comes from the dependence of the b-tagging efficiency on the b-quark content of the tagged jet. When b-quarks are produced via gluon splitting, it is very likely that the $b\bar{b}$ pair ends up in the same jet cone. Using Monte Carlo samples, the b-tagging efficiency in case of single b-jets or double b-jets can be calculated. Figure 4.23 shows the inclusive b-tagging efficiency as a function of jet P_T from Monte Carlo (rescaled to match data with the Scale Factor), superimposed to the single b-jet and double b-jet tagging efficiency. As expected, jets containing $b\bar{b}$ pair are more likely to be tagged, and the difference is higher at high P_T.

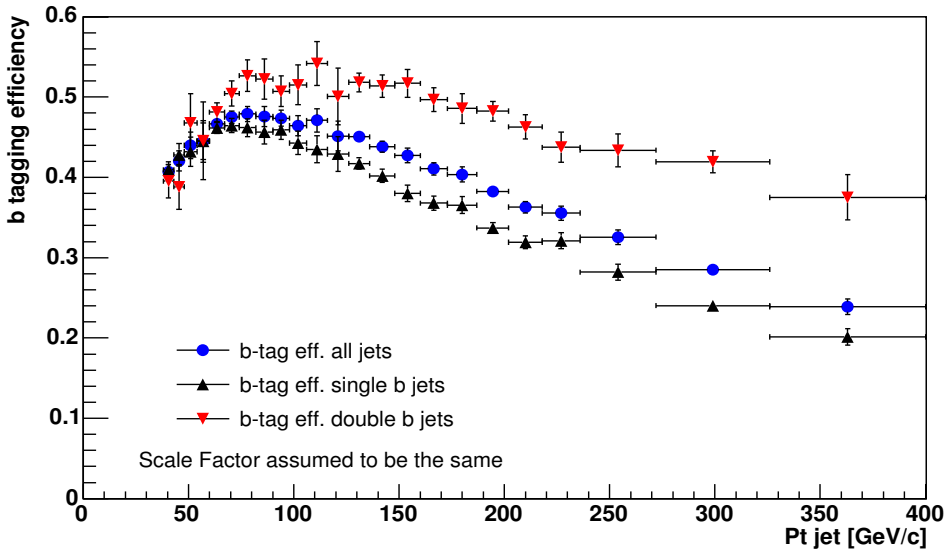

Figure 4.23: B-tagging efficiency for single b-jets and double b-jets

In measuring the inclusive b-jet cross section, the b-tagging efficiency must be measured for b-jets regardless their content in terms of b-quark multiplicity; thus, if the Monte Carlo samples do not reproduce in the correct way the rate of $b\bar{b}$-jets/b-jets, the inclusive b-tagging efficiency could be different. We evaluate this uncertainty by comparing the Pythia $b\bar{b}$-jet/b-jet rate prediction with that foreseen by the NLO theoretical calculation as explained in section 1.3: figure 4.24 shows that the rate of $b\bar{b}$-jets in Pythia Monte Carlo is underestimated with respect to that predicted in a NLO calculation, and on the left the correction factors to be applied are shown. The NLO theoretical expectation is computed for 2 different values of renormalization and factorization scale (in particular $\mu_R = \mu_F = \mu_0$ or $\mu_0/2$): results related to the $\mu_0/2$ scale – that is also the most conservative case – are chosen for the systematic error on b-tagging efficiency.

The superimposition of the b-tagging efficiency distribution for inclusive b-jets, with curves obtained considering the correction factor NLO($\mu_0/2$)/Pythia $b\bar{b}$-jets content variation is

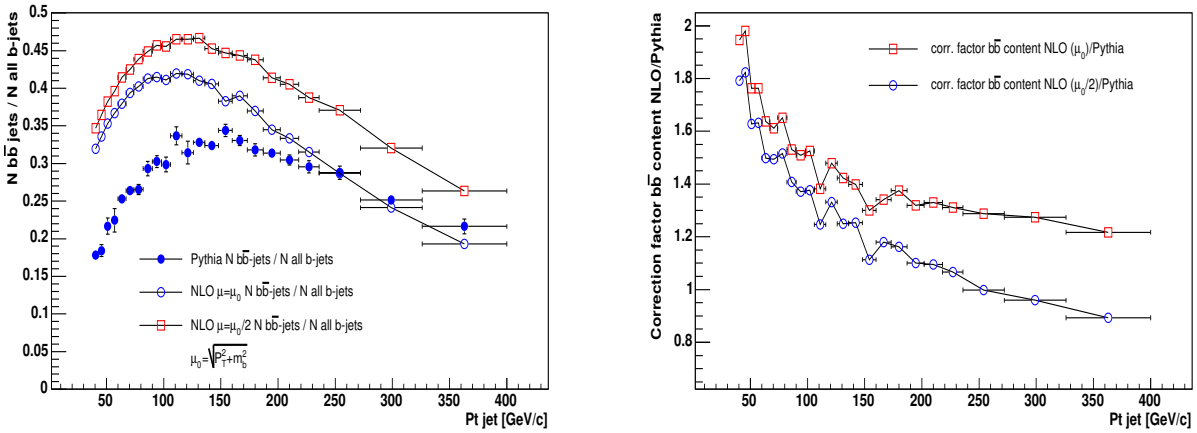

Figure 4.24: On the left: Ratio of number of $b\bar{b}$-jets to the number of all b-jets for Pythia (filled marker) and NLO prediction, as calculated for $\mu_R = \mu_F = \mu_0$(empty blue circle) and $\mu_R = \mu_F = \mu_0/2$(empty red square). On the right: correction factors coming from the NLO/Pythia ratio for both cases: the high values are the ones considered for systematic error.

shown in figure 4.25: the variation is below 2% in the whole P_T range. Finally the effect of this systematic error on the cross section is shown in figure 4.25 (on the right).

Another source of uncertainty might be related to the assumption that the Scale Factor does not depend on the b-quark content of the jet: this has been indirectly studied [42] and no obvious dependence of the SF on the b-quark generation process has been found.

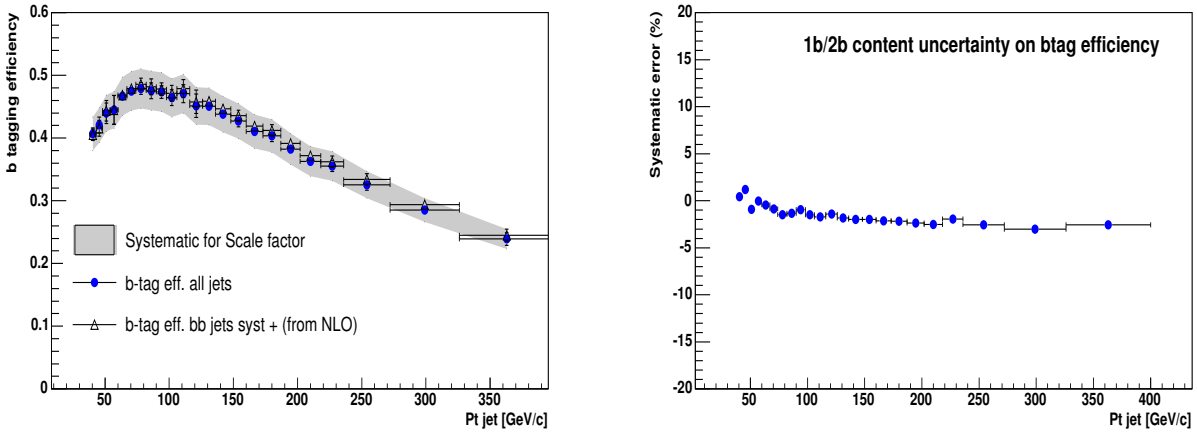

Figure 4.25: Effect of changing the double b content on the inclusive b tagging efficiency (on the left). The resulting uncertainty on the cross section is less than 2% on the whole transverse momentum spectrum (on the right).

4.5 B-flavor content of tagged jets

Several techniques have been developed to determine the heavy flavour content of a tagged jet in order to extract the fraction of b-jets. Here we use, as the discriminating quantity, the shape of the SECVTX vertex mass distribution.

The secondary vertex is usually found for long-lived b or c hadrons. Due to the presence of neutral particles and the energy lost because of detector resolution, a full reconstruction of the hadron invariant mass is not possible. Still, the invariant mass of tracks used to find the secondary vertex constitutes a good discrimination between jets containing b, c or light quarks. Using QCD 2→2 Pythia Monte Carlo, we obtain the b, c and lights-jet distributions (that we will call templates) for secondary vertex masses of positively tagged jets.
The fit is performed considering independently each bin in the corrected jet P_T, since the b-tagging efficiency depends on it as the purity of the tagging procedure.

The b-fraction is the only flavor content of interest, so the c and light jets mass distributions are merged: the secondary vertex mass from the data is fitted to find the coefficients of a linear combination of the 2 components (b and non-b) with the ROOT routine TFractionFitter[44]. The method is stable in the full jet P_T range (a 3-component fit presents problem at high P_T, where difference between c-jet and light-jet templates are small). The down-side of this choice is the Monte Carlo dependence of the c- and light-jet mixing, so we assume as correct the composition of non-b templates in terms of the c-tagged and mis-tagged jet fraction as foreseen by Monte Carlo. A systematic uncertainty is associated to this assumption.

The total error on the fraction extrapolated with TFractionFitter is generally 20% or more per bin, due to a lack in statistics both in data and in Monte Carlo. This problem is unavoidable for data; to improve the statistical error on the Monte Carlo, we checked the possibility of grouping templates of neighbour bins for the c+light template (increase in the b-template statistic is not necessary). The mass of the secondary vertex (m_{secvtx}) is dependent on jet P_T, but if the shape in a given bin is consistent with that of the neighbour, this difference is below the fit sensitivity. Standard Kolmogorov tests are performed to verify the similarity of the histograms with the one resulting from merging. In addition, the c/light mixing fraction must be constant in the P_T range of the merged templates.

This procedure has been applied to the first and the last three bins only. Figure 4.26 shows c and light templates for the three bins in [38-54] GeV/c (left column) and the three in [236-400] GeV/c (right column). The separate distributions (bins named 1, 2, 3 as a function of P_T) are compared with the one resulting from merging (named as All). Kolmogorov test results are also reported on the plots. Table 4.5 shows that the c/light mixing fraction in the bins is almost constant in the two P_T ranges. Results of the b-fraction bin-by-bin are reported in table 4.5: the total error on the fraction for P_T jets below 200 GeV/c, is generally between 10% and 20%, and it increases at higher transverse momentum; the procedure to extract the systematic errors of the last column is described in next subsection.

Figure 4.27 shows the detail of one bin, with the distribution of the mass of secondary

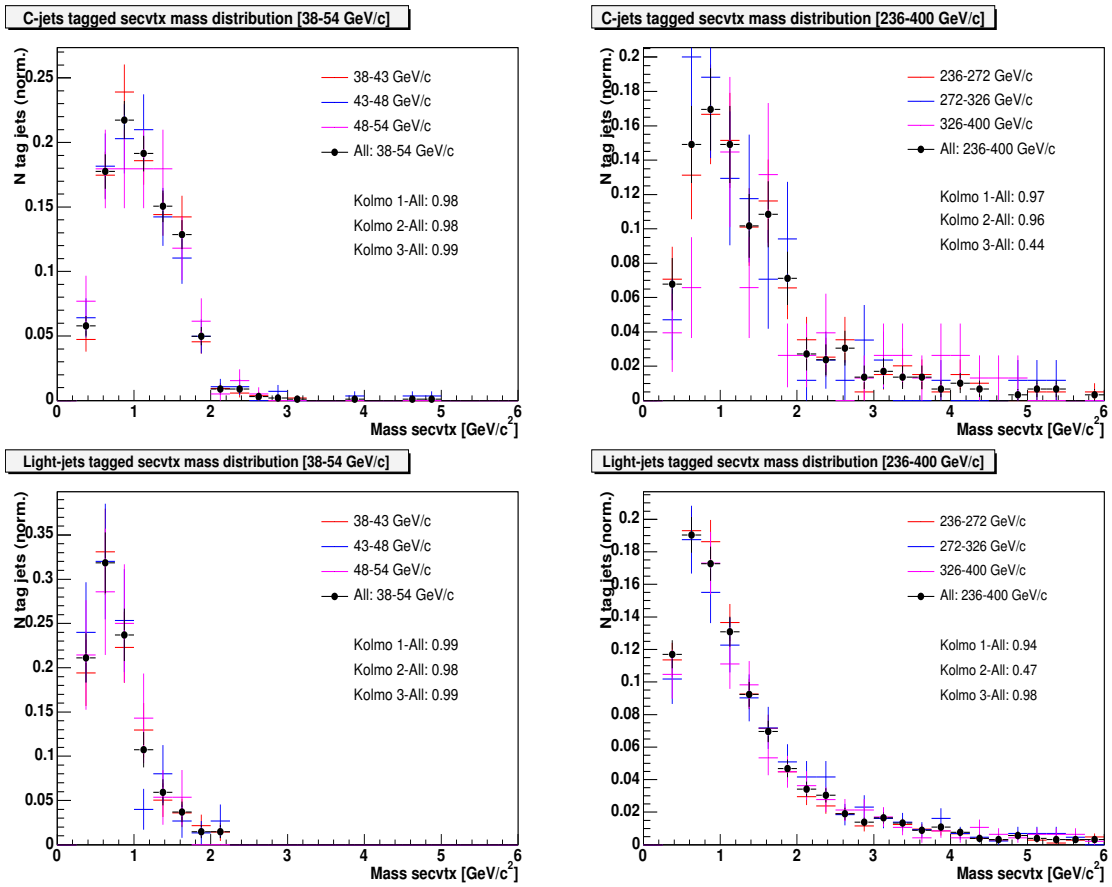

Figure 4.26: Secondary vertex mass distributions in the two bin groups considered: column on the left present 38-54 GeV/c P_T range, column on the right 236-400 GeV/c range. Results of Kolmogorov tests between single bin distribution (named as 1, 2, 3 as function of P_T) and merged distribution (named as All) are also reported.

38-43 GeV/c 1.7±0.2	43-48 GeV/c 1.8±0.3	48-54 GeV/c 1.7±0.3	Tot: **38-54 GeV/c** **1.7±0.1**
236-272 GeV/c 0.19±0.01	272-326 GeV/c 0.20±0.02	326-400 GeV/c 0.17±0.02	Tot: **236-400 GeV/c** **0.19±0.01**

Table 4.6: Fraction of c/light tagged jets for single and grouped(last column) bins.

vertex as extracted from data, compared with the fit prediction and the b and non-b mass templates rescaled to the fraction resulting from the fit. Finally, figure 4.28 shows the b-tagged jets fraction as a function of jet P_T: the statistical error and the total systematic error are reported.

P_T **range [GeV/c]**	$\mathbf{f}_b$ ± err(stat+syst)	stat	syst TOT (%)
38-43	0.35 ± 0.07	0.05	+14/-15%
43-48	0.38 ± 0.08	0.07	+10/-14%
48-54	0.40 ± 0.10	0.08	+15/-16%
54-60	0.305 ± 0.043	0.024	+12/-14%
60-67	0.345 ± 0.044	0.030	+9/-11%
67-74	0.306 ± 0.050	0.037	+11/-12%
74-82	0.287 ± 0.050	0.045	+8/-9%
82-90	0.318 ± 0.029	0.014	+8/-10%
90-98	0.303 ± 0.029	0.017	+8/-10%
98-106	0.291 ± 0.036	0.020	+10/-11%
106-116	0.286 ± 0.043	0.024	+11/-13%
116-126	0.275 ± 0.043	0.020	+14/-15%
126-136	0.263 ± 0.054	0.028	+18/-19%
136-148	0.251 ± 0.046	0.034	+12/-14%
148-160	0.212 ± 0.039	0.017	+16/-18%
160-173	0.221 ± 0.03	0.022	+10/-12%
173-187	0.218 ± 0.047	0.026	+18/-20%
187-202	0.195 ± 0.055	0.035	+22/-24%
202-218	0.135 ± 0.074	0.042	+31/-33%
218-236	0.18 ± 0.08	0.07	+31/-33%
236-272	0.14 ± 0.08	0.08	+28/-33%
272-326	0.18 ± 0.13	0.12	+28/-33%
326-400	0.26 ± 0.20	0.16	+47/-50%

Table 4.7: Fraction of b-jets among tagged jets as result of fitting on the secondary vertex mass distribution from Monte Carlo (templates for b and c+light jets)

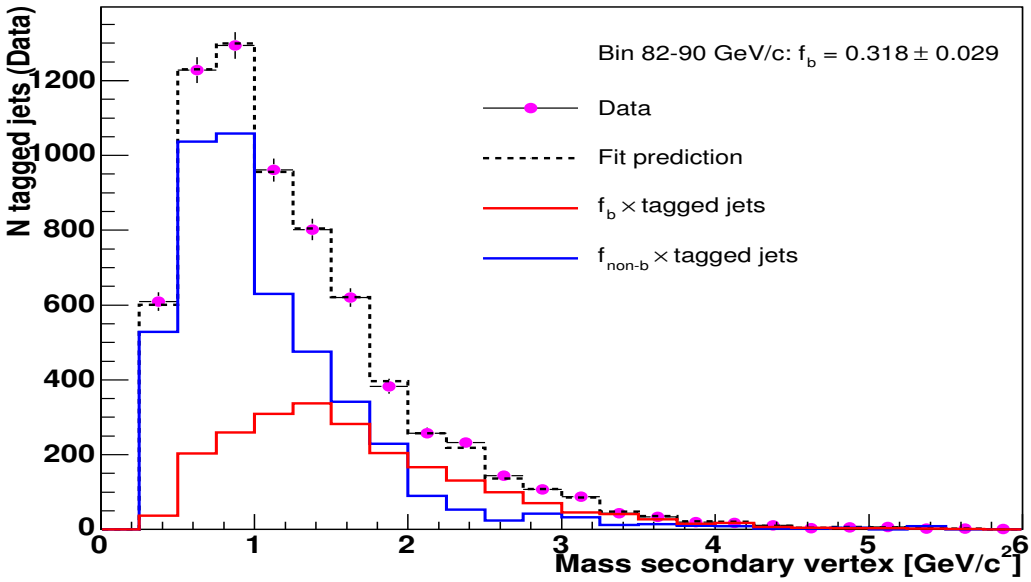

Figure 4.27: Mass of secondary vertex distributions for data and fit prediction superimposed to Monte Carlo templates of b and non-b jets, for jet P_T bin 82-90 GeV/c.

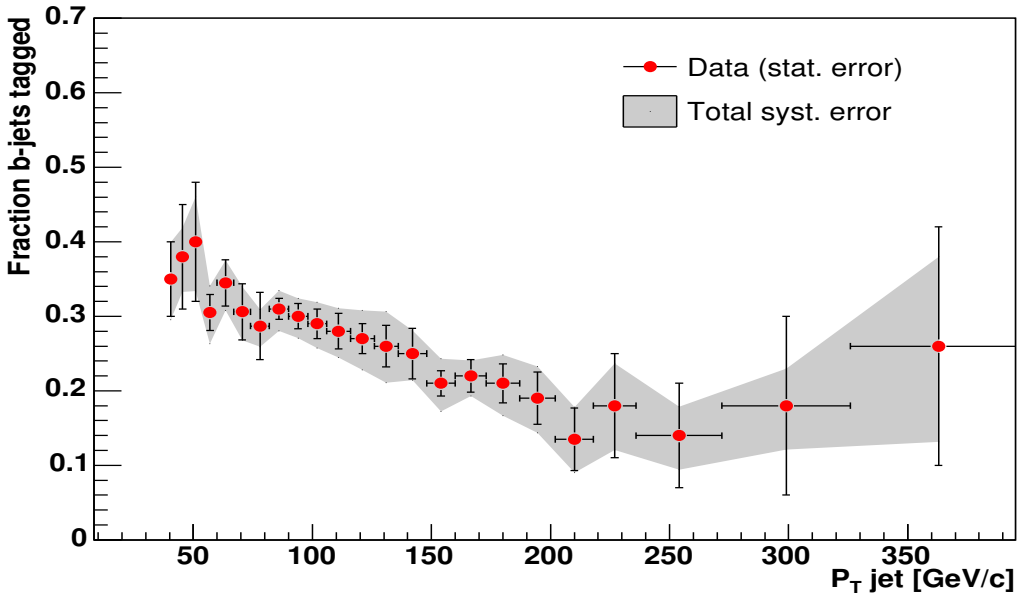

Figure 4.28: Fraction of b-jets tagged for data as a function of jet P_T: the total error from the fit is quoted, and superimposed is the total systematic errors (added contributions are listed in the next subsection).

4.5.1 Systematic error on b-fraction

The main sources of systematic error considered are listed below:

- the uncertainty due to templates statistics and stability of the fitting algorithm.
  The routine TFractionFitter used to perform the fit of secondary vertex mass gives a total error that is a combination of the statistical error on the data and on Monte Carlo samples. The latter component is a source of systematic error for the b-jet tagged fraction, so it is necessary to disentangle the two components to have a correct error propagation. A simple way implemented for this purpose is to artificially increase the integral of the templates for b and c+light jets, to reduce the statistical error related to the Monte Carlo and derive the real statistical error (from data). The overall assumption is that the error is proportional to $\sqrt{N}$, where N is the integral of the template histograms. Due to limits of the fitting procedure, the maximum factor usable for this artificial increase is 10^3. The Monte Carlo systematic error is then given by the following expression:

$$syst^{MC}_{stat} = \sqrt{(Err^{fit}_{TOT})^2 - (Err^{fit}_{10^3})^2}$$

  To check the internal consistency of the method, the same artificial increase and decrease has been applied to the data: figure 4.29 shows the correlation between the data statistical error (Δ N = $\sqrt{\mathrm{N}}$) and the total error on the fraction from the fit. There is, as expected, an anti-correlation between Δ N and $\Delta \mathrm{f_b}$, but the total error reaches a plateau that is in agreement with the systematic error on the Monte Carlo samples previously found.

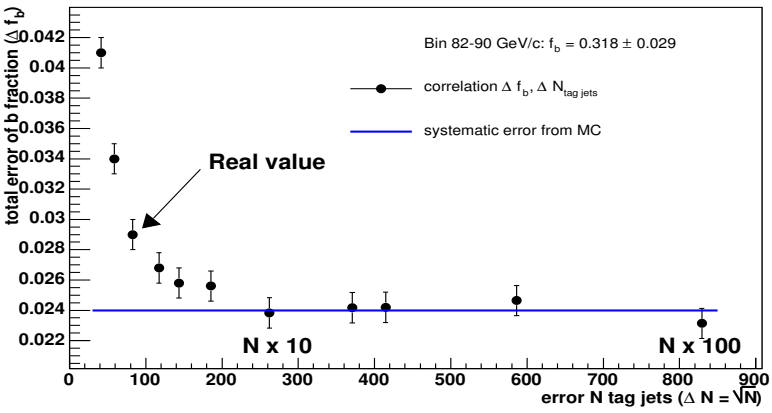

Figure 4.29: Correlation between total error on the b-fraction and the statistical error of the data sample for one of the bins [P_{T}: 82-90 GeV/c]: the horizontal line is the systematic component of the total error on the fraction, extracted in an independent way.

- c/light jets mixing.
  The fit is performed using templates from b-jet and c+light jets. The shape of

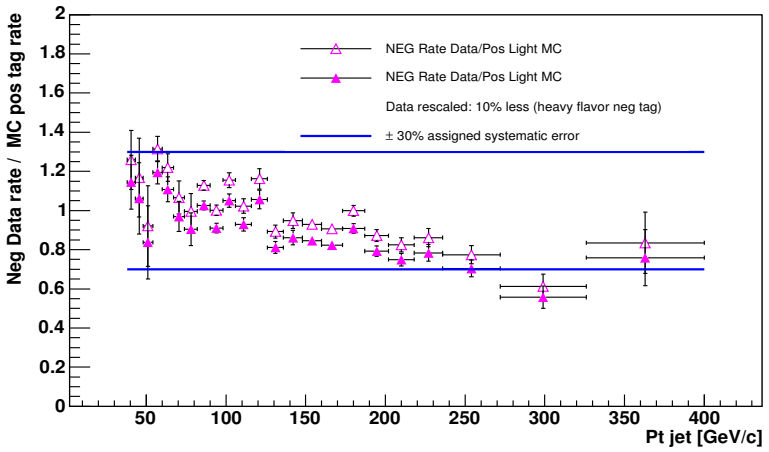

Figure 4.30: Ratio between the negative tag rate in the data and the positive mis-tag rate in Monte Carlo (full marker): the ratio with the data rate reweighted to remove the heavy flavor content is superimposed (empty marker).

the secondary vertex mass from c and light jets is different, thus it is important to adopt the correct mixing when merging the templates. The c/light tagged jet fraction relies on the prediction of Monte Carlo, so an uncertainty might be related to this assumption. Since the shape is only sensitive to the relative amount of c and light jets, it would be enough to evaluate how well the Monte Carlo is able to reproduce the light tagged jet population. The positive mis-tag rate of Monte Carlo is compared to the negative tag rate in data: in figure 4.30 the ratio, shown over the full P_T spectrum, is about 1 but with fluctuations of the order of 20%. Besides, it is necessary to take into account that, among negatively tagged jets in data, the content in heavy flavor jets is unknown but not negligible, and past dedicated studies [45] reported a b+c jet fraction of 10-15%. Thus we estimate the heavy flavor fraction in data negative tagged jets as of the order of 10%, and the corresponding ratio Data/Monte Carlo is also shown in the figure.

A 30% uncertainty band includes the ratios over the all P_T range and this is taken as systematic error related the c/light jets mixing although it is quite conservative. The final effect on the b-jets fraction is generally of the order of $\pm$5%, to increase to 10% for P_T above 200 GeV/c.

- b/c quark multiplicity in b/c tagged jets.
  It has already been observed that the Pythia Monte Carlo underestimates the ratio of $b\bar{b}$/single b-jets. In the same way, the ratio of $c\bar{c}$/single c-jets is not expected to be well described by Monte Carlo. The effect on the evaluation of the fraction derives from the different shape of the secondary vertex mass distribution for jets with 1 or 2 heavy quarks into the cone.

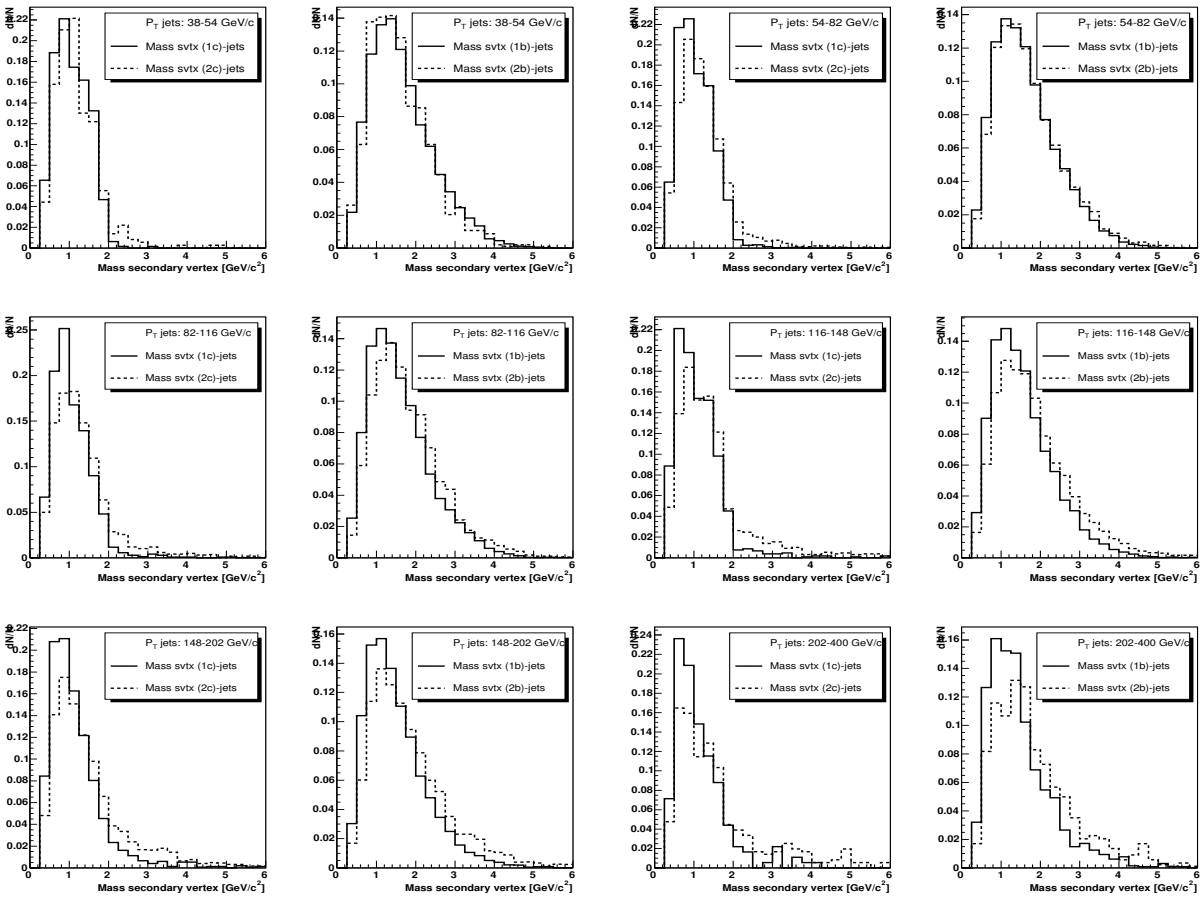

Figure 4.31: Mass secondary vertex distributions for c-tagged and b-tagged jets considering separately single (solid line) and double (dashed line) heavy-flavor content: from top-left to bottom right, 6 ranges in P_T of the jets are considered.

Using the same procedure applied to evaluate the systematic uncertainty on the b-tagging efficiency, the variation on the b-tagged jet fraction related to the contribution of $b\bar{b}$ and $c\bar{c}$-jets is found to be between +2 and -5% in the whole P_T range. Figure 4.31 shows the comparison of secondary vertex mass distributions as extracted from Monte Carlo, for tagged jets with one or two heavy quarks within the cone: 6 regions in the P_T spectrum are shown, although the systematic effects have been studied bin-by-bin. In particular, a clear tail in the $c\bar{c}$ jet mass distributions can be noticed at all transverse momentum, and the $c\bar{c}$ jet rate is the dominant component in the systematic uncertainty calculation. The asymmetric effect on the fit fraction result is related to the fact that $c\bar{c}$-jets can fake a b-jet so that a lower fraction is measured considering an increased amount of those kinds of jets. On the other hand, the effects related to an increased $b\bar{b}$-jet rate might move the fraction in the opposite direction. The final uncertainty results from the combination of the two effects.

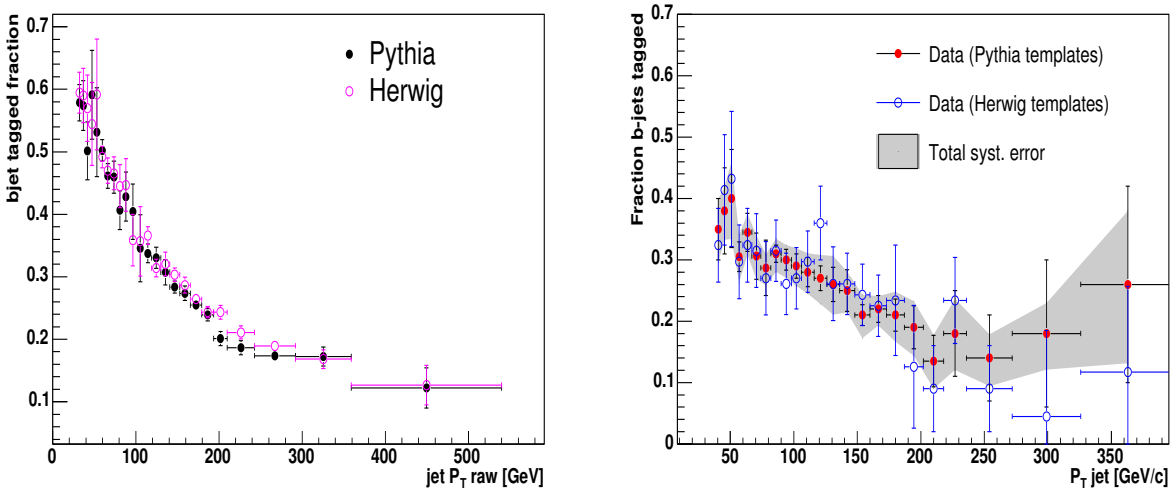

Figure 4.32: *On the left:* Comparison b-tagged jets fraction prediction from Herwig and Pythia Monte Carlo. *On the right:* Comparison of the b-tagged jet fraction as calculated from Data, using Pythia or Herwig templates.

- Pythia/Herwig comparison.
  To test the dependence of the results on the Monte Carlo generator, the whole procedure of fitting can been repeated using a Herwig MonteCarlo dijet sample. The statistics of Herwig samples is lower than the statistics for Pythia Monte Carlo samples. Nevertheless, good agreement is found when comparing the predicted fraction of b-tagged jets as a function of P_T (figure 4.32 – left). The associated systematic can be calculated as:

$$syst^{MC}_{H/P} = \sqrt{(\Delta f_{H/P})^2 - (syst^{MC\,Pyt}_{stat})^2 - (syst^{MC\,Her}_{stat})^2}$$

  where $\Delta f_{H/P}$ is the difference between the central values of the data fit results using Pythia and Herwig templates respectively. In order not to overestimate the error because of the Monte Carlo statistics, the associated errors for both Monte Carlo samples have to be subtracted. Since the difference of the two sample is found to be only statistical ($(\Delta f_{H/P})^2 > ((syst^{MC\,P}_{stat})^2 + (syst^{MC}_{stat})^2)$), the relative uncertainty is considered to be zero.

- Fragmentation model used in Monte Carlo samples.
  To check the effect of changes in the fragmentation model, a comparison of the Secvtx mass has been performed comparing default Pythia b-filtered samples (Lund fragmentation model, ϵ^{fragm}=0.0025) and Pythia b-filtered samples produced with Peterson model and $\epsilon^{fragm} = 0.06$: no significant difference in distributions has been found except for the first 2 bins of the cross section ([38-43] and [43-48] GeV/c in P_T jets). The difference between the central values of the fraction as obtained using the two templates is of the order of 1%. Figure 4.33 shows the secondary vertex mass distribution for b-jets tagged in both Pythia Monte Carlo samples, for the first two bins

and for two different ranges in transverse momentum: above 50 GeV/c any effect of fragmentation is negligible as expected.

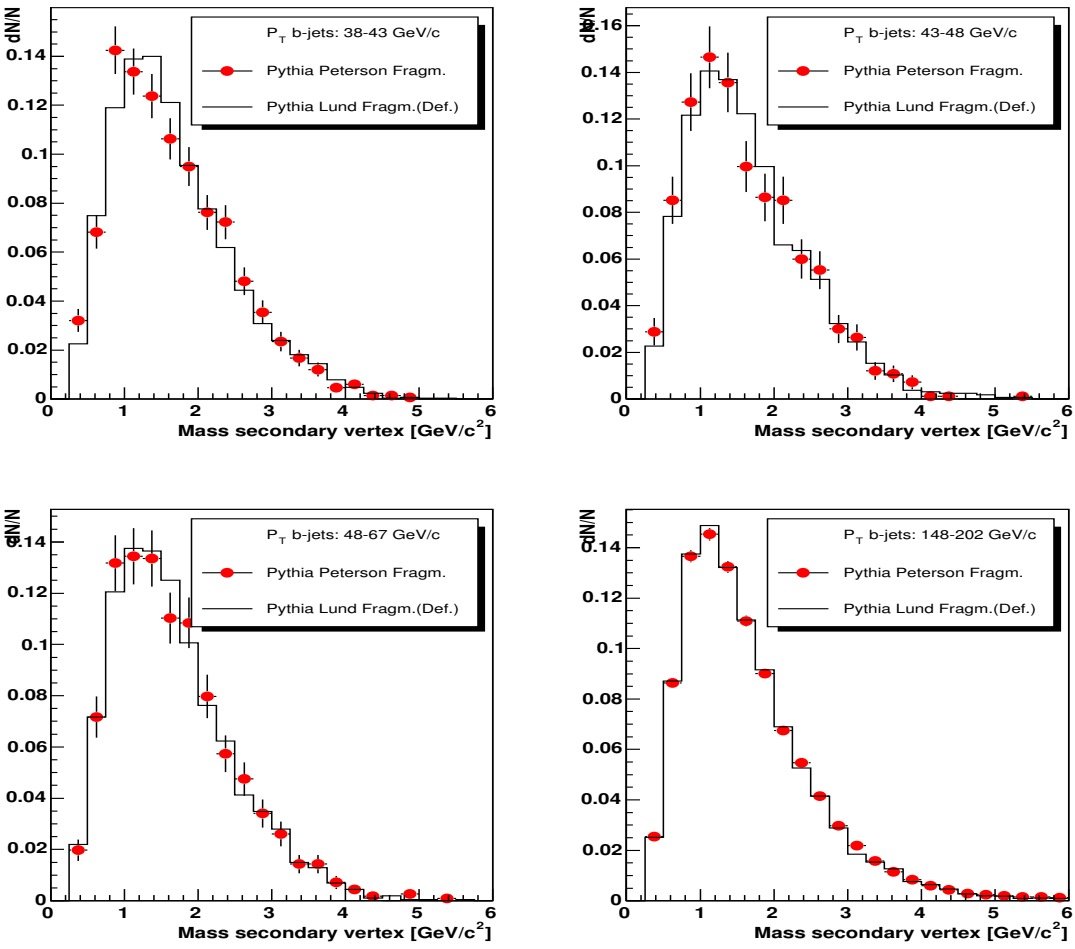

Figure 4.33: Mass of secondary vertex distributions for b-tagged jets for the first two bins(on the top) and for higher transverse momentum jets(on the bottom) as extracted from Pythia Monte Carlo samples generated with Lund fragmentation model (default, solid line) and from Pythia Monte Carlo samples generated with Peterson model (red circles).

Further checks have been made to ensure that the CDF detector simulation models well the secondary vertex mass distribution. These checks are presented in Appendix A.

Chapter 5

Results and theory comparison

In this Chapter we present results for the measurement of the inclusive b-jet production cross section in a corrected jet transverse momentum range between 38 and 400 GeV/c, covering almost 7 orders of magnitude. The jets tagged by the SecVtx algorithm are counted and the b-flavor content is extracted for each jet P_T bin, as described in the previous chapter. To have a cross section of b-jets at particle level, as presented in 5.1, further correction factors are required, as described in section 5.2. Systematic errors are discussed in 5.3, and the final results are described in section 5.4 as well as a comparison with Leading Order Monte Carlo. Finally, a preliminary comparison of the cross section with the theoretical predictions at Next-to-Leading Order (NLO) is presented (section 5.5) using the algorithm described in the first Chapter. Correction factors extracted from Pythia Monte Carlo to take into account hadronization and underlying event effects that are not taken into account by the theory, are used for the comparison.

5.1 The raw b-jet cross section

The raw inclusive cross section for b-jets is:

$$\left.\frac{d^2\sigma_{\mathrm{b-jet}}}{dp_T dY}\right|_i = \frac{N^i_{\mathrm{tagged}} f^i_b}{\epsilon^i_{\mathrm{b-tag}} \Delta Y \ \Delta p^i_T \int \mathcal{L}}$$

for each bin i in jet transverse momentum corrected for detector effects, where

- N^i_{tagged} is the number of the tagged jets using b-tagging algorithm,
- f^i_b is the fraction of b-jets among tagged jets as extracted from the data,
- $\epsilon^i_{\mathrm{b-tag}}$ is the b-tagging efficiency ($= \epsilon^i_{\mathrm{b-tag\,MC}} \times$ SF),
- ΔY is the jet rapidity range, equal to 1.4,
- Δp^i_T is the size of the bin in jet transverse momentum,

- $\int \mathcal{L}$ is the integrated luminosity defined for each dataset and weighted with the related prescale factor; the correction factor 1.019 (for combined CDF and D0 luminosity measurements) [46] is applied in the final calculation.

The statistical uncertainty of the measured cross section is calculated as

$$\delta\Big(\frac{d^2\sigma_{\mathrm{b-jet}}}{dp_T dY}\Big)\Big|_i = \frac{\delta(N^i_{\mathrm{tagged}} f^i_b)}{\epsilon^i_{\mathrm{b-tag}} \Delta Y \ \Delta p^i_T \int \mathcal{L}}$$

$$= \frac{d^2\sigma_{\mathrm{b-jet}}}{dp_T dY}\Big|_i \times \sqrt{(\delta N^i_{\mathrm{tagged}}/N^i_{\mathrm{tagged}})^2 + (\delta f^i_{b\,\mathrm{stat.}}/f^i_b)^2}$$

where $(\delta N^i_{\mathrm{tagged}}/N^i_{\mathrm{tagged}})$ comes from the counting of the tagged jets and $(\delta f^i_{b\,\mathrm{stat.}}/f^i_b)$ comes from the statistical component of the error due to the b-tagged jets fraction. Luminosity and b-tagging efficiency errors are considered as purely systematic uncertainties. Although there is an anti-correlation between the two terms of statistical error contributions (see figure 4.29), the impact of $\delta f^i_{b\,\mathrm{stat.}}$ is much larger than that due to the bin statistics (15% *vs* <1%): thus the formula above is considered to be a conservative estimate of the statistical error.

5.2 Unfolding procedure

In addition to the average correction applied to the jet P_T, the measurement has to be corrected for the acceptance, for smearing and for effects due to the b-flavor content in the jet, in order to measure a particle level b-jet cross section free of detector effects. The impact of this correction, generally referred to as *unfolding* and carried out bin-by-bin using Monte Carlo samples, is quite important.

The procedure applied to find the unfolding correction factors is summarized as follow:

- Hadronic and calorimetric jets are reconstructed using HEPG final state particles and calorimetric towers respectively.
- The related b-jet cross sections are reconstructed with the requirement that the hadronic (calorimetric) jet must be identified as a b-jet, that is that a B-hadron is found inside the jet cone within a distance below 0.7 from the jet axis.
- Apart for the rapidity range, no selection cuts are applied on the hadronic b-jets.
- The ratio of the *true* particle (hadronic) level cross section to the average corrected P_T^{jet} is taken on a bin-by-bin basis so that the unfolding factors are defined as:

$$C^i_{\mathrm{unfold}} = \frac{d^2\sigma_{\mathrm{b-jet}}/dp_{\mathrm{T,\,HAD}}dY_{\mathrm{HAD}}}{d^2\sigma_{\mathrm{b-jet}}/dp_{\mathrm{T,\,COR}}dY_{\mathrm{CAL}}}\Big|_i = \frac{N^{b-jets}_{hadron\ level}}{N^{b-jets}_{cal\ level}}\Big|_i$$

  where $\mathrm{N}^{b-jets}_{hadron\ level}$ is the number of particle b-jets in the i^{th} bin and $\mathrm{N}^{b-jets}_{cal\ level}$ is the number of calorimetric b-jets in corrected P_T.

The bin-by-bin factors are applied to the previous b-jet cross section and:

$$\left.\frac{d^2\sigma_{\mathrm{b-jet}}}{dp_T dY}\right|_i^{\mathrm{unfold}} = \frac{N^i_{\mathrm{tagged}} f^i_b C^i_{\mathrm{unfold}}}{\epsilon^i_{\mathrm{b-tag}} \Delta Y \ \Delta p^i_T \int \mathcal{L}}$$

is the b-jet cross section at particle level. Figure 5.1 on the left shows the ratio between data and Monte Carlo (Pythia) cross sections once the data are unfolded following the explained procedure: the shape of this ratio – fitted with a third order polynomial – indicates a clear difference between the P_T spectrum in the Monte Carlo and that in the data.

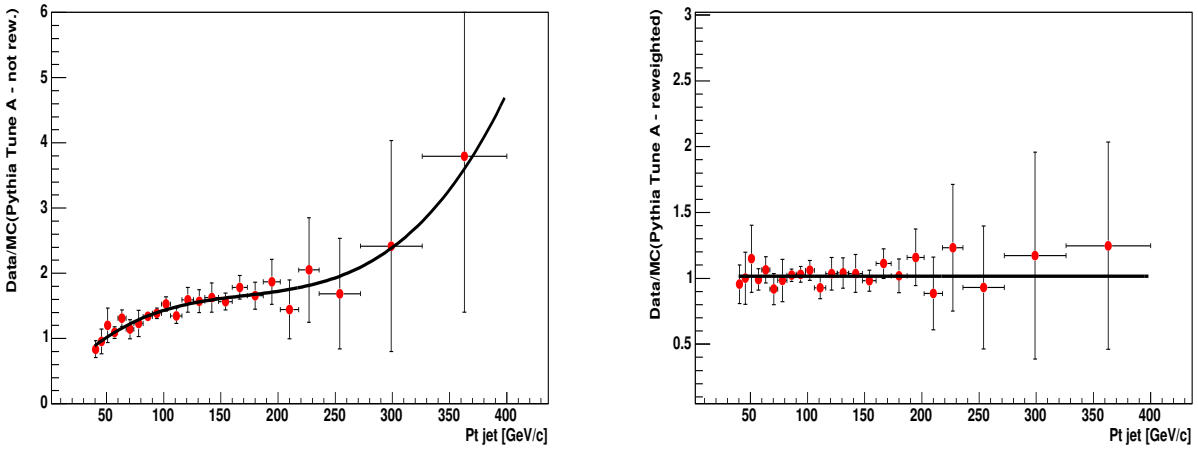

Figure 5.1: Data/MC ratio of b-jet cross section: on the left, unfolding factors from Pythia not reweighted, on the right unfolding factors from reweighted Pythia.

This effect, normally associated with the P_T shape given by CTEQ5L PDF function implemented in Pythia, could cause a bias when calculating the unfolding factors, that must be reduced to make the measurement independent from the Pythia spectrum in transverse energy. Then, a Monte Carlo reweighting procedure has been adapted: for each event, the $\hat{p_T}$[1] is extracted, and each event is then reweighted by this third order polynomial applied in $\hat{p_T}$. Figure 5.1 on the right shows the new ratio Data/MC, with unfolding factors from the reweighted MC: the shape is flat and consistent with a straight line (constant fit: $\chi^2/NdF = 0.24$, to be compared to a third polynomial fit: $\chi^2/NdF = 0.25$). Thus, a second iteration is not necessary.

The unfolding factors obtained by reweighting the Monte Carlo are applied, and the difference with the non-reweighted Pythia factors is taken as a systematic error, added in quadrature with the uncertainty from Monte Carlo statistics. Figure 5.2 shows the comparison of reweighted and non-reweighted Pythia unfolding factors, whilst in 5.3 the ratio is reported, considering the statistical error from MC only once.

[1] $\hat{p_T}$ is defined as the transverse momentum of the final parton in the 2→2 hard process

The bin-by-bin unfolding factors are on average 1.7 for jets with transverse momentum below 150 GeV/c, and they increase up to 2 and above for very high P_T. Two different effects contribute to these factors: the correction for the acceptance of the event selection cuts, and the real smearing convoluted with the specific correction for b-flavor jets. The acceptance contributes only about 10%, mainly because of the Z vertex cut, so that smearing and b-specific jet corrections are dominant. This is expected, since the average P_T jet correction procedure has been implemented for general tagged jets (thus with several charged tracks passing P_T cuts) and not for inclusive b-jets; thus, together with the bias due to the tagger, we have to consider, for example, that about 23% of b-hadrons decay semileptonically (e, μ, τ), resulting an underestimation of the parton energy due to lost neutrinos.

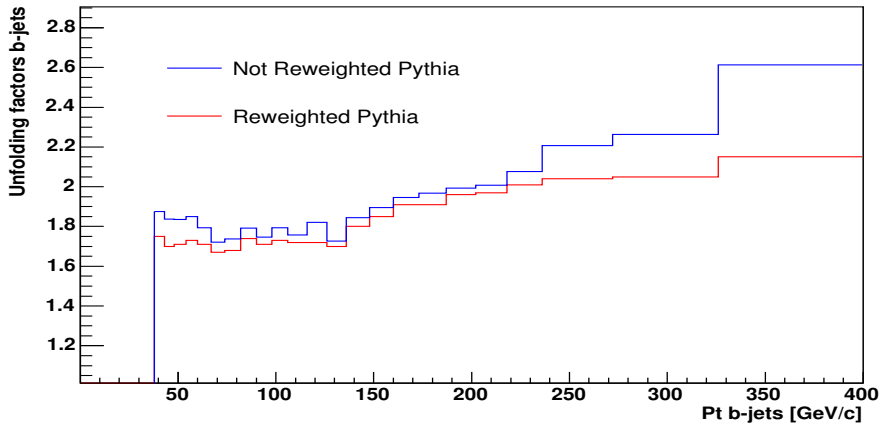

Figure 5.2: Unfolding factors as obtained without and with reweighting Pythia MC.

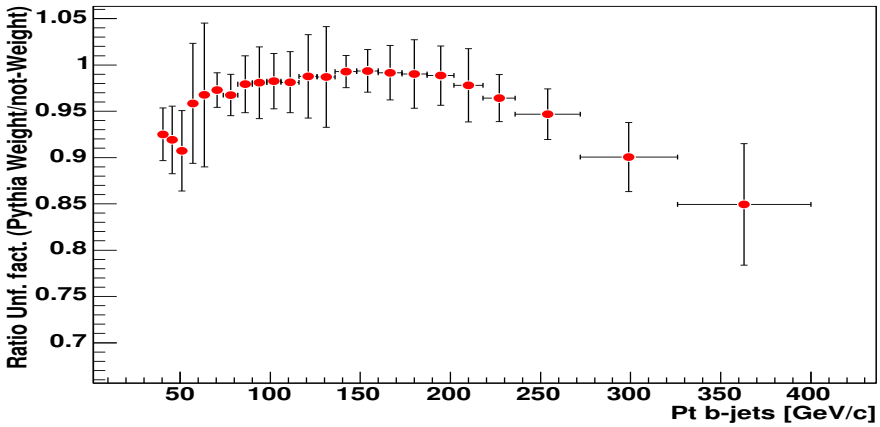

Figure 5.3: Ratio of unfolding factors as obtained with Pythia weighted/ Not weighted.

5.3 Systematic Uncertainties

The systematic uncertainties on the measured b-jet cross section result from five sources: calorimeter response, resolution, b-tagging, unfolding factors and luminosity. While the uncertainty on the luminosity has no transverse momentum dependence, the other systematic errors are found as a function of jet P_T. The different contributions are presented below:

- Absolute Jet Energy Scale: it is evaluated varying the measured $P_T^{\rm jet}$ in data (leaving Monte Carlo unchanged) by $\pm 3\%$. This quantity has been evaluated for common use in CDF [47] and arises from the calorimeter simulation, modelling of the fragmentation by the Monte Carlo, and stability of the calorimeter. The effect on the cross section is between $^{+10\%}_{-8\%}$ for lowest P_T bin and $^{+39\%}_{-22\%}$ for the highest one.

- Jet energy resolution: once the jets are corrected, the jet energy resolution, $\sigma(P_T^{jet})$, is derived from MonteCarlo. Figure 5.4 shows the resolution as a function of $P_T^{\rm HAD}$, passing from 15-20% at low P_T to 10% at high P_T. The error associated to the energy resolution has been evaluated in [48] and it is of the order of 10% for Pythia Monte Carlo. Thus, to calculate the corresponding systematic, the $P_T^{jet}(HAD)$ for each jet is smeared by the observed resolution $\sigma(P_T^{jet}(HAD))$ and by $1.1\times\sigma(P_T^{jet}(HAD))$ and $0.9\times\sigma(P_T^{jet}(HAD))$. To be conservative, we take as systematic uncertainty, the highest value between the positive and negative fluctuation: this error is around $\pm 6\%$.

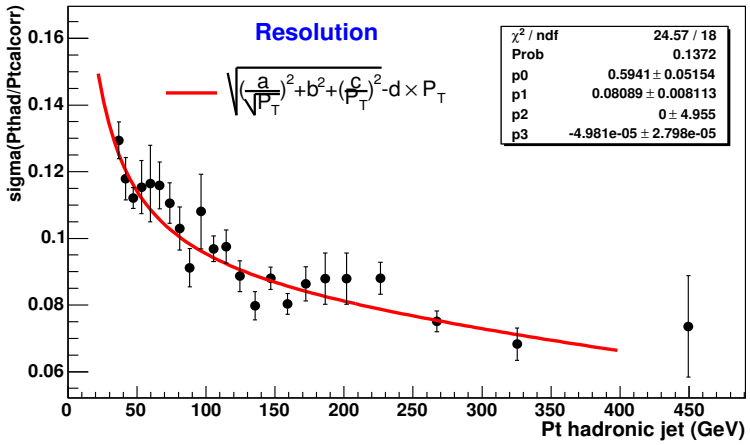

Figure 5.4: Energy resolution as derived from Pythia Monte Carlo: values for a, b, c, d parameters of fitted function are reported on the plot, as $p0$, $p1$, $p2$, $p3$ respectively.

- Multiple interactions: contributions to the jet energy due to multiple interactions is removed from raw jets. The 15% systematic uncertainty on the correction covers the luminosity dependence of the measurement and has a negligible impact on the P_T distribution both at high and low P_T.

- B-tagging efficiency: the total systematic error on b-tagging efficiency is the result of the combination of the uncertainties described in section 4.4: mis-tage rate, semileptonic *vs* hadronic decay, P_T dependence and b-quark multiplicity in the jet cone. The effect on the cross section is almost constant in transverse momentum – since the only P_T dependent error source is the b-quark multiplicity – and it is around 7.5%.

- B-fraction: as already explained in section 4.5.1, the systematic error on the b-fraction depends on many factors. The main contributions arise from the template statistical uncertainty convoluted with the fitting procedure stability, from uncertainty on the light-quark content in Monte Carlo samples, and on the b-quark multiplicity in the jet cone. The global uncertainty on the cross section is $^{+14\%}_{-15\%}$ for the first bin, $^{+47\%}_{-50\%}$ for the last bin. The lowest error is found for jets of the intermediate P_T region – about 90 GeV/c – and is $^{+8\%}_{-10\%}$.

- Unfolding: we consider two sources of systematics affecting the unfolding factors: Monte Carlo statistics and changes in the factors after the iteration procedure. The latter is the dominant contribution, and the error is around 15% for jets in the range 38-54 GeV/c, but below 4% for intermediate P_T jets. It increases up to 40% for the last bin.

- Luminosity and Prescale: the integrated luminosity enters in the cross section as a normalization factor. Thus, its uncertainty enters directly in the cross section. The official CDF 6% uncertainty on the luminosity value is used.

  An additional 2% has been assigned, for the P_T jet range [38-54] GeV/c, due to the uncertainty on prescale factor of ST05 for runs < 147879 – because of dynamic L2 prescale. For the other samples, no error is required for the prescale.

Fractional contributions to the total systematic error are presented in figure 5.5: the absolute energy scale and the b-tagged jet fraction are the major contribution in the whole P_T spectrum, but at high momentum the error related to the unfolding is comparable.

The overall systematic error is shown in figure 5.6: the uncertainty is $^{+25\%}_{-25\%}$ for the first bin, $^{+73\%}_{-68\%}$ for the last bin. The lowest error is found for jets of the intermediate P_T region – about 90 GeV/c – and is $^{+17\%}_{-20\%}$.

5.4 Results

Figure 5.7 shows the inclusive cross section for b-jets at the particle level. For the first two bins (that use data of ST05 sample), each jet is weighted by the correspondent efficiency value (below 99%) as extracted from the function fit to take into account the trigger bias. The differential cross section is measured for P_T jets between 38 and 400 GeV/c, covering almost 7 orders of magnitude. Data are reported in Table 5.4.

In figure 5.8 data are also compared with the hadronic b-jet cross section as extracted from Pythia and Herwig MC (in figure 5.9 the ratio Data/Pythia and Data/Herwig is

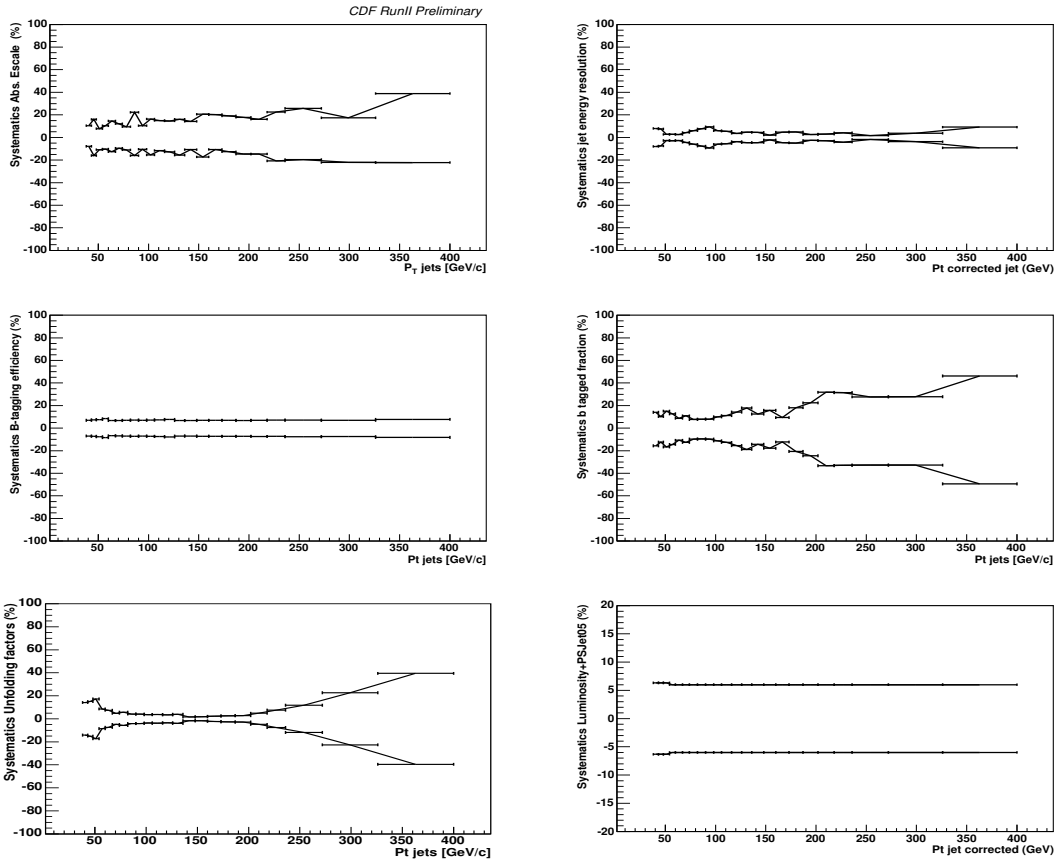

Figure 5.5: Systematic errors (from top, left: Energy scale, energy resolution, b-tag efficiency, b-tag fraction, unfolding factors, luminosity and prescale).

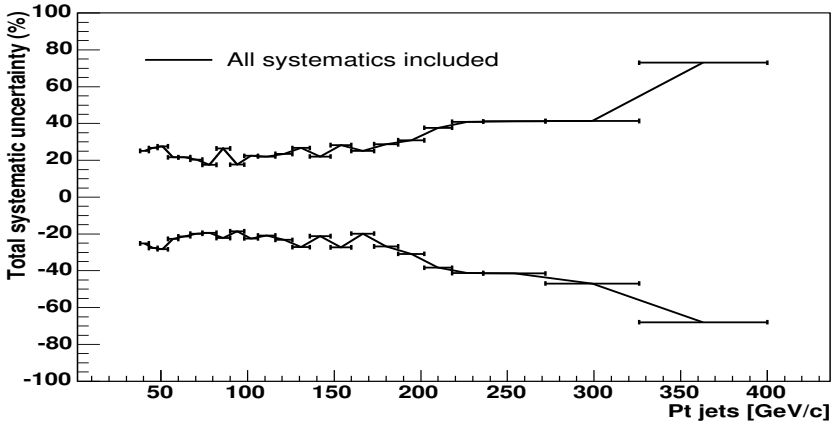

Figure 5.6: Total systematic error on b-jet cross section at particle level.

shown). Both Pythia and Herwig are leading order Monte Carlo calculations together with a probabilistic algorithm for initial- and final-state radiation: the difference in the ratio is mainly related to the implementation of the parton shower (Pythia uses the String Model with Bowler fragmentation functions, Herwig uses a cluster model), and to the underlying event contributions. While Pythia is tuned on RunI CDF data (Tune A) to correctly reproduce underlying events, Herwig is not.

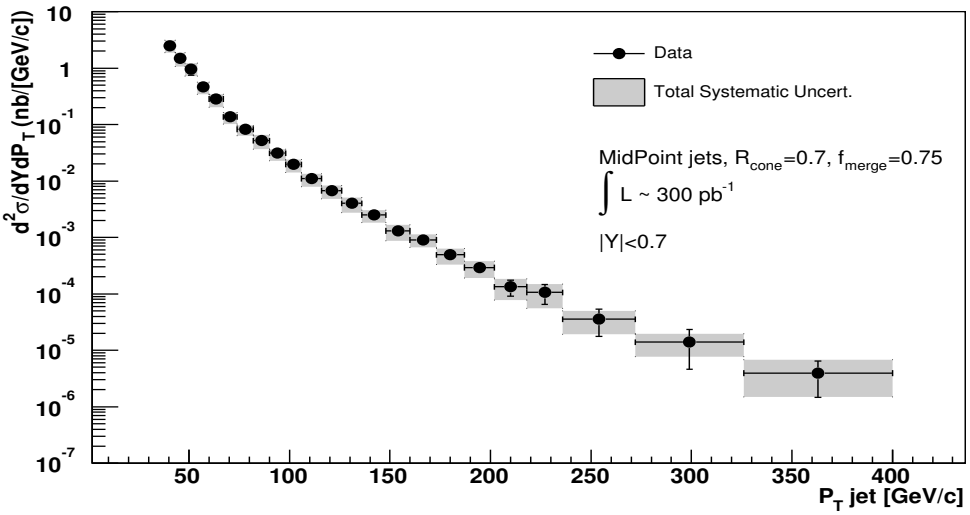

Figure 5.7: Differential b-jet cross section corrected at particle level.

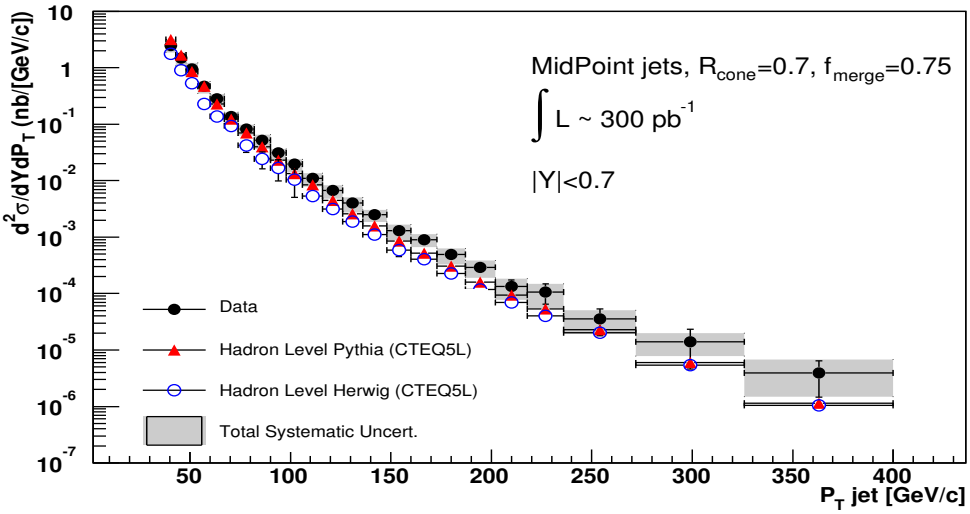

Figure 5.8: Differential b-jet cross section corrected at particle level compared with Pythia and Herwig Monte Carlo.

p_T^{b-jet} [GeV/c]	$\frac{d^2\sigma_{bjet}}{dp_T dy} \pm$ stat. $\pm$ syst. $[\frac{nb}{GeV/c}]$	$C_{HAD}^{b-jet} \pm$ stat.
38 - 43	$(2.48 \pm 0.38^{+0.62}_{-0.62})\times10^{0}$	1.169 ± 0.016
43 - 48	$(1.48 \pm 0.29^{+0.40}_{-0.41})\times10^{0}$	1.144 ± 0.022
48 - 54	$(9.6 \pm 2.1^{+2.7}_{-2.7})\times10^{-1}$	1.058 ± 0.025
54 - 60	$(4.7 \pm 0.4^{+1.0}_{-1.1})\times10^{-1}$	1.098 ± 0.036
60 - 67	$(2.8 \pm 0.3^{+0.6}_{-0.6})\times10^{-1}$	1.088 ± 0.008
67 - 74	$(1.4 \pm 0.2^{+0.3}_{-0.3})\times10^{-1}$	1.077 ± 0.011
74 - 82	$(8.3 \pm 1.0^{+1.5}_{-1.6})\times10^{-2}$	1.091 ± 0.014
82 - 90	$(5.2 \pm 0.2^{+0.9}_{-1.1})\times10^{-2}$	1.062 ± 0.017
90 - 98	$(3.1 \pm 0.2^{+0.7}_{-0.6})\times10^{-2}$	1.034 ± 0.012
98 - 106	$(2.0 \pm 0.1^{+0.4}_{-0.4})\times10^{-2}$	1.029 ± 0.014
106 - 116	$(1.1 \pm 0.1^{+0.2}_{-0.2})\times10^{-2}$	1.028 ± 0.017
116 - 126	$(6.7 \pm 0.8^{+1.5}_{-1.5})\times10^{-3}$	1.010 ± 0.006
126 - 136	$(4.0 \pm 0.4^{+1.0}_{-1.1})\times10^{-3}$	1.011 ± 0.008
136 - 148	$(2.5 \pm 0.3^{+0.55}_{-0.52})\times10^{-3}$	1.007 ± 0.009
148 - 160	$(1.3 \pm 0.1^{+0.36}_{-0.35})\times10^{-3}$	1.005 ± 0.012
160 - 173	$(9.0 \pm 0.1^{+2.2}_{-1.8})\times10^{-4}$	1.010 ± 0.010
173 - 187	$(5.0 \pm 0.6^{+1.4}_{-1.3})\times10^{-4}$	1.0 ± 0.012
187 - 202	$(3.0 \pm 0.5^{+0.9}_{-0.9})\times10^{-4}$	1.0 ± 0.015
202 - 218	$(1.3 \pm 0.4^{+0.5}_{-0.5})\times10^{-4}$	0.996 ± 0.010
218 - 236	$(1.1 \pm 0.4^{+0.5}_{-0.5})\times10^{-4}$	1.0 ± 0.013
236 - 272	$(3.6 \pm 1.8^{+1.5}_{-1.5})\times10^{-5}$	0.983 ± 0.013
272 - 326	$(1.4 \pm 0.9^{+0.6}_{-0.7})\times10^{-5}$	0.994 ± 0.008
326 - 400	$(3.9 \pm 2.5^{+2.8}_{-2.7})\times10^{-6}$	1.020 ± 0.016

Table 5.1: Differential inclusive b-jet cross section at particle level as a function of p_T^{jet} for jets with $p_T^{jet} > 38$ GeV/c and $|y^{jet}| < 0.7$. The C_{HAD}^{b-jet} factors are applied to the NLO pQCD prediction: the methodology to define these factors is explained in section 5.5.1

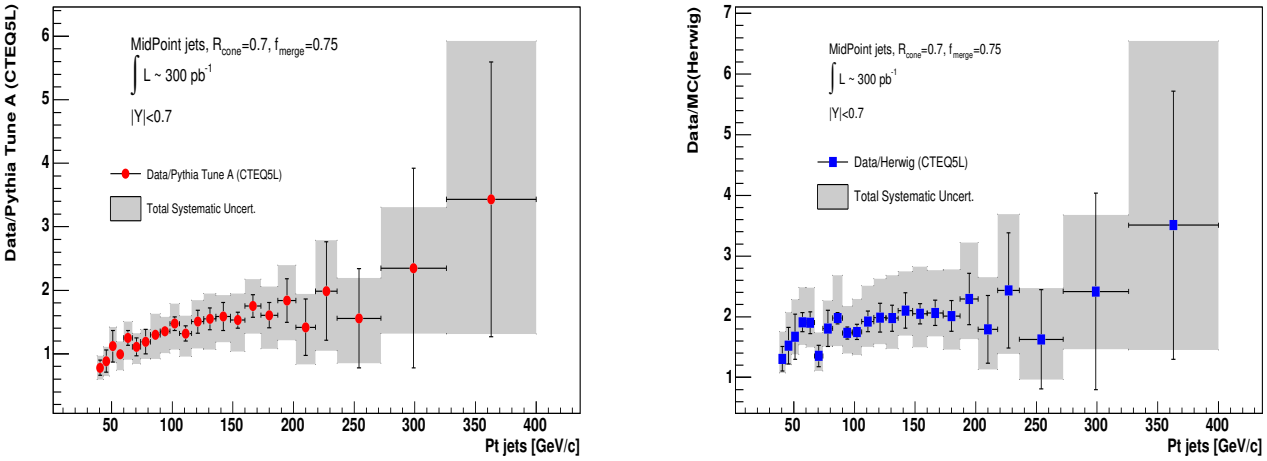

Figure 5.9: Ratio of differential b-jet cross section corrected at particle level with Pythia (on the left) and Herwig Monte Carlo (on the right).

5.5 Comparison to NLO pQCD

The Next-to-Leading Order algorithm for the b-jet cross section calculation, described in Chapter 1, has been adapted to match the data, giving a differential cross section in jet rapidity and P_T. Jets produced in $|Y| < 0.7$ are considered, in order to correctly reproduce the acceptance of the data analysis. The default parameters entering in the calculations are listed below:

- b-quark mass: m_b=4.75 GeV/c^2 Given the high energy jets considered, the b-mass dependence of the theoretical result (m_b varying between 4.5 GeV/c^2 5.0 GeV/c^2) is negligible.

- renormalization and factorization scale: we always consider μ_R=μ_F=μ, being μ=μ_0/2, and $\mu_0 = \sqrt{p_T^2 + m_b^2}$. This choice is mainly driven by the scale used in NLO pQCD calculation for inclusive jet cross section at CDF[49, 50] (P_T^{jet}/2). However, it must be considered that, rather than the scale being proportional to the natural scales of the process (m_b, P_T^{b-jet}), no theoretical constraints exist, as well for the choice of $\mu_R = \mu_F$.

- cone size of the jet: A cone size R=0.7 is used, but a separation factor [51] is also considered (R$_{sep}$=1.3), to mimic the merging/splitting mechanism of a jet-cone algorithm. The NLO calculation uses a Snowmass-like scheme, different from the E-scheme implemented for data jets. Thus, the P_T spectrum of the b-jet is affected by unknown uncertainties due to this difference in jet definition. The factor R$_{sep}$=1.3 is also chosen in analogy with inclusive jet cross section studies, but a new theoretical calculation is needed to allow a more conclusive comparison.

- Parton distribution function: we use CTEQ6M – and the related uncertainties – as shown in section 1.4. The CTEQ6M PDFs are the published most recent sets of parton distribution functions (a later version has been recently released, namely CTEQ6.1M, providing a global fit that is almost equivalent to the CTEQ6M). Differences are mainly on some parton distributions (*e.g.*, the gluon) that may deviate from CTEQ6M in some kinematic ranges, but the amount of this deviation is well within the specified uncertainties.

5.5.1 Corrections for Underlying Event and Fragmentation

Particle jets are much more complicated objects with respect to the parton jets considered in the pure NLO calculation, because of fragmentation effects and because of underlying events (UE). Fragmentation brings a loss of energy from the jet cone, whereas the underlying event adds additional energy into the jet cone. In order to compare NLO predictions to the data, these effects must be accounted for: here the contribution of UE is added to the theory curve, while fragmentation contributions is subtracted.

Since the correction factors do not depend on the hard scattering, Pythia Tune A is used to derive them. Concerning the underlying event, in Pythia two contributions can be distinguished: from Multiple Parton Interactions (MPI) and from beam remnants, the first being dominant. Thus, the global underlying event / fragmentation correction factor is the ratio of inclusive b-jet cross section obtained running the jet reconstruction algorithm at hadron level on MC samples in which MPI are turned ON, on one hand, and running it at parton level on MC samples where MPI is turned OFF. Thus:

$$C_{\rm had} = \frac{\sigma(\text{hadron level with MPI})}{\sigma(\text{parton level no MPI and no Beam remnants})} \tag{5.1}$$

The corrections can be factorized based on the two different contributions:

$$C_{\rm had} = C^{\rm MPI}_{\rm Hadron\,Level} \times C^{\rm Fragm\&BR}_{\rm No\,MPI} \tag{5.2}$$

where

$$C^{\rm MPI}_{\rm Hadron\,Level} = \frac{\sigma(\text{hadron level with MPI})}{\sigma(\text{Hadron level no MPI})} \tag{5.3}$$

is effectively the correction due to underlying event only, and

$$C^{\rm Fragm\&BR}_{\rm No\,MPI} = \frac{\sigma(\text{hadron level no MPI})}{\sigma(\text{parton level no MPI and no Beam remnants})} \tag{5.4}$$

is the correction due to fragmentation and BR correction only. The factors are reported in the figure 5.10 superimposed to the two separate contributions: a 18% correction is applied for the lowest P_T jet bin, whilst it is negligable for jet transverse momenta above 120 GeV/c.

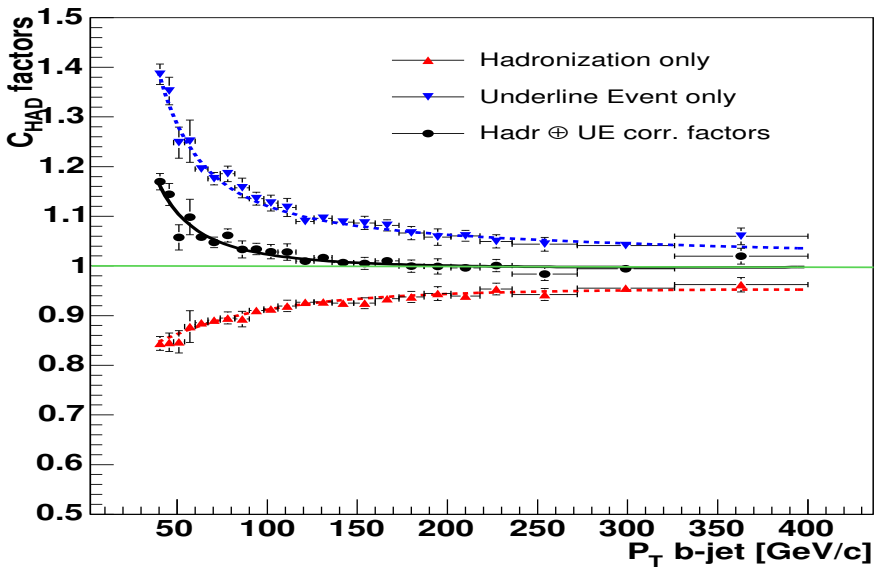

Figure 5.10: Correction factors for fragmentation and underlying event, for b-jets, as extracted from Pythia Tune A Monte Carlo.

5.5.2 Results data *vs* NLO

The superimposition of data and the NLO prediction corrected at hadron level for the renormalization and factorization scale equal to $\mu_0/2$ is shown in figure 5.11. The grey band refers to the total systematic error in data, while the dotted line is the theory uncertainty. The reported systematic error on the theoretical prediction is related to four different sources:

- PDF: extracted using the 20 eigenvector basis sets of CTEQ6M as from equation 1.4, the corresponding uncertainty on the cross section is between 7% for the lowest P_T bin and 20% for the last one;
- R_{cone}: due to the merging/splitting issue and to different implemented algorithms in data and theory, we assing a 10% uncertainty, equal to the difference of b-jet cross sections as found for R_{sep}=1.3 and =1;
- Hadronization factors: the correction factors for fragmentation and underlying events are extracted from Pythia Monte Carlo samples. We consider as systematic uncertainty the statistical error on this factor: the effect is below 2%, and thus almost negligeble with respect to the other systematic errors.
- Scale variation: the renormalization and factorization scales μ are simultaneously varied between $\mu_0/4$ and μ_0: the overall effect is between 40% and 20%(the latter for P_T jets above 250 GeV/c).

The first three contributions are added in quadrature and are referred to below as $\Delta_{\mathrm{PDF}\oplus\mathrm{R_{cone}}}$. The upper and lower bands, referred to as the total theoretical uncertainty, are derived considering also the scale dependence, and are given by:

- upper: $(\sigma^{NLO}_{b-jet}(\mu_0/4) + \Delta_{\mathrm{PDF}\oplus\mathrm{R_{cone}}})$;
- lower:$(\sigma^{NLO}_{b-jet}(\mu_0) - \Delta_{\mathrm{PDF}\oplus\mathrm{R_{cone}}})$.

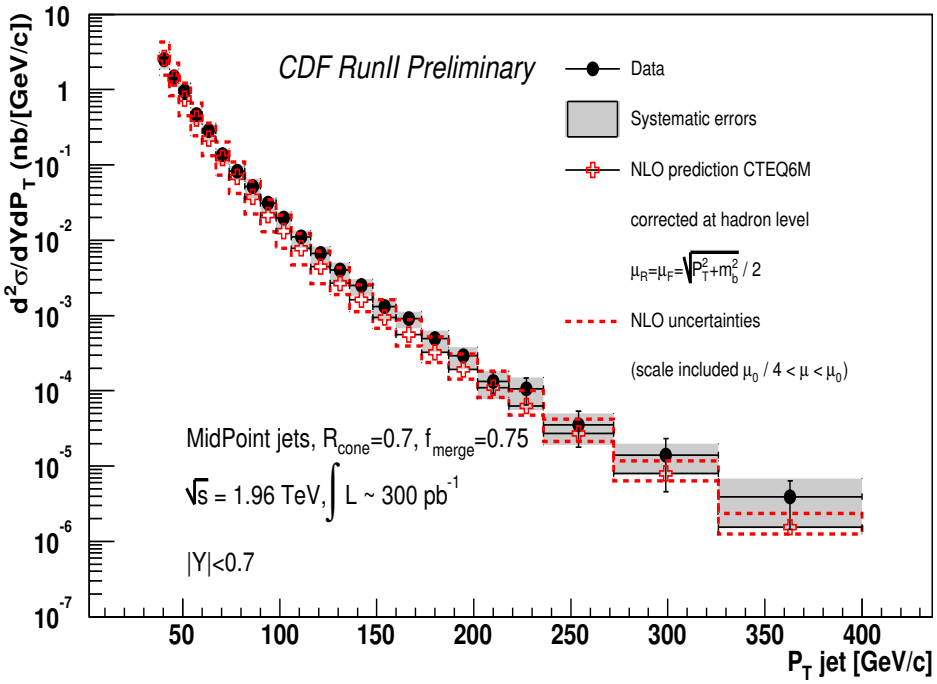

Figure 5.11: Differential cross section as measured in data and as obtained from NLO calculations. The systematic error of the theoretical curve refers to PDF, $\mathrm{R_{cone}}$ and scale uncertainties.

Since the renormalization and factorization scale dependence is not strictly speaking a systematic uncertainty, figure 5.12 first shows the ratio data/NLO considering the systematic error on the NLO prediction plotted around one, and including only PDF and cone uncertainties. They grey band is again the total systematic error from the data; the data contribution also dominates for the statistical error.
For jets having transverse momentum below about 90 GeV/c, there is good consistency between the measured cross section and the theory, while above 90 GeV/c there is agreement only within the systematic uncertainties. Obviously, the overlap region increases when considering the scale variation: figure 5.13 reports the ratio of data/NLO as before, again with uncertainties plotted around one. Similarly to figure 5.11, the upper and lower bands result from the combination of systematic uncertainty on PDF and R_{cone} ($\Delta_{\mathrm{PDF}\oplus\mathrm{R_{cone}}}$) with the NLO predictions, using scales μ_0 and $\mu_0/4$.

The bands have been obtained as follow:

- upper: ratio $(\sigma^{NLO}_{b-jet}(\mu_0/4) + \Delta_{\mathrm{PDF}\oplus\mathrm{R_{cone}}})$ / $(\sigma^{NLO}_{b-jet}(\mu_0/2))$;
- lower: ratio $(\sigma^{NLO}_{b-jet}(\mu_0) - \Delta_{\mathrm{PDF}\oplus\mathrm{R_{cone}}})$ / $(\sigma^{NLO}_{b-jet}(\mu_0/2))$;

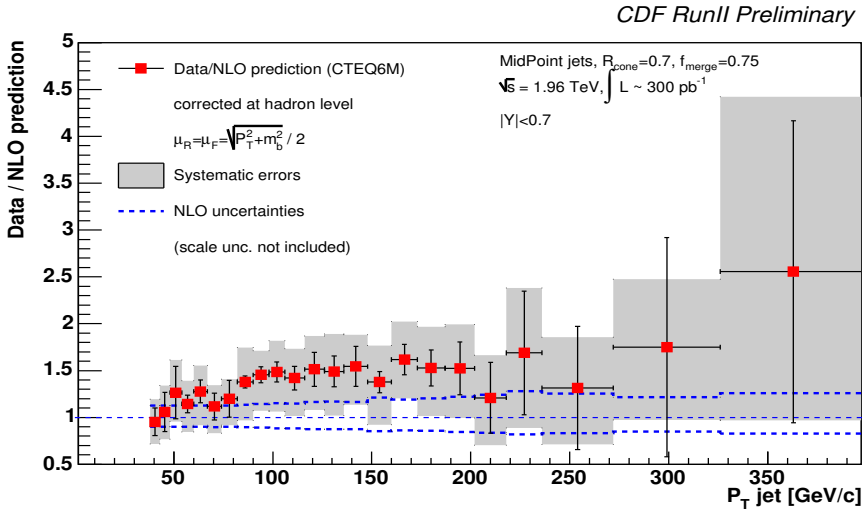

Figure 5.12: Ratio data/NLO prediction: the systematic error of the theoretical curve refers only to the PDF and the $\mathrm{R_{cone}}$ uncertainties and are plotted around one.

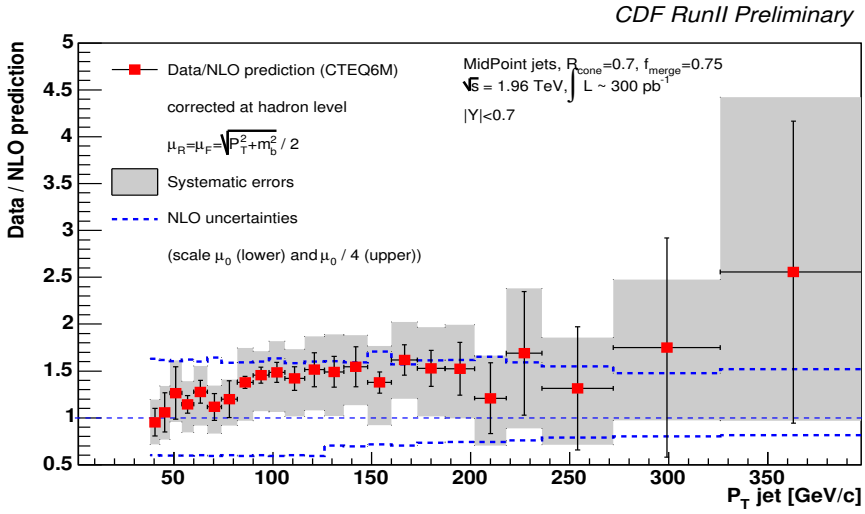

Figure 5.13: Ratio data/NLO prediction: the central value refers to the default choice of scale, $\mu_0/2$. Upper and lower band results from the combination of systematic uncertainty on PDF and R_{cone} with the NLO predictions, as found using scales μ_0 and $\mu_0/4$:
upper: ratio $(\sigma^{NLO}_{b-jet}(\mu_0/4) + \Delta_{\mathrm{PDF}\oplus\mathrm{R_{cone}}})$ / $\sigma^{NLO}_{b-jet}(\mu_0/2)$;
lower: ratio $(\sigma^{NLO}_{b-jet}(\mu_0) - \Delta_{\mathrm{PDF}\oplus\mathrm{R_{cone}}})$ / $\sigma^{NLO}_{b-jet}(\mu_0/2)$;

5.6 Discussion

It is interesting to compare the behaviour of the b-jet cross section measured in CDF RunII, with respect to the theory, with previous measurements at hadron colliders. The differential cross section for b-jet production has been measured in RunI by the DØ experiment[52], in an energy range limited to 100 GeV. A direct comparison between CDF and DØ results cannot be performed, due not only to the change in the center of mass energy between RunI and RunII, but also to the different jet algorithms implemented and to the different rapidity range covered by the measurement. Nevertheless, the same NLO pQCD algorithm [13] has been used by DØ for theoretical comparison.Thus, it is possible to perform an "indirect" comparison via the theory.

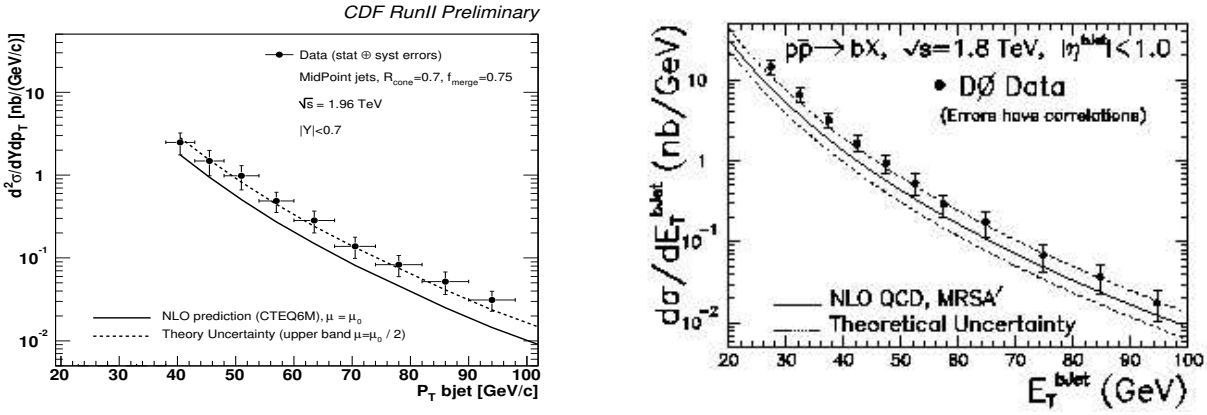

Figure 5.14: Left: zoomed view of the CDF differential cross section for b-jet production for jets P_T below 100 GeV/c. Right: the differential cross section, integrated over $|\eta|$ <1, for b-jet production performed by DØin RunI.

Using the same choice of scale DØ had made for the central value of the theory calculation (μ=μ_0), figure 5.14 on the left shows a zoomed view of the b-jet cross section as found in the present study at CDF RunII . The upper band of the theoretical uncertainties (lower band not reported) is the NLO calculation with μ=μ_0/2; PDF and R_{cone} uncertainties are also included in quadrature. For jets below 100 GeV/c, the same general pattern is observed as the DØ measurement.

The strong dependence on the choice of renormalization and factorization scale shows that higher order contributions could play a major role: considering perturbation theory beyond NLO, events would have more partons in the final state and a better description of its transverse momentum would be achieved thanks to the multiple radiation of initial states. For instance, in a NLO pQCD calculation, gluon splitting only appears at leading order: while at low P_T effects are expected to be small, logarithmic – $\log(P_T/\mathrm{m})$ – enhancements of the higher order contribution due to this process could be very important at high P_T.

Thus, a next-to-leading order calculation might not be considered conclusive for a precise theoretical comparison with the measured high-P_T b-jet production cross section: however, considering both the theoretical and experimental systematic errors, the measured points are compatible with predictions of NLO perturbative QCD.

Part II

Development of silicon microstrip detectors for the ATLAS Silicon Tracker

The second part of this thesis work reports some of the crucial tests performed during the development of the silicon microstrip detectors composing the Semi Conductor Tracker (SCT) in 2001 and 2002. LHC operating conditions result in very challenging performance specifications for the SCT modules and the limitations mainly concern the accepted noise and noise occupancy level, the tracking efficiency, the timing and the power consumption. A series of several end-cap module pre-production prototypes have been built and extensively tested on single module test benches as well as on beam tests. The present work has led to the definition of a final forward module design (K5), judged satisfactory by the SCT collaboration to pursue the real module production. In addition, an alternative module layout (KB) has been studied: a functional design of this kind provided the SCT with a viable back-up solution in case the development of a fully functional baseline module had not been achieved.

Results presented here have been partially published as Nuclear Instruments Method papers.

Chapter 6

The ATLAS experiment and the SCT detector

The Large Hadron Collider (LHC) is currently being built in the former LEP tunnel at CERN. The LHC tunnel is 27 km long and it is situated in Geneva. The machine will accelerate protons to energies of 7.0 TeV, then collide them head-on to have a centre of mass energy of $\sqrt{s} = 14$ TeV. Superconducting magnets of 8.33 Tesla define the trajectory of the 7 TeV protons along the LHC tunnel.

In this Chapter a brief introduction of the ATLAS experiment at the LHC hadronic collider is presented, together with a more detailed description of the Semi Conductor Tracking (SCT) detector of ATLAS. Finally some highlines related to the physics potential of the Inner Tracking Detector are reported.

6.1 ATLAS

The ATLAS detector [53] is one of the two general purpose experiments to be built in the LHC accelerator, optimised to be sensitive to a wide range of physics signatures. The ATLAS dimensions are 12 m radius, 44 m length and a weight around 7000 tons.

The principal aim of ATLAS is the discovery of the Higgs particle, but a major additional goal is the search for new particles coming from theories beyond the Standard Model (SM). The study of b-quark disintegrations and precision measurements of top quark mass are among the experiment objectives for a better understanding of the SM.

The basic design considerations for ATLAS can be summarised as follows:

- very good electromagnetic calorimetry for electron and photon identification and energy measurements, complemented by hermetic jet and missing E_T calorimetry;
- efficient tracking at high luminosity for lepton momentum measurements, for b-quark tagging, and for enhanced electron and photon identification, as well as τ and heavy-flavor vertexing and reconstruction capability of some B decay final states at lower luminosity;

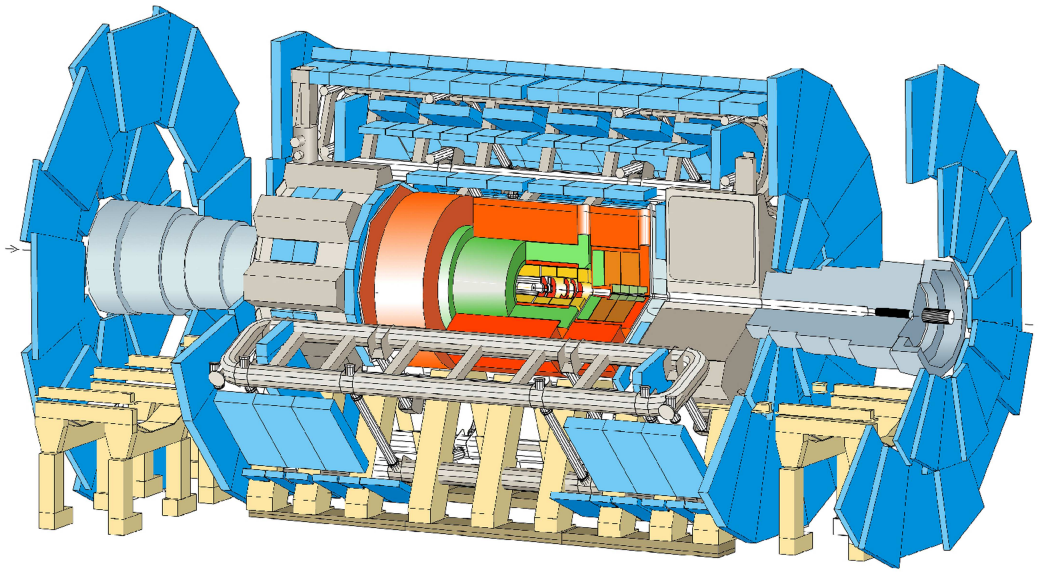

Figure 6.1: Simulated view of the ATLAS detector

- high-precision muon momentum measurements, with the capability to guarantee accurate measurements at the highest luminosity using the external muon system alone;
- large acceptance in pseudorapidity with almost full azimuthal angle (ϕ) coverage;
- Triggering and measurement of particles at low p_T thresholds, providing high detector efficiency.

Figure 6.1 shows the simulated view of the future detector. The ATLAS detector is composed by 3 main different sub-systems, from outside to inside: the muon system, the calorimeters and the inner detector tracking. These are briefly introduced in the next section.

6.1.1 Inner detector

The Inner Detector (ID) is a high performance tracker, that has been developed to provide efficient tracking in the severe conditions of short bunch crossing and strong radiation conditions. It consists of several layers of position sensitive detectors of three different technologies: silicon pixel detectors occupy the radii between 5 and 12 cm from the interaction point (for the barrel part), micro-strip detectors (SCT) cover the intermediate layers – at radial distances of 27 to 56 cm –, and a transition radiation detector (TRT) occupies the outer layers. These subsystems are enclosed inside a solenoidal magnet with a 2 Tesla magnetic field, used for charged particle momentum measurement. The Inner Detector will cover up to $|\eta| \leq 2.5$.

The main problems for the ID will be the large occupancies and high radiation doses. The design has been optimised to overcome these difficulties and give a precise tracking of particles. A most detailed description of the inner detector of ATLAS can be found in [53] and [54].

Figure 6.2 shows a simulated view of the Inner Detector. Starting from the smallest radii, the three main sub-structures can be summarized as follow:

- **Pixels detector**: designed to achieve high granularity and obtain track measurements with high precision. Sensors are placed very close to the interaction point: the first layer has a radius of 5 cm, while the outer barrel layer is at 12.25 cm from the interaction point. The system provides up to three high resolution points per track. The layer at lowest radius (called the B-layer because of its prominent role to improve the secondary vertex resolution for b-tagging) comprises the full rapidity range $|\eta| < 2.5$. Barrel layers two and three cover pseudo-rapidities $|\eta| < 1.7$ and three end-cap disks are used to provide space points in the forward regions $1.7 < |\eta| < 2.5$. Each layer is equipped with modules of 61 mm long and 16 mm wide, each one composed by around 46,000 pixel detectors consisting of a silicon n^+n diode segmented in pads or pixels with dimensions $50 \times 400\ \mu m^2$.
  Charged particles traversing the diode deposit a small signal through ionisation. Applying a reverse bias voltage the liberated carriers drift to the segmented readout plane of the detector. Each pixel is bump-bonded to a readout channel in the front-end chips that are mounted on the diode. The total number of channels is 140 millions, with a silicon area of 2.3 m^2.

- **Semiconductor Tracker**: intermediate layers of the ATLAS Inner Detector. It provides four three-dimensional space-points on tracks at radial distances[1] in the range 27 cm to 56 cm. Good spatial resolution is required to provide a precise transverse momentum measurement in the bending direction of the 2 T magnetic field of the Inner Detector solenoid. For a detailed description see section 6.2

- **Transition Radiation Tracker**: placed in the outermost part of the Inner Detector, from 56 cm of radius to 115 cm. The pseudorapidity coverage of the TRT is $|\eta| < 2.5$, with the barrel region covering $|\eta| < 0.7$. Averaged over the full pseudo-rapidity range, 36 hits per track are generated. The TRT is composed of several hundred thousand straw tubes (50000 in the barrel part, each divided in two at the center in order to reduce the occupancy, and 320000 in the end-cap), for a the total number of read out channels around 420000. Each straw is a 4 mm diameter cylindrical tube. The inner surface of each straw is covered in aluminium, and acts as high voltage cathode. In the middle of the straw there is an anode wire made of gold-plated tungsten, from which the signal is read out. The straws are filled with 70% Xe, 27% CO_2 and 3% O_2. The potential difference between the wire and the straw is used to collect the charge liberated by the passage of charged particles through the gas. The

[1]The ATLAS geometry is best described in terms of a cylindrical coordinate system with its origin at the interaction point and its z-axis parallel to the beam line.

resolution obtained with straws is 170 μm.
The straws are also embedded in a medium with an abruptly varying refractive index. Transition radiation is produced when a relativistic particle traverses an inhomogeneous medium, in particular the boundary between materials of different electrical properties. The intensity of transition radiation is roughly proportional to the particle energy $I = m/\sqrt{1-\beta^2}$, where m and $\beta = v/c$ are respectively the mass and the velocity of the particle. Thus transition radiation allows the identification of highly relativistic particles. Electron/hadron discrimination is possible for momenta bigger than ~ 1 GeV/c. Transition radiation is emitted in the X-ray regime, *i.e.* between 10 and 30 KeV and the resulting photons are collimated in the forward direction. These allow the detector to discriminate between tracking hits (ionisation inside straws), which pass a lower threshold, and transition radiation hits, with a larger one.

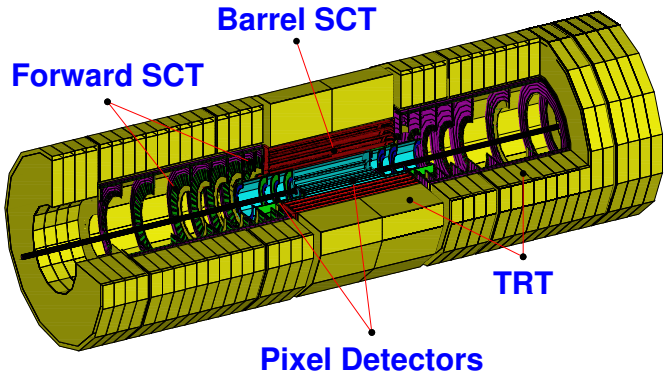

Figure 6.2: Simulated view of the inner detector of ATLAS composed of: Pixel detector, Semiconductor Tracker (SCT) and Transition Radiation Tracker (TRT).

The three subsystems composing the ID provide 7 high precision measurements (3 pixels and 4 SCT) and ~ 36 measurements in the TRT. The whole ID is confined inside a 2 Tesla solenoidal field bending the charged particles. Using the measured space-points, the helical trajectory of the track is reconstructed. With simulations of the inner tracker response to minimum ionising particles (MIP) the expected resolution of the helix parameters gives a momentum resolution:

$$\sigma\left(\frac{1}{p_T}\right) = 0.36 \oplus \frac{13}{p_T\sqrt{\sin\theta}} \qquad (\mathrm{TeV}^{-1}) \tag{6.1}$$

where θ is the polar angle and p_T transverse momentum in GeV. The parameters that give the track direction are azimuthal angle, ϕ, and polar angle, θ. The Z axis of the system is defined by the beam axis. The other helix parameters correspond to the longitudinal (z_0) and the transversal (d_0) impact parameters. The expected resolution in the transverse impact parameter is:

$$\sigma(d_0) = 11 \oplus \frac{73}{p_T\sqrt{\sin\theta}} \quad (\mu m) \tag{6.2}$$

The errors on the resolutions come from different sources. In particular, for particles with $p_T < 36$ GeV (most of the tracks in B-physics are in this range), effects related to multiple scattering in the detector material dominate the p_T resolution. Particles change their trajectory due to Coulomb interactions with material degrading not only p_T resolution but also their angular resolution. Scattering also dominates the resolution in the transverse impact parameter, d_0, for $p_T < 6$ GeV. In addition to these processes, electron bremsstrahlung contributes to the resolution deterioration.

One of the goals of the Inner Detector is also to keep high tracking efficiency. In the range $|\eta| < 2.5$, the acceptance region for high precision physics, > 95 % of the minimum ionizing particles (MIPs) with $p_T > 5\ GeV$ are expected to be reconstructed. The probability to reconstruct fake tracks should be less than 1 %. These requirements are relaxed slightly in the vicinity of the high p_T candidates. Nevertheless, the efficiency can be reduced, degrading the detector performance, because of low energy particle absorptions in the material. To avoid these effects, the material composing the ID should be kept as low as possible. This has been partially fulfilled with a careful design of the active detectors and by the use of low Z-materials (such as aluminium for the power cables, and carbon-fibre for support structures), although an increase of material in the whole range of η values has occurred with respect to the initial Inner Detector Technical Design Report.

6.1.2 Calorimetry

The ATLAS calorimeter system [55] is designed to measure the energy (and $\theta - \phi$ direction) of all particles and jets formed in the collision. The energy measurement of calorimeters is based on the formation of a shower, a cascade of particles, when a relativistic particle transverses dense matter. The energy resolution for the calorimeters is dominated by the stochastic or sampling term which decreases with $1/\sqrt{E}$.

Electrons and photons create a shower through pair production, $\gamma \to e^+e^-$ and $e \to e\gamma$ (bremsstrahlung) in the electric field of the nucleus. The energy loss for a given material is characterised by the radiation length X_0. The lateral development of the shower is determined by the Moliere radius.

Hadrons produce a cascade of hadron-nucleus interactions. The longitudinal development of the shower is determined by the interaction length of the material. Hadronic showers contain a variable electromagnetic component from radiation of photons (bremsstrahlung) and π^0 decays. The shower shape of hadronic showers is more irregular than in pure electromagnetic showers.

Since the nuclear interaction length is about an order of magnitude greater than X_0, ATLAS, as CDF and other experiments, has two different calorimetry systems: an electromagnetic (ECAL), placed in the innermost part of the system, and an hadronic calorimeter (HCAL), see Figure 6.3.

- **Electromagnetic calorimeter:** it is a high granularity lead/liquid argon (LAr) sampling calorimeter with a specific geometry that provide complete ϕ symmetry without cracks. The total thickness of ECAL is around 24 to 36 radiation lengths.

The sub-system has a first part acting as a *pre-shower* detector (with around 1.5 X_0), enhancing particle identification (γ, π^0, e) and providing a precise measurement of η. An excellent invariant mass resolution is needed for many physics measurement: for a 1% mass resolution, the energy resolution requirement for the sampling and constant terms becomes:

$$\sigma(E) \simeq \frac{10\%}{\sqrt{E}} \oplus 1\% \tag{6.3}$$

where the energy is expressed in GeV; the energy measurement is based on the determination of the ionisation energy loss by the charged component of the shower (electrons and positrons) in the thin (2-6 mm) gaps between the absorber plates, filled with the liquid argon. The total coverage of the ECAL extends up to $|\eta| < 4.9$.

- **Hadronic calorimeter:** it uses different technologies in each rapidity region. The barrel and *extended barrel* regions consist of steel plates which are sampled by plastic scintillator tiles. These are placed perpendicular to the beams, and are grouped into cells at approximately constant η. The structural material and iron absorber together form the return yoke for the central solenoid. In the end-cap, where radiation damage would severely degrade the scintillator, a parallel-plate Cu/LAr hadronic sampling calorimeter covers $1.5 < |\eta| < 3.2$. The jet energy resolution is required to be measured with a precision given by:

$$\frac{\Delta E}{E} = \frac{50\%}{\sqrt{E}} \oplus 3\%, \ |\eta| < 3 \tag{6.4}$$

$$\frac{\Delta E}{E} = \frac{100\%}{\sqrt{E}} \oplus 10\%, \ 3 < |\eta| < 5 \tag{6.5}$$

where the energy E is expressed in GeV. The ATLAS calorimeter performance technical design reports present the results of detailed simulation studies of the hadronic calorimeters, showing that the energy resolution requirements of previous equations are met by the current design. Besides, beam tests of prototype modules have confirmed these conclusions.

6.1.3 Muon spectrometer

Many of the physics processes of interest involve the production of muons. Their identification provide an important signature for the event selection of the experiment, especially because of the high density environment of hadronic colliders. For instance, muons coming from the disintegration of heavy quarks can be identified and give the trigger to such events. Muons are the only charged particles able to go through all sub-detectors and reach the detector external layers, where is placed the muon system [56].

The muon system consists of muon detectors and toroidal magnets. The magnet system for the muon chambers is composed of eight superconducting air-coils in the barrel region and eight in each end-cap. The magnet generates a toroidal magnetic field, that goes from

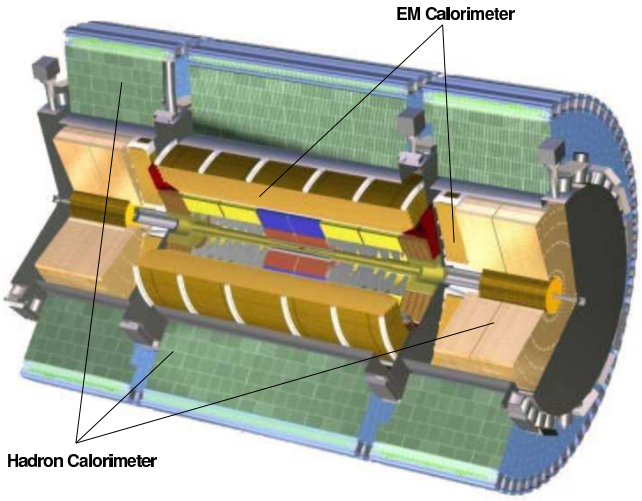

Figure 6.3: 3D view of the calorimetry system of ATLAS. In the central part is placed electromagnetic calorimeter (ECAL). In the outer part is formed by the hadronic calorimeter (HCAL).

3.9 Tesla in the barrel part to 4.1 in the end-caps. The inner diameter of the barrel toroids is 9.4 m, the outer diameter is 19.5 m and the length is 26 m.

There are three measurement chambers or *stations* for muons in the barrel and in the end-cap region, giving high precision space points for the measurement of the sagitta of the track. Over most of the pseudo-rapidity range, measurement is given by Monitored Drift Tubes (MDT) and, for large pseudo-rapidities ($|\eta| < 2$) and close to the interaction point ($2 < |\eta| < 2.7$) by Cathode Strip Chambers (CSC). The resolutions achieved with these systems is around 80 μm and around 60 μm respectively. The final ATLAS muon reconstruction uses the combined information from the high resolution measurements in the muon spectrometer an the inner detector.

Dedicated muon detectors with fast response time and less precision will give a rough measurement of p_T and trigger. The trigger chambers are Resistive Plate Chambers (RPC) in the barrel part and Thin Gap Chambers (TGC) in the forward region.

6.1.4 Trigger

The ATLAS trigger and data acquisition [57] is a technological challenge due to the large number of channels ($\sim 10^8$ channels), the high crossing frequency (40 MHz) and the LHC luminosity. At the high luminosity of LHC a total of 10^9 interactions per second will occur, each event with a raw data size of 1 MByte. Current data storage technology limits the amount of data that can be stored to the order of 100 MB/s. This corresponds to a maximum trigger rate of $\sim$ 100 Hz. Thus it is necessary a very fast trigger, able to reduce in 7 orders of magnitude the frequency of storage, but also able to preserve all interesting

events, with an open design for unknown physics channels.

The trigger is structured in three levels (LVL1, LVL2, Event Filter), see figure 6.4. Each of the levels is more complicated and slower than the previous one: the frequency achieved in each level of trigger is also showed in the figure.

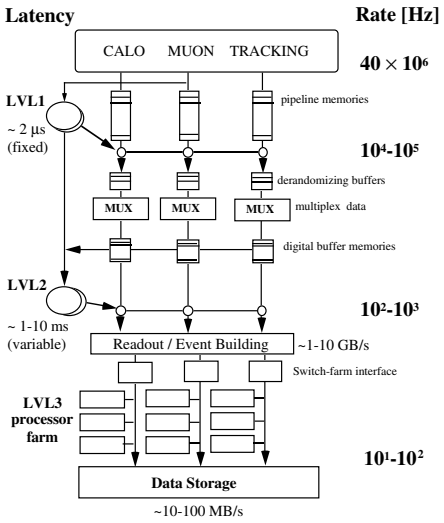

Figure 6.4: Representation of the ATLAS trigger.

The Level-1 (LVL1) trigger uses information from a relatively small number of detectors[2], to achieve a fast turn-back time; it takes data at each beam crossing at a frequency of 40 MHz (25 ns), having only 3 μs to reach a decision on the validity of the event. This leaves a maximum frequency for the next level of 100 KHz, that is the capacity of LVL2. During the trigger latency the data from the detector is stored locally in pipelines. At this level, the trigger decision is entirely based on an analysis of the data from the dedicated parts: fast muons stations (Thin Gap Chambers and Resistive Plate Chambers) and the calorimeter data with reduced granularity.

The Level-2 (LVL2) reduces the processing frequency from 100 KHz to 1 KHz. Information from Level-1 is used to identify regions with electromagnetic clusters with high p_T, (electrons or photons), jets and muons. Thus, Level-2 has data coming from a small part of the detector, with a latency less than 10 ms.

Both the LVL1 and LVL2 algorithms as well as efficiencies and frequencies for several signal to noise rates have been evaluated with detailed physics and detector simulations. Processors used in trigger issues will be fully programmable. In this way, selection criteria will be able to be changed depending on the physics results.

The third stage, the Event Filter, is placed after the event builder. At this point detailed alignment and calibration data are available. The definition of an abstract event data model allows the use of offline algorithms in the event filter. A software based event reconstruction

[2]Inner Detector is not used in this level due to the complexity of the events at high luminosity.

is done in PC farms at this level. Event reconstruction will not be longer than 1 s, and events will be stored for later analysis. The Event Filter will have a storage capacity around 100 MB/s.

6.2 The Semi Conductor Tracker

The Semiconductor Tracker (SCT) is one of the ATLAS Inner Detector elements which aims to track charged particles in the ATLAS experiment. The SCT is divided in three regions, one barrel and 2 end-cap zones.

The barrel area is composed by four cylindrical layers of detection modules around the beam axis and covering the full azymuthal range. The layers go from a radius of 27 to 56 cm, and they are 149 cm long, covering a rapidity range up to $|\eta| < 1.0$.

Each of the end-cap regions is composed of 9 carbon-fiber wheels placed perpendicular to the beam: they provide measurements in the region from $z = 80$ cm to $z = 270$ cm, covering the full azimuthal range and a rapidity range up to $|\eta| < 2.5$ and with a half length of 279 cm.

In both areas, end-cap and barrel, sensor modules are arranged with an overlap between modules, avoiding problems with dead zones in the detector.

The SCT is populated with a total of 4088 silicon micro-strip detector modules. The modules are constructed from one or two pairs of micro-strip sensors (wafers) glued back-to-back with a 40 mrad stereo-angle: in this way the measurement of the particle position can be obtained as the intersection of the strips with signal (information from both sides). The assembly and gluing of the sensors should fulfil certain limits [58] to have a reliable and precise position reconstruction.

In both barrel and end-cap geometries, the azimuthal angle ϕ - essential to the transverse momentum determination - is measured with high precision. The barrel modules also provide a measurement with limited resolution in the coordinate z along the beam axis, and the endcap modules in the radial distance R from the beam axis. In both cases the third coordinate is given by the sensor position. The barrel modules are all identical whereas the radial coverage of the endcaps requires three geometrically different versions [59]. End-cap module geometries have denominations: *Inner* (in the ring closer to the beam axis), formed with a single wafer of 61.06 mm length, *Middle* and *Outer* (ring closer to TRT) with an active strip length of 121.1 mm and 116.7 mm respectively. The outer rings have 52 outer modules and 40 modules middle and inner rings. The inner modules are composed by only 2 wafers, whereas for outer and middle 4 wafers are needed. The different layouts are showed in figure 6.5 and 6.6. There are basic differences between the two modules design, barrel and end-cap, both in the geometrical concept and in the different components.

Barrel modules are rectangular, composed of four wafers with the same size; end-cap modules are wedge shaped. The readout electronics position is centered for barrel and at one end for the end-caps, where the connexion between strips and readout electronics is made through a pitch adaptor or fan-in structure. The hybrid itself is one of the main differences between barrel and forward modules, although the same type of chips are implemented in

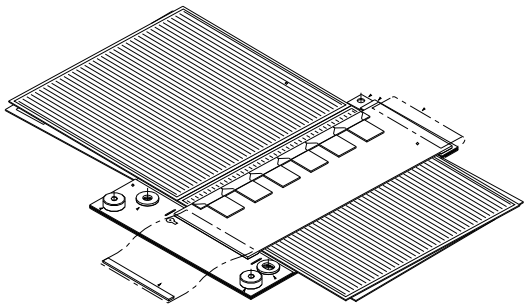

Figure 6.5: Barrel module layout

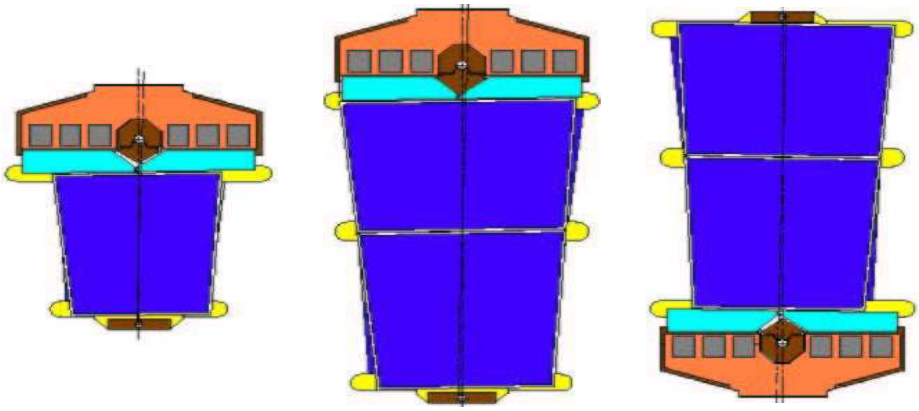

Figure 6.6: The three forward module layouts: from left to right, inner, middle and outer modules.

both cases (see section 6.2.2). Each chip has 128 channels, so that 6 of them are necessary for a single module plane read-out. Chips are glued on the hybrid circuit, with analog and digital part, based on a carbon-carbon flex. Different versions of the end-cap module hybrid were designed. The final version, called K5, is the one used for the production of end-cap modules. Detailed results of electrical tests performed on K5-equipped outer modules are reported in Chapter 7.

In an end-cap module, planes are glued on a both sides of a Thermal Pyrolytic Graphite (TPG) and AlN spine. This spine plays 2 different roles, being a support structure for silicon wafers and also responsible for meeting the thermal and electrical conductivity specifications. Besides, the spine contributes to the homogeneity of the module temperature. The gradient on the module should be smaller than 5^oC [53] (silicon properties depend on the temperature). The spine is also responsible for the module cooling transfer: a cooling block is attached to the spine and to the cooling pipes in the support frames (wheels). Thanks to the cooling an operating temperature of -7^oC in the wafers will be achieved. The spine is not present on barrel modules, and a TPG baseboard supplies the same functions. Fan-in structures are replaced by a small pitch adaptor located on the hybrid.

Among the 3 end-cap geometries, few main differences exist. The electronics are situated in the narrower region of the wedge for the outers and in the opposite side for middle and inner modules. As mentioned, the inner module is composed by only 2 silicon wafers.

All the silicon sensors are of 285 μm thick n-type $< 111 >$ material with a resistivity of 4-8 k Ω·cm. Each sensor has 768 active micro-strips formed by implanting p^+ material. The strips on the barrel sensors have a pitch of 80 μm, while the strip pitch on endcap modules varies from 54.4 to 94.8 μm with the fan geometry. A detailed description of the sensors is given in [60]. Table 6.1 shows values for angles between strips and pitch for end-cap and barrel wafers.

The SCT will use around 20000 silicon wafers, 10900 rectangular in the barrel and 8700 wedge shaped in the end-cap. In total 6 different geometries are used, 5 of them in the end-cap (2 geometries for the outer, 2 for the middle and 1 for the inner). The dimensions of wafers vary from 38 cm^2 to 42 cm^2. The next section explains the general performance of the micro-strip detectors.

Wafer type	Pitch
Barrel	80 μm
Forward Outer	0.161 mrad
Inner, Middle	0.209 mrad

Table 6.1: Geometrical characteristics for the SCT silicon wafers.

6.2.1 Micro-strips detectors

Historically, the first operative micro-strip detector was built in the seventies for the study of short lived particles in hadronic interactions. Since then, these devices have became essential for most experiments in particle physics.

The basic device of a micro-strip detector is the so called reverse biased pn junction (diode): figure 6.7 shows a sketch of a transversal cut. At the bottom of the device a metal layer (aluminium) is deposited to protect the semiconductor material. The highly doped n-type part over the metal is placed to prevent depleted zone to reach the bottom and to guarantee a good ohmic contact. Thus, the bulk is composed by a n-type semiconductor material and highly doped strips p-type are produced in this substrate. Over all is situated an insulator material (SiO_2), to protect the silicon of the wafer. Aluminium is deposited on the p-type zones over the insulator and is used to connect the pn-junction to the electronics and collect the charge.

Silicon micro-strip detectors are basically a set of reverse biased diodes or more precisely a set of parallel pn-junction strips separated by a small distance. The reverse-biased pn-junction generates a region without free carriers, called depleted zone. When a charged particle passes through the depleted zone, it creates electron-hole pairs by ionisation. The initial ionisation is limited to a cylinder of radius around 1 μm, being electron-hole pair

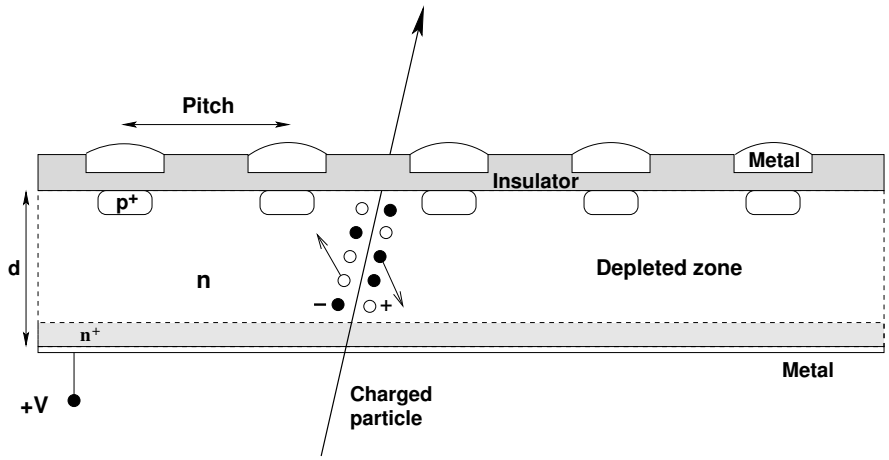

Figure 6.7: Schematic view of a transversal cut of a micro-strip detector.

produced uniformly along the particle trajectory. The generated pairs drift in the electric field originated by the applied bias: if the pn detector is fully depleted, the passage of a charged particle creates about 20,000 e-hole pairs, the holes drifting to the strips p^+ and the electrons to the backplane. During the drift, spatial distribution of the cloud of carriers is dominated by diffusion, while the contribution due to the repulsion between carriers of the same type is insignificant. The resulting width of the cloud for a typical device is small, around 10 μm for a 280 μm thick detector at room temperature and biased at 50 V. The width can be calculated as: $\sigma = \sqrt{2\frac{\kappa T}{q}\mu t}$, where κ is the Boltzmann constant, T is temperature, q is electron charge, μ is carrier mobility and t is the charge collecting time. Using this approximation, the spatial distribution of the drifting carriers is the same for electrons and holes. The typical full deposited charge collected in a readout strip is about 4 fC. The signal produced is proportional to deposited energy, so it increases with the width of the depleted region. If the depleted zone is increased and extended to the whole thickness of the sensor with a larger bias, more signal is collected, and the width of the electron-holes cloud is reduced (5 μm for 200 V bias in the case above). The bias needed to fully deplete a pn junction can be calculated as:

$$V_d = \frac{q}{2\epsilon_s} N_D d^2 = \frac{d^2}{2\epsilon_s \mu_e \rho} \tag{6.6}$$

where N_D is the donor (substrate) concentration, d is the thickness of the wafer and ρ resistivity of the less doped zone (substrate). ϵ_s is the dielectric constant of silicon and μ_e is the electron mobility.

The signal collected on the strips gives the particle crossing point. Thus, the separation between strips or pitch determines the resolution of such devices. Equation 6.7 show the

expected resolution for a micro-strip device with binary readout, as in the case of SCT.

$$< \Delta x^2 >= \frac{1}{p} \int_{-\frac{p}{2}}^{\frac{p}{2}} x^2 dx = \frac{p^2}{12} \tag{6.7}$$

Considering the ATLAS case for barrel modules with a constant pitch of 80 μm, a resolution $\sigma \sim 23$ μm is obtained (see results for SCT modules in test beam chapter).

There are many advantages of semiconductor as a detecting medium, for instance:

- reduced ionisation energy: only 3.6 eV are needed to create a electron-hole pair, compared with 5 eV to ionise a solid insulator and 30 eV to ionise a gas;
- the energy lost per length unit is large due to the high density (2.33 g/cm^3): thus, sensors can be very thin and produce a clear signal;
- despite the density, electron and holes can move almost freely and very fast. Charge from carriers can be collected in less than 20 ns;
- electronics can be integrated inside or very close to the detector.

In table 6.2 the specifications for the ATLAS micro-strip detectors are listed. These properties are checked by the manufacturers and by the SCT institutes. Detectors that do not fulfill the requirements are rejected. The leakage current and depletion voltage are measured for all wafers, the other parameters are only verified in a sample of them (10 %). The percentage of wafers rejected is well below 2 %.

Property		Specification	Conditions
Leakage current	I (μA)	< 6	$V_{bias} = 150$ V
Leakage current	I (μA)	< 20	$V_{bias} = 350$ V
Current stability	ΔI (μA)	< 2	$V_{bias} = 150$ V, 24 hours
Depletion voltage	V_D (V)	< 150	
Substrate resistivity	ρ ($K\Omega/cm$)	$3 < \rho < 8$	
Metal strip resistance	R_{msr} (Ω/cm)	< 15	
Bias resistance	R_{bias} ($M\Omega$)	1.25 ± 0.75	
Inter-strip capacitance	C_{inter} (pF/cm)	< 1.1	$V_{bias} = 150$ V, 100 kHz
Coupling capacitance	C_c (pF/cm)	≥ 20	1kHz

Table 6.2: Specifications for the SCT detectors.

6.2.2 Front-end electronics

A signal of 4 fC is the typical deposited charge in the silicon, and external amplification is in general needed before further processing of the signal. The read-out electronics is located very close to the silicon sensors to avoid loss of noise performance and large input capacitance due to long cabling.

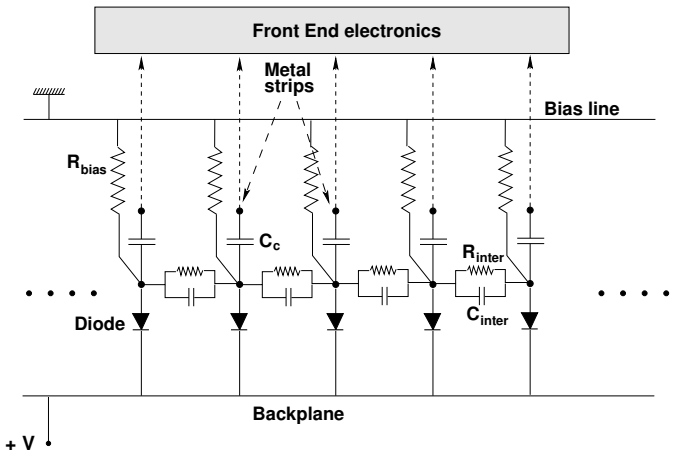

Figure 6.8: Equivalent diagram of SCT micro-strip detector.

A silicon pn micro-strip detector can be represented with a simplified equivalent diagram as in figure 6.8. The bias resistance, R_{bias}, is a poly-silicon resistance situated between the bias line and the front-end electronics. The main goal of the R_{bias} is to ensure a low current in the electronics. The value is chosen to have a small contribution to electronics noise. C_{inter} and R_{inter} are the inter-strip capacity and resistance. C_{inter} has the largest contribution to the load capacitance C_{load}, where the load capacitance is the equivalent capacity of the hole strip and is the capacity seen by the readout electronics connected to the strip. C_{load} is responsible of most of the electronics noise, being dominant when increasing the strip length. Micro-strip detectors can have DC-coupling or AC-coupling. In the direct coupling or DC, the readout electronics is connected directly to the p^+n junction of the strip, whereas in AC coupling, a capacitor (C_c) is placed after the junction. For the SCT detectors, AC-coupling has been chosen. The p^+ implant is AC coupled to a metalized strip on the sensor surface, which is connected to a channel of the readout electronics. The coupling capacitance C_c has a value around 20 pF/cm. AC-coupling between the strips and the electronics prevents current generated in the reverse-biased diode (leakage current) to enter in the electronics.

The SCT front-end integrated circuit - the radiation-hard ABCD3T [61] - has 128 channels. The ABCD3T is the final design of the single chip implementation of binary read out architecture, realized in the radiation-hard DMILL technology. The ABCD integrates the analog and digital functionality of the binary read-out architecture in a single chip: the front end circuit, discriminator, binary pipeline, derandomizing buffer, data compression logic and the read-out control logic. The design and performance of these chips are mostly detailed in [61, 62, 63, 64]. Figure 6.9 shows a block diagram of the chip, while the schematic of a single channel is shown in figure 6.10.

Signals coming from the strips are amplified and integrated with a semi-gaussian shaping. The shaper optimises the signal to noise ratio of the front-end. The transfer function

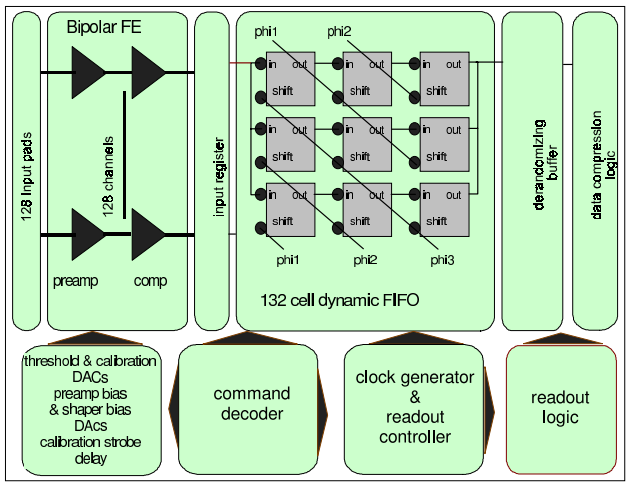

Figure 6.9: Block diagram of the analogue front-end circuit.

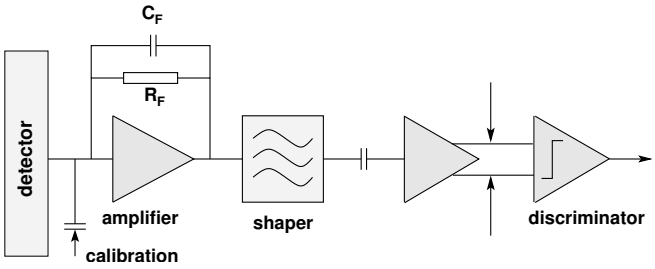

Figure 6.10: Schematic diagram of the analog stages of a single channel as implemented in the ABCD chips (C_F and R_F are the feedback capacitor and resistance respectively).

of an ideal $CR(RC)^3$ is:

$$h(t) = (\frac{t}{\tau})^3 e^{-t/\tau} \tag{6.8}$$

where τ^3 is the shaping time. The design peaking time of the shaper is 20 ns. The response of the shaper to a certain input is obtained by convoluting the time resolved input pulse with the transfer function $h(t)$, but a more realistic description of the ABCD shaper is obtained by taking into account an extra differentiation step with an RC time of 150 ns. This results in an faster fall-off of the pulse tail. Some additional details are given in section 9.6.

In the binary readout scheme, the pulse obtained is reduced to one bit of digital information by comparing it with a selected threshold. The non-uniformity of the amplifiers is corrected at this point by adjusting a 4 bit digital-to-analogue converter (trimDAC) for each channel. This feature has been implemented especially to cover the increasing spread between channels after irradiation and will be further described in the chapter dedicated to electrical tests on the modules.

Parameter	Specification	Comments
Gain	50 mV/fC	Unirradiated
Linearity	Better than 5 %	Range 0-4 fC
Noise	$< 1500\ e^-$ ENC $< 1800\ e^-$ ENC	Unirradiated Irradiated
Noise occupancy	5×10^{-4}	Even after Irradiation
Peaking time	20 ns	
Time-walk	≤ 16 ns	
Double pulse resolution	≤ 50 ns	For 3.5 fC signal

Table 6.3: ABCD chip specifications.

The shaped signal is compared in the discriminator. One important feature of the ABCD discriminator is that it can be operated in two modes: level sensing (returns 1 if the signal is above the threshold) and edge sensing (1 is saved only if a transition low to high occurs). Operating the discriminator in edge sensing reduces the tail of the shaped signal, thus the probability that ghost hits appear in the consecutive beam crossing.

The resulting hit pattern is then transferred and stored into a binary pipeline (FIFO memory), 132 cells deep, until a level-1 trigger sygnals readout (trigger latency $\simeq 3.2\ \mu s$). The output data of 3 bits (the precedent, the required bit and subsequent) is compared to a compression pattern. If the hit pattern satisfies the requirement, it is added to the data stream. Three different algorithms (or compression modes) are available:

- ANYHIT compression: $1XX \quad | \quad X1X \quad | \quad XX1$
- LEVEL compression: $X1X$
- EDGE compression: $01X$

where 1 means that a hit has been recorded in the register, 0 no hit and X could be 0 or 1. These three bit combinations are the type of patterns read out by each of the algorithms. In ANYHIT compression, channel information is considered if the signal was over threshold in any of the three bits (three different clock cycles). This mode is used for test and in ATLAS beam will be synchronised with trigger request. The LEVEL and EDGE compressions uses this information to provide an additional noise rejection.

The ABCD chips present an integrated calibration circuit that allows a fast and accurate characterization of the module: details on this circuit, used for electrical tests, will be given in chapter 7.

The main characteristics of the ABCD chip are summarised on Table 6.3.

To read-out every strip, 6 chips have to be associated to each side of a module; they are mounted on a specific structure called *hybrid*. A fully assembled hybrid consists of a six layer copper-polyimide flex circuit, a substrate, SMD components (connectors, resistors, capacitors, and a thermistor), twelve ABCD3T read-out chips and one DORIC (Digital

optical receiver integrated circuit) chip for the optical links[3].

The first chip on each side of the module, designed as the master chip, is responsible for the electrical transmission of data. Within the module a token passing scheme is used to control the transfer of data to the master chip for onward transmission. This scheme incorporates several redundancy options such that, should any single chip fail, the remaining chips can still be read out.

Each SCT module is connected to its own programmable low voltage and high voltage power supply channels. The power distribution system includes three patch panels and three lengths of conventional cable, the innermost section being formed by low mass power tapes to minimise the material in the tracker volume. In the end-cap module the power tapes connect directly to the hybrid on which the opto communication chips are mounted. In the barrel region the interface between the module, power tapes and optical signals is provided by a further copper/kapton flex circuit.

The final version of the end-cap hybrid chosen by the SCT community is the already mentioned K5 hybrid, and a picture (front and back) is showed in figure 6.11.

The performance of prototype K5-hybrid-equipped modules, built in preparation for SCT production, will be discussed in the next chapter.

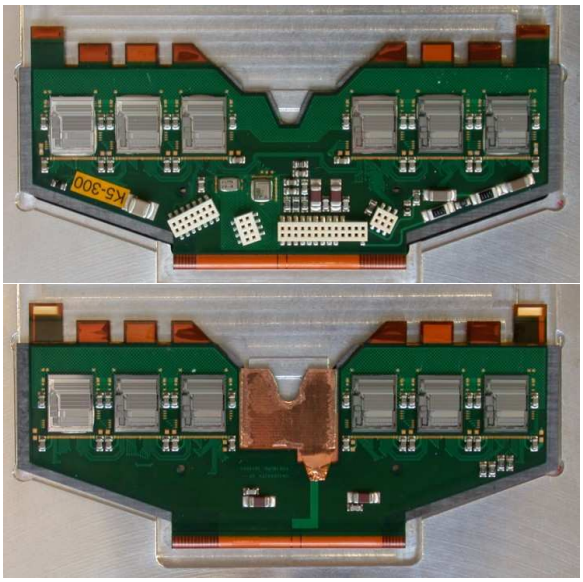

Figure 6.11: K5-300 hybrid front and back view.

[3]The SCT will be read-out and supplied with clock and control signals optically, with approximately 8000 data- and 400 control-links. These numbers come from the fact that each silicon module will require one control and two readout links.

6.3 Physics potential of the Inner Detector

The high granularity region made of pixels and microstrips in the Inner Detector provides a unique opportunity for the detection of B-Hadrons whose decay pattern can be resolved with high efficiency. The rate of B-hadron production at the LHC is enormous thanks to the large hadronic cross-section for b-quark and the high luminosity of the machine: about one collision in every hundred will produce a $b\bar{b}$ pair, which results in an yield of about 10^{10} $b\bar{b}$ in the first year of operation, the so called low luminosity run (10^{33} cm^2 s^{-1}).

B physics is a crucial part of Standard Model and beyond in many respects.

- Concerning QCD, a precision measurement of b-jet production, for instance, allows to subtract, when associated to a prompt photon, one of the main backgrounds to the photon charm production at large P_T: for instance, this is important since related to the estimate of the intrinsic charm content of the proton and provides by itself, when associated to W production, an accurate estimate of the strange quark parton density.

- Υ can be measured even at very low P_T, where the cross section increases, allowing to discriminate among the color singlet production models; moreover, the study of $b\bar{b}$ correlations and asymmetries allows to subtract a source of background to CP violation effects in b-decays.

- A good b detection will lead to a good estimate of the top mass, thus to stringent limits, if not evidence, of Higgs masses. Also, top decays will be study to check possible supersimmetric signatures such as charged higgs, with $t \to H^+ b$ channel.

- Higgs decay mode into $b\bar{b}$ pairs and its associated production with other particles as W or Z or $t\bar{t}$, are relevant for light Higgs searches. Moreover, the Higgs coupling to b-quarks in supersymmetric extensions grows with tanβ parameter and adds interest to the b driven decays/production modes, reinforced by the expectation, in Minimal SuperSymmetric Model, of a lightest Higgs in the W mass range, below roughly 120 GeV.

The Inner Detector, and the SCT as part of it, besides its central role in B physics, will also be essential for searches for leptonic decays of new massive particles, characterized by large P_T isolated electrons.

Chapter 7

Baseline end-cap modules

Eighteen end-cap module prototypes using the K5 hybrid version [65, 66] have been assembled between February and November 2002 in several institutes of the SCT collaboration, in order to prove the reliability of the baseline hybrid performance before starting the real production. Inner, middle and outer modules have been built and extensively tested electrically and thermally [67]. In this chapter, we focus on the electrical performance of the K5 outer modules. The basic electrical requirements for SCT end-cap modules will be reported in the first section, followed by a description of the electrical test set up and a summary of the results obtained with the prototype modules. Some of the end-cap modules have been irradiated between May and October 2002 with the CERN PS 24 GeV proton beam, using the SCT T7 facility [68]: details on the tests performed are presented in section 7.5.

7.1 Standard electrical module tests

7.1.1 Electrical requirements for the ATLAS-SCT end-cap module

The LHC operating conditions result in very challenging performance specifications for the SCT modules and the limitations mainly concern the accepted noise and noise occupancy level, the tracking efficiency, the timing and the power consumption. The complete end-cap module electrical specifications are described in [54] and only the most important ones are reported here.

- The equivalent noise charge (ENC) for the front-end system, including the silicon strip detector attached to the hybrid, should be less than 1500 e- ENC for non irradiated modules, and less than 1800 e- ENC for irradiated ones. However, the total effective noise results not only from the front-end electronics contribution, but also from the channel-to-channel threshold matching. It can be parametrized as the addition in quadrature of this ENC for the front-end electronics with the contribution of the channel-to-channel threshold spread.

- The noise occupancy is required to be significantly less than the real hit occupancy to ensure that the noise hit rate does not affect the data transmission rate or track reconstruction. The foreseen noise occupancy limit of 5×10^{-4} requires that the discriminator level in the front-end electronics is set to 3.3 times the rms noise.

  To achieve this condition at the foreseen ATLAS operating threshold of 1 fC, the total equivalent noise charge should never be greater than 1900 e- ENC: assuming 3.3 fC median charge, that corresponds to a median signal-to-noise ratio of 10:1.

- To minimise the data to be read out and to simplify tracking, each hit has to be associated with a unique bunch crossing. The silicon charge collection time of 10 ns therefore requires edge-sensing discriminators with a maximum *timewalk* of 16 ns for the nominal threshold settings and full range of input signals. The fraction of outputs shifted to the wrong beam crossing is required to be less than 1%.

- The double pulse resolution, which directly affects the efficiency, is required to be 50 ns, to ensure less than 1% data loss at the highest design occupancy. Thus, the detection of two tracks that are incident on the same strip is possible providing the separation time is at least two bunch crossings.

- For the power consumption, the nominal values for the power supplies of the chips are:

  - power supply for the analogue components: V_{cc} = 3.5 V ± 5%;
  - power supply for the digital components: V_{dd} = 4.0 V ± 5%;
  - detector bias HV, up to 500 V with a maximal leakage current of $2\mu A$ per channel, that is an maximum "average" of about 3 mA.

  The nominal power consumption for the chips is foreseen to be 4.75 W during operation at 1 fC comparator threshold with 1% occupancy and 100 Khz trigger rate (L1 rate). Including the optical readout, the maximal power dissipation should be 7.0 W for the hybrid and the heat generated in the detectors just before run away should be 2.6 W for outer module wafers and 1.6 W for inner ones[1] [67].

7.1.2 Set-up description and characterization tests

Standard electrical tests aim to verify the hybrid and detector functionality after the module assembly and to demonstrate the module performance with respect to the required electrical specifications.
The system used to perform electrical tests and data acquisition includes the VME units listed below and shown in figure 7.1.

- The MuSTARD [69] (Multichannel Semiconductor Tracker ABCD Readout Device) is a VME module designed to receive, store and decode the data from up to 6 detector

[1] This does not take into account the high voltage (HV) supply, which may limit the power to lower values.

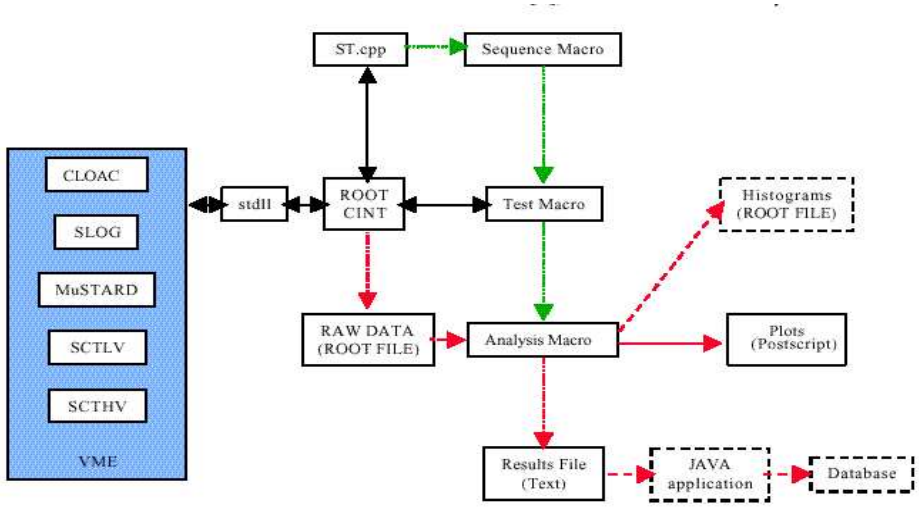

Figure 7.1: Schematics of SCTDAQ system.

modules decoding the events and histogramming the data. Individual events may be transferred to the host computer if more detailed analysis is required.

- The SLOG [70] (SLOw command Generator) allows the generation of slow commands for the control and configuration of ATLAS SCT front-end chips. It also distributes the clock and the fast command signals generated by the CLOAC to up to 12 detector modules.

- The CLOAC [71] (CLOck And Control) module generates the clock, fast trigger and reset commands for the SCT modules, in the absence of the Timing, Trigger and Control system.

- The SCTLV module provides low voltage power[72] for the digital and analogue part of the chips (V_{dd} and V_{cc}) and the optical components, for up to 2 detector modules;

- The companion module SCTHV[73] provides detector bias up to 500 V for four detector modules.

The VME crate is interfaced to a PC running Windows NT or Linux: the SCT module configuration and data acquisition is performed by the SCTDAQ software package. Static libraries written in C handle the basic communication with the VME boards. Higher level functions are implemented in a small number of C++ classes, linked with the static libraries and some libraries of the ROOT framework, to form a shared library. Within ROOT, the system is started by running an interpreted macro that calls upon the functions of the shared library to initialize the VME boards and configure the SCT detector modules to their default operating conditions. The methodology of each test implemented in SCTDAQ and the subsequent data analysis are described in [74]. A single module is tested

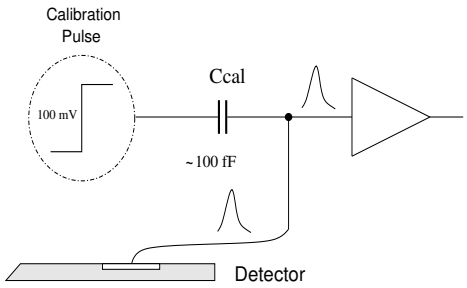

Figure 7.2: Schematic representation of the chip read-out.

to check the functionality and performance stability, and to verify if the specifications are met. An integrated calibration circuit implemented on the chips allows a fast and accurate characterization: a Digital to Analog Converter (DAC) and a chopper circuit generate a voltage step of defined height (see figure 7.2 for a simplified representation of electronics of the chip). This voltage step is applied to a 100 fF calibration capacitor, this creating a fast (less than a few ns) charge pulse that is injected into the input of the preamplifier. By scanning the threshold voltage over a large range and registering the binary response, the so-called *s-curve* – efficiency – can be reconstructed in terms of counts over threshold versus threshold voltage. The s-curve for a fixed charge and Gaussian noise is described by a complementary error function. The threshold where 50% efficiency is obtained (VT50) is the threshold corresponding to that input charge. The width of the S-curve is a measure of the output noise.

The procedures commonly used in the module test are outlined below.

- Digital tests are executed to identify chip or hybrid damage;

- An optimization of the delay between trigger and signal is performed on a chip by chip basis;

- To minimize the impact of the threshold non-uniformity across the channels on the noise occupancy, the ABCD3T design foresees the possibility to adjust the discriminator offsets. A threshold correction using a digital-to-analogue converter (Trim DAC) per channel with four selectable ranges, has been implemented in the chips (ASICs). The so called *trimming* procedure allows an improved matching of the discriminator thresholds; this is an issue especially for irradiated modules, due to the increasing of threshold spread with radiation dose;

- The gain and electronic noise (ENC) are obtained channel by channel with threshold scans performed with 10 injected charges in a range from 0.5 to 8 fC (ResponseCurve procedure, RC). For each charge injected, the corresponding value in mV is extracted as the 50% point of the threshold scan fitted with an s-curve. The gain, input noise and offset are deduced from the correlation of injected charge in fC versus the voltage output (mV).

- A threshold scan without any charge injection is performed to yield a direct measurement of noise occupancy at 1 fC. The extracted parameters from previous response curve are used to fit a straight line to a plot of ln(occupancy) vs. Qthreshold^2 (fC^2) to yield a measurement of the total effective ENC noise. Deviations from this line, notably at higher thresholds, are indicative of non-Gaussian behaviour such as the presence of common mode noise.

- To determine the timewalk a dedicated scan is also executed: setting the comparator threshold to 1 fC, for each value of injected charge (over a range of 1.25 to 10 fC), a complementary error function is fitted to the falling edge of a plot of efficiency vs. the setting of the delay register, to determine the delay at which the efficiency is 50%. The timewalk is given by the difference between delays calculated for 1.25 and for 10 fC charge injected.

The endcap prototype modules are tested in custom designed aluminium boxes which provide mechanical support as well as cooling. In these boxes, the modules are mounted on two aluminium surfaces, one beneath the hybrid, the other one at the far end of the detectors. Both surfaces are cooled with an alcohol-water mixture provided by a Huber chiller.

7.2 Correction factors

Two types of corrections have to be taken into account to compare modules with each other and with the real SCT conditions in ATLAS.

7.2.1 Calibration factor and relative charge spread

As described in the previous section, the module characterization uses a calibration circuit that generates a voltage step pulse which is coupled to the front-end via a calibration capacitor (Ccal). To take into account variations of the capacitance from the design value, estimations of the correction factors (C.F.) are deduced from oxide thickness measurements of test capacitors placed all over the ASIC wafer. The real (corrected) gain and noise ENC are then given by:

$$\text{Real gain} = \text{Meas. gain}/\text{C.F.}; \qquad \text{Real ENC} = \text{Meas. ENC} \times \text{C.F.}$$

The typical value of the calibration factor is about 1.1 or below. Front end paramenters after irradiation can change quite dramatically: thus, calibration factor changes after irradiation might have a certain impact on the module performance and further tests are requested to check the impact of this uncertainty.

Figure 7.3 on the right shows an example of irradiated forward module tested injecting 1 fC through the calibration circuit: the spread of the distribution across the channels is of the order of 10% after the trimming procedure for irradiated prototypes, while it is around 1% for unirradiated prototypes (on the left).

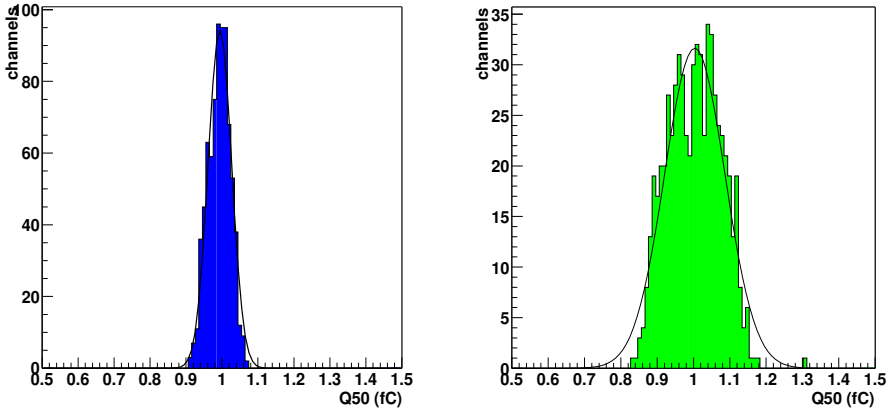

Figure 7.3: 1 fC injected charge for one of the two sides of a non irradiated (on the left) module and a fully irradiated one (on the right).

7.2.2 Temperature dependence

The second important correction concerns the temperature at which the measurements are made. The goal during SCT operation is to provide the most beneficial temperature conditions for positive annealing of the silicon detectors. Therefore the aim is to cool the detectors to -7°C in nitrogen atmosphere, using a two phase evaporative refrigerator cycle system, based on C_3F_8. Following simulations performed on the thermal conditions for the SCT, this corresponds to a temperature around +2 °C on the hybrid, measured by a thermistor placed on it.

To make electrical test results performed in the laboratory comparable with each other and with the real experiment conditions, front-end parameters sensitive to the temperature, such as gain and ENC noise, need to be normalized. Unirradiated modules are usually tested in an atmosphere at room temperature and are cooled with a liquid mixture at +15 °C provided by a chiller: the measured thermistor temperatures are in a range from 30° to 40 °C (hybrid temperature), while the detector temperature can be considered the same as the ambient. For irradiated modules, a cold environment is necessary to keep the detector temperature reasonably low to reduce the leakage current and prevent reverse annealing. A climate chamber set to -7 °C has been used to host the module, in addition to the chiller set to -16 °C (effective coolant temperature $\sim$ -14.5 °C).

Measurements performed on outer unirradiated modules (see figure 7.4 on the left) show the correlation between noise and thermistor temperature which can be fitted linearly with a slope of 5.8 e^- ENC/°C. Similar measurements have been performed for unirradiated inner modules, that lead to a correction of about 4.7 e^-/°C (see figure 7.5).

The low accuracy both in the measured noise (ENC error estimation $\sim$ 30 e^- ENC [75]) and in the thermistor temperature (T error $\sim$ 1°C) lead to an error on the slope of $\sim \pm$ 1.0 e^- ENC/°C.

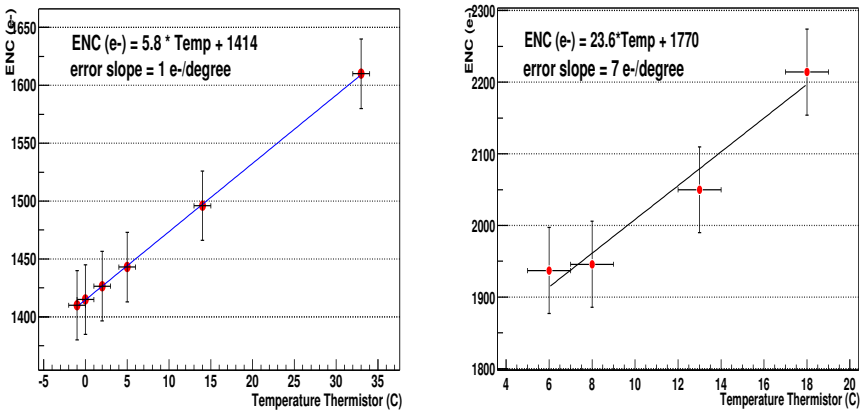

Figure 7.4: Left: Temperature dependence of the noise is 5.8 $e^-/°C$ for an unirradiated outer module (ambient temperature at about +20 °C, V_{bias} = 150 V). Right: The same plot for an half dose irradiated module with ambient temperature at - 7 °C and constant V_{bias} = 350 V: the slope extracted from a linear fit is ∼24 e^- ENC/°C.

For outer half dose irradiated and full dose irradiated modules (for details on irradiation see 7.5, the study has been performed using a constant temperature of -7°C for the environment. For half irradiated modules (figure 7.4 on the right), the slope of a linear fit results in a temperature dependence of the noise around 24 e^- ENC/°C with an uncertainty of ± 7 e^- ENC/°C, due also to the large error on the ENC values (± 60 e^- ENC). For a fully irradiated module, the results obtained for the ENC noise extracted from the response curve (RC) and from the noise occupancy are shown in figure 7.6: in particular, the left hand side plot is the ENC from the noise occupancy scan, obtained assuming that all sources of noise are gaussian, and fitting the occupancy as a function of the threshold by:

$$NO(t, ENC) = \frac{1}{2}\,\mathrm{erfc}\left(\frac{t}{ENC\sqrt{2}}\right) \tag{7.1}$$

where NO, ENC and t are the noise occupancy, ENC noise [2] and threshold values respectively. It can be seen that the variation of ENC with temperature is not linear. Fitting by a straight line gives slopes varying between 17 or 24 $e^-/^oC$ (RC and NO respectively) when the fit range is the whole interval [-6^{o}C;-2^{o}C], and 30 $e^-/^oC$ when fitting only the last part of the plots. The temperature range of the measurements is limited from below by the chiller capacity, and from above by the fact that the module trips due to the 5 mA power supply limit, when the chiller temperature is set higher than about -15^oC ($T_{hyb} \approx -2^oC$).

The fact that the module cannot run at the expected temperature of 2^{o}C is due to an

[2]It is worth noticing that this ENC noise value differs from that obtained by the response curve. The ENC deduced from the noise occupancy includes the contribution of both electronics noise and channel-to-channel variation. It therefore includes the threshold spread.

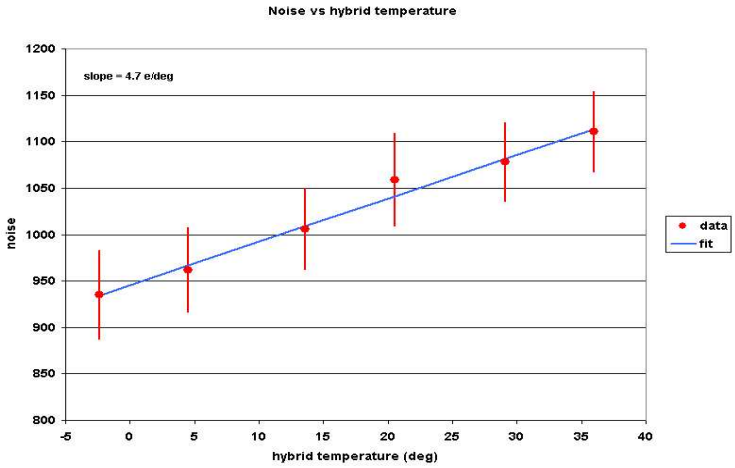

Figure 7.5: Temperature dependence of the noise for an unirradiated inner module at V_{bias} = 150 V.

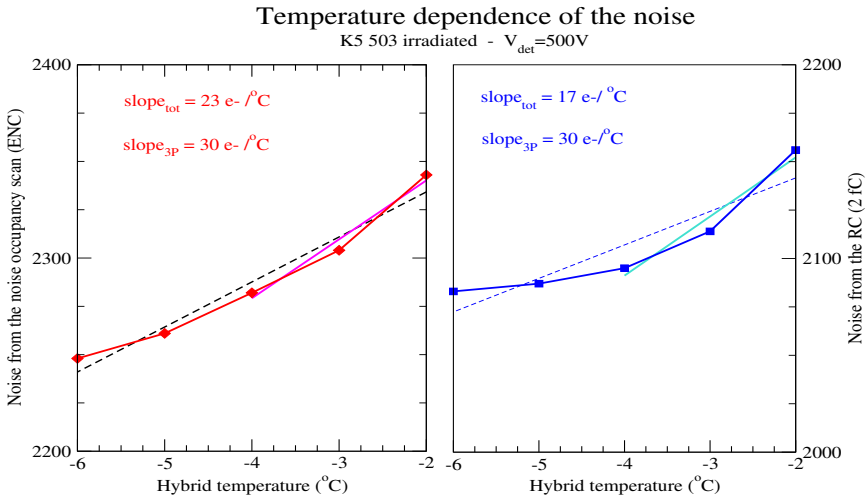

Figure 7.6: Temperature dependence of the ENC for irradiated K5 503. On the left: ENC from the noise occupancy; on the right: ENC from the RC. Values are corrected for the calibration factor and fitted by a straight line. The first value of the slope corresponds to a fit over the whole range of temperature, and the second one over the last part of the plots.

unexpected self-heating of the detectors, as can also be seen on figure 7.7, where leakage current measurements performed at different temperatures (hybrid also powered) are shown. This also explains that the variation of ENC versus temperature measured doesn't match the one calculated using analytical expressions for the total ENC.

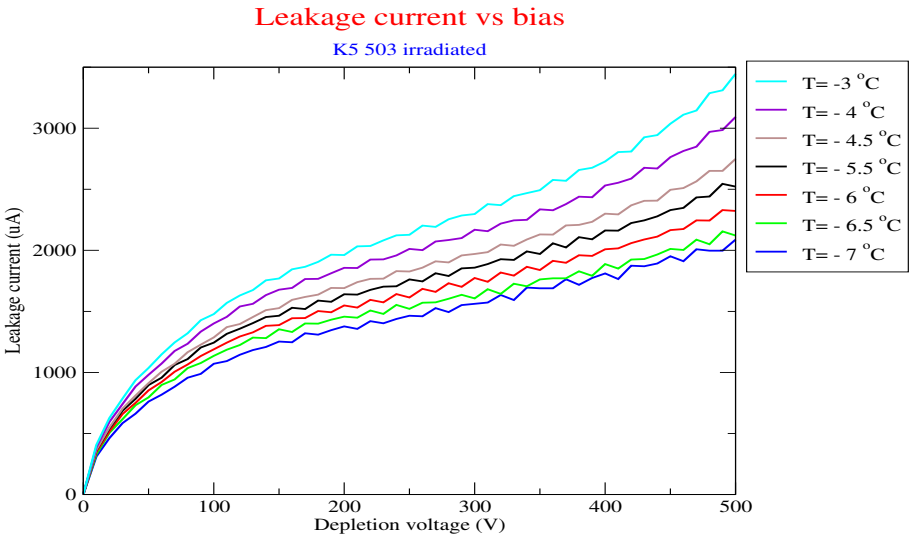

Figure 7.7: IV curves at different temperatures, with hybrid powered on.

Five different contributions to the noise can indeed be isolated:

$$
\begin{aligned}
ENC_{Ic} &= \frac{e^3}{12\sqrt{3}}\sqrt{\frac{2kT}{g_m}}\frac{C_e + C_d + C_F}{\sqrt{t_{peak}}}\frac{1}{q} \\
ENC_{Ib} &= \frac{e^3}{36}\sqrt{\frac{5}{3}}\sqrt{t_{peak}}\sqrt{\frac{2qI_C}{\beta}}\frac{1}{q} \\
ENC_{det} &= \frac{e^3}{36}\sqrt{\frac{5}{3}}\sqrt{t_{peak}}\sqrt{2qI_{leak} + 4kT\left(\frac{1}{R_F} + \frac{1}{R_{bias}}\right)}\frac{1}{q} \\
ENC_{rbb} &= \frac{e^3}{12\sqrt{3}}\sqrt{4kTR_{bb}}\frac{C_d + C_F}{\sqrt{t_{peak}}}\frac{1}{q} \\
ENC_{corr} &= \frac{e^3}{12\sqrt{3}}\sqrt{\frac{4kT}{g_m}}\sqrt{\frac{(C_d + C_e + C_F)C_C}{t_{peak}}}\frac{1}{q}
\end{aligned}
$$

where $e = 2.718...$, q is the electron charge, k the Boltzmann constant, β is the current gain (between 150-200 for a non irradiated module and 20-50 for an irradiated one), T is the temperature measured in K, either of the chips, or of the detectors for ENC_{det}. $C_F = 120f$F is the feedback capacitor, $C_e = 0.6p$F is the internal input capacitance of the chip, $C_d \approx 18p$F is the detector capacitance, $C_c = 20p$F/cm is the coupling capacitor, I_C is the collector current per channels (about 110 μA per channel for irradiated modules), $g_m = qI_C/kT$ is the transconductance of the transistor and $t_{peak} = 20$ ns is the peaking time. Typical values for the resistances are $R_{bb} = 180\Omega$, $R_F = 80k\Omega$ and $R_{bias} = 1M\Omega$. ENC_{Ic} is the collector current shot noise, ENC_{Ib} is the base current noise, $ENC_{R_{bb}}$ is the base spread resistance noise, ENC_{corr} is the correlation term, and ENC_{det} is the detector contribution. The main uncertainties are the detector and chip temperatures. The temperature of the

detectors are taken to vary between -15^{o}C and -7^{o}C and the chips are supposed to be 20 degrees warmer. These are plausible values, even if there is no way from the previous measurements to deduce directly the chips and detector temperature. The results are however not very dependent on the detector temperature range, and are summarized in figure 7.8.

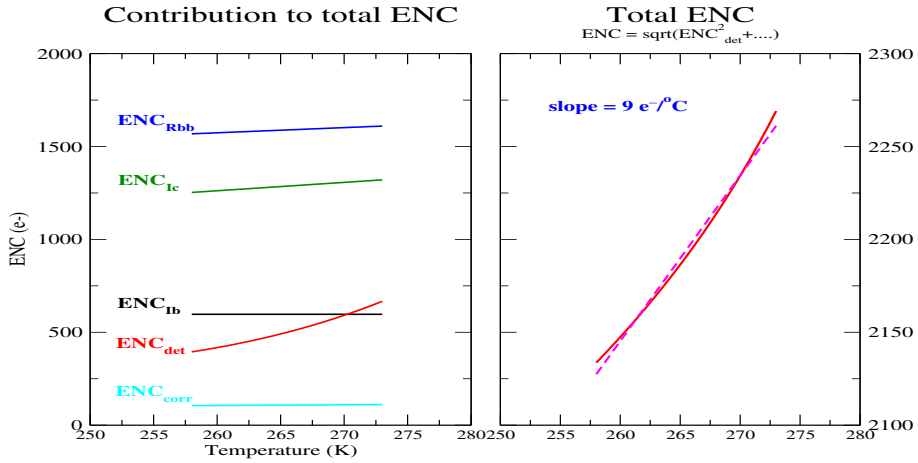

Figure 7.8: Different contributions to the total ENC noise, plotted vs detector temperature.

The measurements and this estimation are thus not consistent, since the slope deduced from the measurements is around 30 e$^-$/^{o}C, whereas the estimated one is around 9 e$^-$/^{o}C. The same self-heating phenomenon is true for the half-irradiated modules. However, the measurements were performed in a test box without split cooling block. The coupling between the hybrid and the detectors is thus more important than what it should be in the experiment. In addition, a liquid cooling has been used, instead of the foreseen C_3F_8 evaporative cooling [67]. Nevertheless, since this temperature correction is needed to compare module with each other in the laboratory tests performed, the results are presented using a correction of 24 e$^-$ ENC/^{o}C and 30 e$^-$ ENC/^{o}C for half-irradiated and irradiated modules respectively.

The gain variation with temperature has also been measured and turns out to be negligible.

7.3 Results from electrical tests of non-irradiated modules

A total of eighteen modules have been tested during 2002 in all the involved institutes. It should be noticed that the outer module type corresponds the least favorable case in terms of noise, due to the higher contribution of longer detector strips ($\simeq$ 1500 e$^-$ ENC noise to be compared to the $\simeq$ 1200 e$^-$ for the inner module): results are shown in table 7.1.

Module	*Gain*	*Thr. spread*	*T*	*Noise(ENC)*		*Occ.@1fC×10^{-4}*		*Masked*
	(mV/fC)	*@1fC (ENC)*	*(°C)*	*Meas.*	*Corr.*	*Meas.*	*Corr.*	*Chann.*
K5 300 M	47.8	167	38	1407	1329	0.13	0.05	0
K5 301 M	50.1	160	40	1421	1333	0.15	0.05	10
K5 302 O	47.5	188	38	1419	1423	0.08	0.09	4
K5 303 O	48.1	207	33	1382	1439	0.03	0.07	8
K5 305 O	48.1	193	35	1393	1440	0.15	0.32	0
K5 308 O	47.1	182	47	1552	1438	0.40	0.11	4
K5 309 O	47.9	160	33	1435	1417	0.04	0.03	12
K5 310 O	48.1	144	31	1442	1437	0.20	0.21	0
K5 312 O	46.9	240	46	1524	1441	0.25	0.09	10
K5 501 O	49.5	358	38	1581	1420	0.34	0.04	17
K5 502 O	52.4	191	38	1552	1390	0.48	0.07	11
K5 503 O	49.3	153	39	1602	1435	0.43	0.06	2
K5 504 O	49.8	139	41	1634	1457	0.61	0.08	0
K5 304 I	51.5	118	44	1204	1212	$<10^{-7}$	$<10^{-7}$	1
K5 307 I	47.5	127	48	1276	1251	$<10^{-7}$	$<10^{-7}$	16
K5 313 I	50.5	150	44	1190	1106	$<10^{-7}$	$<10^{-7}$	10
K5 314 I	51.1	124	41	1134	1120	$<10^{-7}$	$<10^{-7}$	4
K5 316 I	51.8	142	42	1119	1099	$<10^{-7}$	$<10^{-7}$	4

Table 7.1: Module parameters as measured for unirradiated end-cap modules (middle, outer and inner). It is noted that K5-502, 503 and 504 have been tested on a prototype disk.

The average module gain is about 49 mV/fC, corrected for each module with the appropriate calibration factor; using this correction and normalizing to the SCT temperature, the ENC noise in all outer modules is about 1430 e^-, while the average for the middle and the inner are 1330 and 1160 e^-, respectively. In addition, the table reports the channel-to-channel threshold spread at 1 fC: non-uniformity across channels acts as an effective contribution to the noise; this has been calculated considering the rms of the gaussian distributions of figure 7.3. The occupancy due to the effective noise at 1 fC is summarized in the last column of table 7.1 (see also figure 7.9). The column labeled as *corr* indicates the noise occupancy values corrected for the calibration capacitance variation and for the temperature, as mentioned in section 7.2.2. This correction was performed by fitting the occupancy as a function of the threshold, by the complementary error function (7.1), assuming that the noise is purely gaussian. Inverting this complementary error function leads, for a given value of the noise occupancy, to a value of the ENC noise. This ENC noise is then corrected as specified above, and the corrected noise occupancy is obtained using once more the interpolation (7.1). It has to be noticed that the prototype hybrids have been equipped with non perfect – that is 1-dead channel – chips, except for K5 503 and 504, whose chips were perfect ones. The unirradiated modules are well inside the requested specifications, having average noise ENC < 1500 e^-, noise occupancy below the foreseen limit 5×10^{-4} and efficiency in terms of working channel $> 99\%$. Figure 7.10 shows a representative timewalk scan. The typical timewalk that has been measured varies between 11 and 14 ns.

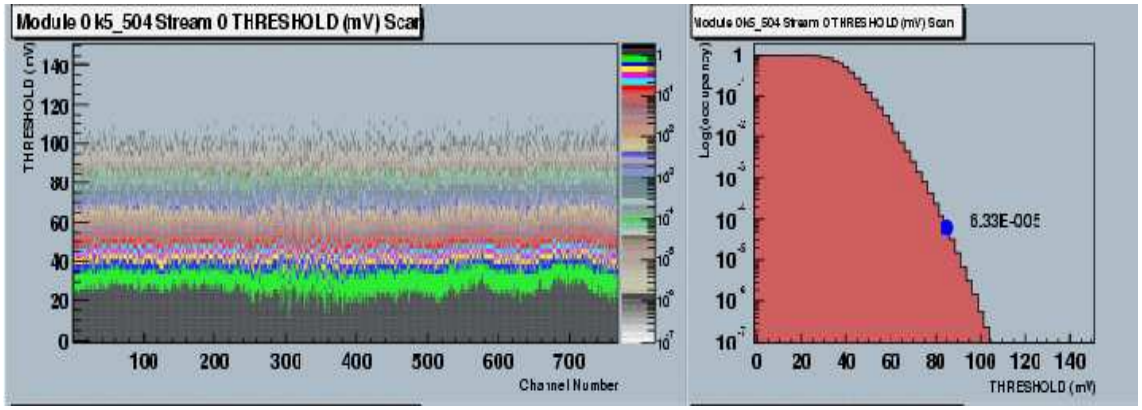

Figure 7.9: Example of Noise Occupancy for the upper link of an unirradiated module: on the left hand side the 2D distribution of occupancy *vs* threshold per channel is shown, on the right hand side the projection of the occupancy in logarithmic scale for the whole link, that shows the expected shape. The dot indicates the 1 fC point as identified in the trimming procedure.

7.4 Forward system test

The results described above on unirradiated modules have been obtained testing one single module at the time. Moreover, no optical readout has been used. The system test at

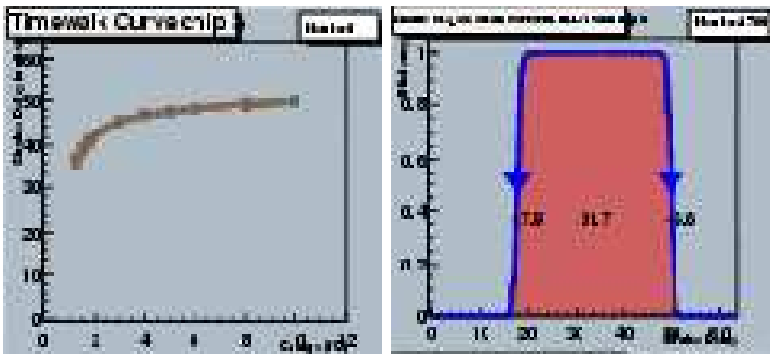

Figure 7.10: Representative timewalk curves for one chip of an unirradiated module. On the left: for each injected charge, a chip by chip scan of efficiency vs. delay is performed to extract the 50% point of the falling edge. The corresponding delay (DAC units) is plotted vs. the injected charge and the timewalk is the difference between delay values at 10 fC and 1.25 fC. On the right: to convert DAC units to ns, the efficiency curve vs. delay (DAC units) is used. The width of the plateau, calculated as difference between the 50% point of falling and raising edge, should be 25 ns, so the conversion factor is extracted.

CERN, was set up to study the performance of the SCT modules when mounted in a similar configuration to the one of the real experiment. The forward(end-cap) system test was based around a carbon fiber sector, equivalent to one quarter of a disk. This was mounted on an aluminium support frame within a copper enclosure representative of the thermal shield. A total of 13 outer modules and 10 inner modules could be mounted on the front of the sector and 10 middle modules on the back. Opto-hardness comprising optical fibres were used to provide clock and control signals for groups of 5/6 modules. A comparison of ENC noise measurements performed with outer modules operated on the sector and off the sector in (single boxes) is shown in figure 7.11.

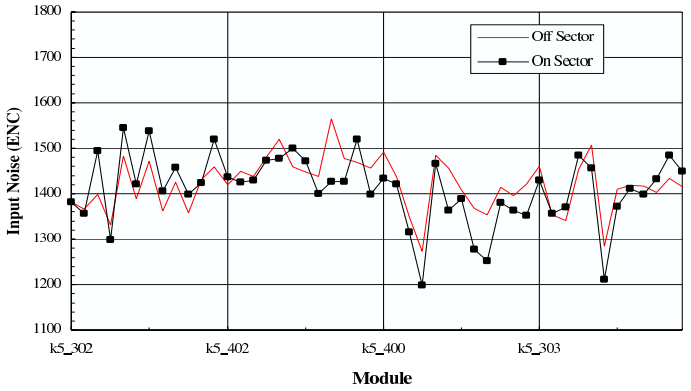

Figure 7.11: ENC noise of four outer modules measured when contemporary mounted on the sector and in single tests out of the sector.

The tests performed aimed for instance to study grounding and shielding scheme to prevent common mode noise: the binary architecture of the SCT dictates that great attention must be paid to the system design, since an excess of common mode noise could render the detector blind. Details on these tests, performed in 2001-2002, can be found elsewhere[65].

7.5 Irradiated modules

SCT barrel and end-cap modules are required to remain operational after 10 years of LHC running. The highest accumulated radiation levels expected in the ATLAS SCT are reproducible irradiating the modules with a 24 GeV proton beam at the CERN PS. Irradiation nominal fluence is 3×10^{14} protons/cm^2, distributed on a period of about 10 days. The irradiation is then followed by a 7 days period of annealing at 25 °C.

Seven of the modules have been irradiated at different fluences, with the 24 GeV proton beam of the CERN PS using the SCT irradiation facility. Four of them (K5 305, 308, 503, 504) have been irradiated with the nominal fluence of about 3×10^{14} protons/cm^2– simulating approximately 10 years of ATLAS operation. Two of them (K5 310, K5 303) have been irradiated to half the dose (fluence of about 1.5×10^{14} protons/cm^2). The remaining module (K5 312) has undergone a full irradiation in two steps: the first one was up to half the dose, and the second one four months later, to reach the total fluence [68]. We summarize in this section the electrical performance of these irradiated end-cap modules, after a brief general introduction of the radiation effects on front-end electronics and silicon detectors.

7.5.1 Radiation effects

Radiation damage involves both the read out electronics and the silicon detectors.

ABCD chips are realized in BiCMOS technology both for the analogue and the digital part, so they are sensitive to ionization effects as well as to displacement damage[76]. The DMILL technology is qualified as a radiation resistant one, however, the radiation levels expected for the SCT detector exceed the upper limits of those specified for the DMILL process, i.e. 10 Mrad of total ionising dose and 1×10^{14} n/cm^2 1 MeV equivalent neutron fluency for the displacement damages. On top of the general requirement that the chip should be fully functional after irradiation up to the maximum specified levels, there are some particularly critical issues of the ABCD design, which should be considered carefully with respect to radiation effects. The most critical aspects are summarised below:

1. The performance of the front-end circuit is affected by the major radiation effect in bipolar transistors, i.e. degradation of the current gain factor β. From radiation tests performed[76], β of the input transistor is expected to change of a factor of 4 during the ATLAS experiment lifetime. As a result, the shot noise contribution increases, raising the equivalent input noise in ENC from $\sim 1500\ e^-$ to $\sim 1800\ e^-$.

2. An increase of the offset spread in the discriminator is expected. The offset spread

increases by a factor 3-4 after proton irradiation and by a factor about 2 after neutron irradiation.

3. Concerning the digital part of the ABCD, degradation of the maximum clock frequency is foreseen: after full dose of 10 Mrad the maximum clock frequency is 52 MHz, to be compared with the nominal 40 MHz. In order to cover possible variation of the process parameters, the digital part of the ABCD chip is designed to work at least at a clock frequency of 80 MHz before irradiation.

Silicon detectors are subject to both surface and bulk radiation damage. The first is mostly due to an accumulation of charges in the interface between silicon oxides and bulk; it affects for instance interstrip capacitance, the main contributor to the parasitic capacitance for the amplifier noise. The bulk is mostly damaged by displacement that leads to an increase of the leakage current proportional to the fluence and the silicon volume.

In the description of the effects of radiation on devices, two mechanisms should be distinguished:

- **Ionisation**: Most of the energy of charged particles is lost through this mechanism. For creating a electron-hole pair, 3.6 eV are needed. A charged minimum ionising particle crossing a 300 μm silicon detector creates $\sim$ 22000 pairs, depositing a charge of 3.5 fC. Ionisation damage is caused by charged particles that ionise the Silicon atoms, liberating charge carriers.

- **Non-ionising Energy Loss (NIEL)**: The fraction of the energy transferred by the incident particle to the lattice not via ionisation is called non-ionising energy loss. Deposited energy goes to the atoms in the lattice, resulting in general in a displacement of atoms. The energy required for a displacement of a single atom is 13-30 eV in a direct collision with the atom and the energy transfer could be up to 130 KeV in the case of 1 MeV neutron collision. Photons in the range of 1-7 MeV and electrons of few MeV can create damage compared to 1 MeV neutrons effect. Simulations predict for the innermost layer of SCT a 1×10^{14} 1 MeV equivalent per cm^2 fluences during the 10 years of operation of LHC. Although non-ionising events are relatively rare, they are the dominant source of damage for bulk silicon in the detectors.

Defects created by radiation can be of different types: vacancies, interstitials, divacants, etc but the overall effect of the damage on the micro-strip devices is an increase of acceptors concentration. As the irradiation proceeds, the effective doping of the material changes and at some point the acceptors concentration due to defects exceeds the initial doping; thus the n-type silicon of the bulk has undergone *type inversion*. The evolution of concentration with fluency is described by:

$$N_{eff}(\phi) = N_{eff}(0)e^{-c\phi} - \beta\phi \tag{7.2}$$

where $N_{eff}(0)$ is the concentration of effective dopants [3] before irradiation and ϕ is the fluence. The first term accounts for donor removal, hence the dependence on the initial dopant concentration $N_{eff}(0)$. The second reflects the creation of new acceptor states. The contributions of these two processes is given by the c and β constants, dependent on particle types and energy.

Once irradiated, dopant concentration changes with time depending also on the storage temperature. Radiation defects are not stable, but evolve with time. Different types of defects can combine to create new states or recombine: this effect is know as *annealing*. Two different effects take place: short term annealing, called beneficial, reduces the concentration of acceptors. Long term annealing, or inverse annealing, increases acceptors states. Figure 7.12 represents the evolution of the effective concentration with fluency of equation 7.2: for a certain fluency, depending on the initial concentration, a type inversion is observed, substrate n to p. That transition will change the operational method of the pn ATLAS sensors. The pn junction will not be situated on the strips anymore, but on the backplane. Depletion will start from backplane to strips, although micro-strip detector can still be operational by diffusion of the generated pairs, even if the detector is not fully depleted.

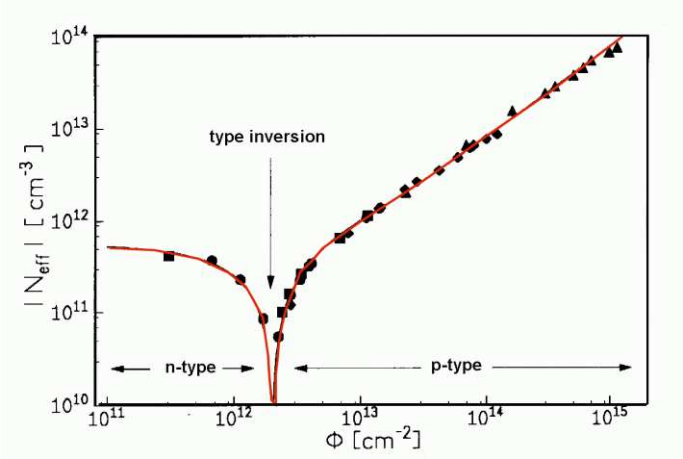

Figure 7.12: Effective dopants number versus radiation fluency. For a fluency around 2 10^{12} 1 MeV n_{eq} cm^{-2} the type is inverted, from n to p type.

Another effect correlated with bulk damages is the increase in leakage current of the detector, that can be parametrized by:

$$I = \alpha\phi \times v_{det} \tag{7.3}$$

where α is the current damage factor, ϕ is fluence and v_{det} is the detector volume. To predict the leakage current using bulk radiation damage parametrization it is necessary to

[3] N_{eff} is defined as $N_D - N_A$ with N_D the donors concentration and N_A the acceptors concentration.

combine the effects of both the change in effective carrier density and the increase in the leakage current, and also considering the behaviour at low and high fluence separetly. The typical depletion voltage before irradiation for a 300μm-thick detector is around 80 V. If the detector is biased when irradiation begins, the donor removal term in eq. 7.2 initially causes the effective carrier density, and hence the full depletion voltage, to decrease and the detector remains fully depleted with a constant volume. Therefore eq.7.3 implies a linear relationship between detector current and fluence at low fluences, assuming the initial detector current before irradiation to be negligible: $I \propto \phi$. At high fluences (above 10^{14} protons per cm^2) the acceptor creation term in eq. 7.2 dominates and to a good approximation $|N_{eff}|=\beta\phi$. This results in a full depletion voltage greater than the applied bias voltage, the detector is no longer depleted and the active volume is now a function of the fluence:

$$v_{det} = Aw = A\sqrt{\frac{2\epsilon}{e}\frac{V_{bias}}{|N_{eff}|}} = A\sqrt{\frac{2\epsilon}{e}\frac{V_{bias}}{\beta\phi}} \tag{7.4}$$

where A is the area of the detector, w is the depletion width of the detector, ϵ is the dielectric constant of silicon, e is the electron charge and V_{bias} is the bias voltage applied to the detector. Thus, from eq. 7.3, the detector current at high fluence should be proportional to $\phi^{1/2}$.

As a result of the rise of leakage current, operational temperature increases, being more necessary a good heat removal and cooling.

7.5.2 Electrical test results

Unless otherwise specified, the measurements with irradiated modules have been performed in a climate chamber with environment at -7^oC. The modules are inside their test box with cold nitrogen flux; thermal grease is applied on both cooling points and the coolant, provided by a chiller, is at a temperature of -14.5^oC.

Figure 7.13 presents the leakage current as a function of the bias voltage, when the hybrid is unpowered, to avoid the hybrid heating. The curves are clearly consistent with the fact that irradiations have been performed at two fluences, since the leakage current is doubled in the case of a full irradiation with respect to the partial (half) irradiation.

As consequence of the β factor degradation, the optimum values for shaper and preamplifier currents decrease; two 5-bit DAC implemented on the ASICs permit to change these values and the working point estimation is done checking different combinations of preamplifier and shaper current. Each chip can be independently adjusted and the front-end settings have therefore been re-optimized to obtain a high gain, but making a compromise to lose as few channels as possible. This procedure, the so-called *current scan*, is done as first step of the electrical tests, followed by the trimming test. For irradiated modules, the trim procedure is especially important, due to the increase in the ABCD discriminator threshold spread: more channels have to use large-range trimDAQ settings, where the correction step-size is coarser.

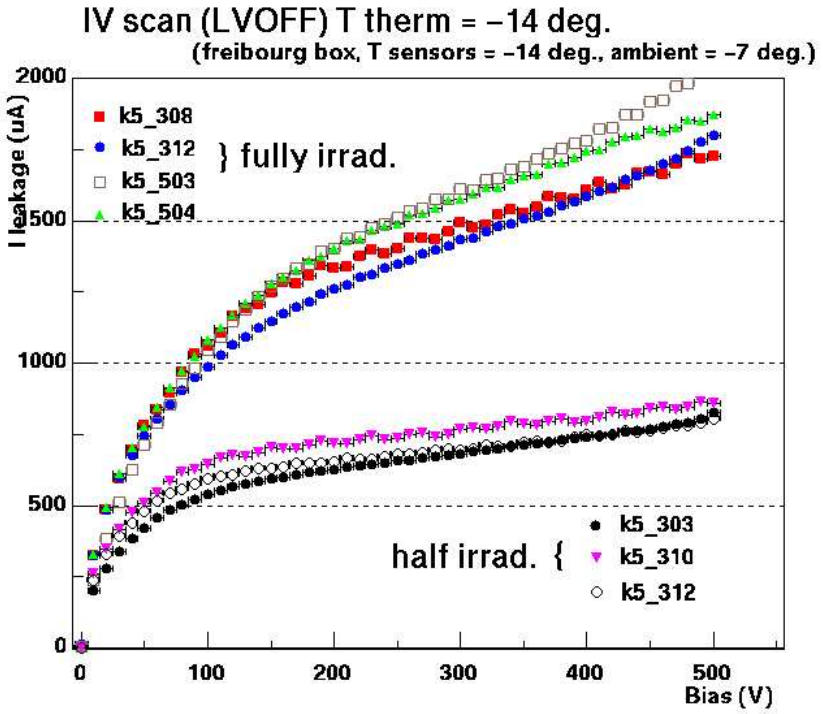

Figure 7.13: Leakage current for half and fully irradiated modules.

The data presented are corrected both for calibration capacitor variation and for temperature, as explained in Sections 7.2.2 and 7.3. Measurements of the calibration DAQ after irradiation show that there is no major change in the calibration capacitor [77] and the same (unirradiated chips) values for the calibration factors are then used. The bias voltage has to be increased after irradiation and all tests presented are performed biasing the detectors at 500V. In Table 7.2 are displayed the gain, threshold spread, noise and noise occupancy of the half irradiated modules. Number of masked channels is also specified, since it has a direct influence on the module efficiency. No more than 1% of the channels should be lost on a module, which turns out to be satisfied by K5 303 and 312. However, K5 310 had one masked chip (128 channels) due to read-out problems.

Module	*Gain*	*Thr. spread*	*T*	*Noise (ENC)*		*Occ.@1fC×10^{-4}*		*Masked*
	(mV/fC)	*@1fC (ENC)*	*(°C)*	*Meas.*	*Corr.*	*Meas.*	*Corr.*	*Chann.*
K5 303	43.0	459.5	2	1528	1899	0.58	5.0	10
K5 310	37.0	479.2	7	1775	1995	5.03	8.7	43+128
K5 312	37.8	529.0	-1	1717	2115	3.31	15.6	16

Table 7.2: Front-end parameters as measured for half-irradiated outer end-cap modules. (Fluence $\simeq 1.5 \times 10^{14}$ protons/cm^2). K5 310 has a masked chip due to readout errors. The specifications are 5×10^{-4} for the noise occupancy, 15 masked channels at most, and an ENC not exceeding $1800e^-$.

Module	*Gain*	*Thr. spread*	*T*	*Noise (ENC)*		*Occ.@1fC×10^{-4}*		*Masked*
	(mV/fC)	*@1fC (ENC)*	*(°C)*	*Meas.*	*Corr.*	*Meas.*	*Corr.*	*Chann.*
K5 305	27.6	614.0	1	2052	2433	54.8	158	7
K5 308	30.5	633.7	-1	1934	2208	27.3	71.8	5
K5 312	29.0	536.5	-2	1815	2140	5.33	27.0	20
K5 503	29.0	655.4	-6	2123	2427	46.9	107	29
K5 504	27.7	697.2	-5	2036	2307	40.5	89.8	17

Table 7.3: Front-end parameters as measured for fully-irradiated outer end-cap modules. (Fluence $\simeq 3.0 \times 10^{14}$ protons/cm^2)

As can be seen in this table, the noise occupancy values are between 5.0×10^{-4} and 15.6×10^{-4} at 1 fC threshold, and ENC noise is between $\approx$ 1899 and $\approx$ 2115. Considering the fact that the luminosity will initially be lower, it can be expected from the previous results that the end-cap modules will reach the specification limits after about 7 years [54], if operated at the above threshold.

The front end parameters of the five fully irradiated modules are instead summarized in table 7.3. The noise level is between $\approx$ 2140 and $\approx$ 2430 e$^-$ ENC, and the noise occupancy between 27 and 160 $\times10^{-4}$, while the specifications are 1800 e$^-$ ENC and 5×10^{-4} respectively. To reach the noise occupancy level required by the specifications, a threshold of at least 1.2 fC is necessary, as verified by plotting the noise occupancy distribution per channel (see Figure 7.14). Test beam analyses are then required to determine whether it is possible to use this threshold while maintaining the specified efficiency level [78].

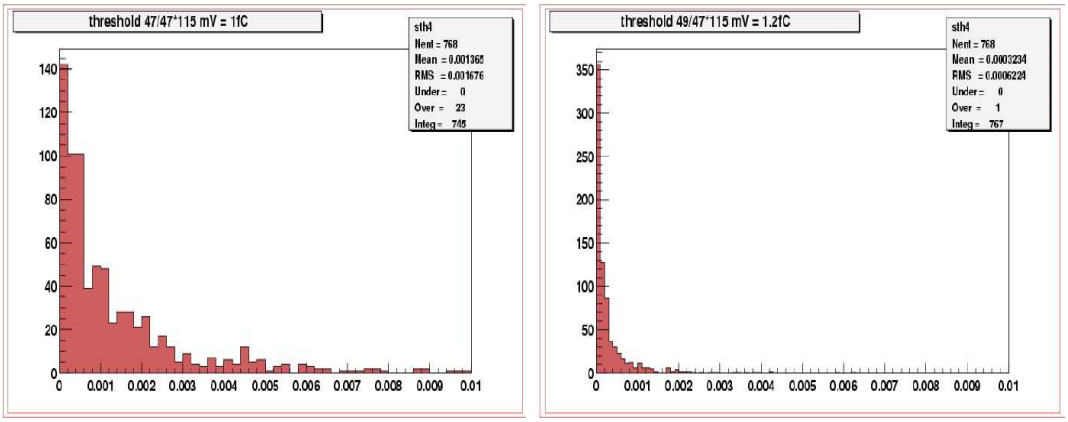

Figure 7.14: Noise occupancy distribution of K5 503 (link0) fully irradiated, for two different values of the threshold discriminator: 1 fC (left hand side) and 1.2 fC (right hand side). Taking into account the outliers, not shown in these plots, the mean noise occupancy values non corrected are 9.10^{-3} and 5.10^{-4} respectively, which corresponds to $1.7.10^{-2}$ and $2.2.10^{-3}$ when corrected for the calibration factor and the temperature dependence.

The gain and ENC noise variation with the irradiation dose is summarized in figure 7.15.

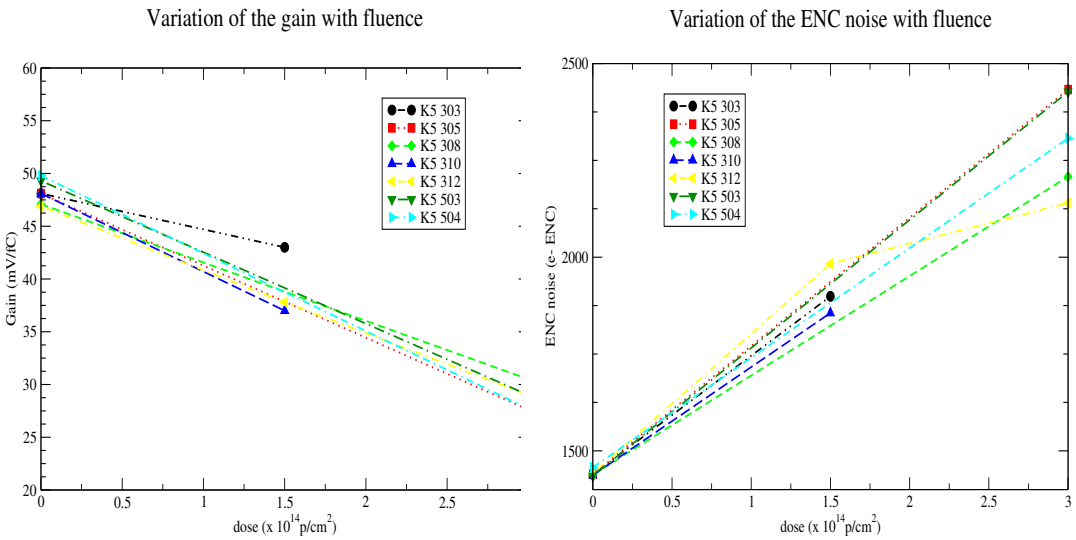

Figure 7.15: Variation mean gain, noise as a function of the irradiation dose.

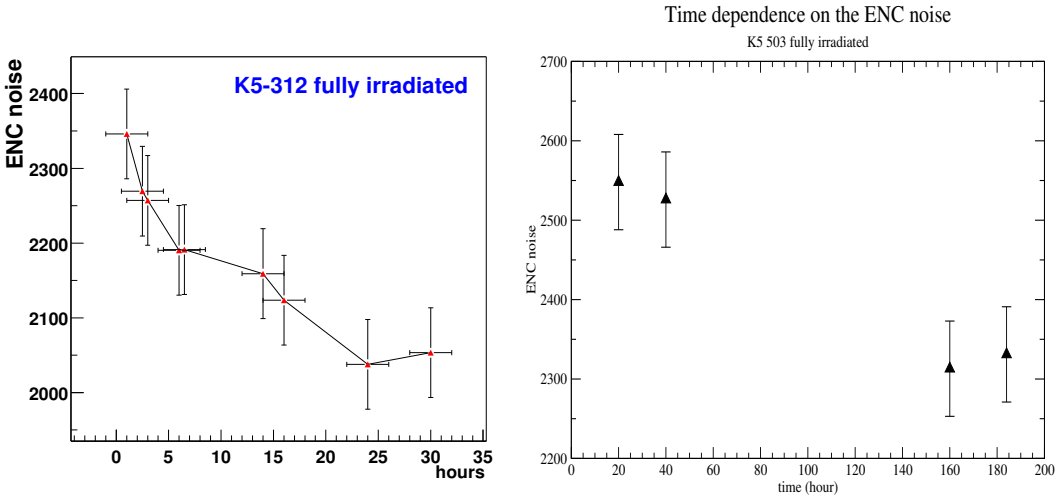

Figure 7.16: Variation of the ENC noise (corrected) with the time of bias for K5 312 (left hand side) and K5 503 (right hand side). The bias voltage is 500V.

ENC noise measurements have been performed on a long time scale to evaluate the dependence of the noise on the time of bias. The results are displayed in Figure 7.16 for K5 312 (when fully irradiated) and K5 503, left biased at 500V. A $\approx$ 36 hours time scale study was performed with K5 312, while K5 503 has been biased during more than six days. It can be clearly seen from Figure 7.16 that the noise is decreasing very slowly, as it was already observed in [79]. Between the first and the last measurement performed on K5 312, the ENC varies by more than 300 e^- ENC. In case of K5 503, the same decrease is indeed noticeable only on a longer time scale, making very difficult the extrapolation of a general

estimation of the time dependence.

The time walk of fully irradiated K5 312, representative of the timewalk results for the irradiated modules, is displayed in figure 7.17. It shows a high number of channels with large timewalk: 746 channels out of the 1536 have a timewalk larger than the specification of 16 ns, 11 being in another bunch crossing (that is above 25ns).

The degradation in timing performance is correlated with radiation effects in the analog part of the ABCD circuit. Thus, modifying the digital power supply V_{dd} did not lead to any improvement of the timewalk. On the contrary, the high number of slow channels can be significantly reduced by increasing the analog voltage, V_{cc}, supplied to the chips. The time walk profiles for V_{cc} = 3.5V and V_{cc} = 3.8V are compared in figure 7.18. Table 7.4 shows the influence of increasing V_{cc} from the nominal value of 3.5V to 3.8V by step of 0.1V. For this latter value, the timewalk distribution becomes flat across the chips and only

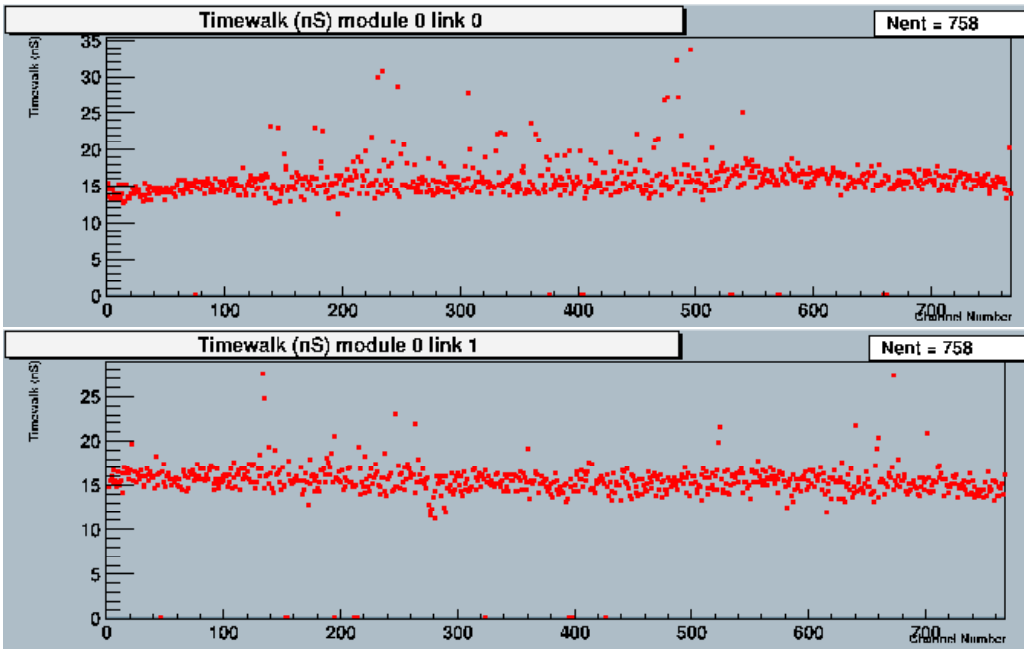

Figure 7.17: Timewalk distribution of K5 312 fully irradiated, for link 0 and link1.

Vcc *V*	*TW>16ns* *# of ch.*	*TW>20ns* *# of ch.*	*TW>25ns* *# of ch.*
3.5	746	32	11
3.6	380	8	3
3.7	311	2	0
3.8	190	0	0

Table 7.4: Dependence of the timewalk as a function of the analog voltage V_{cc} of the chips. The results are given for module K5 312.

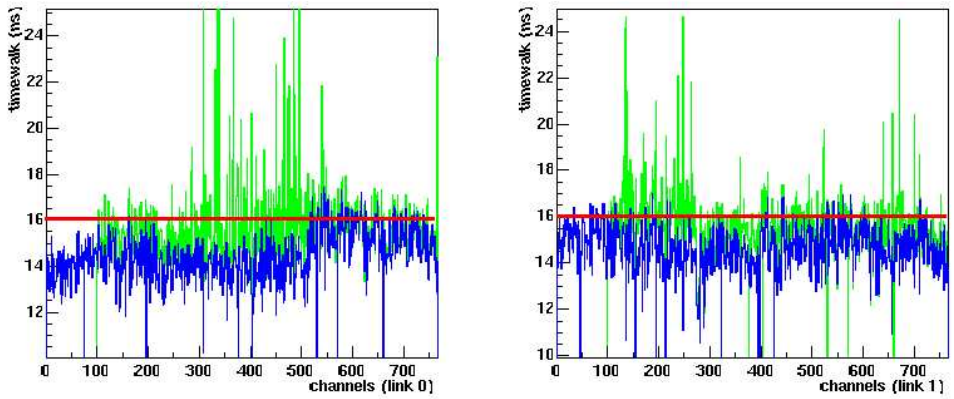

Figure 7.18: Comparison of timewalk distributions across the channels (both sides) with V_{cc} =3.5 V (light line) and V_{cc} =3.8 V (dark line). The horizontal line corresponds to the specification requirement of 16 ns as maximal limit for timewalk.

190 channels are above the required 16 ns, all of them having a timewalk less than 20ns.

In addition to significantly reducing the discriminator timewalk for many channels, operating the ASICs at V_{cc} = 3.8V instead of the nominal value also slightly improves the front-end parameters, as can be seen in Table 7.5; in particular, the gain is on average 3 mV/fC higher and the noise occupancy is slightly reduced. It also allows the recovery of some channels, masked mainly because of the impossibility of being adjusted by the trimming procedure. However, the gain still remains non-uniform across the chips, as shown in figure 7.19 (on the left nominal V_{cc}, on the right increased V_{cc}).

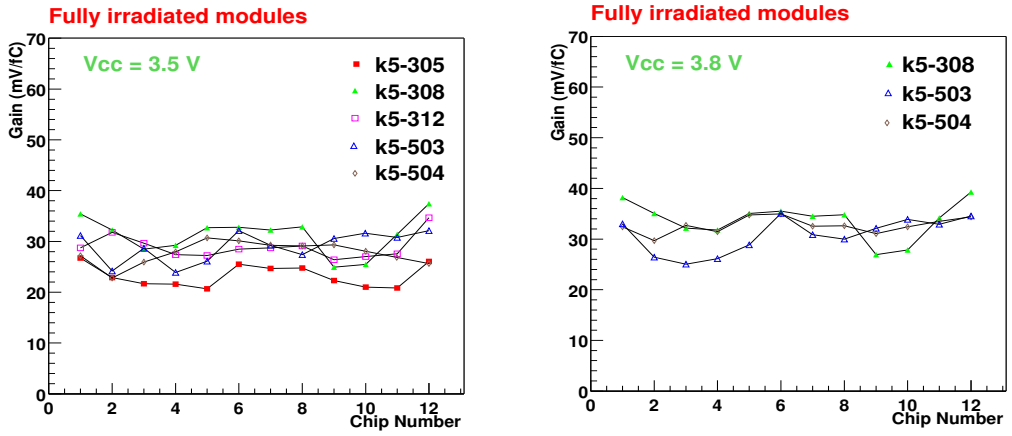

Figure 7.19: Gain distribution across the chip for irradiated modules K5 308, 503 and 504 operating at V_{cc}= 3.5 V (left) and 3.8 V.

The main issue in increasing the analog voltage when running irradiated modules concerns the power consumption of the module. This latter should not exceed 7W on the hybrid, and 2.6 W (1.6W) for the outer module wafers (inner module wafers) [67]. Since the front-end bias currents of irradiated modules are smaller than the ones of non irradiated, the power consumption can be maintained within this limit, as shown in table 7.6, where the maximal power consumption for all irradiated modules, for $V_{cc} = 3.5$V and $V_{cc} = 3.8$V, is evaluated.

Module	*Gain (mV/fC)*	*Thr. spread @ 1fC (ENC)*	*Noise (e^- ENC)*	*Occ.@1fC $\times 10^{-4}$*	*Masked Chann.*
K5 308	30.5/33.7	634/582	2208/2204	71.8/24.9	5/5
K5 503	29.0/31.6	655/661	2427/2300	107/42.6	29/12
K5 504	27.7/32.7	697/577	2307/2316	89.8/55.6	17/3

Table 7.5: Comparison of front-end parameters operating the modules with $V_{cc} = 3.5V$ or $V_{cc} = 3.8V$. The first (second) number of each column corresponds to $V_{cc} = 3.5V$ ($V_{cc} = 3.8V$).

Module	*Average*		*Maximal*		*Power Consumption*	
	I_{cc} (V)	I_{dd} (V)	I_{cc} (V)	I_{dd} (V)	*Aver (W)*	*Max (W)*
V_{cc} = 3.5 V, V_{dd} = 4.0 V						
K5 308	670	690	760	850	5.4	6.0
K5 312	620	810	680	950	5.1	6.2
K5 503	670	620	770	800	4.8	5.9
K5 504	660	640	760	830	4.9	6.0
V_{cc}= 3.8 V, V_{dd} = 4.0 V						
K5 308	710	680	820	870	5.6	6.7
K5 312	690	620	—	—	5.1	—
K5 503	700	610	750	840	5.1	—
K5 504	670	600	740	830	4.9	6.1

Table 7.6: Power consumption using the nominal $V_{cc} = 3.5$ V (on the top of the table) and $V_{cc} = 3.8$ V (on the bottom), keeping the digital bias at the nominal value 4.0 V. The maximum power consumption is calculated as $I_{cc}^{max} \times V_{cc} + I_{dd}^{max} \times V_{dd}$.

7.6 Summary of electrical performance

The electrical performances of end-cap pre-production prototypes, have been described in this Chapter. Given the fact that up to eighteen modules have been studied, the results obtained are representative of the typical performance of the end-cap module prototypes.

The non irradiated modules are well within the specifications, with a noise occupancy not exceeding 4×10^{-5} and a mean ENC noise of 1440 e^- ENC in the least favorable case of outer modules. Two outer modules have been irradiated to the level of approximately 1.5×10^{14} protons/cm^2, corresponding to half the fluence expected during ten years of the ATLAS life time. The noise occupancy then reaches values between 5 and 16 $\times10^{-4}$ and ENC noise between 1900 and 2115 e^- ENC.

Five modules have been irradiated at the full dose, resulting in a noise occupancy level between about 27×10^{-4} and 160×10^{-4}, and an ENC noise in the range 2140-2430 e– ENC, while the specifications are respectively 5 $\times10^{-4}$ and 1800 e^- ENC. The nominal noise occupancy limits would be met by increasing the threshold of the discriminator up to at least 1.2 fC. The characterization of these irradiated modules has been made over a period of several days. The ENC noise in particular decreases sensibly, over several days under bias (few hundreds of electrons). At the nominal value of the analog voltage of the front-end chips, many channels have a time walk larger than 16 ns, and a significant number of channels are even in another bunch crossing. However, it is worth noticing that increasing the analog voltage from 3.5V to 3.8V reduces considerably the discriminator time walk for many of them, thus permitting the recovery of almost all channels. In addition, when operating the ASICs at this increased voltage, there is a slight improvement of the gain (3mV/fC) and the noise occupancy.

The results obtained from the electrical and beam tests (described in Chapter 9), have been judged satisfactory by the SCT collaboration to pursue the real module production, and the SCT end-cap modules passed a Final Design Review in December 2002.

The mass production of the 1976 SCT end-cap modules began in mid-2003 at various production sites around the world. The CERN-Geneva assembly system has proved its ability to deliver the necessary yield of good modules within the time expected by the SCT collaboration. Many efforts were put into improving the production procedure, infrastructure, equipment, manpower and tools as more experience was gained and more new problems were encountered. At the University of Geneva 659 modules for the outer rings have been assembled and tested before shipment to the CERN quality assurance site. The end-cap modules are now being mounted on disks and the global SCT will be ready in 2006.

Chapter 8

An alternative project: the KB module

The four first hybrid versions foreseen for end-cap modules showed unacceptable instabilities of some chips – particularly towards the outer edge of the hybrid – and extensive reworking requirements that were not consistent across the fabricated modules. The possibility of building an end-cap module based on the barrel hybrid, the so-called "KB", assembled in an end-tap configuration with the forward detectors, was therefore considered by some institutes of the SCT collaboration.

A first prototype (later called b048) was successfully built in September 2001, followed by eight other outer modules in a final design configuration, assembled and fully tested. These included two irradiated modules, one of these latter being used for thermal tests only [80]. In this chapter, the module layout and particularities of its design are presented, together with the different assembly steps. The results of standard electrical tests[81] for unirradiated and irradiated KB modules are detailed, while relative test beam results are reported in next Chapter.

8.1 Motivation

Since the development of a fully functional hybrid, which performs to SCT stringent thermal and electrical requirements, is often complicated by the complexity and sensitivity of the readout electronics, and is therefore a technical challenge, it deemed advantageous to study an alternative module layout.

Looking at the history of the K-X hybrids developed between 1998 and 2002, the idea of a "KB project" was born after the problems observed on modules built with K4 hybrids. K4 hybrid had been also designed to overcome some deficiencies detected in the previous version of the hybrid and it was delivered at the beginning of 2001.

Twelve modules had been built: while input noise was quite close to the SCT specifications, some discontinuities were observed in the s-curves above 0 fC threshold, and especially around the 1 fC point, that is supposed to be the operation threshold (see figure 8.1). The

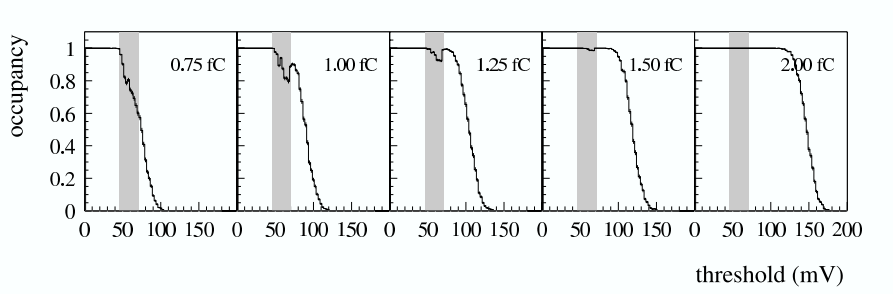

Figure 8.1: S-curves of a single channel of a K4 module, measured using different test input charge. The bands show the position of the features is independent of the shape of the S-curve or the input charge.

problem was related to the whole hybrids, involving most of the chips and thus indicating a global effect. These discontinuities were studied in a systematic way trying to explore all possible origins, as analog and digital grounding, dependence on the strip capacitance etc. Afterwards, it was found they suffered from feedback effects [82], most likely due to the CMOS-amplifiers after the comparator.

8.2 Module layout

The KB module consists of 3 component groups:

- the central spine, serving as structural support and which provides cooling for detectors and hybrid,
- the silicon detectors, glued to the spine,
- the electronics hybrid which is also glued to the spine.

Figure 8.2 shows the exploded view of the module and its components, while in figure 8.3 a photograph of a KB is reported. The module is mounted and cooled at the rear end behind the hybrid. The cooling contacts is 7 mm wide and extends over the full module width. The total module length is 156 mm.

The spine consists of a long central piece of thermal pyrolithic graphite (TPG)(part 1a), below the detector and hybrid, and two pieces of TPG(part 1b), in the area where the hybrid is attached to the spine. The TPG pieces provide the main cooling to detectors(part 1a) and hybrid(part 1b)

The central TPG(1a) has an in-plane heat conductivity of about 1700 W/mK, necessary to dissipate the heat generated in the irradiated detectors, due to the high leakage current. The TPG has been wedge shaped to allow a better dissipation, as the heat load carried by it increases gradually from the module top end to the end closer to the cooling contact. Its good electrical conductivity is also used to distribute the backplane voltage to the four

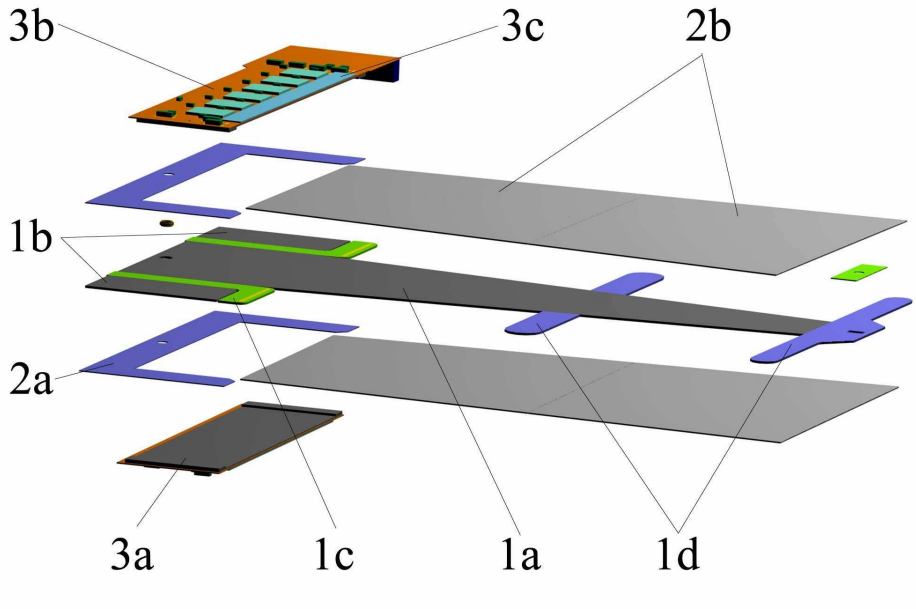

Figure 8.2: Schematic layout of the KB outer module

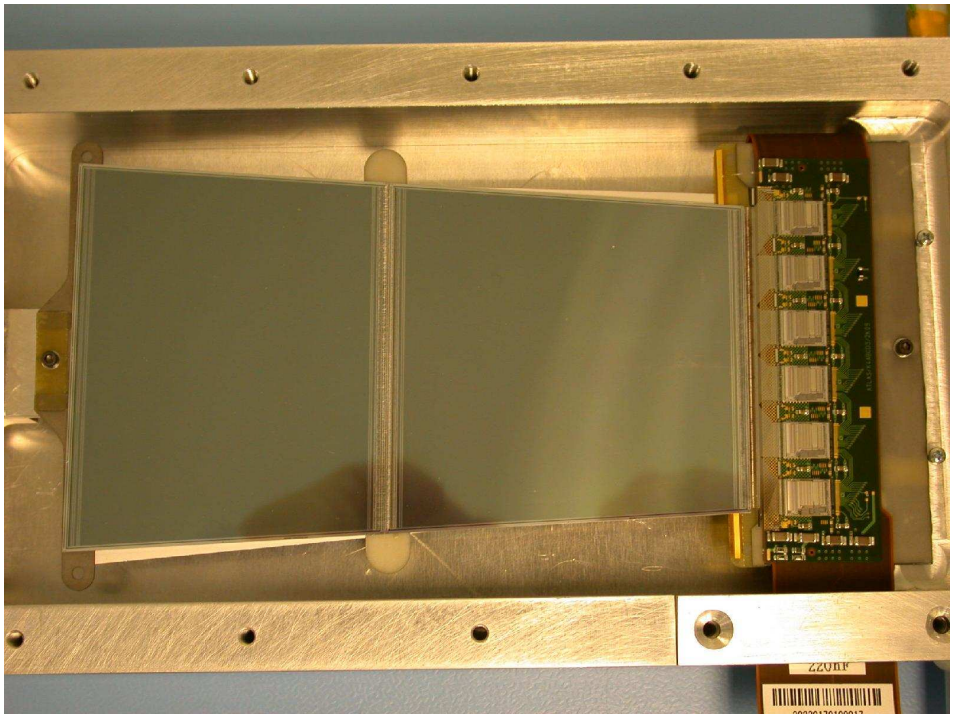

Figure 8.3: Photograph of a KB outer module

detector backplanes. The small TPG pieces (1b) remove the heat from the hybrid and conduct it to the cooling contact. The central TPG is separated from the smaller TPG pieces by two "L"-shaped parts of PEEK(part 1c), and they also serve as structural reinforcement between spine and detectors. At the place where the detectors are daisy-chained and at the far detectors end, the edges are supported by pieces of AlN ceramics (parts 1a-d), as it is required for bounding reasons and for a second module mounting point. All the central pieces have a nominal thickness of 450 μm.

The hybrid used for the KB module has the same structure of the one used for the barrel SCT modules, with some modification related to the different implementation of the hybrid on the module, since in the KB case it is bonded at the end of the sensors, rather than in the centre of the module as for barrels.

For further details on the KB module layout see for instance [83].

8.3 Assembly steps

In order to study the feasibility and function of this module layout we assembled a prototype series of eight "outer" KB modules. Outer module types were chosen as their layout is the most demanding for thermal and electrical performance.

Five of the assembled modules have been constructed according to SCT mechanical specifications and were surveyed to verify the mechanical precision of the assembly. All constructed module were electrically functional and were consequently used for tests.

Aim of the assembly procedure definition was on decoupling functions of all module components in order to simplify the technical specification for each part and allow the parallel construction of the module components groups. In particular we tried to decouple the construction of the hybrid from the assembly of the rest of the module.

The module is constructed in four phases, none of them presenting problems during the prototypes assembly:

1. the components in the center part (TPG,PEEK and AlN pieces - parts 1a-e) are aligned relative to each other and locked on a vacuum jig. Aluminum precision fittings are glued to the module as mounting and reference points.

2. the two detectors on one side and the AlN ceramic facing (part 2a) are aligned on a separate vacuum jig. After having precisely fitted the two jigs holding the two sides of the module, the detectors plus spine are glued together, thus the detector strips are bonded together and electrical tests are performed.

3. the hybrid is pre-assembled separetly with fles-circuit, supports, FE chips and pitch adapters and it is tested electrically as a separate unit. Afterwards, the hybrid is glued on one side of the forward extension of the AlN, and then wrapped around to the other side of the module.

4. in the last step the detector strips are bonded to the pitch adapter, and the detector p^+ bias line is bonded to the hybrid, thus the detector backplane connection is made.

Following the module assembly, the prototypes have been subjected to a standardized quality control procedure: it consists of verifying detector leakage current at different points of the assembly and a XYZ metrology survey to verify mechanical precision.

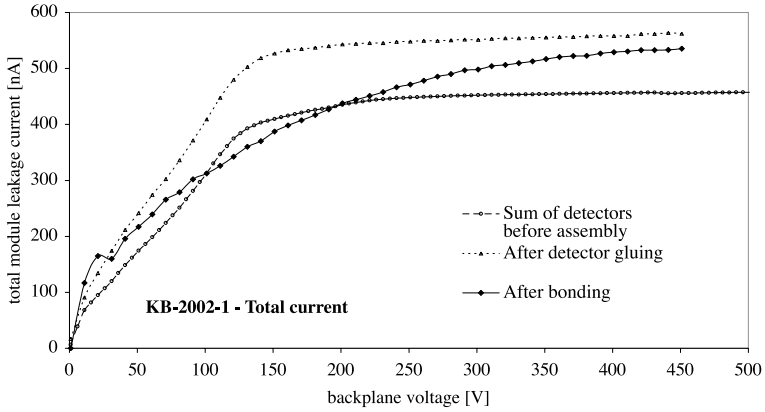

Figure 8.4: Total module leakage current,*i.e.* sum of four detectors, before assembly, after detector gluing and after bonding.

Figure 8.4 shows the total module leakage current for one module (sum of four detectors) before assembly, after gluing of sensors to the spine and after bonding. None of the five precision modules revealed detector current problems or breakdown.

The XY survey for module 1 to 4 showed very good results which are within the module specifications. The only deviation of one parameters ("MidYF": translational shift of the front-to-back detector pairs orthogonal to the strip orientation) for module 5 is still within the tolerances, and it has been anyhow due to loss in vacuum on one of the alignment jigs. The Z survey, that measures the planarity of the detector surface, has given also satisfactory results.

After the assembling, most of the KB modules were used for an intense test program, both from electrical and thermal point of view. Results of electrical tests are the subject of the next session, while for thermal test results see [80].

8.4 Electrical performance of non irradiated modules

For the non irradiated modules, similarly to the baseline module tests, the measurements have been performed with a minimal cooling, that is a chiller, providing a liquid coolant at +15°C, which corresponds to a temperature on the hybrid[1] between 28 and 35°C. The KBs were mounted in a dedicated test box (Al frame) that supports both ends of the module and cools it along its AlN facing at the rear with a cooling contact of $\sim 78\times8\text{mm}^2$.

[1] as in K5 hybrids, the hybrid temperature is monitored by two thermistors glued onto the hybrid.

Two types of corrections have to be taken into account to compare modules with each other, as for the K5 modules: corrections related to the calibration factors as in section 7.2.1 (values for 4 of the KBs reported in table 8.4 as example), and effects due to the temperature.

Module	*Cal. factor*	*Module*	*Cal. factor*
KB 048	1.13	KB 104	1.12
KB 100	1.12	KB 105	1.167
KB 102	1.13	KB 106	1.167
KB 103	1.13	KB 108	1.12

Table 8.1: KB calibration factors

As in case of baseline modules, the noise values have to be normalized to a given temperature. Evaluations of the SCT cooling system have led to an expected temperature on the baseline module hybrid of about 2°C. Even if the extrapolation in the KB case is not straightforward, we choose to normalize the KB results to this same conventional value. The noise versus temperature dependence has been measured on two KB modules. As shown in figure 8.5, the ENC variation is linear with temperature and the correction to apply turns out to be about 5.5 e- ENC/^oC (non corrected for calibration factor) for non irradiated modules. This temperature dependence is similar to the one found for prototype barrel modules [75].

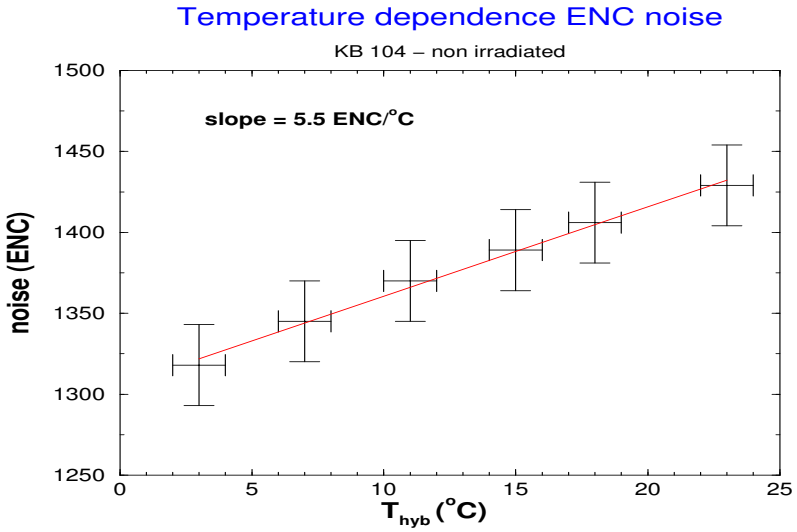

Figure 8.5: Temperature dependence of the ENC noise for non irradiated KB 104 and 105. The slope is approximately 5.5ENC/°C, including the calibration factor.

In table 8.2 the main electrical characteristics of KB modules are summarized, and both measured and corrected values of ENC and noise occupancy are displayed. The noise

occupancy correction was performed by fitting the occupancy as a function of the threshold, by the complementary error function 7.1, assuming that the noise is purely gaussian and threshold values respectively. Inverting this complementary error function leads, for a given value of the noise occupancy, to a value of the ENC noise. This ENC noise is then corrected as specified above, and the corrected noise occupancy is obtained using once more the interpolation (7.1).

Module	*Gain*	*Thr.spread*	*T*	*Noise(ENC)*		*Occ.@1fC* $\times 10^{-4}$		*Masked*
	(mV/fC)	*@1fC (ENC)*	*(°C)*	*Meas.*	*Corr.*	*Meas.*	*Corr.*	*Chann.*
b048	48.7	136	28	1410	1450	0.05	0.09	7
KB 100	47.8	138	34	1448	1446	0.11	0.11	3
KB 102	49.0	203	35	1300	1287	0.02	0.02	1
KB 103	48.5	156	33	1416	1430	0.05	0.06	30
KB 104	50.1	170	28	1370	1391	0.04	0.06	1
KB 105	50.9	139	-	1357	-	0.06	-	0
KB 106	50.0	156	30	1380	1430	0.02	0.04	2
KB 108	50.0	138	29	1318	1328	0.03	0.04	13

Table 8.2: Electrical performance of the non-irradiated KB modules. The values of noise and noise occupancy indicated as *corr* are corrected for calibration factor and normalized to the SCT operating temperature, that is 2°C on the hybrid thermistor. The gain is corrected as well by the respective calibration factors. Note that b048 is the first KB prototype that had been built with a slightly different geometry [83].

The noise occupancy of these modules at 1fC threshold is between $\approx 2 \times 10^{-6}$ and $\approx 10^{-5}$ – that is well inside the required specifications – with a gain of $\approx$ 50mV/fC and a (corrected) mean noise value of 1410 e- ENC. Figure 8.6 shows the noise occupancy plot of KB 104, together with the response curve and the dependence of gain on the threshold for one chip, representative of the results obtained with KB modules.

No instabilities were observed, as can be seen in Figure 8.7, where a set of four typical s-curves – superimposed – is displayed.

We can note that the number of masked channels is well below the 1% level required by the specifications, except for KB 103 for which the bonding procedure happened to be imperfect. In addition to these satisfactory mean values of noise and ENC, figure 8.8 shows that the ENC noise and the gain are very uniform across the modules, for all the tested KB modules.

Furthermore, the timewalk, not displayed here, is between 10 and 13 ns. The results are thus very satisfactory, and close to the barrel module performance [84].

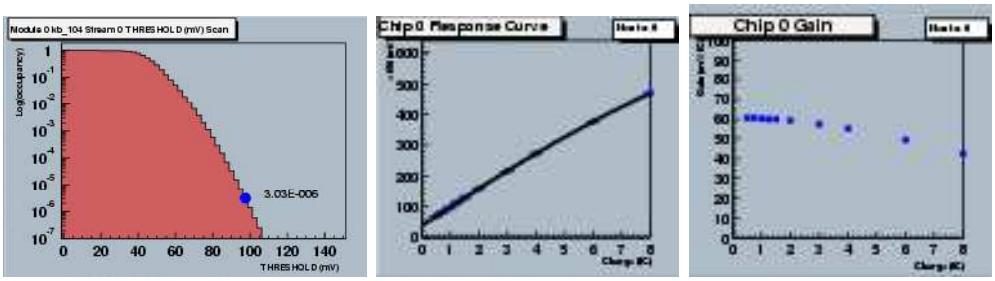

Figure 8.6: Typical noise occupancy, response curve and gain vs threshold plots of a KB module.

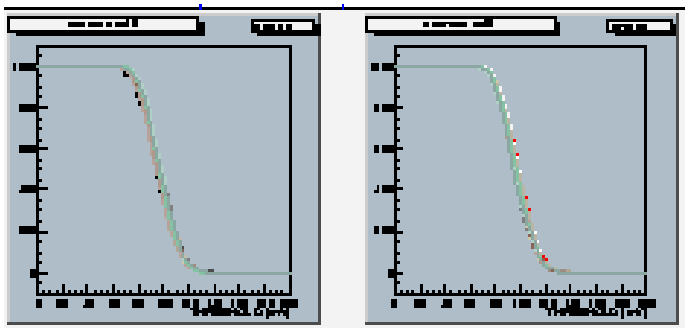

Figure 8.7: Example of scurves of an unirradiated KB module: for all single read out channel, a correspondent 0.5 fC charge in mV is injected and a threshold scan is performed. This plot shows S-curves of four channels superimposed.

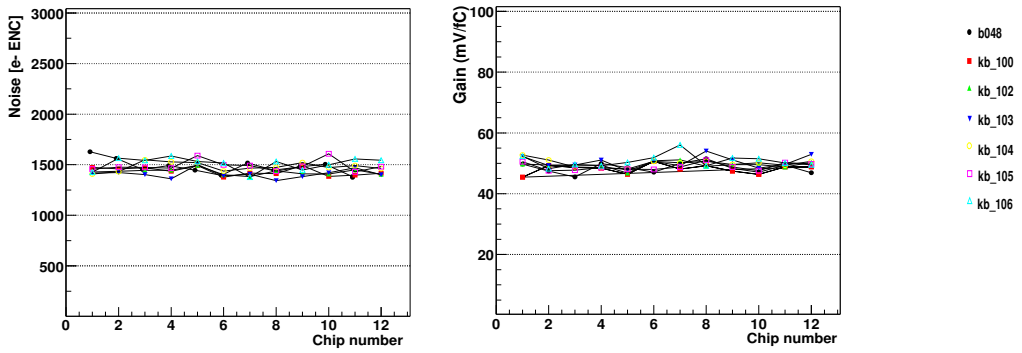

Figure 8.8: *(a)* on l.h.s. plot: Measured Noise (e- ENC) distribution per each ASIC for all unirradiated KB modules tested in the same environment. All reported values are corrected for the calibration factor and normalized to $2°C$. *(b)* on r.h.s. plot: Gain distribution per ASIC, corrected with the calibration factor.

8.5 Irradiated module performance

The KB 100 module was irradiated in October 2002. The module was mounted on a plastic cradle and the hybrid was fully powered, while silicon detectors were biased at 100 V. Indications of the temperature conditions were given by thermistors mounted on the hybrid and during the whole period it didn't exceed 25 °C .

Online tests were performed using the standard SCTDAQ test facility, to check the functionality of the ASICs and to monitor occurrence of possible failures of chips readout. After irradiation, the module was annealed for 7 days at 25 °C monitored temperature, in order to stabilize the detector properties.

The module was subsequently tested in a climate chamber set at -7 °C; cold nitrogen was fluxed inside the metal box holding the module (N_2 flux $\simeq$ 1 l/min) and a Huber chiller set at -17 °C was also connected to the box providing a liquid coolant passing below the hybrid. Figure 8.9 shows a measurement of the leakage current made with the electronics unpowered: at 500 V bias voltage, the value that was used during all electrical tests, the leakage current stabilized around 1500 μA, and increased up to 2600 μA when the ASICs were turned on, due to the extra-heating transmitted by conduction from the hybrid to the detectors.

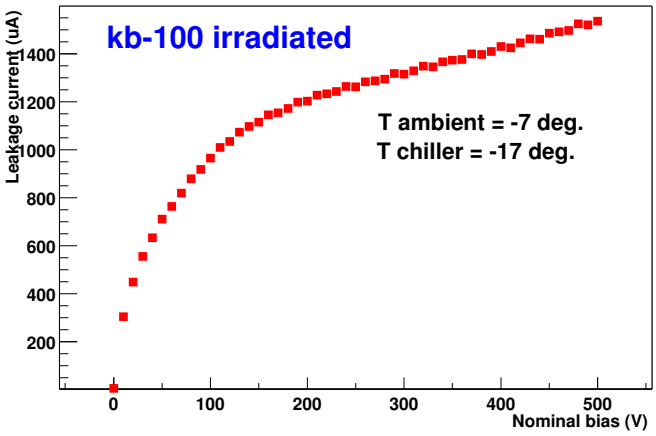

Figure 8.9: Leakage current for the irradiated module KB 100 (chips unpowered): the measurement has been performed setting the environment temperature at -7 °C (foreseen ATLAS condition) and providing liquid cooling through a chiller set at -17 °C (correspondent coolant temperature $\simeq$ -15 °C).

In addition to the standard electrical procedure described in the previous section, tests required to optimize the working conditions of the ASICs has been performed. Each chip Front End settings are independently adjusted and typical values found for KB-100 were 120 or 140 μA for the input transistor current, 27 or 30 μA for the shaper bias. This current scan procedure was made as the first step of the electrical tests, followed by a trimming

test.

Table 8.3 shows the front-end parameters as measured on the KB module: noise in ENC and noise occupancy at 1 fC have been corrected with a calibration factor of 1.12, supposed to be the same before and after irradiation (no temperature normalization is applied (T(therm.) = +1 °C)). In figure 8.10 the gain and ENC noise distributions across the channels are also presented: the noise is around 1980 e- and the efficiency in terms of number of working channel is > 99.5 %.

A timewalk scan has been performed to evaluate possible degradation in the speed of the ASICs (see figure 8.11): 10 chips out of 12 are in the specifications, with an average timewalk of < 16 ns, only one chip on the bottom side having a mean time walk of about 18 ns.

Gain	*Thr. spread*	*T*	*Noise (e- ENC)*		*Occ.@1fC* $\times 10^{-4}$		*Masked*
(mV/fC)	*@ 1fC (ENC)*	*(° C)*	*Meas.*	*Corr.*	*Meas.*	*Corr.*	*Chann.*
30.0	586.0	1	1765	1978	15	40	6

Table 8.3: Front-end parameters as measured for the irradiated KB module. The occupancy at 1 fC threshold is higher than what is expected from the electronic noise and threshold spread. The measurements were affected by common mode noise due to the fact that they were performed in a very noisy environment (climate chamber) without an appropriate grounding - see also test beam section.

8.6 Summary

The KB module layout had been designed, prototyped and tested for the end-cap of the ATLAS SCT detector. It aimed on integrating identical read out electronics and hybrid for barrel and end-cap modules in the geometry of the forward SCT detector and it was developed when the performance of K-X hybrids were not yet satisfactory.

Being the electronics hybrid one of the most complex component of the entire module, the described module design provided a valid backup solution in case a dedicated forward hybrid was not completed in time.

The module was designed to follow the stringent SCT requirements for electrical performance and with emphasis on excellent thermal management. The design was validated in a prototype assembly of eight modules. This prototype run also allowed to develop and demonstrate the assembly procedure, which was found to be simple yet precise and reliable.

Results on KB modules in beam tests are reported in the next Chapter.

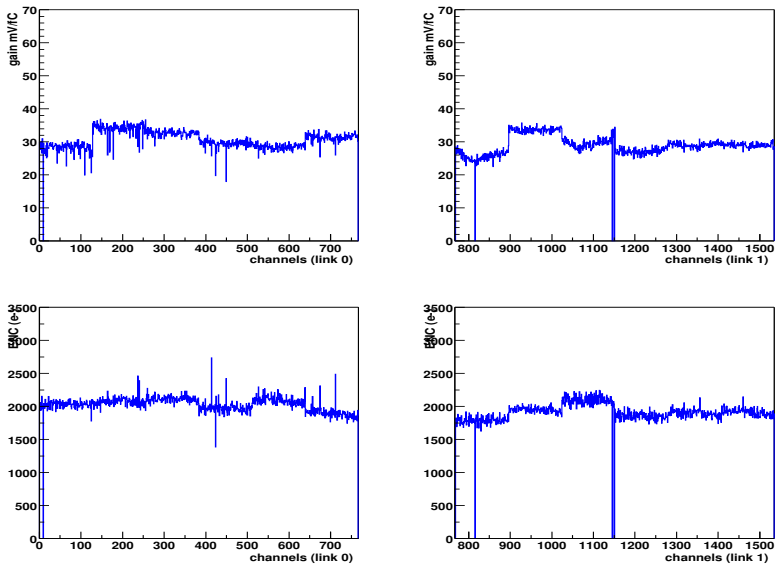

Figure 8.10: Gain (on the top) and Noise ENC (on the bottom) distributions across the channels for KB 100 irradiated module: left and right plots refer to the two module sides.

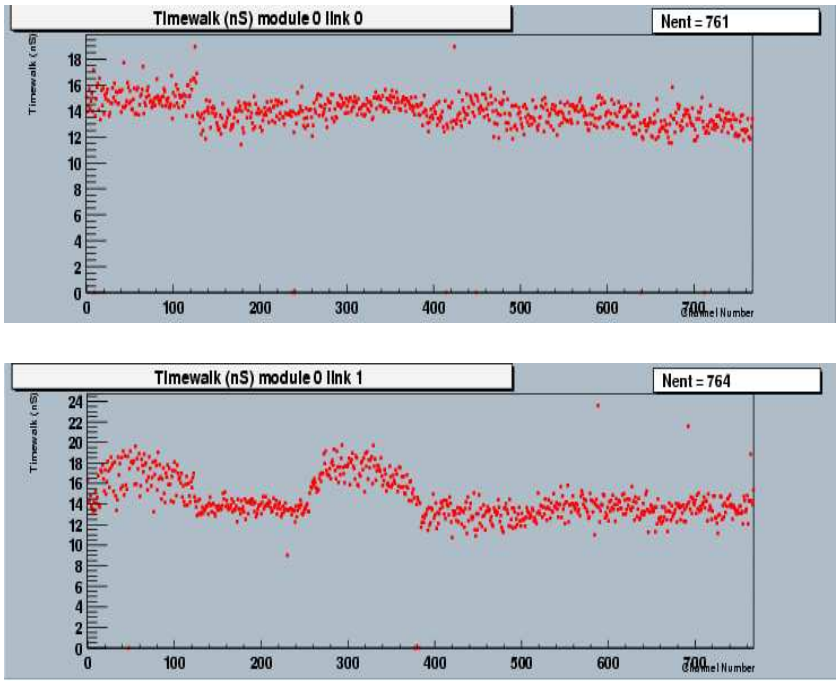

Figure 8.11: Timewalk distribution of KB 100 irradiated, for link 0 and link 1.

Chapter 9

Test beam results

ATLAS SCT silicon micro-strip detectors have been tested in test beams at the H8 area of the CERN SPS. For each beam test (see for instance [85], [86], [78]), a maximum of 12 modules are installed in the beam area. Modules of four SCT geometries are used: rectangular barrel modules and the three types of wedge-shaped end-cap modules. To estimate the performance at the end of the ATLAS experiment, modules irradiated as described in previous chapters are included.

In the beam period, the operating conditions are scanned over standard ranges. In the binary readout scheme adopted by the SCT, a fine-grained scan of the discriminator threshold is needed to recover the charge distribution; the charge collection efficiency is characterised by the median of the charge distribution.

The dependence of the performance on particle incidence angle, detector bias voltage, and analog supply voltage is studied by performing nested scans of the operating parameter and the discriminator threshold. The effect of a strong magnetic field is also tested by inserting the complete setup in the superconducting 1.56 T Morpurgo magnet. The deviation of the charge carriers due to the Lorentz effect has been studied in detail, yielding a precise measurement of the Lorentz angle.

In this chapter, an overview of the test beam setup and methodology and the most important results will be given, with a special attention to forward K5 irradiated modules and to KB modules performance. In section 9.1 the system setup is briefly introduced, while in section 9.2 the module calibration procedure is briefly reported, being very similar to tests already described in previous chapters. In section 9.3 the offline preprocessing steps of the raw data is outlined. Section 9.4 refers to the most important results as efficiency at operating threshold, noise occupancy, median charge, for unirradiated and irradiated modules. Bias voltage dependence, pulse shape studies, efficiency as function of interstrip position and spatial resolution are described in section 9.5, 9.6, 9.7 and 9.8 respectively, while angle scan, magnetic field effects are reported in 9.9. Section 9.10 is dedicated to a summary of KB modules results, while section 9.11 presents briefly the studies performed using SCT irradiated modules for track pattern recognition. Finally, these and other results not reported, together with their impact on the ATLAS tracking system performance, are summarized in section 9.12.

9.1 Setup

The H8 test area at CERN received a secondary beam from the 450 GeV SPS. Several particle types and beam energies were available. A standard beam for tests of SCT modules consists of 180 GeV charged pions with a minor contamination of muons. The test beam setup used in the last years is depicted in figure 9.1. The arrangement of the devices under test corresponds to the August 2002 beam test in the H8 beam line.

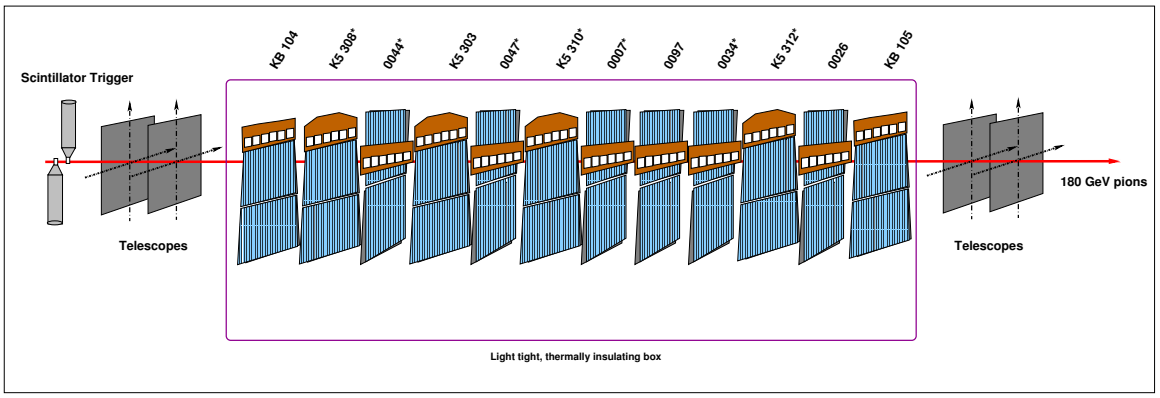

Figure 9.1: Arrangement of the SCT prototype modules in the beam line during the August 2002 beam test.

The complete test setup can be introduced in a 1.56 Tesla magnetic field from the super-conducting Morpurgo magnet, the magnetic field points being vertically downward, *i.e.* parallel to the readout strips of the detectors in the standard module configuration. The most important systems - binary readout and control, beam telescope, trigger and cooling - are briefly described below:

- **Trigger**: two scintillator detectors read out by Photo Multiplier Tubes are used to detect the passage of beam particles and trigger the readout system. The scintillator response is sufficiently fast to control the jitter of the trigger signal to 1-2 nanoseconds. The acceptance of the scintillator detectors is typically $2 \times 2cm^2$, large enough to contain typical beam spots and comparable in size to the acceptance of the beam telescope. The SCT modules have a sensitive area of 6×12 cm^2.

- **Beam telescope**: the telescope is used to reconstruct the trajectories of incoming beam particles. Provided that the alignment of the system of telescope and modules is known, tracks can be interpolated to the plane of the modules under test. The alignment of the test beam system is discussed in section 9.3. The telescope is composed of four modules mounted in pairs on either side of the thermal enclosure of the modules under test. Each of the four telescope modules consists of a two perpendicular Silicon Micro-Strip sensors with a strip pitch of 50μm. The detectors are read out by VA2 analog multiplexed readout chips with 1μs peaking time. The spatial resolution obtained is well below 5μm. Routinely, an SCT module is read out as an

anchor module. This means the module is left at a fixed threshold and bias voltage optimized for high efficiency and low noise.

- **Binary readout and control**: the SCT prototypes receive clock and commands and their data are received and decoded by a suite of custom VME modules as in the laboratory system setup described in previous chapters. The clock and control module (CLOAC) provides a central 40 MHz system clock that is distributed to all modules. It is also used to send short commands - resets and the L1 trigger - to the modules. A slow command generator module (SLOG) assembles and sends slow commands. These are used to configure the readout chips on six binary modules and load the settings for the DACs that control the bias to the Front End circuit, the threshold and the trim DACs. The MuSTARD module is capable of reading out both sides of six SCT modules through the spy connectors.

- **Cooling**: the devices under test are held in a light-tight thermally insulating box. The box is flushed with cold nitrogen to ensure a dry atmosphere. Each of the modules is contained in its own aluminium test box. The module boxes are equipped with mounting points and cooling contacts similar to those to be employed in ATLAS. The modules are cooled individually by a water-ethanol (60:40) mixture at -15^o C flowing through a cooling pipe in the module box, immediately under the cooling point. The liquid flow from a chiller is sufficient to remove the maximum power of 7 W dissipated by the front-end electronics. The resulting hybrid temperatures, measured with a PT1000 or thermistor at the edge of the hybrid, are monitored continuously. Hybrid temperatures range between -5 and 5^o C. The differences between modules are small compared to the variation across the hybrid and should not lead to significant differences in electronics noise. The leakage current of irradiated detectors is in the range from 1 to 3 mA, depending on the bias voltage. The non-irradiated modules have tiny currents of the order of 1μA.

9.2 Module calibration

A full characterisation of the module front end parameters as gain and noise, is made in situ prior to the beam test using the ABCD's on board calibration circuit following the same procedure of laboratory tests.

The usual corrections for calibration capacitor effects and temperature dependence discussed in Chapter 7 are considered. In particular, during the test beam, modules have been kept to a temperature within a range of 7-8 degrees, between -7^{o}C (irradiated barrel modules) and 0 ^{o}C (irradiated endcaps). Not normalizing to 2^{o}C, the signal-to-noise might be affect by a maximal error of the order of 5%.

In addition to the standard electrical procedure, tests required to optimize the working conditions of the ASICs for irradiated modules have been performed. The degradation in timing performances of fully irradiated endcap modules has been studied with beam tests and effects related to V_{cc} changes are discussed later in this Chapter.

9.3 Analysis

During the beam test, data from all sub-systems - telescope modules, binary modules, TDC - are assembled into events and written to a binary data file. To facilitate the analysis, these raw data are processed off-line into summary files, named DSTs (for Data Summary Tape). The summary files present the data in an easily accessible n-tuple format. The off-line processing includes the internal alignment of telescope and module planes and the reconstruction of tracks using the measurements of the beam telescope.

9.3.1 Alignment and track reconstruction

The beam telescope provides four very precise measurements in two perpendicular space coordinates. The reconstruction of the track and the interpolation to the plane of the prototype require a precise knowledge of the relative alignment of all detectors in the setup.

The internal alignment of the analog telescope and detectors under test is very roughly limited by the mechanics of the test beam system. Detailed knowledge of relative positions and angles is obtained by a software alignment using the beam particle tracks. As a first step the reference frame is fixed by choosing two pairs of telescope planes and minimising the deviation of the tracks with respect to the Z-axis. All other planes are then aligned with respect to the first two by optimisation of the residuals. The SCT modules are composed of four separate silicon wafers. Both stereo-planes of each module are aligned independently. Under the condition that the beam is contained in a single wafer per plane, the alignment procedure is insensitive to the module assembly precision, *i.e.* the wafer-to-wafer and the front-to-back alignment. A more detailed description of the algorithm can be found in [85]. The alignment procedure is repeated each time the setup is accessed and whenever the magnetic field is changed.

The off-line pre-processing of the data includes the reconstruction of the tracks using the space points measured by the telescope.The measurements on the two perpendicular planes of each telescope module are combined into three-dimensional space points. Track segments are constructed by combining all space point measurements on the most upstream and downstream telescope modules. Space points of the remaining two telescope modules are included in the track candidate if the distance between the track segment and the space point is less than 50 microns. All tracks with at least three space points are stored. A number of track quality indicators are available to select a sample of tracks with a predefined efficiency and purity. The most important are: the number of space points in the track fit, the χ^2 of the fit, the track gradients with respect to the beam axis and the efficiency of the anchor module. After applying these cuts, a large fraction of the track statistics remains, while the effect of fake tracks on the efficiency measurement is well below 1 %. In the H8 beam tests the position where the tracks were incident on each module is interpolated from the telescope hits with a precision of $\sim 5\mu$m, being the dominant error due to track multiple scattering in the setup.

9.3.2 Event selection

During the beam period a large number of runs[1] are taken with variable operating conditions: discriminator threshold, bias voltage, incidence angle and magnetic field. The first step in the analysis is the selection of the event sample. To select a sample of clean, unambiguous events, a number of event selection criteria are applied:

- **Single track events**. In a small fraction of events (depending on the beam intensity, generally of the order of 5 %) more than one track is reconstructed from the telescope information. As the integration time of the binary modules is much shorter than that of the telescope modules the second track is generally not detected in the binary system. To avoid ambiguities, events with more than one track are rejected from the analysis. Events where no track has been reconstructed are rejected as well.

- **Track quality**. From the remaining sample, only those events where the track satisfies the quality criteria are accepted. Most analyses require a minimum number of points in the track fit and set maximum values fro the χ^2 of the fit and the slopes of the track with respect to the beam axis. In general, a hit close to the track in the anchor module is required. This combination of cuts efficiently removes fake tracks and tracks suffering a large deflection due to multiple scattering inside the setup. The loss of statistics in this stage depends on the values of the cut, but is in general of the order of 10-30 %.

- **Masked channels**. During the characterisation of the modules a number of faulty channels is masked. Events where the track points to one of these "bad" channels or immediate neighbours (± 1 strip) are rejected from the analysis. In recent prototypes the fraction of masked channels is always below 1 %. The loss of statistics in this step is therefore small.

- **Time window**. A final cut removes those events where the trigger phase falls outside the optimum window. The window is optimised separately for each module. Only binary hits in one clock cycle are maintained. Thus, the data taken in ANYHIT compression is converted off-line into the equivalent of LEVEL compression. This cut is expensive in terms of statistics: for a 10 ns window only 40 % of the events are retained.

9.4 Results

9.4.1 Efficiency and noise occupancy

The most important benchmark properties of the binary modules are efficiency and noise occupancy at the operating threshold, envisaged to be 1 fC. The *real* position of the track

[1] The *run* is the smallest unit of data in the beam test. It contains 10.000 to 30.000 events for a fixed set of operation conditions.

on the module plane is interpolated from the telescope measurements: a detector plane is considered efficient if a binary cluster center is located within $100\mu m$ of the real track position. In the binary readout scheme, a scan of the discriminator threshold through the charge distribution is performed to reconstruct the full signal distribution. The s-curve – efficiency as a function of threshold – measures the integrated charge distribution. The *collected* charge distribution is described by the Landau distribution of the *deposited* charge convoluted with the Gaussian noise distribution and the effect of charge sharing between neighbouring strips. The median charge is measured, on the s-curve, as the charge corresponding to the threshold where 50 % efficiency is obtained. In practice, the threshold is expressed in equivalent charge and the value for the median charge is obtained directly from a fit with a skewed error function:

$$\epsilon = \epsilon_{max} f(x \cdot [1 + 0.6 \frac{e^{-\epsilon x} - e^{\epsilon x}}{e^{-\epsilon x} + e^{\epsilon x}}]) \tag{9.1}$$

where f denotes the complementary error function. The median charge μ, the width σ and the maximum efficiency ϵ_{max} are free parameters and $x = (thr - \mu)/\sigma^2$. This parameterisation describes the data quite accurately.

The detector bias voltage is set to its expected nominal value, 150 Volts for non-irradiated modules and 350 (or 500) Volts for modules irradiated to 3×10^{14} p/cm^2. The efficiency is quoted at a corrected threshold of 1.0 fC, with the noise occupancy at the same threshold. Typical efficiency s-curves for an unirradiated and irradiated module are shown in figure 9.2 on the left.

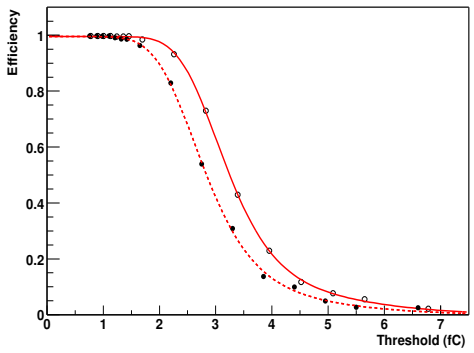

Figure 9.2: Typical efficiency s-curves for unirradiated *solid* and irradiated *dashed* modules

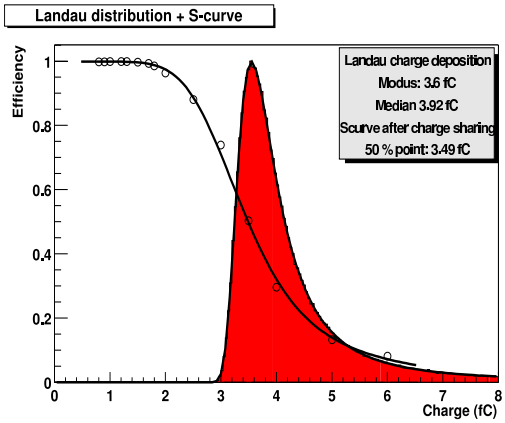

Figure 9.3: Theoretical charge deposition distribution and simulated s-curve after charge sharing and noise

The median collected signal at nominal bias voltage varies significantly from one module to another. For non-irradiated barrel modules the charges range from 3.2 to 3.6 fC. The irradiated modules collect less charge when the detectors are biased to 350 V, between 2.7 and 3.1 fC (the highest values obtained only for barrel modules). In this case, the beam is incident perpendicularly on the modules and no magnetic field is applied. Considering the

180 GeV/c charged pions beam, the expected median charge for a silicon module as the SCT ones is 3.9 fC (see figure 9.3) as extrapolated from Landau theory and 4.0 fC from GEANT4 simulation. An attempt to evaluate the reason for the 0.5 fC not collected is given in [87], and it is summarized below.

The binary readout scheme is essentially single-strip. The charge deposited on neighbouring readout strips cannot be recovered by clustering neighbouring channels. In [87] three mechanisms that lead to signal leaking into the neighbouring strips are identified:

- Diffusion: for tracks incident on the central region between two strips, diffusion of the charge carriers as they drift towards the read-out plane can lead to significant charge sharing.
- Cross talk: The capacitative coupling of the strips – the inter-strip capacitance – leads to the induction of a signal on the neighbouring strips.
- δ-electrons: In a fraction of the interactions a large momentum transfer takes place between the incident particle and an electron in the medium. Electrons with energies of several tens or hundreds of KeV can travel significant distances ionising the medium along their trajectory.

Multi-strip clusters due to diffusion of the charge carriers only occur when a track is incident on a narrow region exactly between read-out strips. This property is used to disentangle the diffusion component from the remaining two mechanisms. From a set of events two samples are formed: the first samples contains the full statistics, while in the second sample only tracks that are incident close to (within 20 μm of) a readout strip are accepted. The multi-strip cluster probability for the full sample - with contributions from the three mechanisms - and the reduced sample - where diffusion no longer plays a role - is shown as a function of threshold in figure 9.4.

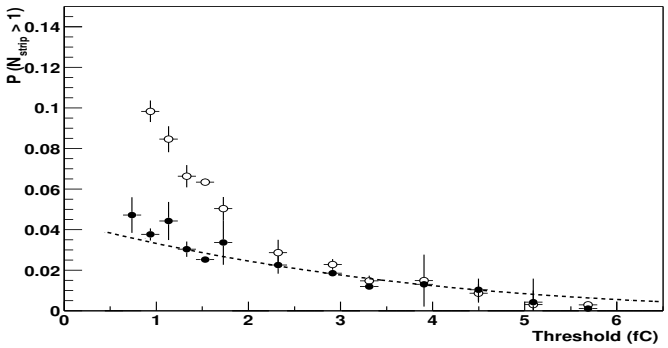

Figure 9.4: Probability of multi-strip clusters close to the track. The open markers correspond to the analysis considering all tracks, while filled markers refer to tracks very close to the read-out strips. The dashed curve represents a calculation of the multi-strip probability using GEANT4.

Charge sharing due to diffusion is found to lead to a significant increase in the multi-strip cluster probability only at low threshold. From the difference in median charge obtained on both samples the charge loss due to diffusion of the carriers can be estimated. For all module types the charge difference is found to be 0.13-0.16 fC.

The charge loss due to cross talk cannot be measured in the beam test. The fraction of the signal that is induced on neighbouring strips can be estimated from the inter-strip capacitance. Ignoring the impedance of the amplifier and assuming the capacitor on the hybrid that joins the detector backplane and HV ground is sufficiently large the following result is obtained for the signal induced on the neighbouring strips:

$$I_{neighbours} = \frac{I_s C_i}{C_c + C_i + C_b} \tag{9.2}$$

Using measured values for the coupling, inter-strip and strip-to-backplane capacitances of $C_c = 120$ pF, $C_i = 6$ pF and $C_b = 1.7$ pF, the charge loss due to cross talk is expected to be of the order of 6%, i.e. ~ 0.26 fC.

The leakage of charge to neighbouring strips due to δ-electrons is found to dominate the multi-strip cluster probability at high thresholds. Also in this case, the effect on the median charge cannot be directly estimated from test beam data. Model (GEANT4) calculations show that even though the tail of the charge distribution becomes less pronounced as δ-electrons carry energy away from the central strip, the median of the distribution is not significantly affected.

The total charge loss due to the three charge sharing mechanisms is thus expected to be ~ 0.4 fC. Signal loss due to charge sharing accounts for (most of) the discrepancy between the observed median charge (3.5 fC) and the theoretical expectation (4.0 fC). The error on the median charge is dominated by the uncertainties in the calibration. The variation of the calibration from one chip to the next is evaluated in the beam test by pointing the beam to areas of the detector read out by different chips and measuring the median charge of each chip separately. For non-irradiated modules the chip-to-chip spread in the median charge is of the order of 4%. After irradiation the spread increases to nearly 10% on forward modules. Correcting the charge of each chip by measurements of the calibration DAC output improves the uniformity, suggesting that the spread in median charges is due to variations in the components of the calibration circuit. Therefore, the random error of a single median charge measurement is of the order of 0.1 fC for non-irradiated modules and 0.3 fC for irradiated modules. In practice, the signal-to-noise ratio, the ratio of median charge and the equivalent noise charge, removes most of the calibration dependence, greatly facilitating comparison between the different modules.

In addition to the ENC noise measurement performed in-situ during module calibration, the noise hits are counted in noise events taken in the periods without beam between two spills of the accelerator. Thus, the noise events are taken in exactly the same operating conditions as the beam events. The occupancy is defined as the probability to find a hit due to noise on a channel in a given clock cycle.
When the modules are operated with sufficient over-depletion, the noise occupancy is a

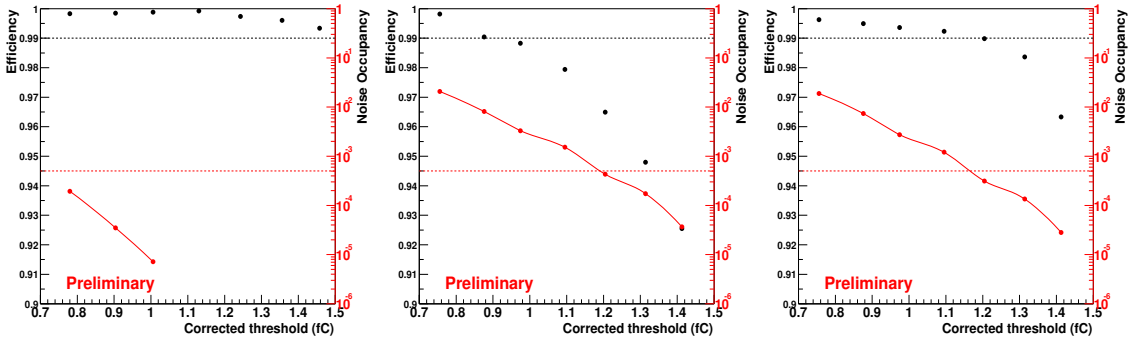

Figure 9.5: Results of the efficiency (left axis) and noise occupancy (right axis) versus corrected threshold in fC in the region near the nominal 1.0 fC operating point. The dashed lines indicate the module specifications for efficiency (99%) and noise occupancy (5×10^{-4}) at the nominal operating threshold. The leftmost figure corresponds to a non-irradiated barrel module, the middle figure to a forward module irradiated to the reference fluence of 3×10^{14} p/cm^2 and with nominal bias voltage 350 V, the rightmost figure to the same module biased at the limit value of 500 V.

rapidly falling, nearly Gaussian function of threshold, independent of bias voltage. The occupancies are found to coincide rather accurately with the expectation from the equivalent noise charges measured during the characterization.

Figure 9.5 shows efficiency and noise occupancy on the same plot for unirradiated (left) and irradiated forward modules (middle and right, for V=350 V and 500 V respectively): after irradiation, the noise occupancy is considerably higher for a given threshold, in agreement with increased noise charge, and this has been noticed especially for forward modules, as already shown in tests performed in the laboratory.
The SCT specifications require over 99 % tracking efficiency and a noise occupancy of less than $5 \cdot 10^{-4}$ (both requirements are indicated as dashed lines in the figure): the operating range is defined as the range in thresholds where the efficiency and noise occupancy specifications are both met. It is clear that the efficiency for irradiated forward modules fall off at a lower threshold than for similar non-irradiated modules; thus, irradiated modules do not meet the specification but in a narrow window [from 1.1 to 1.2 fC] and only if bias voltage is raised to 500 V (nominal bias after few years of irradiation is 350 V). For non-irradiated modules of the four geometrical types, the operating range extends from $\sim$ 0.8 fC up to $\sim$ 1.5 fC.

9.5 Detector Bias Voltage

The bias voltage of the detector is an important operating parameter. For the non-irradiated detectors a plateau is reached, collecting the full deposited charge a few tens of Volts after depletion voltage. For irradiated detectors, the collected charge continues to increase,

although slowly, even tens of volts after depletion.

On the other hand, the maximum voltage is limited by the detector breakdown voltage (greater than 500 Volts for SCT detectors), the limit of the power supplies (450-500 Volts) and the limit posed by the cooling system. Therefore, a good characterisation of the performance versus detector bias voltage is essential.

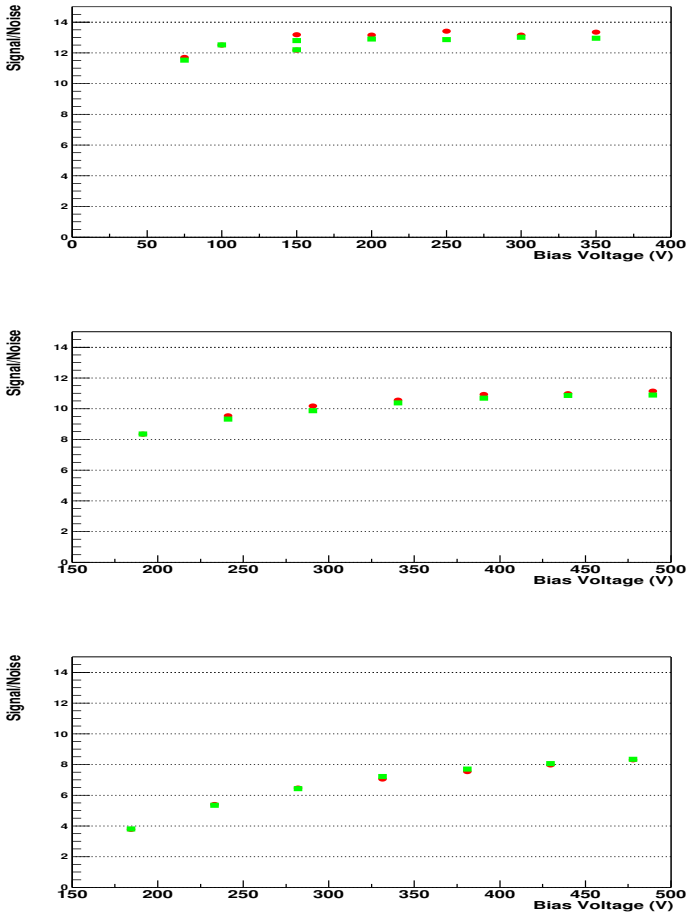

Figure 9.6: Median signal-to-noise ratio versus bias voltage. Top: non-irradiated module (all types are similar.) Central: half dose-irradiated endcap outer module. Bottom: fully irradiated endcap outer module. In all figures, the round and square markers correspond respectively to the readings on the front and back wafers of the module. In cases where the area of the sensor hit by the beam was read out by more than one chip, the results of each chip are indicated separately.

Figure 9.6 shows the dependence of the median signal-to-noise S/N (median collected charge over equivalent noise in fC) on the detector bias voltage. From top to bottom we present the S/N for an unirradiated, an half-dose irradiated and a full-dose irradiated forward module. The degradation in performance after irradiation is clear, the S/N passing from a 13 average value to 8. Each point in bias corresponds to two S/N value, one for each

side of the module. No error bars are reported, although a 5% error should be considered per each S/N value.

For the non-irradiated modules the S/N (and the median charge) is nearly constant from 150 Volts upwards, since both the collected charge and noise do not depend strongly on the bias. The charge difference between the reference voltage of 150 V and the highest voltage (300 V) is 0.15 fC, the S/N difference of the order of 5%. As the bias voltage approaches the depletion voltage (around 75 Volts in these modules) the median charge gradually decreases. This can be explained as a ballistic deficit of the shaper, i.e. the integration window of the front-end electronics is no longer large compared to the charge collection time of the detector, leading to charge loss. The charge collection time for non-irradiated *pn* detectors of thickness d is approximately given by:

$$T = \frac{d^2}{\mu V_{bias}} \tag{9.3}$$

where μ is the mobility of the majority carriers. Just above depletion voltage (80 V), one obtains 22.5 ns for thin detectors, 29 ns for thick detectors. The shaper of the Front End has a peaking time of 25 ns. Therefore, one would expect some amount of charge to be lost due to ballistic deficit. The charge loss at the lowest voltages can be described by a simple model of the relative ballistic deficit (RBD) in a third order CR(RC) shaper by:

$$RBD = 0.125\frac{T^2}{\tau^2} \tag{9.4}$$

where τ is the shaper peaking time. In under-depleted operation, only the charge deposited in the active, depleted region of the detector is being collected. For a detailed discussion of charge collection times, see references [88, 89].

The relation between signal and bias voltage for irradiated modules is more complicated. The collected charge does not saturate until the maximum available bias voltage in the beam test, 500 V, is reached, and S/N passes from 4 to 8. The depletion voltage is estimated to be around 250 V for these detectors.

For modules irradiated to the reference fluence of $3 \cdot 10^{14} p/cm^2$ the combined effect of a certain charge loss and a significant increase of the noise yields signal-to-noise ratios between 8 and 11 for a bias voltage of 470 V. Various possible explanations exist for the high over-depletion needed to reach full charge collection. Measurements by the ROSE collaboration [90] indicate that there is considerable charge loss due to trapping of the charge carriers in radiation-induced lattice defects. Assuming a constant trapping probability per unit time, the effect is bias voltage dependent (through the charge collection time). For small over-depletion, the different field distribution across the Silicon in type-inverted bulk material might lead to a ballistic deficit of the shaper.

In order to quantify the uncertainties due to the spread in chips behaviour after irradiation, scans at the same voltage, but with the beam pointing to different chips were taken. Figure 9.7 shows the values for charge and S/N across the module for fully-irradiated outer module K5 308.

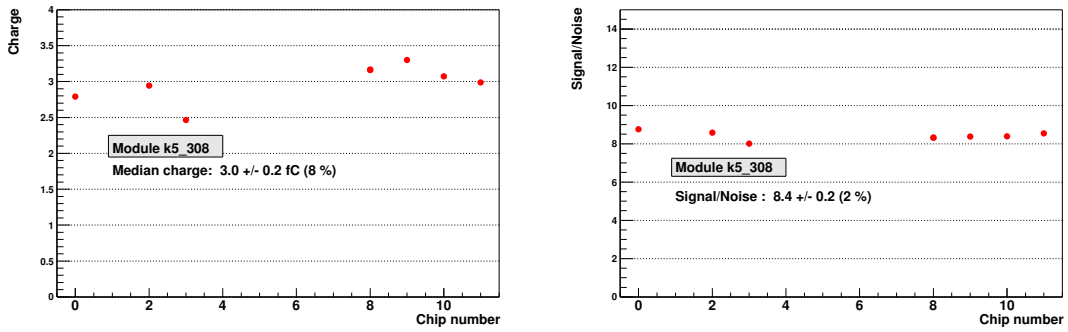

Figure 9.7: Values of the charge in fC (left) and S/N (right) for the chips of the module K5 308 measured in the test beam.

Table 9.1 shows the mean value of median charge and S/N for half-irradiated K5 310 and K5 312 outer module, and for fully-irradiated K5 308. For comparison, an unirradiated forward module (K5 303) is also included in the table. The spread in observed charges is quite large for irradiated modules, because of the error due to variations in the calibration of the chips: it is estimated to be around 0.2 fC. The variation in the S/N from different chips (standard deviation) is instead smaller than the variation of either charge or noise: this reflects the cancellation of the absolute scale of the calibration in the ratio, and the error is around 2%.

Module	*Charge (fC)*		*S/N*	
K5 308*	3.0 ± 0.2	(8%)	8.4 ± 0.2	(2%)
K5 310*	3.3 ± 0.3	(8%)	11.2 ± 0.2	(2%)
K5 312*	3.21 ± 0.08	(2%)	11.4 ± 0.3	(2%)
K5 303	3.76 ± 0.11	(2%)	13.1 ± 0.3	(2%)

Table 9.1: Mean values for charge in fC and signal to noise ratio of the irradiated outer modules (half dose and full dose) at 500 V. An unirradiated outer module is also included for comparison (V_{bias}=350 V). The standard deviation and the equivalent percentage of the error are also reported.

9.6 Pulse-shape studies

When the charge measurements are repeated for a range of sampling times, the median pulse of the shaper can be reconstructed. In the laboratory the delay between generation of the charge and sampling can be controlled explicitly using the calibration circuit. In asynchronous beam tests this control is not possible, but a method was developed (described in more detail in reference [91]) to reconstruct the pulse shape using the delay between the raw trigger and the clock. Another method can be used with synchronous beams, see [92].

The pulse shape is reconstructed with a Time to Digital Converter (TDC) information that includes the influence of the detectors. For the case of the reconstruction with the calibration circuit, the input pulse cannot be changed. Thus, the input to the shaper/amplifier electronics is very close to a delta pulse. The theoretical response of the shaper/amplifier of the ABCD chips to a delta pulse is given by:

$$a(t) = [\gamma \cdot t^2 + \beta \cdot t + \alpha] \cdot e^{-0.1 \cdot t} - \alpha e^{-0.005 \cdot t} \tag{9.5}$$

where t is time in ns, $\alpha = -5.83\ 10^{-3}$, $\beta = 5.54\ 10^{-4}$ and $\gamma = 5.26\ 10^{-4}$. The input delta pulse is assumed to come at $t = 0$, in order to describe the experimental data. Amplifier response can be parametrised as:

$$b(t) = A \cdot a\left(19.1\frac{t-d}{\tau_p}\right) \tag{9.6}$$

where A is the amplitude of the pulse, d the delay and τ_p the amplifier peaking time of the electrons.

The signal at the discriminator is the time convolution of the collected detector signal and the amplifier-shaper time response. Therefore, the increase of carriers velocity with increasing voltages makes better the delta pulse approximation shown in Equation 9.6. In the following discussion, when beam test results on peaking times are reported, it should be interpreted as an effective peaking time due to the convolution of the detector signal and the electronics response.

In asynchronous beam tests the pulse shape is reconstructed using the TDC information. The measured time range is extended to cover 75 ns (3 bunch crossings) using the hit information from the previous and next clock cycles provided by the ABCD. Dividing the time range in 1 ns slices and performing a fit with the function in Eq. 9.1 of the efficiency versus threshold (s-curves), the median charge is obtained for each of the slices. Figure 9.8 shows an example of the pulse shape for a non irradiated and an irradiated module (superimposition of the two shapes). Bias voltages used in the two cases are 150 Volts (non-irradiated) and 500 Volts (irradiated).

The first thing to notice is that the continuous line (fit ABCD function) is not an exact description of the data. For the non-irradiated modules the fit is quite good, indicating that detector effects do not distort much the pulse. But, the irradiated module shows a clear *shoulder* that can not be reproduced by the function. This effect is thought to be due to the overdrive needed by the comparator. When irradiation degrades the comparator the effect becomes more pronounced. This effect remains even for the highest bias voltage (the one used on the plot). As a result, the fitted value of the peaking time is pushed up and will tend to overestimate the difference between non-irradiated and irradiated modules.

The appearance of the shoulder in pulse shapes determined with the internal calibration circuit suggests that this effect is due to the degraded power of the discriminator. The response of the shaper itself can also be slower. These are purely electronics effects and should not depend on the bias voltage. On the other hand, the structure of the detector signal is quite different in irradiated, type-inverted sensors. This has been studied in some

detail in [91]. However, test beam results do not allow to disentangle between the various explanations.

In order to achieve a better understanding of the module performance after irradiation, studies on the electronics were realised. As already underlined, irradiation of electronics readout degrades the characteristics of electrical circuits *i.e.* preamplifier and calibration circuits. In the case of the preamplifier, increases the noise and decreases gain. On the other hand, the effect on the calibration circuit is to increase differences (spread) across chips. In Chapter 7, the effects due to change of analogue voltage V_{cc} from 3.5 Volts (nominal for the SCT modules in ATLAS) to 3.8 Volts has been shown. In the test beam, tests using the two different front-end settings were probed in the irradiated end-cap modules to see the influence for instance in the pulse shape. A comparison using different working parameters was done for an irradiated end-cap module (k5-308): the two different calibration corresponds to configurations A and B respectively. An evidence of improvement in timing performance for the configuration B with respect to A is observed. and it is visible in the pulse shape of Figure 9.9.

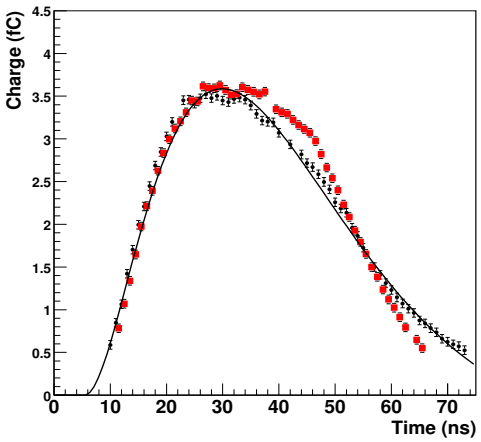

Figure 9.8: Example of the reconstructed pulse shape done with test beam data for two modules, a non-irradiated (black circles) and a irradiated one (red squares) for bias voltages 150 Volts and 500 Volts.

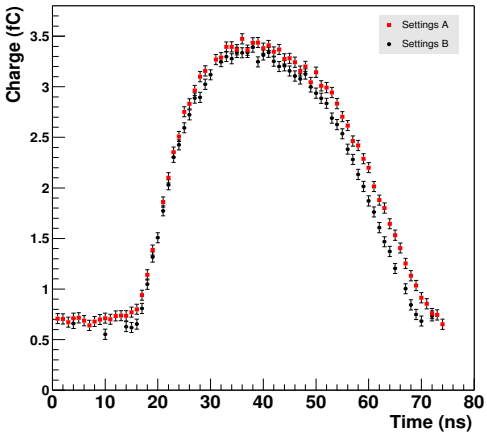

Figure 9.9: Pulse shapes for the two front-end setting configurations A *and* B, for the full-dose irradiated end-cap module K5 308: it is visible the better timing response in case of higher analogue voltage.

9.7 Spatial resolution

A fundamental issue for silicon strip detector is the spatial reconstruction capability. With a single strip, resolution in the rϕ plane) is the residual, calculated as the difference between where the track has crossed the centre of the silicon wafer (extrapolated from telescope system) and the centroid of the binary cluster. This value should be around pitch/$\sqrt{12}$

as from equation 6.7, that for a barrel module is $\sim$ 23 μm and for an endcap depends on the track position since the pitch variates along the module. In a stereo module, where u and v are the fired strips in the two planes, the real spatial point could lie anywhere in the cross-hatched region showed in figure 9.10. Combination of a hit in each plane defines a parallelogram whose axis is rotated by half of an angle α as defined in the figure. Inside this region, the probability to find the space point coordinates is given by the triangular probability function. The corresponding resolution in $R\phi$ (perpendicular to the z axis as defined in the TDR) is:

$$\sigma_{\perp} = \frac{\sigma_1}{\sqrt{2}cos\frac{\alpha}{2}}$$

where $\sqrt{2}$ is a statistical term arising from two residual measurements σ_u and σ_v here assumed to be equal and denoted by σ_1. The resolution in z is

$$\sigma_{||} = \frac{\sigma_1}{\sqrt{2}sin\frac{\alpha}{2}} = \sigma_{\perp}cot\frac{\alpha}{2}$$

For barrel modules, where the strips are parallel, α is simply the stereo angle of 40 mrad; for forward module the situation is slightly more complicated, since we should combine the angles that come from rotation of each strip with respect to the line of symmetry. In both cases it is possible to consider the approximation for small α:

$$\sigma_{\perp} = \frac{\sigma_1}{\sqrt{2}}, \quad \sigma_{||} = \frac{\sqrt{2}\sigma_1}{\alpha}$$

In a test beam, the modules are perpendicular to the beam in both z and $R\phi$, so we redefine z as the beam axis and ($\perp$,||) as (x,y). This orientation of the coordinate system presents y along the direction of $\alpha/2$ as shown in figure 9.10 (u-v layout). X and y can be calculated from the u and v coordinates as:

$$x = \frac{u+v}{\sqrt{2}cos\frac{\alpha}{2}} \qquad y = \frac{v-u}{\sqrt{2}sin\frac{\alpha}{2}}.$$

Figure 9.11 shows resolutions for both non-irradiated and irradiated modules at 1.5 fC threshold, with beam perpendicular to the modules and without magnetic field. Effects related to not perpendicular tracks and to magnetic field are discussed in section below.

The x resolution is found to be about 17 μm, while y resolution is around 800 μm, as expected from TDR specifications [54].

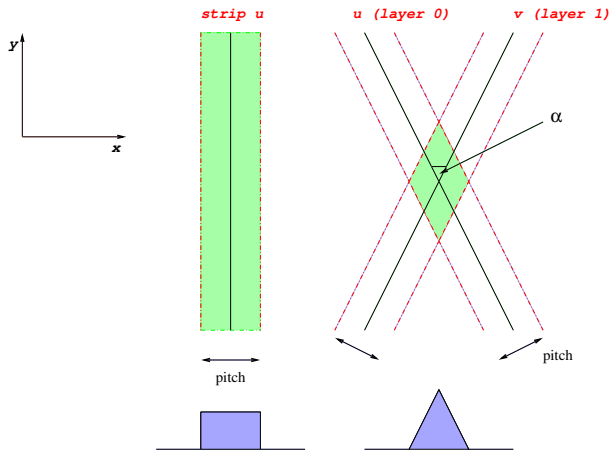

Figure 9.10: Measurements given by (*Left*) a single strip and (*Right*) a stereo layer. In this case, for each plane one strip fires (u and v) and the real space point could lie anywhere in the parallelogram given by single strip resolution (residuals).

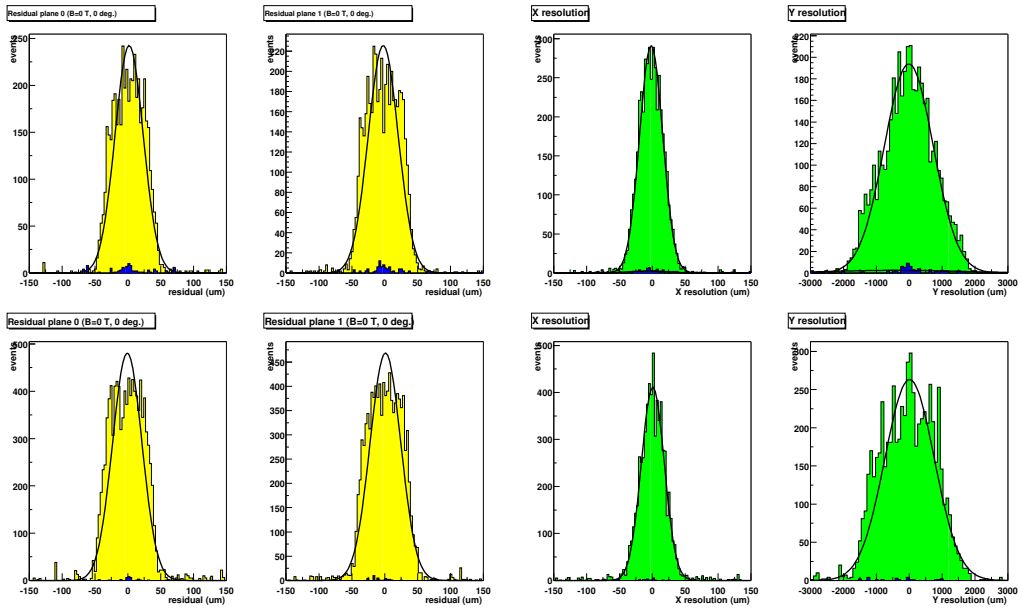

Figure 9.11: Residuals in u,v and resolution in x,y for combination of single (light fill area) and double clusters (dark fill area) on both stereo planes. On the top, example of non irradiated module, on the bottom example of irradiated module.

9.8 Inter-strip distribution

The good resolution of the analog telescope can be used to study the dependence of the efficiency on the inter-strip position of the track.

In detectors with analogue readout the charge on multiple consecutive strips is measured and the position is determined from the centroid of the cluster. The clustering procedure yields a quasi-continuous position measurement.

In the binary readout scheme signal is stored in one strip only if charge collected is above the readout threshold. In this way charge below threshold is lost with the corresponding loss of signal. Thus, binary readout pitch has been chosen for having most of the charge reaching only one strip. The position measurement that comes out is discrete. This could lead to non uniformities in the response depending on the position of the track with respect to the two closest strips, particularly in the inter-strip region.

Figure 9.12 shows the efficiency as a function of the reconstructed track position between two strips as fraction of the pitch for different values of threshold. Each step in the distribution is about 6 μm as set by the telescope track resolution: interstrip position 0.5 corresponds to a track crossing the silicon layer at equal distances from the 2 neighbour strips.

If there is no charge sharing, all the charge carriers locally generated around the incident particle trajectory are collected on a single strip and, with binary readout, the Signal-to-Threshold is maximised in this condition. When the track crosses the detector between two strips, the released charge could be partially deposited on neighbouring strips (usually not more than 2 strips per cluster with perpendicular beam). There is observed an inefficiency around the middle inter-strip position where the charge sharing is greatest, decreasing the effective pulse height measured by the two single strips. This effect of charge sharing plays a role above 1.5 fC for intermediate values of threshold but not below, thus the loss in efficiency for operating threshold of 1 fC is negligeble.

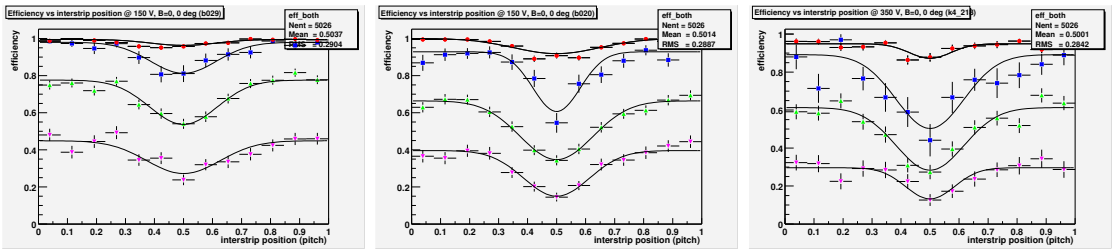

Figure 9.12: B field OFF, perpendicular beam: Efficiency *vs* inter-strip position at four different thresholds (1.5, 2, 2.5 and 3 fC). *Left*: non-irradiated barrel module; *center*: irradiated barrel module; *right*: irradiated forward module.

9.9 Incident angle and magnetic field effects

In the ATLAS detector the SCT modules will be subject to a 2 Tesla magnetic field. Also, tracks are in general not perpendicularly incident on the detector plane. Therefore, an

important subject of study in beam tests is the influence of magnetic field and of a non-perpendicular incidence angle on the performance of the modules. Effects related to a strong magnetic field are due to the Lorentz force that deviates the drifting carriers. Figure 9.13 shows how the Lorentz force is equivalent to a rotation by a small angle $\Theta_L = \mu^H B = r_H \mu B$, where μ^H is the Hall mobility, the conduction mobility μ multiplied by the Hall scattering factor r_H, and B is the magnetic field perpendicular to the incident particles.

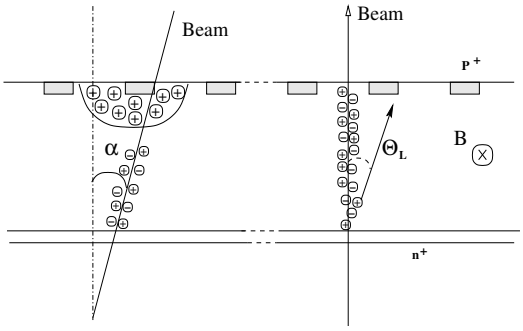

Figure 9.13: Representation of the effect of the incidence angle and the application of a magnetic field.

When a beam particle hits the detector with a non-perpendicular incident angle α, the charge sharing increases. A measure of the amount of charge sharing is the distribution of cluster size also as function of position between two strips (fraction of pitch) where a track hits the detector: the average number of strips involved increases in the central inter-strip position.

If a magnetic field is applied, the deviation of the track with respect to the perpendicular plane induces an increase in the cluster size. Figure 9.14 shows a comparison of cluster size for irradiated and non-irradiated modules at different angles and with/without magnetic field: the increase in charge sharing is clearly visible.

Hence, the cluster size dependence on angle in the magnetic field is used to determine the Lorentz angle. Figure 9.15 shows cluster size *vs* incident angle for unirradiated (left) and irradiated (right) modules, with and without magnetic field. The Lorentz angle Θ_L is determined as the difference in the minimum of the fit between magnetic field ON and OFF. The error of the Lorentz angle is taken to be the standard deviation of all the measurements for a set of modules. With this method Θ_L is obtained for both groups: non-irradiated and irradiated modules.

$$\Theta_L(150 Volts) = 3.3^\circ \pm 0.3^\circ \tag{9.7}$$

$$\Theta_L(350 Volts) = 2.1^\circ \pm 0.4^\circ \tag{9.8}$$

As the irradiated modules are biased at a higher voltage, the observed difference could be due to an electric field dependence of the Lorentz angle or a change in the properties of the charge carriers due to irradiation. In the literature, the effect of proton irradiation on the mobility and thus Lorentz angle of holes is found to be compatible with no effect [93, 94]

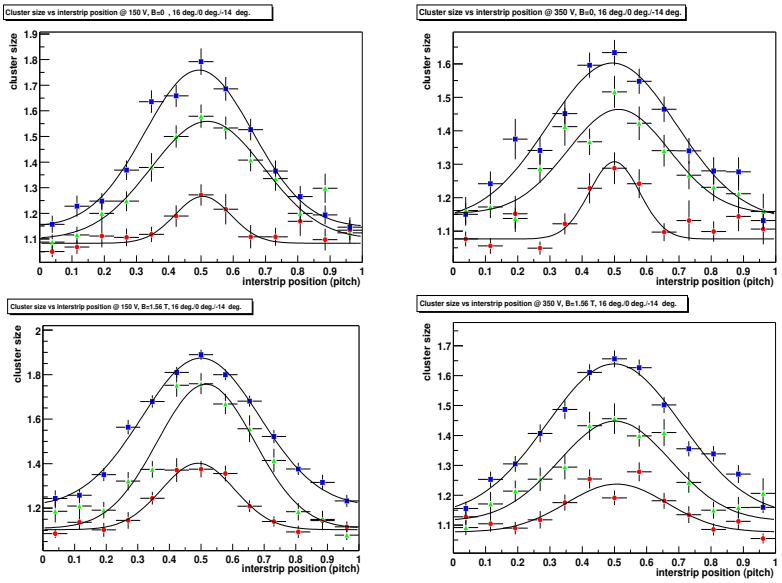

Figure 9.14: Cluster size *vs* inter-strip position for different incident angle of the beam, without (top) and with magnetic field B=1.56 T (bottom): red circles are perpendicular beam, blue squares 16 degree angle, green triangles -14 degree angle. Non irradiated (on the left) and irradiated modules (on the right) are presented.

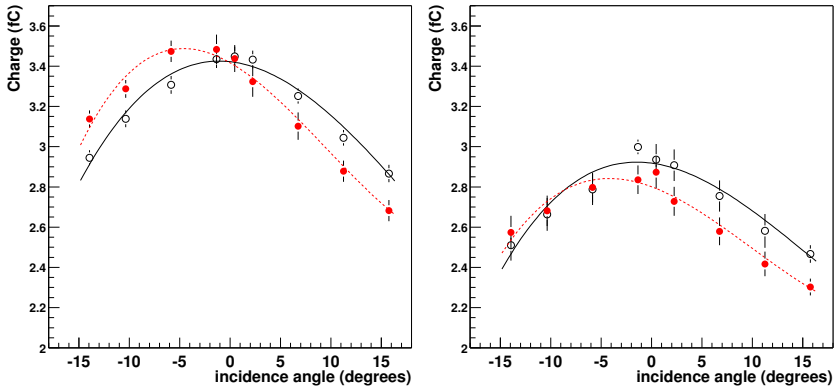

Figure 9.15: Median charge versus angle for non-irradiated (left) and irradiated (right) modules. Filled marker are measurements in a 1.56 T magnetic field, open markers without field

or very small, of the order of 2%. The difference in voltage, that is electric field inside the detector, has the effect of changing the Θ_L through the electric field dependence of the carrier mobility μ. Theoretical models applied to beam test conditions (silicon temperature $T = 261$ K, thickness $d = 285$ μm and magnetic field $B = 1.56$ T), predict values[95, 96] of $\Theta_L(150\text{V}) = 3.3°$ and $\Theta_L(350\text{V}) = 2.4°$ in agreement within errors with our measurement.

Having established the Lorentz angles for irradiated and non-irradiated modules, the combined effect of magnetic field and non-perpendicular incidence on the module performance was studied in more detail.

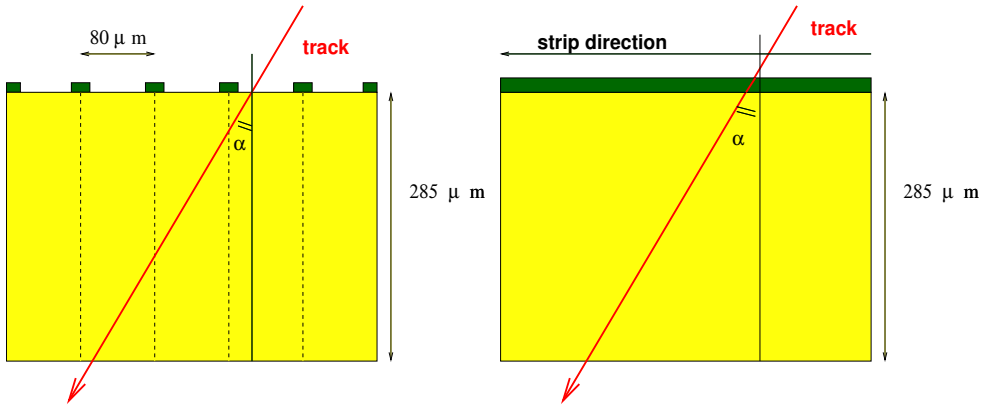

Figure 9.16: On the left, case ***(a)***: the incidence angle α of the beam on the detector is equivalent to a rotation of the module onto the axis parallel to the strip direction, fixing the track direction. On the right, case ***(b)***: in a similar way, that is equivalent to a rotation of the module onto the axis parallel to the strip direction, respect to the track direction.

Figure 9.16 shows the two possible cases that have been distinguished to evaluate effect of non-perpendicular tracks: in respect to a fixed beam direction, the first scenario *(a)* is equivalent to a rotation of the module onto the axis parallel to the strip direction; the second one *(b)* is equivalent to a rotation around an axis in the detector plane, but perpendicular to the readout strip. In the real experiment, case *(a)* will occur as an effect of the track curvature in the solenoidal magnetic field; moreover, the end-caps geometry of ATLAS will lead to incidence angles up to 34 degrees on the outer ring of the first disk, as in case *(b)*.

In both conditions, the path length through the silicon detector is longer than with perpendicular tracks and, in first approximation, the deposited charge increases linearly by a factor $1/\cos\alpha$. On the other hand, with a binary readout system, when a track crosses two or more strips, the released charge could be deposited in neighbouring strips: already with perpendicular beam, a lack in efficiency in the middle inter-strip position of the track is measurable. The effect of charge sharing increases with non-perpendicular tracks, resulting as a significant loss of median charge that has been measured in 2001 test beam, where incidence angle between 0 and 15 ^{o} have been used and the results, as reported in detail in [86], have showed a maximal decrease in terms of collected charge of about 0.6 fC.
The narrow range of incidence angle (due to mechanical limits in the geometry of the main box where the modules are usually arranged) has been extended in the August 2002 test beam (see also [97]), using an additional box in which few prototypes could be arranged in different positions. In particular two modules are considered in the following analysis, placed with the two explained orientations, using an incidence angle α of about 35: module KB-105 has been arranged as for case *(a)*, module B053 as for case *(b)*.

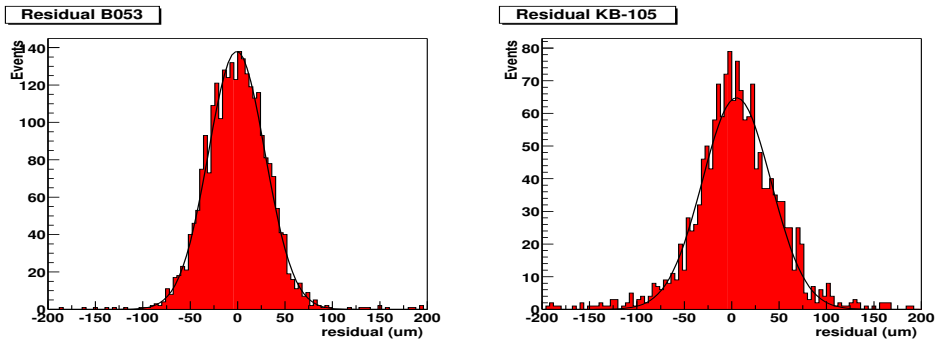

Figure 9.17: Residuals measured @ 1 fC: due to the long distance between the modules and the telescope system, the reconstructed tracks compared to the hit position of the modules have a poor resolution and the obtained residuals are wide. On the left, B053 and on the right KB-105, both @ 1fC threshold and with nominal bias 150 V.

Figure 9.17 shows the residual distributions as measured for B053 (on the left) and KB-105 (on the right): in both case the residuals, calculated as the difference between where the track has crossed the centre of the silicon wafer and the centroid of the binary cluster, are wider than for the prototypes arranged in the main box. The track position is extrapolated by the telescope system, in this case placed far from the two under study modules, so that the effect of analog telescope modules resolution is not negligible anymore. In particular, while charge sharing between neighbouring strips should have a slight beneficial effect on the spatial resolution in case *(a)*, KB-105, placed even further, presents a resolution of about 38μm (resulting from a gaussian fit), worse than B053 ($\sigma \simeq$30 μm). On the other hand, the measurement of efficiency and median charge are only slightly affected by the poor resolution, since it implies a lower number of good tracks, so a lower statistic.

Table 9.2 shows a comparison between median charge measured at 150 V and 350 V of bias voltage, with perpendicular beam and with track having incidence angle 35^o. Residuals and average cluster size are also reported.

Module	*Qmed @ 0^o Bias=150V*	*Qmed @ 35^o Bias=150V*	*Qmed @ 0^o Bias=350V*	*Qmed @ 35^o Bias=350V*	*Res.*	*Clus. @1fC*
B053	3.29	4.02	3.45	4.34	29.8	1.2
KB-105	3.30	1.65	3.40	2.05	37.5	1.42

Table 9.2: Median charge for perpendicular tracks and for incidence angle α of 35^o at 150 V and 350 V. Residuals and cluster size @ 1 fC are also reported: no difference is notable between the two different bias voltage.

- **case *a***: the median charge of module KB-105 (s-curves at 150 V and 350 V reported in figure 9.18), is much lower than what it has been measured with perpendicular track. The effect of charge sharing is significantly high and it translates in a lack of

efficiency and consequently of collected charge, that could be compared with what had been measured in previous test beams with incidence angle α between -14^o and +16^o. Circle points of figure 9.19 show the correlation between median charge and incidence angle α for barrel module B018 as measured in 2001 test beam: adding the KB-105 measurement (last point, squared),and extrapolating the curve, Q is low as expected; an uncertainty of about 10% has to be considered on the KB-105 median charge value because of the low statistic. No normalization has been applied, since the median charge with perpendicular beam is the same ($Qmed$=3.3 fC) for both barrel and KB module.

- **case *b***: as mentioned above, the end-caps geometry of ATLAS will lead to incidence angles up to 34 degrees on the outer ring of the first disk. The median charge of module B053 is as high as expected, with an increase by a factor 1/cosα respect to the perpendicular charge Q(α=0). Figure 9.20 shows the correlation between median charge and incidence angle for another module (B029) as measured in 2001 test beam in addition to the point refereed to B053, fitted with function 1/cosα. The median charge is normalized to the value found in perpendicular scan, 3.19 fC for B029 and 3.29 fC for B053 respectively.
  Moreover, the measured median charge with a bias voltage of 350 V is 4.34±0.15 fC, to be compared to the expected one 4.20±0.18 fC, where the uncertainty is dominated by the error of ±3^o on the incidence angle.

Effects of incident angle and magnetic field can be observed also in the correlation between efficiency *vs* inter-strip position: the dip in the central interstrip region becomes significant in a wide zone, as shown in distributions of figures 9.21 and 9.22.

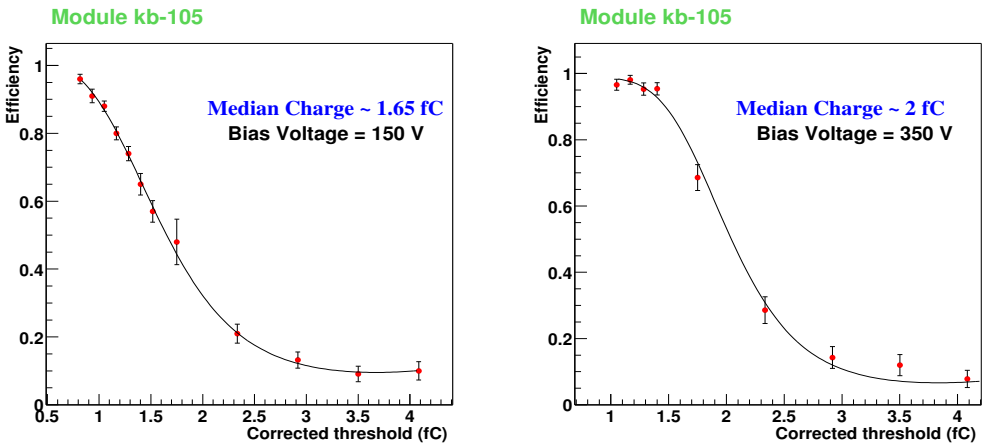

Figure 9.18: Efficiency s-curve for unirradiated module kb-105, placed with an incidence angle of α=(35^o±3^o) equivalent to a rotation of the module onto the axis perpendicular to the strip direction respect to the beam direction. The left plot refers to 150 V nominal bias, the right one reports s-curve with module biased at 350V.

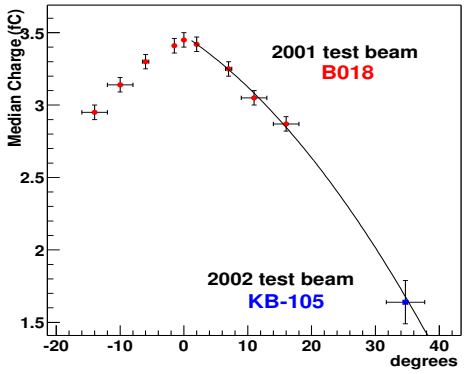

Figure 9.19: Correlation between median charge and incidence angle of the beam: the red circle refers to module B018 as measured in 2001 test beam, the blue squared correspond to KB-105 resulting from the high angle scan performed in 2002. The parabolic fit shows that the median charge is low as expected.

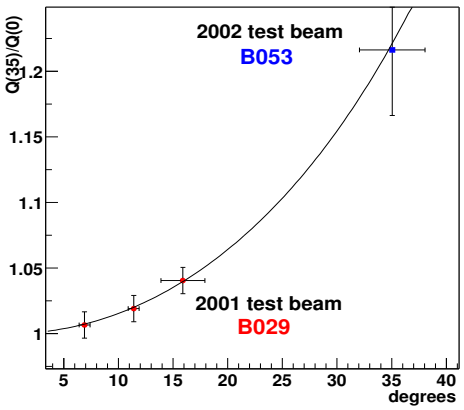

Figure 9.20: $Q(\alpha{=}35^o)/Q(\alpha{=}0^o)$ versus incidence angle: the latest point at 35^o results from the 2002 test beam, while the other measurements refer to barrel module B029 measured in 2001. The plot is fitted with the function $1/\cos\alpha$ as expected from theory.

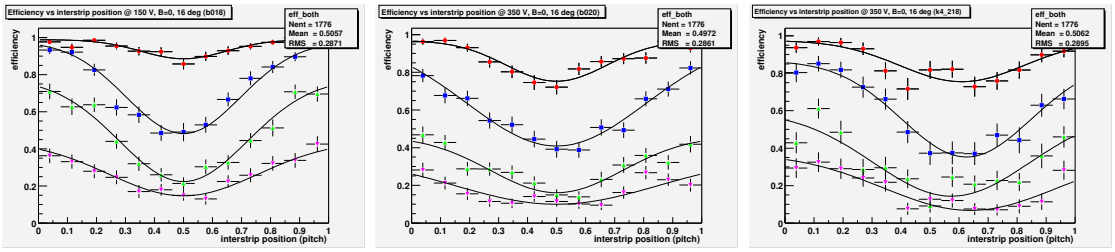

Figure 9.21: B field OFF, beam with incident angle of 16°: Efficiency *vs* inter-strip position at four different thresholds (1.5, 2, 2.5 and 3 fC). *Left*: non-irradiated barrel module; *center*: irradiated barrel module; *right*: irradiated forward module.

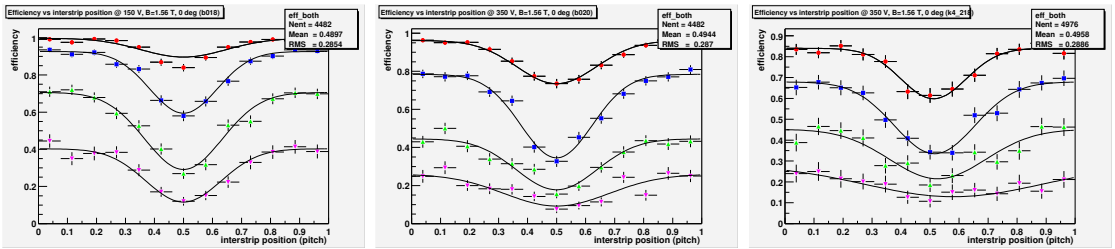

Figure 9.22: B field ON, perpendicular beam: Efficiency *vs* inter-strip position at four different thresholds (1.5, 2, 2.5 and 3 fC). *Left*: non-irradiated barrel module; *center*: irradiated barrel module; *right*: irradiated forward module.

9.10 The KB module

A first prototype (b048), after electrical tests and standard characterization, was included in the October 2001 testbeam: this module was built with a total strip length $\approx$ 8 mm longer than for the baseline outer endcap module. In 2002 a series of 4 modules was tested: figure 9.23 on the left shows typical s-curves for KB modules: for all prototypes tested, the efficiency value at 1 fC threshold is over 99% while median charge range is from 3.3 to 3.5 fC.

Efficiency and noise occupancy with SCT specification as reference, for one of the KB prototypes, is shown on the right of figure 9.23 and table 9.3 summarizes general results overall the modules. During the test beam, two of them have been affected by an excess of occupancy due to the noise – almost one order of magnitude compared to laboratory performances. A dedicate offline analysis identified this extra noise source as a non-gaussian common mode noise. Further investigations have been performed, showing that a careful grounding connection of the hybrid avoid excess in sensitivity to noise pick up.

Module	*Eff@1fC*	*NO@1fC* $\times 10^{-4}$	*Qmed (fC)*	*S/N*	*Plane res.*	*Clussize @1fC*
kb-100	99.7	0.7	3.4	14.2	22.5	1.08
kb-102	99.8	1.2	3.3	13.6	23.0	1.05
kb-103	99.3	1.1	3.3	13.9	22.8	1.1
kb-104	99.7	0.8	3.4	14.1	23.7	1.07

Table 9.3: Front-end parameters as measured for unirradiated *kb end-cap modules* .

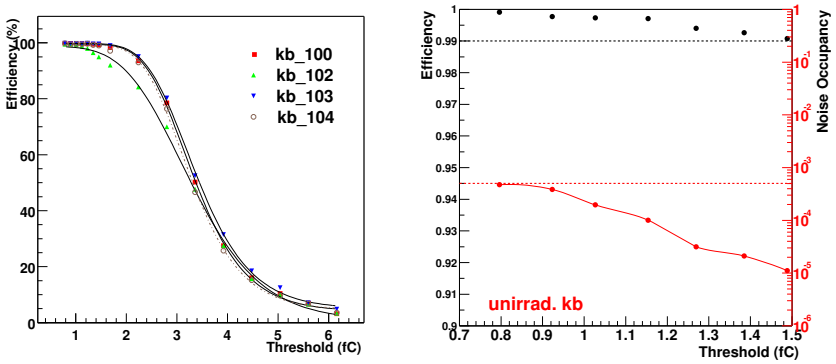

Figure 9.23: efficiency for 4 KBs and noise occupancy and zoom efficiency

Few bias scans has been performed during summer test beams, over a voltage range between 100 V and 350 V: an example is shown in figure 9.24, where efficiency at 1 fC (left) and median charge (right) at different bias values are reported. It is visible an initial loss of charge at 100 V (below the nominal value) due to ballistic effect, and a plateau from 150 V up to 350 V.

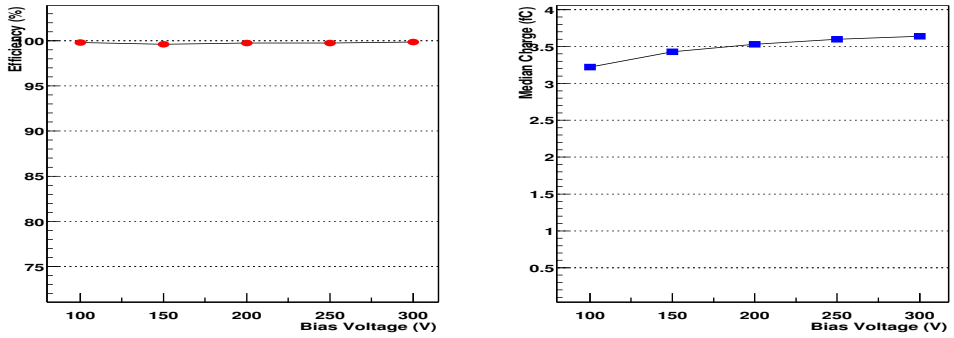

Figure 9.24: Efficiency at 1 fC (a) and median charge (b) for a bias scan performed on one of the unirradiated KB modules.

Figure 9.25 on the left shows the efficiency as a function of the reconstructed track position with respect to two neighbour strips: each step in the profile is about 6 μm, as in previous plots. A lack in efficiency is observed around the middle inter-strip position, where the charge sharing is maximized and the effective pulse height is decreased: the superimposed curves referred to different thresholds, showing how the effect is visible for threshold above 1.5 fC, well far from the operating value of 1 fC. The average cluster size as a function of the track position between two strips is also a measurement of the amount of charge sharing (see 9.25 on the right). The spatial resolution for a single plane is shown in

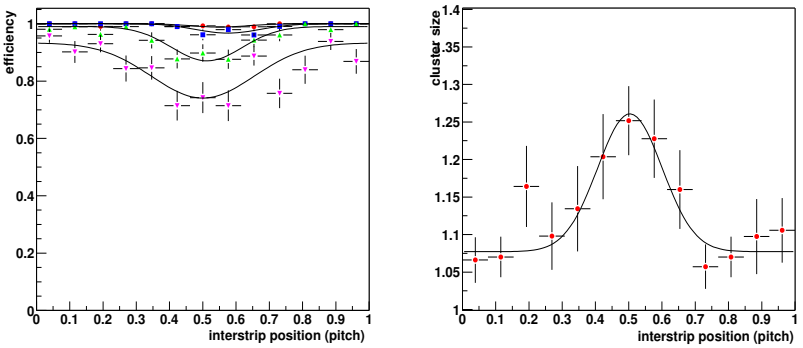

Figure 9.25: On the right, cluster size distribution vs interstrip position; on the left Eff Vs interstrip position.

figure 9.26: on the top, an example of residuals for two planes of an unirradiated KB, where the resolution is given by the rms of the gaussian fit. The expected value for a 1 strip cluster size event, given by pitch/$\sqrt{12}$, is quite close to the obtained value (23μm). Operating on single plane residuals, the real spatial resolution in XY is showed on the bottom of figure 9.26: we find $\sigma_x \simeq 17\mu$m, $\sigma_y \simeq 750\mu$m.

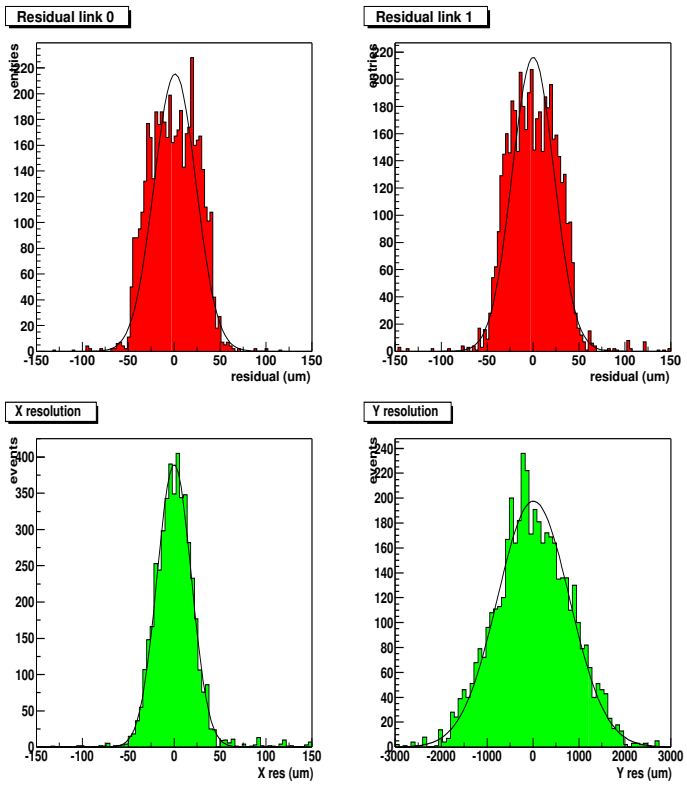

Figure 9.26: Residuals (plane 0 and 1, on the left) and Spatial resolution (X and Y, on the right) for one of the KB modules.

9.11 Tracking with SCT modules

Due to the high multiplicity of charged tracks, the ATLAS inner detector is a challenging environment for pattern recognition and tracking algorithms. During high luminosity operation the occupancy of real tracks, from the trigger event plus a number of pile up events (underlying minimum bias events), is expected to be as high as 0.6 % in certain regions of the SCT.

Detailed simulations have been performed and were reported in the inner detector Technical Design Report [54]. The pattern recognition is expected to be quite robust as long as the noise occupancy is maintained below a tolerable level. Radiation damage of the detector during operation is expected to lead to a noise increase and a deterioration of the collected charge. To maintain a tolerable noise occupancy, the discriminator threshold may have to be increased above the nominal 1.0 fC.

In the 2002 beam test the set of modules irradiated to the higher dose (3×10^{14} protons/cm^2) were read out simultaneously. These data provide an opportunity to check the tracking performance on a irradiated system, when the charge collection and noise performance have been deteriorated due to radiation damage.

The event selection criteria are the same as discussed in section 9.3.2. Tracks were reconstructed with 4 irradiated modules, positioned as in the SCT barrel system for $\eta \sim 0$.

The telescope was used in the analysis only for comparison with the test system. For the analysis only events with one point in each of the X-Y telescope planes and perfectly reconstructed were taken. In this way tracks with multiple scattering and events with two tracks were rejected. Figure 9.27, on the left, shows a perfect event, with only one track reconstructed by the analogue telescope and by the modules array. Right part of the figure shows a typical rejected event with two particles crossing the volume where the second particle has been generated by a hard interaction.

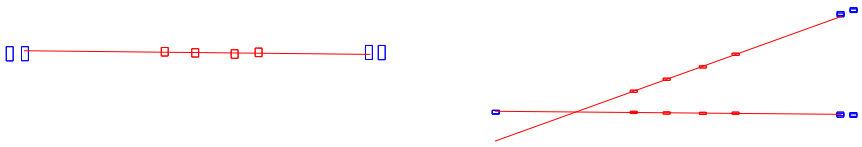

Figure 9.27: Example of a perfectly normal event (left) and an event where a second track is due to a hard interaction in the tracking volume (right), both views are in the XZ plane.

Tracks were fit to the hits in the irradiated modules. The goodness of fit of the track candidate is checked with respect to the telescope tracks:

$$d_{track} = \sum \frac{|a_i^{tel} - a_i^{bin}|}{\sigma_i} \tag{9.9}$$

where the a_i are the track parameters and the σ_i their errors. A track is considered *good* if its distance to the telescope track d_{track} is smaller than 20 sigma. The remaining tracks are labelled as fakes. Figure 9.28 shows the tracking efficiency and fake rate versus threshold (left) and versus bias voltage applied to sensors (right) for a four modules array. The reconstruction efficiency is greater than 97 % for a bias voltage over 450 Volts and 1.2 fC threshold. The efficiency for the array is as expected for single irradiated modules with around 99% efficiency. The fake rate is compatible with zero within the measurement error of 10^{-4} and is independent of the bias voltage.

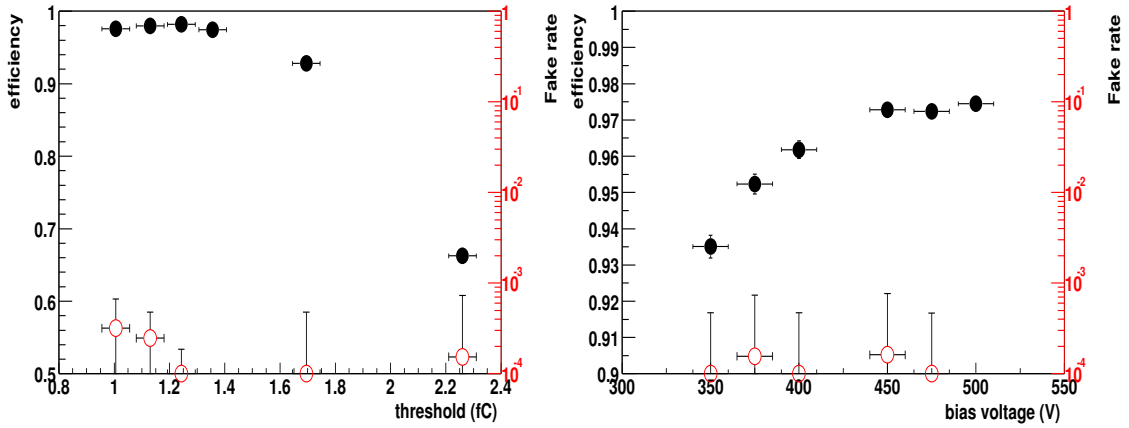

Figure 9.28: Tracking efficiency and fake rate versus threshold (left – bias at 500 V) and bias voltage (right) for a four modules tracking array.

The same analysis has been done using a three modules array. This makes the fake rate slightly more sensitive to the noise occupancy of the individual modules. Whenever the occupancy is around the ATLAS specification (5×10^{-4}), the fake rate is below 10^{-3}. For more details see for instance [99].

9.12 Summary

Beam tests played an important role during the development of the SCT modules. The current module design was found to meet the efficiency and noise occupancy specifications, but not after a full irradiation. The envisaged operating detector bias voltage and discrimination threshold are found to satisfy the requirements for non-irradiated modules. For the reference detector bias voltage of 150 V, the charge collection efficiency is over 95 %. The bias voltage is to be (gradually) increased during the lifetime of the experiment to ensure a good charge collection efficiency. The median signal-to-noise ratio of modules with 12 cm

detectors and unirradiated is ~ 13. Modules irradiated to $3 \times 10^{14} p/cm^2$ collect about 90 % or less of the deposited charge when biased to 350 V. The noise increases significantly as a result of the irradiation. The median signal-to-noise ratio decreases to values in the range 7-11. The reduced signal-to-noise ratio leaves a rather narrow operating range where the efficiency (> 99 %) and noise occupancy ($< 5 \cdot 10^{-4}$), only raising the threshold to 1.2 fC.

The knowledge obtained in beam tests allowed to improve the Monte Carlo simulation of the detector. Part of the beam test results have been incorporated into the *digitisation* step of the SCT module in the GEANT4 simulation of the the ATLAS detector [100]. A realistic description of the bias voltage and incidence angle dependence of the response is implemented for non-irradiated modules. The model is currently being updated using more recent beam test data [101]. The effect of irradiation on the performance is to be implemented as well. The deviation of the drifting carriers due to the Lorentz effect leads to a shift of the apparent position by several μm. A good description of the bias voltage dependence of the Lorentz angle allows for a precise correction of this effect. The measured spatial resolution is also in agreement with the pitch/$\sqrt{12}$ expectation for single strip clusters. Repeated test beams of ATLAS-SCT modules have yielded a wealth of information on the performance of a binary-readout scheme for silicon micro-strip detectors.

Bibliography

[1] C. Quigg, Gauge Theories of the Strong, Weak, and Electromagnetic Interactions, Benjamin-Cummings, Reading, M.A. (1983).

[2] E. S. Abers, B. W. Lee, Gauge Theories, Physics Reports **9C** 1, (1973).

[3] S.L. Glashow Nucl. Phys. 22(1961) 579.

[4] P.W. Higgs Phys. Lett. 12 (1964) 132.

[5] M. Gell-Mann, Phys. Lett. 8(1964) 214.

[6] CERN preprints, CERN-TH 401 and 412 (1964).

[7] D.J. Gross and F. Wilczek, Phys. Rev. D8, 3633 (1973),

[8] W.A. Bardeen *et al.*, Phys.Rev.D18 (1978)3998.

[9] B. Andersson, G. Gustafson and C. Peterson, A semiclassical model for quark jet fragmentation, European Physical Journal C, Vol. 1, Numb. 1-2, pp. 105-116.

[10] See for instance: B. Andersson, P. Andersson, The Lund Model, book published by Cambridge University Press (1998).

[11] J.C. Collins, D.E. Soper, and G. Sterman, Heavy Particle Production in High Energy Hadron Collisions, Nucl. Phys. **B263** (1986) 37.

[12] P. Nason, S. Dawson, R.K. Ellis, The one particle inclusive differential cross section for heavy quark production in hadronic collisions, Fermilab PUB/89/91-T

[13] S. Frixione, M. Mangano, Heavy-Quark Jets in Hadronic Collisions, hep-ph/9605270

[14] M.Mangano and S. Frixione, Private communication.

[15] G. C. Blazey *et al.*, Run II Jet Physics, CDF/PUB/JET/PUBLIC/5293 (1999)

[16] H.D. Politzer, Nucl. Phys. B194 (1984) 493.

[17] J. Chỳla, Renormalization and factorization scale analysis of $b\bar{b}$ production in $p\bar{p}$ collisions, JHEP03 (2003) 042.

[18] J. Pumplin *et al.*, New Generation of Parton Distribution with Uncertainties from Global QCD Analysis, hep-ph/0201195.

[19] See for instance: W. J. Stirling *et al.* MRST Parton Distributions, AIP Conference Proceedings
– February 10, 2005 – Volume 747, Issue 1, pp. 16-21.

[20] S.I. Alekhin, Extraction of parton distributions and α_s from DIS data within a Bayesian treatment of systematic errors, European Physical Journal C, Vol. 10, Numb. 3, pp. 395-403.

[21] C. Albajar, *et al.* Phys. Rev. Lett. B256, 121 (1991).

[22] F.Abe *et al.* Phys. Rev. Lett. 71, 500 (1993).

[23] F.Abe *et al.* Phys. Rev. Lett. 71, 2396 (1993).

[24] F.Abe *et al.* Phys. Rev. Lett. 75, 1451 (1995).

[25] B.Abbott *et al.*, Phys. Rev. Lett. B487, 264 (2000).

[26] The CDF Collaboration, hep-ex/0412071, Published in Phys.Rev.D71:032001 (2005).

[27] M.Cacciari, P. Nason, Phys. Lett. **89**, 122003-1 (2002).

[28] CDF II Coll., FERMILAB-PUB-96/390-E (1996).

[29] A. Bardi *et. al.*, SVT: An online silicon vertex tracker for the CDF upgrade, Nucl. Instrum. Meth. A490 (1998) 658.

[30] Chris Hays *et al.*, The COT Pattern Recognition Algorithm and Offline Code, CDF/DOC/TRACKING/CDFR/6992 (2004)

[31] G.C. Blazey, *et al.*, RunII Jet Physics: Proceedings of the RunI I QCD and Wark Boson Physics Workshop, hep-ex/0005012; P. Aurenche, et al., The QCD and Standard Model Working Group: Summary Report from Les Houches, hep-ph/0005114

[32] R.Brun *et. al.*, Tech. Rep. CERN-DD/EE/84-1, 1987.

[33] G. Grindhammer *et al.*, Nucl. Instrum. Meth. A 290 (1990) 469.

[34] T. Sjostrand *et al.*, Comp. Phys. Comm. 135 (2001) 238.

[35] G. Corcella *et al.*, JHEP 0101 (2001) 010.

[36] H.L. Lai *et al.*, European Physical Journal C12 (2000), pp. 375-392, hep-ph/9903282.

[37] B. Cooper, M. D'Onofrio, G. Flanagan, Multiple interaction corrections, CDF/PHYS/JET/CDFR/7365(2005)

[38] S. D'Auria *et al.*, CDF/DOC/MONTECARLO/CDFR/7055 October 2004.

[39] P. Lujan, H. Bachacou, J. Nielsen, W. Yao, T. Wright, Efficiency of SecVtxB-Tag Used for 2005 Winter Conferences, CDF/DOC/SEC_VTX/CDFR/7343 (2005)

[40] P. Lujan, H. Bachacou, J. Nielsen, W. Yao, T. Wright, Efficiency of SecVtx B-Tag Used for 2005 Winter Conferences, CDF/DOC/SEC_VTX/CDFR/7343 (2005)

[41] T. Wright, SecVtx B-Tag Efficiency using Muon Transverse Momentum, CDF/DOC/SEC_VTX/CDFR/7448 (2005)

[42] A. Holloway *et al.*, SecVtx Tagging Scale Factor for 5.3.3 Analyses, CDF/PHYS/SEC_VTX/CDFR/7445 (2005)

[43] ROOT, An Object-Oriented Data Analysis Framework, Users Guide 3.02c (2005)

[44] R. Barlow and C. Beeston, Fitting using finite Monte Carlo samples

[45] H. Bachacou *et al.*, SECVTX Tag Composition and Heavy Flavor Fraction Studies in QCD Jets, CDF/PHYS/SEC_VTX/CDFR/6739 (2004)

[46] Jaco Koninsberg, Private Communication.

[47] A. Bhatti *et al.*, Determination of the Jet Energy Scale at the Collider Detector at Fermilab, CDF/PUB/JET/PUBLIC/7543 (2005) NIM Paper in preparation.

[48] A.Mehta, Jet Resolution Studies of the H1 Method to Combine Tracks and Calorimeter Towers, CDF/PHYS/JET/GROUP/7468 (2005)

[49] A. Bhatti *et al.*, First Measurement of the Inclusive Jet Cross Section Using the MidPoint Algorithm, CDF/ANAL/JET/CDFR/7206 (2005)

[50] R. Lefevre,M. Martinez,O. Norniella, Measurement of the Inclusive Jet Cross Section using the K_T algorithm in $p\bar{p}$ collisions at $\sqrt{s}$=1.96 TeV, CDFNote 7576 To be published in Phys. Rev. Lett. (2005)

[51] P.M. Stevenson, Phys. Rev. D23, 2961 (1981).

[52] The D0 collaboration, Cross section for b-Jet production in $p\bar{p}$ collisions at $\sqrt{s}$=1.8 TeV, Phys.Rev.Letters Vol. 85, Numb. 24 (11, December 2000)

[53] The ATLAS collaboration. Technical proposal for a general-purpose pp experiment at the LHC at CERN. Technical report, CERN, LHCC 94-43.

[54] The ATLAS Collaboration. ATLAS Inner detector technical design report. Technical report, CERN, LHCC 99-14/15, 1999.

[55] The ATLAS Collaboration. ATLAS Calorimeter performance technical design report. Technical report, CERN, 1996.

[56] The ATLAS Collaboration. ATLAS Muon spectrometer technical design report. Technical report, CERN, 1997.

[57] The ATLAS Collaboration. ATLAS HLT, DAQ and DCS technical design report. Technical report, CERN, 2003.

[58] J. Galagh and S. Snow, How to survey an SCT module, SCT internal communication

[59] T. Kondo et al., Construction and performance of the ATLAS silicon micro-strip barrel modules. Nucl. Instrum. Meth. A485 (2002) 27-42.

[60] D. Robinson et al., Silicon micro-strip detectors for the ATLAS SCT. Nucl. Instrum. Meth. A485 (2002) 84-88.

[61] W. Dabrowski et al., Design and performance of the ABCD chip for the binary readout of silicon strip detectors in the ATLAS semiconductor tracker. IEEE Trans. Nucl. Sci. 47 (2000) 1843-1850.

[62] W. Dabrowski *et al.*, Design and performance of the ABCD chip for the binary readout of silicon strip detectors in the ATLAS Semiconductor Tracker, IEEE Trans. Nucl. Sc., Vol. 47, No 6, Dec. 2000.

[63] W. Dabrowski *et al.*, The ABCD binary readout chip for silicon strip detectors in the ATLAS Silicon tracker, Third Workshop on Electronics for LHC Experiments, CERN/LHCC/98-36, p.175-179.

[64] W. Dabrowski *et al.*, Progress in the Development of the Read-out Chip for the ATLAS Semiconductor Tracker, Proceedings of the Sixth Workshop on Electronics for LHC Experiments (LED2000), Krakow, Sept. 2002

[65] C. Lacasta *et al.*, Electrical Specifications and Expected Performances of the End-cap Module, *ATL-IS-EN-009*, 2002.

[66] M.Mangin-Brinet *et al.* Electrical test results from ATLAS-SCT end cap modules ATL-COM-INDET-2003-008.

[67] M. Donegá et al., Thermal performance measurements on ATLAS-SCT forward modules

[68] P. J. Dervan *et al.*, Irradiation of ATLAS SCT Modules and Detectors in 2002. ATLAS Internal Note, ATL-INDET-2003-001.

[69] M.J. Goodrick and M.C. Morrissey The MuSTARD Module Cavendish Laboratory Preprint, Cavendish-HEP 04/21 (2004)

[70] M. Goodrick and M. Morrissey The SLOG slow command generator
http://hepwww.rl.ac.uk/atlas-sct/mm/slog/

[71] J.M. Butterworth, D.A. Hayes, J.B. Lane, M. Postranecky Timing, Trigger and Control Interface Module for ATLAS SCT Read Out Electronics,
ATLAS Internal Note, ATL-INDET-99-018.

[72] J. Bohm *et al.*, SCT LV3
Institute of Physics, Academy of Science, The Czech Republic
http://www-hep2.fzu.cz/Atlas/WorkingGroups/Projects/MSGC.html

[73] E. Gornicki *et al.*, SCT HV Model HV203 User Manual, Institute of Nuclear Physics (IFJ), Cracow, Poland
http://chall.ifj.edu.pl/ atlas/SCTHV/SCTHV_PAJ.html

[74] P.W.Phillips, L.Eklund, Electrical Tests of SCT Hybrids and Modules.

[75] P.W.Phillips *et al.*, The temperature Dependence of the Electrical Performace of ABCD2T read out chips in Prototype ATLAS SCT Barrel Modules.

[76] W.Dabrowski *et al.* Radiation Hardness of the ABCD Chip for the Binary readout of silicon strip detectors in the Atlas semiconductor tracker.

[77] Measurements of DAQ calibration factor – Valencia group, private communication

[78] A. Barr *et al.*, Beamtest results of ATLAS SCT Modules in 2002, ATL-INDET-2004-006;

[79] A. Chilingarov, Time Dependence of interstrip capacitance, SCT week, June 2002.

[80] M. Donegá *et al.*, Thermal performance measurements on ATLAS-SCT KB forward modules, ATL-COM-INDET-2003-007.

[81] M. D'Onofrio *et al.* Electrical performance of ATLAS-SCT KB end-cap modules ATL-INDET-2003-007; Geneva : CERN, 20 May 2003

[82] Simone Peeters, PhD thesis, NiKhef 2003.

[83] A.G. Clark *et al.*, Design and test of a prototype silicon detector module for ATLAS Semiconductor Tracker endcaps, Published in Nuclear Instruments and Methods in Physics Research Section A, Volume 538, pp 265-280 (11th Feb, 2005)

[84] Barrel Module Final Design Review, SCT-BM-FDR-1 to 9.

[85] A. Barr *et al.* Beam tests of ATLAS-SCT modules in june and august 2000. ATLAS Internal Note, ATL-INDET-2002-005.

[86] A. Barr *et al.* Beam tests of ATLAS-SCT modules in august and october 2001. ATLAS Internal Note, ATL-INDET-2002-024.

[87] M. A. Vos, J. Bernabeu, Z. Dolezal, J.E. Garcia-Navarro, P. Kodys, G.F. Moorhead, M. D'Onofrio, P. Re znicek, Charge collection with binary readout. ATLAS Internal Note, ATL-INDET-2003-011.

[88] T.J. Brodbeck *et al.* Carrier mobilities in irradiated silicon.
Proceedings of 5th Conference on Position Sensitive Detectors, London, September 1999, ROSE/TN/2000-09.

[89] L.J. Beattie *et al.* The electric field in irradiated silicon detectors. Nucl. Instrum. Meth. A 418 (1998) 314-321.

[90] G. Lindstrom F. Lemeilleur and S. Watts. Third RD48 status report. CERN-LHCC-2000-009.

[91] J. Bernabeu *et al.* Beam study of irradiated ATLAS-SCT module prototypes. Nucl. Instrum. Meth. A 485 (2002) 67–72.

[92] A. Barr *et al.* Results from an LHC-structured beamtest of SCT prototype modules ATL-INDET-2002-025; Geneva : CERN, 29 Apr 2002

[93] V. Bartsch et al. An algorithm for calculating the lorentz angle in silicon detectors. CMS IN-2001/027, 2001.

[94] V. Eremin and Z. li. Nucl. Inst. and Meth. A 362 (1995), 338.

[95] T. Lari et al. Lorentz angle variation with electric field for ATLAS silicon detectors. ATLAS Internal Note, ATL-INDET-2001-004

[96] M. Aleppo, A measurement of Lorentz angle of radiation hard pixel sensors. detectors. Nucl. Instrum. Meth. A 465 (2000) 108-111.

[97] F. Campabadal *et al.*, Beam tests of ATLAS SCT silicon strip detector modules Published in Nuclear Instruments and Methods in Physics Research Section A, Volume 538, pp 384-407 (11th Feb, 2005)

[98] M. Vos; M., D'Onofrio; J.E., Garcia-Navarro; G. F. Moorhead, A study of the tracking performance of irradiated SCT prototypes using test beam data. *ATLAS Internal Note*, ATL-INDET-2003-003.

[99] M. Vos, The ATLAS inner tracker and the detection of light supersymmetric Higgs bosons CERN-THESIS-2003-028

[100] S. Gadomski. Model of the SCT detectors and electronics for the ATLAS simulation using GEANT4. ATLAS Internal Note, ATL-SOFT-2001-005.

[101] P. Reznicek. *Test of semiconductor micro-strip detectors of ATLAS detector.* Diploma Thesis, Charles University of Prague, 2003.

Appendix A

One of the systematic uncertainties related to the tagged b-jet fraction should be arised to the uncertainty on the CDF detector simulation. It has already been shown that the b-tagging efficiency include a 0.91 ± 0.06 correction factor to account for remaining imperfections in the simulation and track reconstruction in the Monte Carlo. To evaluate the uncertainty on the secondary vertex mass distributions, we compare data and Monte Carlo performance and check their compatibility concerning quantities used in the tagging procedure. Figure A.1 shows the m_{secvtx} distributions for tagged jets in data and Monte Carlo in each single bin in jet P_T. Histograms are normalized to unity, and, within the statistical uncertainties they look compatible, although not completly overlapped.

To better disentangle real detector simulation effects from other uncertainties (as different b/c-jet content in data and Monte Carlo), the b-enriched dijet sample as described in section 4.4 has been used. A first check is performed on the transverse momentum distributions of the tracks selected with the SecVtx algorithm: such distributions are expected to be not strongly correlated to the heavy flavor content of the jet sample and differences should be arised to simulation effects. Figure A.2 shows the transverse momentum distribution for good, pass 1, pass 2 tracks and tracks effectively used for secondary vertex reconstruction in case of positive tagged jets (electron jets): the latter are those considered in the secondary vertex mass, and in this case a good agreement is observed between data and Pythia Monte Carlo.

To directly test the compatibility between data and Monte Carlo for the secondary vertex mass distributions, events with both away and electron jet tagged are considered. Monte Carlo simulation and fit results (as presented in section 4.4.1) suggest that the amount of b-jets among electron tagged jets is about 100%: comparison between data and Monte Carlo secondary vertex mass distribution is shown in figure A.3, and the agreement is good. A Kolmogorov test is performed on the two histograms, and it results in a 57% probability considering the shape.

As further cross check, figure A.4 presents the relative transverse momentum of the electron with respect to the jet axis direction: this quantity is also sensitive to the B hadron mass within the jet cone. Data and Monte Carlo distributions result as well compatible, with a Kolmogorov probability of 14%, where the result is dominated by the difference in tails due to Monte Carlo lack of statistic.

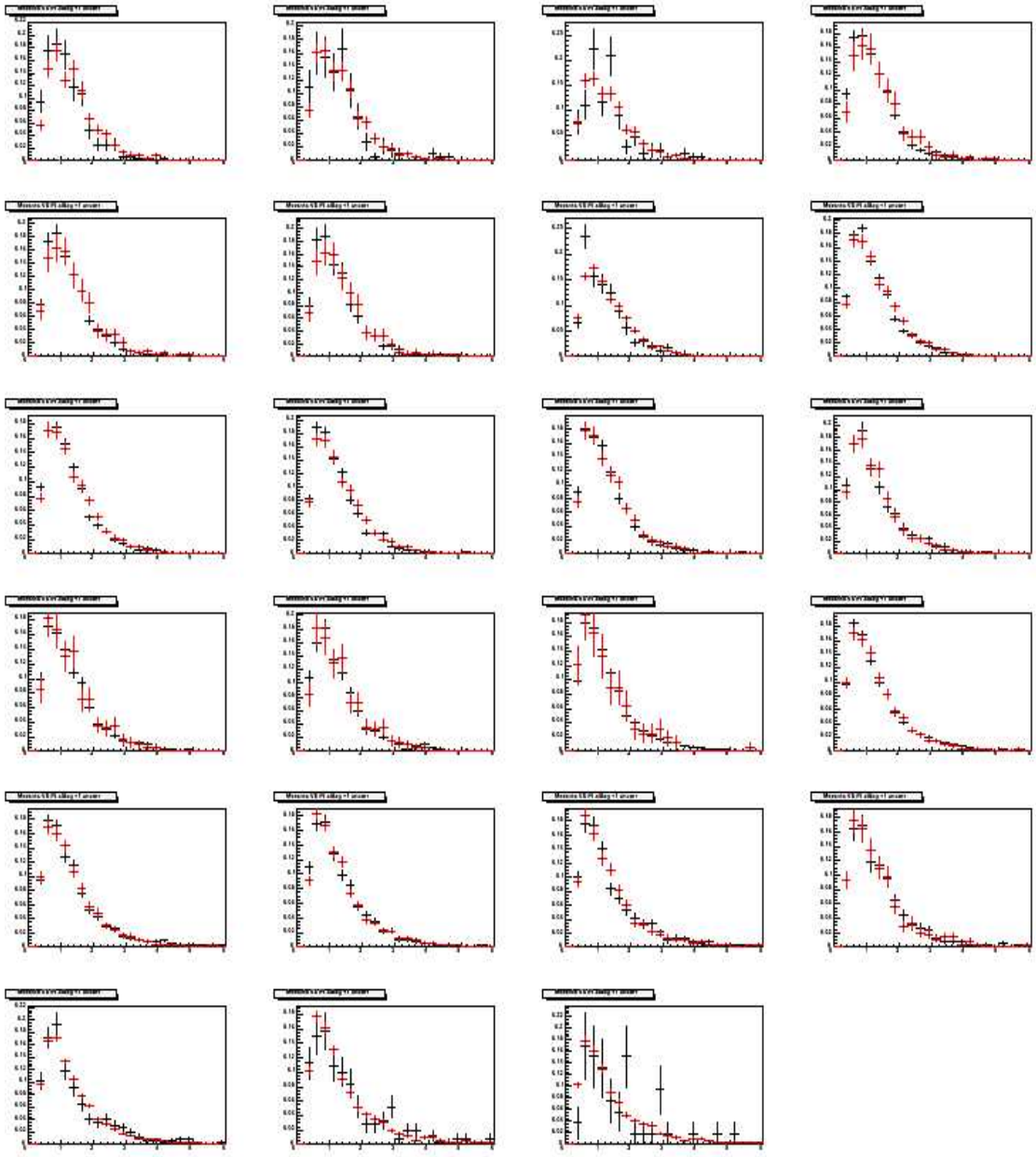

Figure A.1: Mass of secondary vertex distributions for all tagged jets for all bins in transverse momentum: data (black line) and Monte Carlo (red line) distributions are superimposed and normalized to unity.

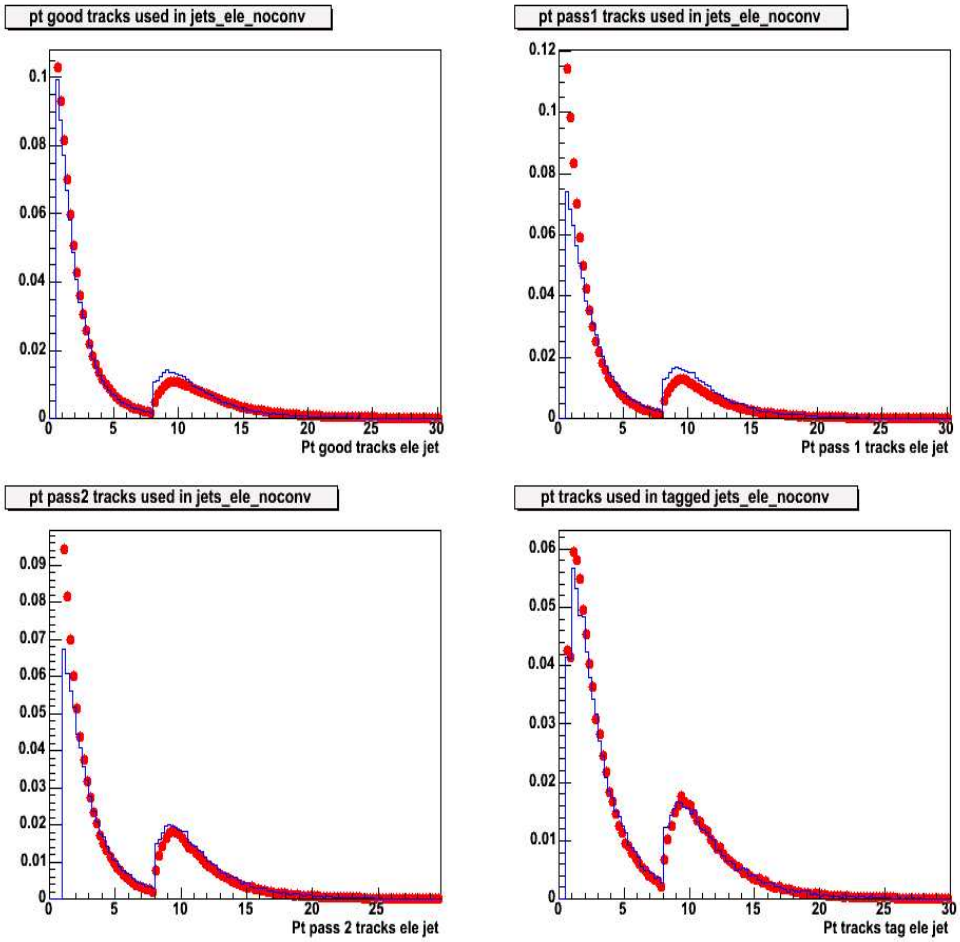

Figure A.2: Transverse momentum distribution for good, pass 1, pass 2 tracks and tracks effectively used for secondary vertex reconstruction in case of positive tagged jets (electron jets): data (red points) and Monte Carlo (blue line) are superimposed.

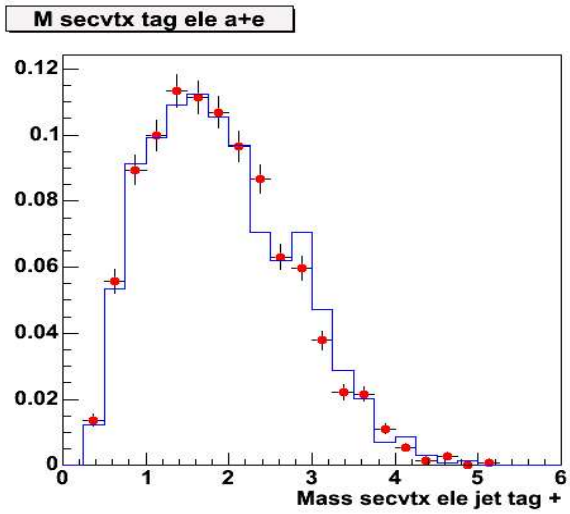

Figure A.3: Mass of secondary vertex distributions for b-tagged electron jets for double tagged events: data (red points) and Monte Carlo (blue line) distributions are normalized to unity and superimposed. Electrons from conversions are removed.

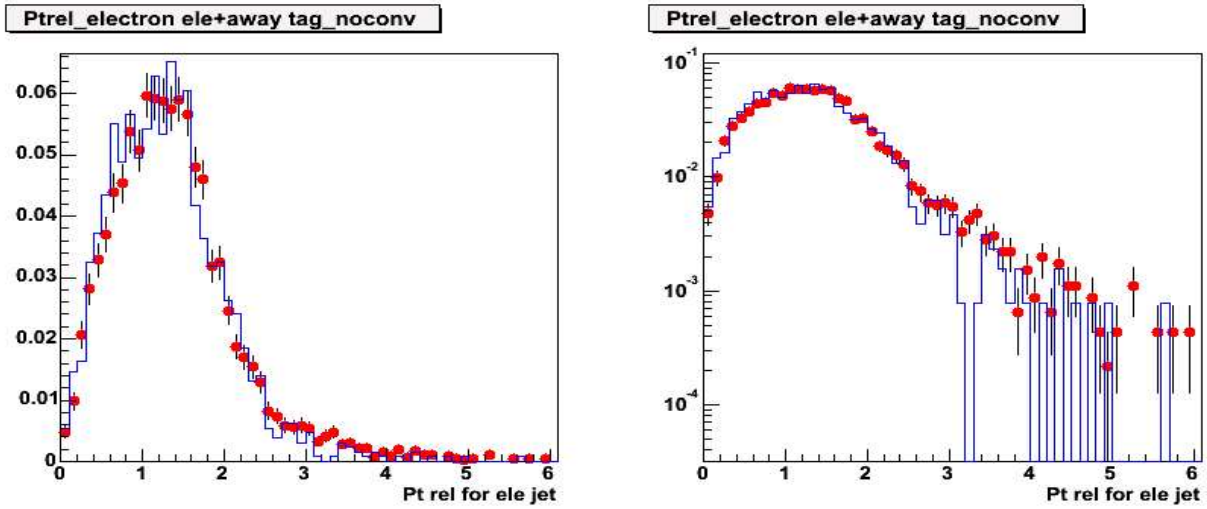

Figure A.4: Relative transverse momentum of the electron with respect to the jet axis direction (Ptrel) for b-tagged electron jets in double tagged events: again, data (red points) and Monte Carlo (blue line) distributions are normalized to unity and superimposed. Linear (left) and logarithmic (right) scale are shown. Electrons from conversions are removed.

Thank you!

When I moved to Geneva to start my PhD, in May 2001, everything was new and strange to me, I was full of fears, and if I think about it now, it sounds so far! Because during this long period I had the chance to meet wonderful people, to work in very exciting environments, to live in places that I love and I always will.... Thus, I would like to thank first of all my supervisor, Allan Clark, for offering me the opportunity to have all this, but also for the way in which he was always supportive and for the trust he had in me! If I think about the time in the SCT, special thanks should go first of all to the member of the old CERN-Geneva "mappet" KB/K5 team, Mariane Brinet, Mauro Donegá, Rainer Wallny and Heinz Pernegger with whom I spent so many days (and nights) fighting with the modules! Thanks to Didier Ferrere and Bettina Mikulec, and, of course, I cannot forget to say thank you to Harris Kagan, for the beautiful (but tiring!) discussions and also for the wonderful dinners at his place, drinking good wine after a long day spent in the clean room. In the tests beam, I had the possibility to work with a great group of people. In particular, I would really like to thank Gareth Moorhead, for his special way of being the coordinator of our team and for his great support; Marcel Vos and Jose Enrique Garcia, for their patience in answering all my questions and my very long emails; to Lars Ecklund and the Czechs, Zdenek, Pavel and Peter Kodis, for the nice collaboration during those years.

To join again CDF was great since the beginning, reminding me the first time, in 2000, I felt part of a real collaboration. First, I would like to thank the people of the Geneva-ETH group, Allan, Xin Wu, Maria Kinzle, Mario Campanelli and Gunther Dissertori for the nice discussions during our weekly meetings. In particular I really thank Mario, always very supporting, that had also the hard task, together with Mauro, to share the CERN office with me in the last years. I was very often in Fermilab, and I had the possibility to work with great people, who have helped me along the way. I still remember the first time I met Mario Martinez, one of the two QCD conveners in 2003. We discussed about the kind of analysis I would be interested in, and he mentioned the b-jet cross section: I still did not know at that time how much this would have been important for me. Thanks a lot, Mario! The whole QCD group was actually always very supportive: together with the conveners coming along during these years, Mario, Jay Dittman, Rick Field, Mary Convery and Regis Lefebre, I would like especially to thank Giuseppe Latino, Anwar Bhatti, Beate Heinemann and Ken Hatakeyama, for their help when I was learning the secrets of jet corrections, Monte Carlo and Stntuple. A great thank you goes also to Alison Lister, with whom I shared some of the efforts to cope with b-tagging, and to Tom Wright and Steve Levy, who have always given precious suggestions to understand it. Finally, I would like to thank

Michelangelo Mangano and Stefano Frixione, for their help and great support to have the unfamous theory comparison.

Some of the people I mentioned above have been (and are) not only collegues for me, but also friends, because life is not only work and work can be also fun.. Many wonderful people have surrounded me and still do, offering me support and love. I would like to thank Sonia and Peo, for being always there for me, and Cristina, Giovanni and all the CERN friends of the first years in Geneva, that taught me how to love this city. A big big kiss and thank you to Shulamit, for her trust, her wise advises and her friendship. Also, I would like to thank some of the other university fellows, to name someone, Sofia and Anna, for the coffee break+cigarette at CERN, Yann, that tried always very hard to convince me that computers are not my enemies, Chiara, Nicolas(x2) and Cyril, for the nice atmosphere we were able to create in the physics class. And, Peggy and *sur tous* Catherine, the secretaries at the University of Geneva: I think nobody could have been more patient with me and my terrible, chronicle allergy to bureaucratic things! And thanks to Alessandro, Paolo and Massimo - the BB5 guys: my last 4 months were the hardest ones, writing the thesis and coping with the analysis, but it was so much fun listening to all your adventures during lunch-time! Thanks to the fermilab friends: Janaya, since 2000, for being warm and sweet and present even when she is at 9 hours time-difference, Eva, Olga and the 'girls', for the crazy nights in downtown but also for the quiet evenings spent just talking, Zoltan (zaza the uncle), Gino and Petra and their wonderful kids, for being always as a family on this side of the ocean. But, the most, I thank Anadi (nani-nani, the aunt), the loyal friend, the one that shared (la condivisione!) with me the worse and the best moments of this last years, and the long nights before the blessing, spent in the trailers or driving on the 59.

Un grazie enorme va ai miei amici di Losanna, con cui ho speso alcuni dei momenti piú belli degli ultimi anni: Renzo e Graziano, i primi con cui ho condiviso la mia avventura svizzera, Franceschina, Saviana, Tania, Dario e tutti gli altri 'losannesi importati'; soprattutto Ilaria e Francesca, le mie streghe preferite, grazie per la vostra amicizia, per il vostro calore, per le canzoni cantate a squarciagola in macchina, e per la vostra pazzia. Grazie alle mie amiche pratesi, Francesca e Elena, per essere sempre pronte a liberarsi da tutti gli impegni appena 'la meteora' torna a casa per le classiche 20 ore totali. Ai miei vecchi compagni di universitá, gli 'amici leggeri', quelli che anche se non ti vedi per un anno sono sempre lí, ad accoglierti a braccia aperte nel momento del bisogno; soprattutto grazie a Laura, per le interminabili chiacchierate ginevrine.

E infine, alla mia meravigliosa famiglia, mamma Anna e babbo Vincenzo, Francesco, Matteo, Marco e la sua moglie Francesca e la mia bellissima nipotina Giulia, un grande, grandissimo grazie, perché senza di voi, senza il vostro sostegno, non sarei qui adesso, felice di aver costruito quello che ho. Mamma e papá, questa tesi la dedico a voi, i migliori genitori che una figlia possa chiedere.